

UNIVERSITY OF SOUTHERN QUEENSLAND



**RADIAL-BASIS-FUNCTION  
CALCULATIONS OF HEAT AND VISCOUS  
FLOWS IN MULTIPLY-CONNECTED  
DOMAINS**

A dissertation submitted by

**LÊ CAO KHOA**

B.Eng.(Hon.), Ho Chi Minh City University of Technology, VietNam, 2003

M.Eng.(Hon.), Ho Chi Minh City University of Technology, VietNam, 2005

For the award of the degree of

**Doctor of Philosophy**

February 2011

# Dedication

*To my family.*

# Certification of Dissertation

I certify that the idea, experimental work, results and analyses, software and conclusions reported in this dissertation are entirely my own effort, except where otherwise acknowledged. I also certify that the work is original and has not been previously submitted for any other award.

---

KHOA LE-CAO, Candidate

---

Date

## ENDORSEMENT

---

A/Prof. NAM MAI-DUY, Principal supervisor

---

Date

---

Prof. THANH TRAN-CONG, Co-supervisor

---

Date

---

Dr. CANH-DUNG TRAN, External supervisor (CSIRO)

---

Date

# Acknowledgments

I would like to express my deepest gratitude to A/Prof. Nam Mai-Duy and Prof. Thanh Tran-Cong, my principal supervisors, not only for their invaluable guidance throughout my research but also for their philosophical attitude which has inspired my research interest. Undoubtedly, without their continuing support and encouragement this thesis would not have been completed.

In addition, I wish to express my sincere thanks to Dr. Canh-Dung Tran for acting his role as external supervisor, and to Prof. David Buttsworth and Ms. Juanita Ryan for their kind supports.

I gratefully acknowledge the financial support provided by the University of Southern Queensland (USQ) and the Commonwealth Scientific and Industrial Research Organisation (CSIRO), including a USQ Research Excellence scholarship, a Faculty of Engineering and Surveying (FoES) scholarship supplement, a Computational Engineering and Science Research Centre (CESRC) scholarship supplement, and a CSIRO Future Manufacturing Flagship Top Up scholarship.

Finally, I would like to dedicate this work to my parents. I am greatly indebted to my family for much unconditional support, understanding and love over the years and for endlessly encouraging me in academic pursuits.

# Notes to Readers

To facilitate the reading of this thesis, a number of files are included on the attached CD to provide animation of some numerical results in this thesis. The contents of the CD include:

1. thesis.pdf: An electronic version of this thesis;
2. Chapter3-Circular-Circular-Annuli-velocity.wmv: An animation showing the evolution of velocity field of the buoyancy flow in a concentric circular-circular annulus using a Cartesian grid  $36 \times 36$  ( $Pr = 0.71, Ra = 10^4$ ) (Section 3.4.3, Chapter 3);
3. Chapter3-Square-Circular-Annuli-velocity.wmv: An animation showing the evolution of velocity field of the buoyancy flow in a concentric square-circular annulus using a Cartesian grid  $36 \times 36$  ( $Pr = 0.71, Ra = 10^5$ ) (Section 3.4.4, Chapter 3);
4. Chapter4-Rotating-cylinder.wmv: An animation showing the evolution of the flow between a rotating circular cylinder and a fixed square cylinder using a Cartesian grid  $26 \times 26$  (Section 4.5.1, Chapter 4).

# Abstract

This PhD research project is concerned with the development of accurate and efficient numerical methods, which are based on one-dimensional integrated radial basis function networks (1D-IRBFNs), point collocation and Cartesian grids, for the numerical simulation of heat and viscous flows in multiply-connected domains, and their applications to the numerical prediction of the material properties of suspensions (i.e. particulate fluids). In the proposed techniques, the employment of 1D-IRBFNs, where the RBFN approximations on each grid line are constructed through integration, provides a powerful means of representing the field variables, while the use of Cartesian grids and point collocation provides an efficient way to discretise the governing equations defined on complicated domains.

Firstly, 1D-IRBFN-based methods are developed for the simulation of heat transfer problems governed by Poisson equations in multiply-connected domains. Derivative boundary conditions are imposed in an exact manner with the help of the integration constants. Secondly, 1D-IRBFN based methods are further developed for the discretisation of the stream-function - vorticity formulation and the stream-function formulation governing the motion of a Newtonian fluid in multiply-connected domains. For the stream-function - vorticity formulation, a novel formula for obtaining a computational vorticity boundary condition on a curved boundary is proposed and successfully verified. For the stream-function formulation, double boundary conditions are implemented

without the need to use external points or to reduce the number of interior nodes for collocating the governing equations. Processes of implementing cross derivatives and deriving the stream-function values on separate boundaries are presented in detail. Thirdly, for a more efficient discretisation, 1D-IRBFNs are incorporated into the domain embedding technique. The multiply-connected domain is transformed into a simply-connected domain, which is more suitable for problems with several unconnected interior moving boundaries. Finally, 1D-IRBFN-based methods are applied to predict the bulk properties of particulate suspensions under simple shear conditions.

All simulated results using Cartesian grids of relatively coarse density agree well with other numerical results available in the literature, which indicates that the proposed discretisation schemes are useful numerical techniques for the analysis of heat and viscous flows in multiply-connected domains.

# Papers Resulting from the Research

## Journal Papers

1. N. Mai-Duy, K. Le-Cao and T. Tran-Cong (2008) A Cartesian grid technique based on one-dimensional integrated radial basis function networks for natural convection in concentric annuli, *International Journal for Numerical Methods in Fluids*, 57, p. 1709–1730.
2. K. Le-Cao, N. Mai Duy and T. Tran-Cong (2009) An effective integrated-RBFN Cartesian-grid discretisation to the stream function-vorticity-temperature formulation in non-rectangular domains, *Numerical Heat Transfer, Part B*, 55, p. 480–502.
3. K. Le-Cao, N. Mai-Duy, C.-D. Tran and T. Tran-Cong (2010) Numerical study of stream-function formulation governing flows in multiply-connected domains by integrated RBFs and Cartesian grids, *Computer & Fluids Journal*, 44(1), p. 32–42.
4. K. Le-Cao, N. Mai-Duy, C.-D. Tran and T. Tran-Cong (2010) Towards the analysis of shear suspension flows using radial basis functions, *CMES: Computer Modeling in Engineering & Sciences*, 67(3), p. 265–294.

## Conference Papers

1. K. Le-Cao, N. Mai-Duy and T. Tran-Cong (2007) Radial basis function calculations of buoyancy-driven flow in concentric and eccentric annuli. In P. Jacobs, T. McIntyre, M. Cleary, D. Buttsworth, D. Mee, R. Clements, R. Morgan and C. Lemckert (eds). *The 16th Australasian Fluid Mechanics Conference*, Gold Coast, QLD, Australia, 3-7 December. *Proceedings of The 16th Australasian Fluid Mechanics Conference* (CD), p. 659–666. The University of Queensland (ISBN 978-1-864998-94-8).
2. K. Le-Cao, C.-D. Tran, N. Mai-Duy and T. Tran-Cong (2009) Direct simulation of two-dimensional particulate shear flows using radial basis functions. In R.P. Jagadeeshan, W. Li, A. Jabbarzadeh, H. See, R. Tanner (Scientific Committee). *The 5th Australian-Korean Rheology Conference*, Sydney, NSW, Australia, 1-4/Nov/2009. Abstract Book, p. 19.
3. K. Le-Cao, N. Mai-Duy, C.-D. Tran and T. Tran-Cong (2010) A new integrated-RBF-based domain-embedding scheme for solving fluid flow problems. In N. Khalili, S. Valliappan, Q. Li and A. Russell (eds). *The 9th World Congress on Computational Mechanics and 4th Asian Pacific Congress on Computational Mechanics (WCCM/APCOM 2010)*, Sydney, Australia, 19-23/Jul/2010. *IOP Conference Series: Materials Science and Engineering*, Vol. 10, Paper No. 012021, 10 pages. IOP Publishing (ISSN 1757-899X (Online) and ISSN 1757-8981 (Print)).
4. K. Le-Cao, N. Mai-Duy, C.-D. Tran and T. Tran-Cong (2010) Integrated-RBF calculations for direct simulation of shear suspension flows. *International Conference on Computational & Experimental Engineering and Sciences (ICCES MM'10)*, Busan, South Korea, 17-21/Aug/2010. IC-CES journal. Tech Science Press (ISSN: 1933-2815 (online)) (accepted, 30/Nov/2010)
5. D. Ho-Minh, K. Le-Cao, N. Mai-Duy and T. Tran-Cong (2010) Simulation

of fluid flows at high Reynolds numbers using radial basis function networks. In G.D. Mallinson and J.E. Cater (eds). *17th Australasian Fluid Mechanics Conference*, Auckland, New Zealand, 5-9/Dec/2010. *Proceedings of 17th Australasian Fluid Mechanics Conference*, Paper No 139, 4 pages. The University of Auckland (ISBN: 978-0-86869-129-9).

# Contents

Dedication	ii
Certification of Dissertation	i
Acknowledgments	ii
Notes to Readers	iii
Abstract	iv
Published Papers Resulting from the Research	vi
Acronyms & Abbreviations	xv
List of Tables	xvi
List of Figures	xx
Chapter 1 Introduction	1

1.1	Governing equations and Discretisation methods . . . . .	2
1.1.1	Governing equations . . . . .	2
1.1.2	Discretisation methods . . . . .	5
1.1.3	Nonlinear solvers . . . . .	8
1.2	Viscous flows in multiply-connected domains . . . . .	9
1.2.1	Problem description . . . . .	9
1.2.2	Numerical simulations . . . . .	11
1.3	Motivation . . . . .	13
1.4	Outline of the Dissertation . . . . .	14

**Chapter 2 1D-integrated-RBFN calculation of heat transfer in multiply-connected domains 17**

2.1	Review of RBFN-based methods . . . . .	18
2.1.1	Conventional direct/differential approach . . . . .	19
2.1.2	Indirect/Integral approach . . . . .	22
2.2	One-dimensional IRBFN method for heat transfer in multiply-connected domains . . . . .	24
2.2.1	Mathematical formulations . . . . .	26
2.2.2	Numerical examples . . . . .	30
2.3	Concluding remarks . . . . .	40

<b>Chapter 3</b>	<b>1D-integrated-RBFN discretisation of stream-function</b>	
	<b>- vorticity (<math>\psi - \omega</math>) formulation in multiply-connected domains</b>	<b>42</b>
3.1	Introduction . . . . .	43
3.2	Governing equations . . . . .	45
3.3	The present technique . . . . .	47
3.3.1	1D-IRBFN discretisation . . . . .	47
3.3.2	A new formula for computing vorticity boundary conditions	51
3.3.3	Numerical implementation of vorticity boundary conditions	54
3.3.4	Solution procedure . . . . .	56
3.4	Numerical examples . . . . .	58
3.4.1	Example 1: Circular shape domain . . . . .	59
3.4.2	Example 2: Multiply-connected domain . . . . .	62
3.4.3	Example 3: Concentric annulus between two circular cylinders . . . . .	64
3.4.4	Example 4: Concentric annulus between a square outer cylinder and a circular inner cylinder . . . . .	72
3.5	Concluding remarks . . . . .	74
<b>Chapter 4</b>	<b>1D-integrated-RBFN discretisation of stream-function</b>	
	<b>(<math>\psi</math>) formulation in multiply-connected domains</b>	<b>78</b>
4.1	Introduction . . . . .	79

---

4.2	Governing equations . . . . .	81
4.3	Brief review of 1D-integrated RBFNs . . . . .	83
4.3.1	1D-IRBFN-4 . . . . .	83
4.3.2	1D-IRBFN-2 . . . . .	84
4.4	Proposed numerical procedure . . . . .	84
4.4.1	Boundary values for stream function . . . . .	85
4.4.2	Cross derivatives . . . . .	87
4.4.3	1D-IRBFN expressions . . . . .	89
4.4.4	Solution Procedure . . . . .	94
4.5	Numerical results . . . . .	95
4.5.1	Example 1: Steady flow between a rotating circular cylinder and a fixed square cylinder . . . . .	97
4.5.2	Example 2: Natural convection in an eccentric annulus between two circular cylinders . . . . .	100
4.5.3	Example 3: Natural convection in eccentric annuli between a square outer and a circular inner cylinder . . . . .	112
4.6	Concluding Remarks . . . . .	117

**Chapter 5 1D-integrated-RBFN-based domain embedding technique** **119**

5.1	Introduction . . . . .	120
-----	------------------------	-----

5.2 Proposed domain-embedding technique . . . . . 121

5.2.1 1D-IRBFN discretisation for extended domain . . . . . 123

5.2.2 Imposition of the boundary conditions on the inner boundaries . . . . . 126

5.3 Numerical examples . . . . . 129

5.4 Concluding remarks . . . . . 139

**Chapter 6 1D-integrated-RBFN calculation of particulate suspension flows 142**

6.1 Introduction . . . . . 143

6.2 Governing equations and sliding frames concept . . . . . 145

6.2.1 Governing equations . . . . . 145

6.2.2 Sliding bi-periodic frames concept . . . . . 149

6.3 Proposed numerical procedure . . . . . 150

6.3.1 1D-IRBFNs . . . . . 152

6.3.2 Sliding bi-periodic boundary conditions . . . . . 155

6.3.3 Boundary conditions on the particles' boundaries . . . . . 157

6.4 Numerical examples . . . . . 161

6.4.1 Example 1: Sliding bi-periodic boundary conditions . . . . . 161

6.4.2 Example 2: A rotating circular cylinder . . . . . 165

---

6.4.3	Example 3: Shear suspension flow . . . . .	168
6.5	Concluding remarks . . . . .	181
<b>Chapter 7</b>	<b>Conclusion</b>	<b>182</b>
7.1	Research contributions . . . . .	183
7.2	Suggested work . . . . .	185

# Acronyms & Abbreviations

1D-IRBFN	One-Dimensional Indirect/Integrated Radial Basis Function Network
BEM	Boundary Element Method
CFD	Computational Fluid Dynamics
DNS	Direct Numerical Simulations
DRBFN	Direct/Differentiated Radial Basis Function Network
FDM	Finite Difference Method
FEM	Finite Element Method
FVM	Finite Volume Method
IRBFN	Indirect/Integrated Radial Basis Function Network
MQ	MultiQuadric
ODE	Ordinary Differential Equation
PDE	Partial Differential Equation
SVD	Singular Value Decomposition

# List of Tables

2.1	Example 1 (boundary value problem - Dirichlet boundary condition - Case 1): Condition numbers of the IRBFN system matrix.	33
2.2	Example 2 (boundary value problem - Dirichlet and Neumann boundary conditions): Overall accuracy of the solution $T$ by the present technique. Condition numbers of the IRBFN system matrix are also included. . . . .	37
2.3	Example 3 (initial-value problem): Relative $L_2$ errors of the solution (grid of $32 \times 32$ ). It is noted that $a(b)$ represents $a \times 10^b$ .	39
2.4	Example 3 (initial-value problem): Relative $L_2$ errors of the solution (grid of $52 \times 52$ ). It is noted that $a(b)$ represents $a \times 10^b$ .	40
3.1	Example 1( circular shape domain): Errors by 1D-IRBFN-2s (Scheme 1) and 1D-IRBFN-4s (Scheme 2) in the computation of second derivatives of $\psi$ at the boundary points. It is noted that $a(b)$ represents $a \times 10^b$ . . . . .	62

3.2	Example 1 (circular shape domain): Overall accuracy of the solution $\psi$ by the present technique employed with two different computational vorticity boundary schemes, namely Scheme 1 (1D-IRBFN-2s) and Scheme 2 (1D-IRBFN-4s). Condition numbers of the IRBFN system matrix are also included. It is noted that $h$ is the spacing (grid size) and $a(b)$ represents $a \times 10^b$ . . . . .	63
3.3	Example 2 (multiply-connected domain): Condition numbers of the system matrix and relative $L_2$ errors of the solution. It is noted that $h$ is the spacing (grid size) and $a(b)$ represents $a \times 10^b$ . . . . .	64
3.4	Example 3 (circular - circular cylinders): Condition numbers of the 1D-IRBFN system matrix by the two formulations. . . . .	67
3.5	Example 3 (circular - circular cylinders): Comparison of the average equivalent conductivity on the inner and outer cylinders, $k_{eqi}$ and $k_{eqo}$ , between the present IRBFN technique using a grid of $52 \times 52$ and some other techniques for $Ra$ in the range of $10^2$ to $7 \times 10^4$ . $KG$ stands for Kuehn and Goldstein . . . . .	69
3.6	Example 4 (square-circular cylinders): Comparison of the average Nusselt number on the outer and inner cylinders, $Nu_o$ and $Nu_i$ , for $Ra$ from $10^4$ to $10^6$ between the present technique (grid $52 \times 52$ ) and some other techniques. . . . .	73
4.1	Example 1 (rotating cylinder): Comparison of the stream-function values at the inner cylinder, $\psi_w$ , for $Re$ from 1 to 1000 between the present technique (grid of $52 \times 52$ ) and finite difference technique. . . . .	98
4.2	Condition numbers of the RBFN matrices associated with the harmonic and biharmonic operators. . . . .	104

- 
- 4.3 Example 2 (symmetric flow, concentric circular-circular annuli):  
Convergence of  $\bar{k}_{eq}$  with grid refinement for the flow at  $Ra = 10^2$ . 104
- 4.4 Example 2 (symmetric flow, concentric circular-circular annuli):  
Convergence of  $\bar{k}_{eq}$  with grid refinement for the flow at  $Ra = 10^3$ . 105
- 4.5 Example 2 (symmetric flow, concentric circular-circular annuli):  
Convergence of  $\bar{k}_{eq}$  with grid refinement for the flow at  $Ra = 3 \times 10^3$ . 105
- 4.6 Example 2 (symmetric flow, concentric circular-circular annuli):  
Convergence of  $\bar{k}_{eq}$  with grid refinement for the flow at  $Ra = 6 \times 10^3$ . 106
- 4.7 Example 2 (symmetric flow, concentric circular-circular annuli):  
Convergence of  $\bar{k}_{eq}$  with grid refinement for the flow at  $Ra = 10^4$ . 106
- 4.8 Example 2 (symmetric flow, concentric circular-circular annuli):  
Convergence of  $\bar{k}_{eq}$  with grid refinement for the flow at  $Ra = 5 \times 10^4$ . 107
- 4.9 Example 2 (symmetric flow, concentric circular-circular annuli):  
Convergence of  $\bar{k}_{eq}$  with grid refinement for the flow at  $Ra = 7 \times 10^4$ . 107
- 4.10 Example 2 (symmetric flow, eccentric circular-circular annuli):  
Comparison of the maximum stream-function values,  $\psi_{max}$ , for two special cases  $\varphi = \{-90^0, 90^0\}$  between the present technique and DQM technique. . . . . 109
- 4.11 Example 2 (unsymmetrical flow, eccentric circular-circular annuli): Comparison of the stream-function values at the inner cylinders,  $\psi_w$ , for  $\varepsilon = \{0.25, 0.5, 0.75, 0.95\}$  and  $\varphi = \{-45^0, 0^0, 45^0\}$  between the present, DQM and DFD techniques. . . . . 109

4.12	Example 3 (symmetric flow, eccentric square-circular annuli): Comparison of the maximum stream-function values, $\psi_{max}$ , for special cases $\varphi = \{-90^0, 90^0\}$ between the present technique and MQ-DQ technique. . . . .	113
4.13	Example 3 (concentric square-circular annuli): Comparison of the average Nusselt number on the outer and inner cylinders, $Nu_o$ and $Nu_i$ , for $Ra$ from $10^4$ to $10^6$ between the present technique (grid of $62 \times 62$ ) and some other techniques. . . . .	113
4.14	Example 3 (unsymmetrical flow, eccentric square-circular annuli): Comparison of the maximum stream-function values, $\psi_{max}$ , for $\varepsilon = \{0.25, 0.5, 0.75, 0.95\}$ and $\varphi = \{-45^0, 0^0, 45^0\}$ between the present technique and MQ-DQ technique. . . . .	114
5.1	Example 1 (boundary-value problem - Case 1): Errors of the solution and condition numbers of the system matrix. . . . .	133
5.2	Example 3 (initial-value problem): Errors of $f$ with $k = 2$ and $k = 3$ by Scheme 1 and Scheme 2 using grid of $40 \times 40$ . It is noted that $a(b)$ represents $a \times 10^b$ . . . . .	140
6.1	Example 1 (sliding bi-periodic boundary conditions): Errors of the solution and condition numbers of the system matrix denoted by $\text{Cond}(A)$ . It is noted that $h$ is the spacing (grid size). . . . .	163
6.2	Example 2 (rotating cylinder): Comparison of the stream-function value at the inner cylinder, $\psi_{wall}$ , between the present technique (grid of $36 \times 36$ ) and finite difference technique for several values of $Re$ . . . . .	167

# List of Figures

1.1	A typical multiply-connected domain . . . . .	9
1.2	A typical boundary fitted mesh . . . . .	11
1.3	A typical domain embedding mesh . . . . .	12
2.1	Differential (left) and Integral (right) approaches . . . . .	22
2.2	1D-IRBFN discretisation and a typical grid line. Points on the grid line consist of interior nodal points $x_i$ ( $\circ$ ) and boundary points $x_{bi}$ ( $\square$ ). . . . .	25
2.3	Example 1 (boundary value problem - Dirichlet boundary condition): Domain of interest and its typical discretisation. Two holes are of circular shapes with the same radius 0.2. The coordinates of the hole centres are $(-0.4, 0.3)$ and $(0.2; -0.3)$ . It is noted that the nodes outside the domain are removed. . . . .	32
2.4	Example 1 (boundary value problem - Dirichlet boundary condition - Case 1): Profile of the approximate solution using a grid of $42 \times 42$ . . . . .	34

---

2.5	Example 1 (boundary value problem - Dirichlet boundary condition - Case 1): Convergence behaviour of the approximate solution with grid refinement. . . . .	35
2.6	Example 1 (boundary value problem - Dirichlet boundary condition - Case 2): A contour plot of $T$ by the 1D-IRBFN method using a grid of $42 \times 42$ (top) and FEM (bottom). . . . .	36
2.7	Example 2 (boundary value problem - Dirichlet and Neumann boundary conditions): Domain of interest and its typical discretisation. It is noted that the nodes outside the domain are removed. . . . .	38
2.8	Example 2 (boundary value problem - Dirichlet and Neumann boundary conditions): Approximate solution using a grid of $42 \times 42$ . This plot contains 21 contour lines whose levels vary linearly from the minimum to maximum values . . . . .	39
2.9	Example 3 (initial-value problem): 1D-IRBFN solution for four values of $k$ at $t = 1$ using a grid of $32 \times 32$ . . . . .	41
3.1	Points on a grid line consist of interior points $x_i$ ( $\circ$ ) and boundary points $x_{bi}$ ( $\square$ ). . . . .	48
3.2	A curved boundary. . . . .	52
3.3	Example 1: Domain of interest and its typical discretisation. It is noted that the nodes outside the domain are removed. . . . .	60
3.4	Example 1 (circular shape domain): Exact solution. It is noted that the exact solution is plotted over the square covering the problem domain. . . . .	61

3.5	Example 2: Multiply-connected domain and its typical discretisation. It is noted that the nodes outside the domain are removed.	65
3.6	Example 2 (multiply-connected domain): Exact solution. It is noted that the exact solution is plotted over the square covering the problem domain.	66
3.7	Computational domains and discretisations: Annulus between two circular cylinders (a) and annulus between inner circular cylinder and outer square cylinder (b).	67
3.8	Example 3 (circular-circular cylinders): Convergence of the temperature (left) and stream-function (right) fields with respect to grid refinement for the flow at $Ra = 10^4$ .	70
3.9	Example 3 (circular-circular cylinders): Convergence of the temperature (left) and stream-function (right) fields with respect to grid refinement for the flow at $Ra = 7 \times 10^4$ .	71
3.10	Example 4 (square-circular cylinders): Iterative convergence. Time steps used are 0.002 for $Ra = 10^4$ , 0.005 for $Ra = 5 \times 10^4$ , and 0.008 for $Ra = \{10^5, 5 \times 10^5, 10^6\}$ . The values of CM become less than $10^{-12}$ when the numbers of iterations reach 10925, 9740, 8609, 15017, and 17938 for $Ra = \{10^4, 5 \times 10^4, 10^5, 5 \times 10^5, 10^6\}$ , respectively. Using the last point on the curves as a positional indicator, from left to right the curves correspond to $Ra = \{10^4, 5 \times 10^4, 10^5, 5 \times 10^5, 10^6\}$ .	75
3.11	Example 4 (square-circular cylinders): Convergence of the temperature (left) and stream-function (right) fields with respect to grid refinement for the flow at $Ra = 5 \times 10^5$ .	76

3.12	Example 4 (square-circular cylinders): Convergence of the temperature (left) and stream-function (right) fields with respect to grid refinement for the flow at $Ra = 10^6$ . . . . .	77
4.1	A curved boundary. . . . .	88
4.2	Points on a grid line consist of interior points $x_i$ ( $\circ$ ) and boundary points $x_{bi}$ ( $\square$ ). . . . .	89
4.3	Example 1 (rotating cylinder): geometry (top) and discretisation (bottom). . . . .	96
4.4	Example 1 (rotating cylinder, $R=0.25$ , $L=1$ ): Velocity field (left) and vorticity field (right) for the flow at $Re = 1$ and $Re = 700$ . . . . .	99
4.5	Example 2 (eccentric circular-circular annulus): geometry. . . . .	100
4.6	Schematic spatial discretisations for an annulus between two circular cylinders (a) and an annulus between inner circular and outer square cylinders (b). . . . .	101
4.7	Example 2 (circular-circular annulus): $61 \times 61$ , decoupled approach, iterative convergence. Time steps used are 0.5 for $Ra = \{10^2, 10^3, 3 \times 10^3\}$ , 0.1 for $Ra = \{6 \times 10^3, 10^4\}$ , and 0.05 for $Ra = \{5 \times 10^4, 7 \times 10^4\}$ . The values of CM become less than $10^{-12}$ when the numbers of iterations reach 58, 154, 224, 1276, 1541, 5711 and 5867 for $Ra = \{10^2, 10^3, 3 \times 10^3, 6 \times 10^3, 10^4, 5 \times 10^4, 7 \times 10^4\}$ , respectively. Using the last point on the curves as a positional indicator, from left to right the curves correspond to $Ra = \{10^2, 10^3, 3 \times 10^3, 6 \times 10^3, 10^4, 5 \times 10^4, 7 \times 10^4\}$ . . . . .	103
4.8	Example 2 (concentric circular-circular annulus): Local equivalent conductivities for $Ra = 10^3$ by 1D-IRBFN and FDM. . . . .	108

- 
- 4.9 Example 2 (concentric circular-circular annulus): Local equivalent conductivities for  $Ra = 5 \times 10^4$  by 1D-IRBFN and FDM. . . . . 108
- 4.10 Example 2 (concentric circular-circular annulus): Contour plots of temperature (left) and stream function (right) for four different Rayleigh numbers using a grid of  $51 \times 51$ . Each plot contains 21 contour lines whose levels vary linearly from the minimum to maximum values. . . . . 110
- 4.11 Example 2 (eccentric circular-circular annuli): Contour plots for the temperature (left) and stream-function (right) fields for several values of eccentricity  $\varepsilon$  and angular directions  $\varphi$  for the flow at  $Ra = 1 \times 10^4$ . Each plot contains 21 contour lines whose levels vary linearly from the minimum to maximum values. . . . . 111
- 4.12 Example 3 (eccentric square-circular domain): geometry. . . . . 112
- 4.13 Example 3 (concentric square-circular annulus): Contour plots of temperature (left) and stream function (right) for four different Rayleigh numbers using a grid of  $61 \times 61$ . Each plot contains 21 contour lines whose levels vary linearly from the minimum to maximum values. . . . . 115
- 4.14 Example 3 (eccentric square-circular annulus): the effects of time-step length on convergence behaviour. . . . . 117
- 4.15 Example 3 (eccentric square-circular annuli): The temperature (left) and stream-function (right) fields for several values of eccentricity  $\varepsilon$  and angular direction  $\varphi$  for the flow at  $Ra = 3 \times 10^5$ . Each plot contains 21 contour lines whose levels vary linearly from the minimum to maximum values. . . . . 118

5.1	A multiply-connected domain. Its extension is a rectangular domain that is represented by a Cartesian discretisation. . . . .	122
5.2	Points on a grid line consist of interior points $x_i$ ( $\circ$ ) and boundary points $x_{bi}$ ( $\square$ ). . . . .	127
5.3	Example 1 (boundary-value problem): Domain of interest and a typical discretisation . . . . .	131
5.4	Example 1 (boundary-value problem - Case 1): A plot of the approximate solution using a grid of $42 \times 42$ . . . . .	132
5.5	Example 1 (boundary-value problem - Case 2): A contour plot of $f_r$ by the 1D-IRBFN method using grid of $40 \times 40$ (top) and FEM (bottom). . . . .	134
5.6	Example 2 (boundary value problem): Discretisation by the present 1D-IRBFN method (top) and FEM (bottom) . . . . .	135
5.7	Example 2 (boundary value problem): A contour plot of $f_r$ by the present 1D-IRBFN method using grid of $80 \times 80$ (top) and FEM (bottom) . . . . .	137
5.8	Example 3 (initial-value problem): Domain of interest and a typical discretisation . . . . .	138
5.9	Example 3 (initial-value problem): Plots of the approximate solution for two values of $k$ using a grid of $40 \times 40$ . . . . .	141
6.1	A particle-fluid system . . . . .	143
6.2	Shear bi-periodic frames. . . . .	147
6.3	A reference frame and its typical Cartesian-grid discretisation. . . . .	151

---

6.4	Nodal points on a grid line consisting of interior points $x_i$ ( $\circ$ ) and boundary points $x_{bi}$ ( $\square$ ). . . . .	151
6.5	A curved boundary of the particle: arclength, and unit normal and tangential vectors. . . . .	158
6.6	Example 1 (sliding bi-periodic boundary conditions): Contour plots of the approximate and exact solutions at different time values. The two plots are indistinguishable. . . . .	164
6.7	Example 2 (rotating cylinder): geometry. . . . .	165
6.8	Example 2 (rotating cylinder): Velocity vector field (left) and vorticity field (right) for the flow at $Re = 100, 200$ and $500$ . . . .	166
6.9	Example 3 (shear suspension): A reference frame (top) and its discretisation (bottom). . . . .	169
6.10	Example 3 (shear suspension): Problem description with two instances during a period of shearing. . . . .	172
6.11	Example 3 (shear suspension): Profile of the angular velocity over the period $K$ . . . . .	173
6.12	Example 3 (shear suspension): Streamlines and iso-vorticity lines at the shear time of 0 and 0.3. . . . .	175
6.13	Example 3 (shear suspension): Variations of the bulk shear stresses over the period $K$ . . . . .	178
6.14	Example 3 (shear suspension): Variations of the bulk normal stress difference over the period $K$ . . . . .	179

---

6.15 Example 3 (shear suspension): Computed bulk viscosity. Analytic results for the dilute case are also included. . . . .	180
---	-----

# Chapter 1

## Introduction

This chapter starts with an overview of the Navier-Stokes equations and conventional numerical methods. A review of the numerical study of viscous flows in multiply connected domains and the motivation for the present study are then presented. Finally, the structure of the dissertation is outlined.

## 1.1 Governing equations and Discretisation methods

### 1.1.1 Governing equations

Computational Fluid Dynamics (CFD) is concerned with the numerical study of the motion of a fluid. The laws of mass and momentum conservation for an incompressible fluid lead to

$$\nabla \cdot \mathbf{u} = 0, \quad (1.1)$$

$$\rho_f \frac{D\mathbf{u}}{Dt} = \rho_f \mathbf{f} + \nabla \cdot \boldsymbol{\sigma}, \quad (1.2)$$

where  $\mathbf{u}$  is the velocity vector,  $\rho_f$  the fluid density,  $\mathbf{f}$  the body force vector per unit mass (e.g. gravitational acceleration),  $\boldsymbol{\sigma}$  the total stress tensor, and  $D[\cdot]/Dt$  the material derivative defined as

$$\frac{D[\cdot]}{Dt} = \frac{\partial[\cdot]}{\partial t} + (\mathbf{u} \cdot \nabla)[\cdot]. \quad (1.3)$$

For an incompressible fluid, e.g. Oldroyd-B, the stress tensor can be decomposed into

$$\boldsymbol{\sigma} = -p\mathbf{1} + 2\eta_1\mathbf{D} + \boldsymbol{\tau}_p, \quad (1.4)$$

where  $p$  is the hydrodynamic pressure,  $\mathbf{1}$  the unit tensor,  $\eta_1$  the solvent viscosity,  $\mathbf{D}$  the strain rate tensor

$$\mathbf{D} = \frac{1}{2}[\nabla\mathbf{u} + (\nabla\mathbf{u})^T]; \quad (1.5)$$

and  $\boldsymbol{\tau}_p$  the polymer-contributed stress tensor

$$\lambda \left( \frac{D\boldsymbol{\tau}_p}{Dt} - \nabla \mathbf{u}^T \cdot \boldsymbol{\tau}_p - \boldsymbol{\tau}_p \cdot \nabla \mathbf{u} \right) + \boldsymbol{\tau}_p = 2\eta_2 \mathbf{D}. \quad (1.6)$$

In (1.6),  $\lambda$  is the relaxation time and  $\eta_2$  the polymer-contributed viscosity. When  $\lambda = 0$ , the Oldroyd-B model reduces to the Newtonian model with the viscosity  $\eta$  being  $\eta = \eta_1 + \eta_2$ .

In this research project, we consider the motion of a Newtonian fluid ( $\lambda = 0$ ) in two dimensions. The stress-tensor equation (1.4) simply becomes functions of the velocity and pressure variables and one can write the governing equations (Navier-Stokes) in the following dimensionless forms.

### Velocity and pressure ( $\mathbf{u} - p$ ) formulation

$$\frac{\partial u}{\partial x} + \frac{\partial v}{\partial y} = 0, \quad (1.7)$$

$$\frac{\partial u}{\partial t} + u \frac{\partial u}{\partial x} + v \frac{\partial u}{\partial y} = -\frac{\partial p}{\partial x} + \frac{1}{Re} \left( \frac{\partial^2 u}{\partial x^2} + \frac{\partial^2 u}{\partial y^2} \right), \quad (1.8)$$

$$\frac{\partial v}{\partial t} + u \frac{\partial v}{\partial x} + v \frac{\partial v}{\partial y} = -\frac{\partial p}{\partial y} + \frac{1}{Re} \left( \frac{\partial^2 v}{\partial x^2} + \frac{\partial^2 v}{\partial y^2} \right), \quad (1.9)$$

where  $u$  and  $v$  are the velocity components,  $p$  the dynamic pressure, and  $Re$  the Reynolds number defined as  $Re = UL/\nu$  in which  $\nu$  is the kinematic viscosity,  $L$  a characteristic length, and  $U$  a characteristic velocity.

The velocities and pressure are regarded as the primitive variables. Since there is no transport equation for the pressure in (1.7)-(1.9), velocity equations (1.8)-(1.9) need be solved iteratively towards the satisfaction of the continuity condition (1.7). Several implementations were reported, including the semi-implicit method for pressure-linked equations (SIMPLE) (e.g. Patankar and Spalding, 1972), the pressure-implicit with splitting of operators (PISO)(e.g. Issa, 1986)

and the fractional step (FS) method (e.g. Le and Moin, 1991).

### Stream-function and vorticity ( $\psi - \omega$ ) formulation

By introducing two new variables, namely the stream function ( $\psi$ ) and the vorticity ( $\omega$ ),

$$\begin{aligned} u &= \frac{\partial \psi}{\partial y}, & v &= -\frac{\partial \psi}{\partial x}, \\ \omega &= \frac{\partial u}{\partial y} - \frac{\partial v}{\partial x}, \end{aligned} \tag{1.10}$$

the primitive variable form, (1.7)-(1.9), reduces to

$$\frac{\partial^2 \psi}{\partial x^2} + \frac{\partial^2 \psi}{\partial y^2} = \omega, \tag{1.11}$$

$$\frac{\partial \omega}{\partial t} + \frac{\partial \psi}{\partial y} \frac{\partial \omega}{\partial x} - \frac{\partial \psi}{\partial x} \frac{\partial \omega}{\partial y} = \frac{1}{Re} \left( \frac{\partial^2 \omega}{\partial x^2} + \frac{\partial^2 \omega}{\partial y^2} \right). \tag{1.12}$$

In comparison with the  $\mathbf{u} - p$  formulation, the continuity equation is satisfied automatically and the number of the field equations is reduced to two.

The given velocity boundary conditions can be transformed into two boundary conditions on the stream function and its normal derivative

$$\psi = \gamma, \quad \frac{\partial \psi}{\partial n} = \xi,$$

where  $n$  is the direction normal to the boundary, and  $\gamma$  and  $\xi$  prescribed functions. It can be seen that boundary conditions are over-prescribed for (1.11) and under-prescribed for (1.12). In practice, the boundary condition on  $\psi$  is used for solving (1.11), while the boundary condition on  $\partial \psi / \partial n$  is employed to derive a computational vorticity boundary condition for solving (1.12).

### Stream-function ( $\psi$ ) formulation

This formulation is obtained by substituting (1.11) into (1.12)

$$\begin{aligned} \frac{\partial}{\partial t} \left( \frac{\partial^2 \psi}{\partial x^2} + \frac{\partial^2 \psi}{\partial y^2} \right) + \frac{\partial \psi}{\partial y} \left( \frac{\partial^3 \psi}{\partial x^3} + \frac{\partial^3 \psi}{\partial x \partial y^2} \right) - \frac{\partial \psi}{\partial x} \left( \frac{\partial^3 \psi}{\partial x^2 \partial y} + \frac{\partial^3 \psi}{\partial y^3} \right) = \\ \frac{1}{Re} \left( \frac{\partial^4 \psi}{\partial x^4} + 2 \frac{\partial^4 \psi}{\partial x^2 \partial y^2} + \frac{\partial^4 \psi}{\partial y^4} \right). \end{aligned} \quad (1.13)$$

The number of the field equations is further reduced to one. As a result, the dimension of the set of resultant algebraic equations is only one half of that by the  $\psi - \omega$  formulation and only one third of that by the primitive variable formulation. Solutions to the  $\psi$  formulation generally converge faster than those to the  $\psi - \omega$  formulation. However, its numerical difficulties lie in the approximation of higher-order derivatives including cross/mixed ones, and the treatment of double boundary conditions.

It is noted that the advantages of the  $\psi - \omega$  formulation and the  $\psi$  formulation, which are mentioned above, are restricted to two-dimensional (2D) problems only.

#### 1.1.2 Discretisation methods

Principal techniques for the discretisation of (1.7)-(1.9), (1.11)-(1.12) and (1.13) can be classified into two groups, namely high-order and low-order.

Low-order discretisation methods, which are widely based on constant and linear interpolants, include finite difference methods (FDMs) (e.g. Harlow and Welch, 1965; Lewis, 1979; Sugiyama et al., 2011), finite element methods (FEMs) (e.g. Hu, 1996; Sammouda et al., 1999; Glowinski, 2008), finite volume methods (FVMs) (e.g. Demirdzic and Peric, 1990; Udaykumar et al., 2001), and boundary element methods (BEMs) (e.g. Kitagawa et al., 1988; Tran-Cong and Phan-Thien, 1989; Beskos, 1997). Each method has some advantages over the others

in certain classes of problems. In FDMs, the computational domain needs be a rectangular one that is usually represented by a uniform grid. In the case of irregular domains, there might be exist suitable coordinate transformations to achieve a rectangular computational domain and the governing equations are then transformed into new forms that are usually more complicated. Derivative terms in the governing equations are simply replaced with equivalent approximate finite-difference expressions based on truncated Taylor series. The methods have been applied to solve fluid mechanics problems (e.g. Lewis, 1979; Noye and Tan, 1989; Prasad et al., 2011). However, because of their domain-shape restrictions and large truncation errors, FDMs still have their limitations in dealing with practical problems. In contrast, FEMs, FVMs, and BEMs, which involve some sorts of integration, are capable of handling irregular geometries directly. In FEMs and FVMs, the problem domain is divided into a finite number of non-overlapping small sub-domains identified as elements or control volumes, i.e. a mesh. The field variables are sought in the form of piecewise continuous polynomials defined over elements. For fluid mechanics problems, FVMs are seen to be more attractive than FEMs. In BEMs, the governing equations are converted into equivalent boundary integral equations. The methods may require the discretisation on the boundaries (lines/surfaces) of the domain only. FVMs, FEMs, and BEMs have achieved a lot of success in solving engineering and science problems (Hortmann et al., 1990; Feng et al., 1994a,b; Manzari, 1999; Sahin and Wilson, 2007; etc.). However, the task of generating a mesh is still difficult, especially for 3D problems or even for 2D problems with complex geometries. In addition, a very dense mesh is generally needed to deal with flows with fine structure in practice (Peyret, 2002).

High-order discretisation methods include spectral methods (e.g. Fornberg, 1998; Peyret, 2002), differential quadrature methods (e.g. Shu and Richards, 1992; Bert and Malik, 1996), and radial basis function network (RBFN) based methods (e.g. Kansa, 1990a; Power and Barraco, 2002; Power et al., 2007; Šarler, 2005, 2009; Šarler et al., 2010; Divo and Kassab, 2007, 2008; Kosec and

Šarler, 2008a,b; Mai-Duy and Tran-Cong, 2001a). These methods are capable of providing accurate simulations for highly nonlinear problems such as buoyancy flows with very thin boundary layers using relatively coarse grids/meshes. In spectral methods, the computational domain also needs to be a rectangular one that is represented by a non-uniform grid. The field variables are sought in the form of truncated Fourier series for periodic problems and Chebyshev polynomials for non-periodic problems (Peyret, 2002). Spectral solutions to problems in fluid dynamics were given in, for instance, (Ghosh et al., 1993; Paik et al., 1994; Peyret, 2002). In RBFN-based methods, the computational domains can be of complex geometries. A network of radial basis functions is used as an interpolant to represent the solution field over a set of data sites that are randomly or uniformly distributed. In order to avoid the problem of reduced convergence rates caused by differentiation, the integral collocation formulation was proposed in (Mai-Duy and Tran-Cong, 2001a). For the integral formulation, highest-order derivatives of the field variable in the partial differential equation (PDE) are decomposed into RBFNs and these RBFNs are then integrated to obtain expressions for its lower-order derivatives and the variable itself (integrated RBFNs (IRBFN)). In (Mai-Duy and Tran-Cong, 2007), IRBFNs were employed on each grid line (1D-IRBFNs) to solve second-order elliptic PDEs. The 1D-IRBFN approximations at a grid node involve only points that lie on the grid lines intersecting at that point rather than the whole set of nodes, leading to a significant improvement in the matrix condition and computational effort. RBFN-based methods are further described in Chapter 2. High-order methods are capable of producing a solution that can converge at a high rate with respect to grid/mesh refinement. However, their matrix is not as sparse as those generated by low-order methods.

### 1.1.3 Nonlinear solvers

The discretisation of (1.7)-(1.9), (1.11)-(1.12) and (1.13) leads to a set of nonlinear algebraic equations because of the presence of the advection/convection terms. In the present project, we only consider the steady state of flows. There are two basic approaches to handle this nonlinearity, namely a steady-state solution approach and a time marching approach (Roache, 1998). Each approach has its own particular strengths.

#### A steady-state solution approach

All time derivative terms in the transport equations are dropped out. Two iterative techniques, namely the Picard iteration (Layton and Lenferink, 1995) and the Newton iteration (Lan, 1994), are widely employed. The former is known to be simpler but converge slower than the latter. It is noted that, in the context of Newton iteration, the trust region dogleg techniques (Conn et al., 2000) are capable of handling the cases where the starting point is far from the solution and the Jacobian matrix is close to singular.

#### A time marching approach

Time derivative terms are widely discretised by means of finite difference. The diffusion and advection terms can be treated implicitly or explicitly. In practice, first-order accurate finite-difference schemes are usually employed to handle the variation of the solution with time. At time  $t = 0$ , one needs to guess the initial values of the field variables, e.g. using a lower- $Re$  solution. In the case of  $Re = 0$ , the initial solution can simply be set to zeros. The solution will then be updated until a steady state is reached.

## 1.2 Viscous flows in multiply-connected domains

### 1.2.1 Problem description

In this thesis, we consider viscous flows in multiply-connected domains. Figure 1.1 shows a typical domain,  $\Pi$ , of rectangular shape with sides  $\{\Gamma_1, \Gamma_2, \Gamma_3, \Gamma_4\}$  and several holes of circular shape. Let  $H_i$  and  $\partial H_i$  be the region of the  $i$ th hole and its boundary, respectively, where  $i = \{1, \dots, N\}$  in which  $N$  is the number of holes. Flows in multiply-connected domains occur in many applications from

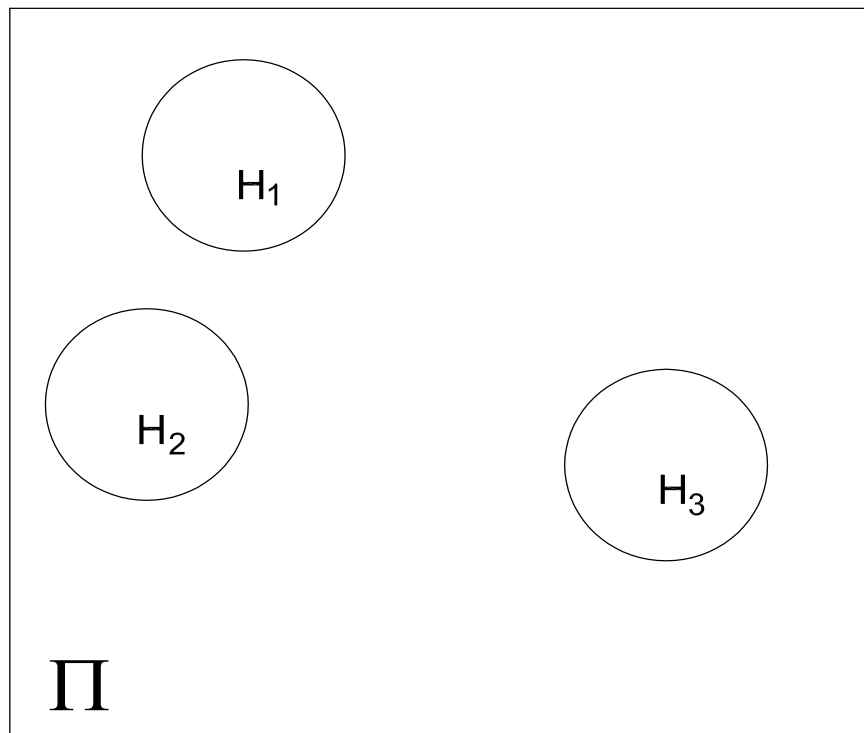


Figure 1.1: A typical multiply-connected domain

industry to biology, such as thermal conductivity for porous materials, natural convection, cooling system, particulate suspension, transport of red blood cells in a vessel, etc. Numerical simulation of such flows faces a lot of numerical difficulties, particularly for the task of generating a mesh (Maury, 2001). Problems to be studied in the project include natural convection flows and particulate

flows.

Natural convection is of great interest in many fields of science and engineering such as meteorology, nuclear reactors and solar energy systems. The problem has been extensively studied by both experimental and numerical simulations. The latter was conducted with a variety of numerical techniques such as finite-difference methods (FDMs) (e.g. Kuehn and Goldstein, 1976; de Vahl Davis, 1983), finite-element methods (FEMs) (e.g. Manzari, 1999; Sammouda et al., 1999), finite-volume methods (FVMs) (e.g. Glakpe et al., 1986; Kaminski and Prakash, 1986), boundary-element methods (BEMs) (e.g. Kitagawa et al., 1988; Hribersek and Skerget, 1999), RBFN-based methods (e.g. Šarler et al., 2004; Divo and Kassab, 2008; Kosec and Šarler, 2008b; Ho-Minh et al., 2009; Mai-Duy and Tran-Cong, 2001b; Mai-Duy et al., 2008) and spectral techniques (e.g. LeQuéré, 1991; Shu, 1999).

Particulate suspensions, which involve transport of rigid particles suspended in a fluid medium, occur in many industrial processes such as slurries, colloids and fluidised beds. There is a need for the numerical prediction of the macroscopic rheological properties of these multiphase materials from their microstructure parameters. Various numerical schemes have been proposed, including Stokesian Dynamics and direct numerical simulations. Examples of direct approaches include the Arbitrary Lagrangian-Eulerian (ALE) moving mesh technique (e.g. Hu et al., 1992; Feng et al., 1994a,b; Hu et al., 2001), the fictitious domain method, in which no-slip boundary conditions were enforced using a distributed Lagrange multiplier (DLM) (e.g. Glowinski et al., 1998; Wan and Turek, 2007; Yu and Shao, 2007; D’Avino et al., 2008), and the lattice Boltzmann method, where the governing equations are derived from microscopic models and mesoscopic kinetic equations, (e.g. Ladd, 1994; Aidun and Lu, 1995; Aidun et al., 1998).

### 1.2.2 Numerical simulations

Discretisation techniques for multiply-connected domain problems can be broadly classified into two categories. The first one is based on the boundary fitted mesh approach, where only the original domain is considered and several nodes lie on the boundary of the domain (Figure 1.2). The second one is based on the domain embedding approach, where the original domain is converted into a simply-connected domain that is then represented by a fixed regular grid/mesh (Figure 1.3).

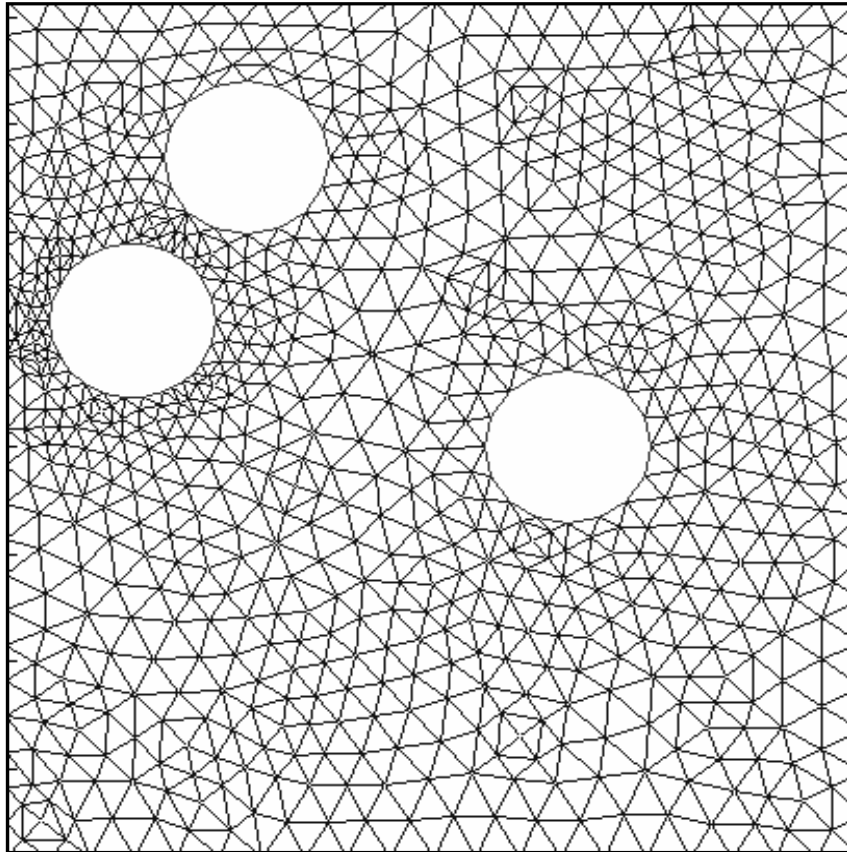


Figure 1.2: A typical boundary fitted mesh

#### Boundary fitted methods

For this category, unstructured meshes/grids are usually used (Figure 1.2). It can be seen that one can use a body fitted mesh to represent a geometrically

complex surface accurately. Moreover, an unstructured finite element mesh can be locally refined in particular regions in order to capture further details of the solution fields. In the case of moving boundary, a distorted mesh needs be regenerated and the flow field is then projected onto a new mesh. Such a task is a sophisticated work. Further details can be found in, e.g., (Hu et al., 1992; Feng et al., 1994a).

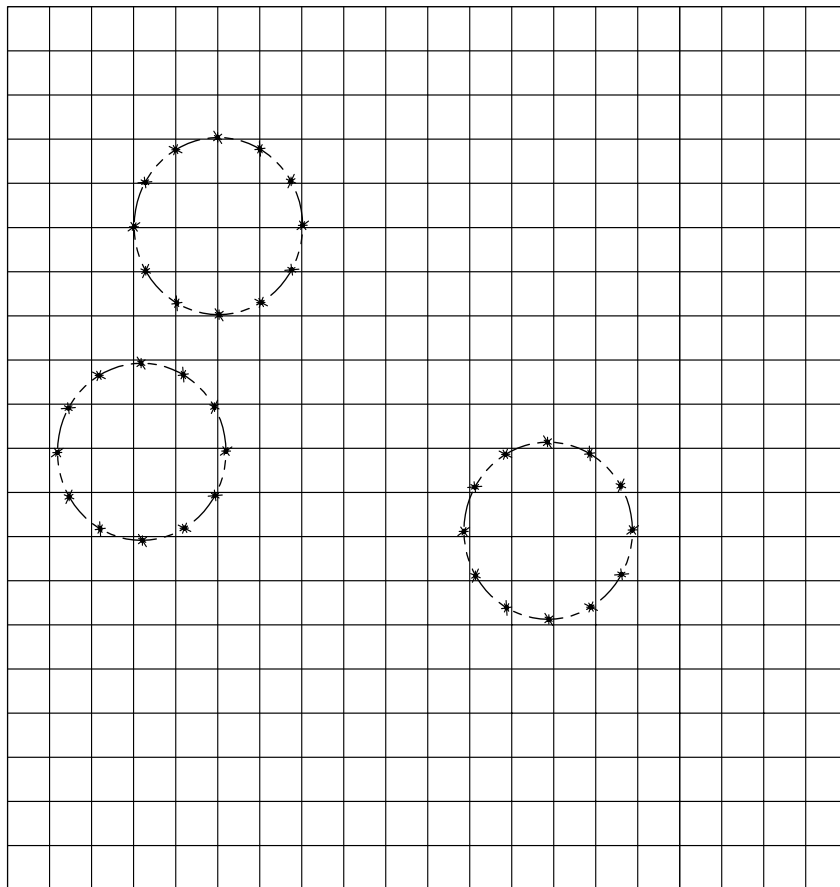


Figure 1.3: A typical domain embedding mesh

### Domain embedding methods

For this category, regular meshes/grids can be used (Figure 1.3). Since the computational domain is simply-connected, one can use fixed meshes and efficient solution methods (e.g. fast direct solvers for elliptic problems on rectangular domains). These are particularly helpful for the handling of moving boundary problems. However, the implementation of boundary conditions on the holes

is conducted in an approximate manner, making the solution less accurate. Further details can be found in (Glowinski et al., 1998; Wan and Turek, 2006).

## 1.3 Motivation

It has generally been accepted that currently-used discrete schemes for solving PDEs defined in multiply-connected domains still face a lot of numerical challenges. For finite-element-based methods (e.g. FEMs and FVMs), the task of generating a finite-element mesh is complicated and time consuming. On the other hand, for certain grid-based methods (e.g. FDMs and pseudo-spectral methods), difficulties lie in the way to find suitable coordinate transformations. This research project is mainly concerned with the development of accurate and efficient discretisation schemes for the simulation of heat and fluid flows in multiply-connected domains. Our objectives include the overcoming of drawbacks associated with other methods as described above.

A high level of accuracy is achieved by means of the following main components.

- High-order RBFNs are employed to represent the field variables in the governing equations. The order of accuracy of conventional low-order polynomials is estimated as  $O(h^\alpha)$ , where  $\alpha$  is a finite small number and  $h$  the mesh size. RBFNs can offer  $O(h^\gamma)$ , where the value of  $\gamma$  is dependent on the smoothness of the solution. For problems having smooth solutions,  $\gamma$  is known to be much greater than  $\alpha$ .
- The integral collocation formulation is utilised to construct the RBFN approximations. For conventional approximation schemes, the approximation order for a  $k$ th derivative is reduced to  $O(h^{\gamma-k})$ . It is expected that the use of integration in IRBFNs can avoid such a reduction.
- The constants of integration arising from the construction of the RBFN

approximations are exploited to impose derivative boundary conditions through the process of conversion of the RBF coefficient space into the physical space. Since the conversion matrix is not over-determined, derivative boundary conditions are incorporated into the RBFN approximations in an exact manner.

A high level of efficiency is achieved by means of the following main components.

- Point collocation is employed to discretise the governing equations. No integrations are involved in the process of transforming the PDEs into sets of algebraic equations.
- Cartesian grids are used to represent the problem domain. It is clear that generating a Cartesian grid is much simpler and easier than generating a finite-element mesh. This benefit is particularly important for the present problems.
- One-dimensional (1D) IRBFNs rather than 2D-IRBFNs are employed to simulate 2D problems in order to achieve some degree of local approximation. The 1D-IRBFN approximations at a nodal point involve nodes on the two associated grid lines only.
- One-dimensional IRBFNs are also introduced into the domain embedding approach towards the handling of moving boundary problems.

## 1.4 Outline of the Dissertation

The dissertation has seven chapters including this chapter (Introduction); each chapter is presented in a self-explanatory way. The outline of the remaining chapters is as follows.

- 
- Chapter 2 gives a brief review of RBFNs including IRBFNs and a description of a new 1D-IRBFN collocation method for solving heat transfer problems governed by Poisson equation in multiply-connected domains. The problem domain is simply discretised by a Cartesian grid. Special attention is given to the handling of Neumann boundary conditions. The proposed method is validated through some test problems with exact solutions.
  - Chapter 3 describes a new 1D-IRBFN collocation method for the discretisation of the stream-function - vorticity - temperature ( $\psi - \omega - T$ ) formulation in multiply-connected domains. Special attention is given to the derivation of computational vorticity boundary conditions for a Cartesian grid. Examples used to validate the proposed method include the buoyancy flows in concentric annuli.
  - Chapter 4 describes a new 1D-IRBFN collocation method for the discretisation of the stream-function - temperature ( $\psi - T$ ) formulation in multiply-connected domains. Special attention is given to the handling of higher-order derivatives, double boundary conditions and unknown values of the stream function on the inner boundaries. Examples used to validate the proposed method include the buoyancy flows in concentric and eccentric annuli and the viscous flows between a fixed outer cylinder and a rotating inner cylinder.
  - Chapter 5 describes a new 1D-IRBFN-based domain embedding method for the solution of Poisson equation in multiply-connected domains. Special attention is given to the handling of boundary conditions on the hole boundaries. The proposed method is validated through several linear boundary-value and initial-value problems.
  - Chapter 6 presents a practical application of the proposed 1D-IRBFN collocation method for numerical prediction of the bulk properties of particulate suspensions under shear conditions. Special attention is given

to the reduction of a very large original domain to a reference computational domain and the implementation of sliding bi-periodic boundary conditions. Results obtained are compared well with those based on finite elements in the literature.

- Chapter 7 gives the closure of the present research and suggests some possible future research developments.

## Chapter 2

# 1D-integrated-RBFN calculation of heat transfer in multiply-connected domains

This chapter consists of two parts. The first gives a brief overview of RBFN-based methods. The second describes a new technique based on Cartesian grids and one-dimension (1D) IRBFNs for solving heat problems governed by Poisson equations in multiply-connected domains. Important features of the proposed method include: (i) Constructing the approximations through integration; (ii) Employing a Cartesian grid to discretise the problem domain; and (iii) Using integrated RBFN approximations in one dimension to represent the approximate solution. These features result in an efficient numerical scheme as (i) the pre-processing is simple; (ii) the associated matrices have condition numbers that are much lower than those yielded through conventional RBFN techniques; and (iii) the reduction of convergence rate caused by differentiation is avoided. Both Dirichlet and Neumann-type boundary conditions are considered. Several test boundary-value and initial-value problems, some of which have exact solutions, are employed to validate the method.

## 2.1 Review of RBFN-based methods

RBFNs have become one of the main fields of research in numerical analysis (Haykin, 1998). They have the property of universal approximation, i.e. an arbitrary continuous function can be approximated to a prescribed degree of accuracy by increasing the number of nodes (Poggio and Girosi, 1990; Park and Sandberg, 1991, 1993). It is noted that some RBFN schemes can offer an exponential rate of convergence (Madych and Nelson, 1988). RBFNs have emerged as a powerful tool for the representation of a function and the solution of an ODE/PDE.

A network of RBFs allows one to convert a nonlinear function representing a physical field in a low-dimensional space (e.g. 1D, 2D and 3D) into a weighted linear combination of RBFs in a very high-dimensional space. It can be mathematically described as

$$y(\mathbf{x}) \approx f(\mathbf{x}) = \sum_{i=1}^m w_i g_i(\mathbf{x}), \quad (2.1)$$

where  $y$  is the exact function,  $f$  the approximate function,  $\mathbf{x}$  the position vector,  $m$  the number of RBFs,  $\{g_i(x)\}_{i=1}^m$  the set of RBFs, and  $\{w_i\}_{i=1}^m$  the set of weights to be found. Common types of RBF include

- the multiquadric function:

$$g_i(\mathbf{x}) = \sqrt{\|\mathbf{x} - \mathbf{c}_i\|^2 + a_i^2}, \quad (2.2)$$

- the inverse multiquadric function:

$$g_i(\mathbf{x}) = \frac{1}{\sqrt{\|\mathbf{x} - \mathbf{c}_i\|^2 + a_i^2}}, \quad (2.3)$$

- the Gaussian function:

$$g_i(\mathbf{x}) = \exp\left(-\frac{\|\mathbf{x} - \mathbf{c}_i\|^2}{a_i^2}\right), \quad (2.4)$$

where  $\mathbf{c}_i$  and  $a_i$  are the centre and the width of the  $i$ th basis function, respectively.

For a large class of RBFs including (2.2)-(2.4), the interpolation matrices derived from (2.1) and a set of distinct data points are proven to be invertible for some  $a_i > 0$  (Micchelli's theorem (Micchelli, 1986)). Moreover, according to the Cover theorem (Haykin, 1998), the higher the dimension of the hidden space (i.e. the number of RBFs used), the more accurate the approximation will be, indicating the property of "mesh convergence" of RBFNs. These important theorems can be seen to provide the basis for the design of RBFNs for the solution of ODEs/PDEs.

### 2.1.1 Conventional direct/differential approach

The application of RBFNs for solving PDEs was first reported by Kansa (1990b), where the RBF construction is based on differentiation (direct/differential approach). In this approach, the field variable is first decomposed into RBFs using (2.1) and all relevant derivatives of the field variable are subsequently obtained by differentiating (2.1). RBFN-based collocation methods are extremely easy to implement and capable of achieving a high degree of accuracy using relatively low numbers of nodal points. Furthermore, they require only a set of unstructured discrete points to support the approximation, which naturally offers the advantage of being meshless (Fasshauer, 2007). In this sense, RBFN-based methods are more suitable for dealing with problems defined on complex geometries. RBFN-based methods have been developed and applied to solve different types of differential problems encountered in applied mathematics, science and engineering (e.g. Zerroukat et al., 1998; Šarler et al., 2004; Šarler,

2005; Šarler et al., 2006; Šarler, 2009; Šarler et al., 2010; Divo and Kassab, 2005, 2006, 2007, 2008; Vertnik and Šarler, 2006; Vertnik et al., 2006; Yun-Xin and Yong-Ji, 2006; Kosec and Šarler, 2008a,b, 2009; Bernal and Kindelan, 2007; Siraj-ul-Islam et al., 2008; Zahab et al., 2009; Chen et al., 2010; Roque et al., 2010). Numerical experience has indicated that the accuracy of an RBFN solution is strongly influenced by the shape parameter  $a_i$ . Unfortunately, there is still a lack of mathematical theories for specifying the optimal values of this free parameter. Moreover, the resultant RBFN matrix is fully populated and its condition number grows rapidly with increasing number of nodes. It was reported in (Li and Hon, 2004) that the system matrix becomes unsolvable when the total number of collocation points are over 1000. Direct applications of RBFNs for large-scale problems can thus be seen to be limited. Several attempts to circumvent these difficulties/limitations have been proposed in the literatures. They include the use of preconditioning, compactly supported RBF, domain decomposition and local approximation.

Works concerning the development of a pre-conditioner for RBFN collocation methods include (Beatson et al., 1999; Ling and Kansa, 2005; Brown et al., 2005; Mai-Duy and Tran-Cong, 2010). A badly conditioned linear system can be replaced with a new system that is in much better condition. It can work well for various values of the shape parameter and a large number of nodes. Another way to improve the matrix condition number is to employ a class of positive definite and compactly supported RBFs proposed by Wendland (1995, 1998).

RBFNs were also combined with domain decomposition (e.g. Li and Chen, 2003; Li and Hon, 2004; Divo and Kassab, 2006; Chinchapatnam et al., 2007; Power et al., 2007). A domain of interest is divided into a set of subdomains, leading to a series of coupled smaller subproblems. These subproblems can be solved separately, which are suitable for parallel computing. Li and Chen (2003) employed RBFN collocation methods in conjunction with domain de-

composition for solving convection-diffusion problems at high Péclet numbers. Li and Hon (2004) presented both overlapping and nonoverlapping domain decomposition methods coupled with the meshless RBF method. Divo and Kassab (2006) developed a domain decomposition RBF method for viscous incompressible fluid flow problems. Chinchapatnam et al. (2007) proposed a numerical procedure, based on RBFNs and Schwarz domain decomposition technique, to solve time-dependent problems. Power et al. (2007) studied the influence of the non-overlapping domain decomposition technique on the symmetric RBFN collocation method.

Several researchers developed local RBFN methods, where only a small sub-region, namely the influence domain, is considered for the construction of the RBFN approximations at a nodal point. It is noted that the influence domain is usually employed with circular/rectangular shape. Local methods lead to a sparse and better-conditioned system matrix. Wu and Liu (2003) proposed a local radial point interpolation method for incompressible flows. Shu et al. (2003) incorporated local RBFNs into the differential quadrature method to simulate incompressible flows. Šarler and Vertnik (2006) localised RBF approximations using a set of overlapping subregions. Vertnik and Šarler (2006) developed a meshless local RBFN collocation method for convective-diffusive solid-liquid phase change problems. Divo and Kassab (2007) presented a localised RBFN meshless method for coupled viscous fluid flow and convective heat transfer problems. Chinchapatnam et al. (2009) proposed a mesh-free computational method based on radial basis functions in a finite difference mode (RBF-FD). Li et al. (2011) improved localised RBFN expansions using Hardy multiquadrics for the desired unknowns. Skouras et al. (2011) coupled local multiquadrics RBFNs with moving least square (MLS).

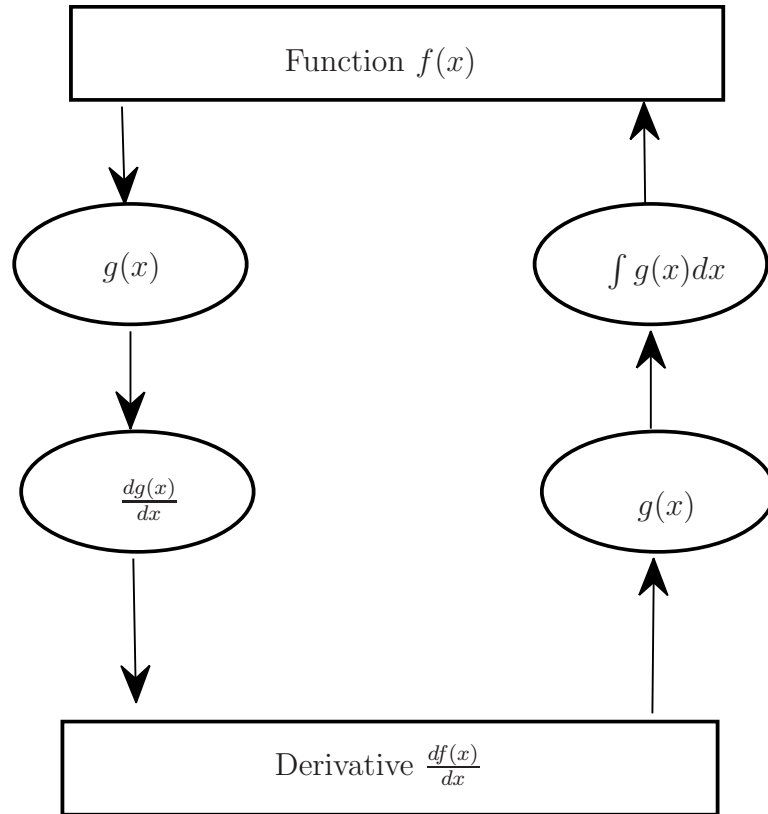


Figure 2.1: Differential (left) and Integral (right) approaches

### 2.1.2 Indirect/Integral approach

Indirect/integrated RBFNs (IRBFNs) were proposed in (Mai-Duy and Tran-Cong, 2001a). In the integral approach, the highest derivatives in a given PDE are first decomposed into RBFs using (2.1), and lower derivatives and the field variable itself are then obtained by integrating (2.1). Figure 2.1 shows a comparison of the ways in which DRBFNs and IRBFNs are constructed. The use of integration, instead of conventional differentiation, to construct the RBFN approximations allows one (i) to avoid the reduction in convergence rate caused by differentiation; and (ii) to make a numerical solution more stable. The constants

of integration in IRBFNs have been found extremely useful in the solution of ODEs/PDEs in several ways: (i) to provide a proper way of implementing Neumann and multiple boundary conditions (Mai-Duy and Tran-Cong, 2007); (ii) to describe irregular boundaries on a Cartesian grid accurately (Mai-Duy et al., 2008); and (iii) to improve the continuity order of the approximate solution across the subdomain interfaces (Mai-Duy and Tran-Cong, 2008). Numerical results have shown that the integral approach performs better than the differential approach for both function approximation (Mai-Duy and Tran-Cong, 2003) and solution of ODEs/PDEs (Mai-Duy, 2004). For simplicity, consider an univariate function  $f(x)$ . The integral approach can be mathematically described as

$$\frac{d^p f(x)}{dx^p} = \sum_{i=1}^m w_i g_i(x) = \sum_{i=1}^m w_i I_i^{(p)}(x), \quad (2.5)$$

$$\frac{d^{p-1} f(x)}{dx^{p-1}} = \sum_{i=1}^m w_i I_i^{(p-1)}(x) + c_1, \quad (2.6)$$

$$\frac{d^{p-2} f(x)}{dx^{p-2}} = \sum_{i=1}^m w_i I_i^{(p-2)}(x) + c_1 x + c_2, \quad (2.7)$$

... ..

$$\frac{df(x)}{dx} = \sum_{i=1}^m w_i I_i^{(1)}(x) + c_1 \frac{x^{p-2}}{(p-2)!} + c_2 \frac{x^{p-3}}{(p-3)!} + \cdots + c_{p-2} x + c_{p-1}, \quad (2.8)$$

$$f(x) = \sum_{i=1}^m w_i I_i^{(0)}(x) + c_1 \frac{x^{p-1}}{(p-1)!} + c_2 \frac{x^{p-2}}{(p-2)!} + \cdots + c_{p-1} x + c_p, \quad (2.9)$$

where  $I_i^{(p-1)}(x) = \int I_i^{(p)}(x) dx$ ,  $I_i^{(p-2)}(x) = \int I_i^{(p-1)}(x) dx$ ,  $\dots$ ,  $I_i^{(0)}(x) = \int I_i^{(1)}(x) dx$ , and  $\{c_1, c_2, \dots, c_p\}$  are the constants of integration. In this thesis, the IRBFN approximation scheme is said to be of  $p$ th-order, denoted by IRBFN- $p$ , if the  $p$ th-order derivative is taken as the starting point.

## 2.2 One-dimensional IRBFN method for heat transfer in multiply-connected domains

The objective of discretisation techniques is to reduce the PDEs to sets of algebraic equations. To do so, the problem domain needs be discretised into a set of finite elements, a Cartesian grid or a set of unstructured points. Among these typical types of domain discretisation, generating a Cartesian grid is seen to be a straightforward task, and hence the computational cost associated with mesh generation is much less than that associated with FEMs. Cartesian grid methods have a long history. Examples of Cartesian grid methods include FDMs and pseudospectral methods. Applications of FDMs and pseudospectral methods to problems defined on non-rectangular domains are not straightforward. One usually needs to use coordinate transformations to convert the problem domain into a rectangular one. In recent years, there has been a great interest in the development of Cartesian-grid-based techniques for dealing with geometrically-complicated domains without the need for coordinate transformations; their applications have become widespread (e.g. Calhoun, 2002; Marella et al., 2005; Ito et al., 2009; Šarler, 2009; Shinn et al., 2009; Udaykumar et al., 2009; Erhart et al., 2010; Liao et al., 2010; Sugiyama et al., 2011).

Inspired by attractive features of Cartesian grid and IRBFNs, we extend 1D-IRBFNs proposed in (Mai-Duy and Tran-Cong, 2007; Mai-Duy et al., 2008) to handle differential problems with more complicated geometries. Consider a multiply-connected domain as shown in Figure 2.2. The problem domain is embedded in a Cartesian grid. Grid points outside the domain (external points) together with internal points that fall very close - within a small distance - to the boundary are removed. The remaining grid points are taken to be the interior nodes. The boundary nodes are points that are generated by the intersection of the grid lines with the boundaries. IRBFNs are employed to represent the field variable on each line of the grid separately (1D-IRBFNs). The construction of

the 1D-IRBFN approximations for a grid node thus involves only nodal points that lie on lines intersecting at that point and parallel to the coordinate axes, rather than the whole set of nodes. The inversion is now conducted for a series of small matrices (each grid line) rather than for a large single matrix (whole domain). This use of 1D-IRBFNs thus leads to a considerable reduction of computational cost in constructing the system matrix over conventional RBFN methods. The meshfree property (i.e. no underlying structured topologies required) of 1D-IRBFNs is exploited to handle irregular boundaries, where the boundary nodes do not generally coincide with grid nodes.

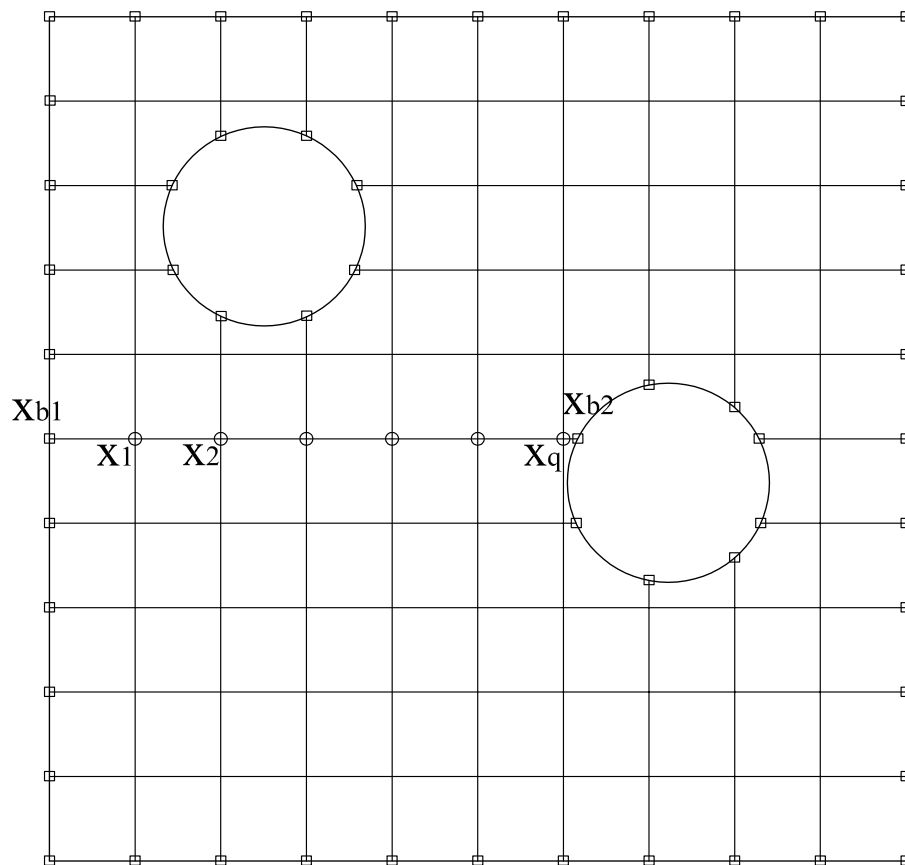


Figure 2.2: 1D-IRBFN discretisation and a typical grid line. Points on the grid line consist of interior nodal points  $x_i$  ( $\circ$ ) and boundary points  $x_{b_i}$  ( $\square$ ).

### 2.2.1 Mathematical formulations

Heat transfer equations usually involve the following term

$$\mathcal{L}_2(T) = \frac{\partial^2 T}{\partial x^2} + \frac{\partial^2 T}{\partial y^2}, \quad (2.10)$$

where  $\mathcal{L}_2$  is the Laplace operator and  $T$  the temperature. As presented earlier, an IRBFN- $p$  scheme permits the approximation of a function and its derivatives of orders up to  $p$ . One can employ IRBFN-2 here to represent  $T$ . Consider a typical grid line as shown Figure 2.2. On this grid line, the following expressions are obtained by using (2.5)-(2.9) with  $p = 2$

$$\frac{\partial^2 T(x)}{\partial x^2} = \sum_{i=1}^m w_i g_i(x) = \sum_{i=1}^m w_i I_i^{(2)}(x), \quad (2.11)$$

$$\frac{\partial T(x)}{\partial x} = \sum_{i=1}^m w_i I_i^{(1)}(x) + c_1, \quad (2.12)$$

$$T(x) = \sum_{i=1}^m w_i I_i^{(0)}(x) + c_1 x + c_2, \quad (2.13)$$

where  $m$  is the number of RBFs on the grid line. It has generally been accepted that, among RBFs, the multiquadric (MQ) scheme tends to result in the most accurate approximation (Franke, 1982). The present technique implements the MQ function whose form is

$$I_i^{(2)}(x) = \sqrt{(x - c_i)^2 + a_i^2}, \quad (2.14)$$

$$I_i^{(1)}(x) = \frac{(x - c_i)}{2} A + \frac{a_i^2}{2} B, \quad (2.15)$$

$$I_i^{(0)}(x) = \left( \frac{-a_i^2}{3} + \frac{(x - c_i)^2}{6} \right) A + \frac{a_i^2 (x - c_i)}{2} B, \quad (2.16)$$

where  $c_i$  and  $a_i$  are the centre and the width of the  $i$ th MQ, respectively;  $A = \sqrt{(x - c_i)^2 + a_i^2}$ ; and  $B = \ln \left( (x - c_i) + \sqrt{(x - c_i)^2 + a_i^2} \right)$ . A set of collocation points  $\{x_i\}_{i=1}^m$  is chosen to be a set of centres  $\{c_i\}_{i=1}^m$ . Such a set is comprised of two subsets. The first subset consists of the interior nodal points ( $\{x_i\}_{i=1}^q$ ) that

are also the grid nodes (regular nodes). The values of the field variable at the interior points are unknown. The second subset is formed from the boundary nodes  $(\{x_{bi}\}_{i=1}^2)$  that do not generally coincide with the grid nodes (irregular nodes).

### Dirichlet boundary conditions

Assume that  $T$  is given at  $x_{b1}$  and  $x_{b2}$ . Unlike the finite-difference and spectral approximation schemes, 1D-IRBFNs have the capability to handle unstructured nodes with high accuracy and thus to deal with irregular boundary in a direct manner.

Evaluation of (2.13) at a set of collocation points results in

$$\begin{pmatrix} \hat{T} \\ \hat{T}_b \end{pmatrix} = \hat{\mathcal{C}} \hat{w}, \quad (2.17)$$

where

$$\begin{aligned} \hat{T} &= (T_1, T_2, \dots, T_q)^T, \\ \hat{T}_b &= (T_{b1}, T_{b2})^T, \\ \hat{w} &= (w_1, w_2, \dots, w_m, c_1, c_2)^T, \\ \hat{\mathcal{C}} &= \begin{bmatrix} I_1^{(0)}(x_1) & \cdots & I_m^{(0)}(x_1) & x_1 & 1 \\ I_1^{(0)}(x_2) & \cdots & I_m^{(0)}(x_2) & x_2 & 1 \\ \vdots & \ddots & \vdots & \vdots & \vdots \\ I_1^{(0)}(x_q) & \cdots & I_m^{(0)}(x_q) & x_q & 1 \\ I_1^{(0)}(x_{b1}) & \cdots & I_m^{(0)}(x_{b1}) & x_{b1} & 1 \\ I_1^{(0)}(x_{b2}) & \cdots & I_m^{(0)}(x_{b2}) & x_{b2} & 1 \end{bmatrix}, \end{aligned}$$

and  $m = q + 2$ .

The obtained system (2.17) for the unknown vector of network weights  $\hat{w}$  can

be solved using the singular value decomposition (SVD) technique

$$\widehat{w} = \widehat{\mathcal{C}}^{-1} \begin{pmatrix} \widehat{T} \\ \widehat{T}_b \end{pmatrix}, \quad (2.18)$$

where  $\widehat{\mathcal{C}}^{-1}$  is the pseudo-inverse of  $\widehat{\mathcal{C}}$ .

Taking (2.18) into account, the values of the first and second derivatives of  $T$  at the interior points are computed by (2.12)

$$\begin{pmatrix} \frac{\partial T_1}{\partial x} \\ \frac{\partial T_2}{\partial x} \\ \vdots \\ \frac{\partial T_q}{\partial x} \end{pmatrix} = \begin{bmatrix} I_1^{(1)}(x_1) & \cdots & I_m^{(1)}(x_1) & 1 & 0 \\ I_1^{(1)}(x_2) & \cdots & I_m^{(1)}(x_2) & 1 & 0 \\ \vdots & \ddots & \vdots & \vdots & \vdots \\ I_1^{(1)}(x_q) & \cdots & I_m^{(1)}(x_q) & 1 & 0 \end{bmatrix} \widehat{\mathcal{C}}^{-1} \begin{pmatrix} \widehat{T} \\ \widehat{T}_b \end{pmatrix}, \quad (2.19)$$

and (2.11)

$$\begin{pmatrix} \frac{\partial^2 T_1}{\partial x^2} \\ \frac{\partial^2 T_2}{\partial x^2} \\ \vdots \\ \frac{\partial^2 T_q}{\partial x^2} \end{pmatrix} = \begin{bmatrix} I_1^{(2)}(x_1) & \cdots & I_m^{(2)}(x_1) & 0 & 0 \\ I_1^{(2)}(x_2) & \cdots & I_m^{(2)}(x_2) & 0 & 0 \\ \vdots & \ddots & \vdots & \vdots & \vdots \\ I_1^{(2)}(x_q) & \cdots & I_m^{(2)}(x_q) & 0 & 0 \end{bmatrix} \widehat{\mathcal{C}}^{-1} \begin{pmatrix} \widehat{T} \\ \widehat{T}_b \end{pmatrix}, \quad (2.20)$$

or in compact forms

$$\frac{\partial \widehat{T}}{\partial x} = \widehat{\mathcal{D}}_{1x} \widehat{T} + \widehat{k}_{1x}, \quad (2.21)$$

and

$$\frac{\partial^2 \widehat{T}}{\partial x^2} = \widehat{\mathcal{D}}_{2x} \widehat{T} + \widehat{k}_{2x}, \quad (2.22)$$

where the matrices  $\widehat{\mathcal{D}}_{1x}$  and  $\widehat{\mathcal{D}}_{2x}$  consist of all but the last two columns of the product of two matrices on the right-hand side of (2.19) and (2.20), and  $\widehat{k}_{1x}$  and  $\widehat{k}_{2x}$  are obtained by multiplying the vector  $\widehat{T}_b$  with these last two columns. It is noted that  $\widehat{k}_{1x}$  and  $\widehat{k}_{2x}$  are the vectors of known quantities related to boundary

conditions.

### Dirichlet and Neumann boundary conditions

It is known that RBFN results for Dirichlet and Neumann problems are generally less accurate than those for Dirichlet problems. To alleviate this problem, several techniques have been proposed. Examples include (i) a properly selected weight method, which is based on the observation of unbalanced errors between domain, Neumann boundary, and Dirichlet boundary least-squares terms (Hu et al., 2004); (ii) a stabilised RBF collocation scheme for Neumann type boundary value problems (Libre et al., 2008); and (iii) a modified equilibrium on line method to impose Neumann boundary conditions (Sadeghirad and Kani, 2009).

In this research, Neumann boundary conditions are presently incorporated into the 1D-IRBFN approximations with the help of integration constants through the process of converting the network-weight space into the physical space. Assume that  $\partial T/\partial x$  and  $T$  are given at  $x_{b1}$  and  $x_{b2}$ , respectively (Figure 2.2). The process of conversion above, i.e. (2.17)-(2.18), is modified as follows.

$$\begin{pmatrix} \hat{T} \\ T_{b1} \\ T_{b2} \\ \frac{\partial T_{b1}}{\partial x} \end{pmatrix} = \begin{pmatrix} \hat{\mathcal{C}} \\ \mathcal{B} \end{pmatrix} \begin{pmatrix} \hat{w} \\ c_1 \\ c_2 \end{pmatrix}, \quad (2.23)$$

$$\begin{pmatrix} \hat{w} \\ c_1 \\ c_2 \end{pmatrix} = \begin{pmatrix} \hat{\mathcal{C}} \\ \mathcal{B} \end{pmatrix}^{-1} \begin{pmatrix} \hat{T} \\ T_{b1} \\ T_{b2} \\ \frac{\partial T_{b1}}{\partial x} \end{pmatrix}, \quad (2.24)$$

where

$$\mathcal{B} = \begin{bmatrix} I_1^{(1)}(x_{b1}) & \cdots & I_m^{(1)}(x_{b1}) & 1 & 0 \end{bmatrix}.$$

One obtains the following nodal derivative values of  $T$  by collocating (2.12) and (2.11) at  $\{x_i\}_{i=1}^q$  and making use of (2.24)

$$\begin{pmatrix} \frac{\partial T_1}{\partial x} \\ \frac{\partial T_2}{\partial x} \\ \vdots \\ \frac{\partial T_q}{\partial x} \end{pmatrix} = \begin{bmatrix} I_1^{(1)}(x_1) & \cdots & I_m^{(1)}(x_1) & 1 & 0 \\ I_1^{(1)}(x_2) & \cdots & I_m^{(1)}(x_2) & 1 & 0 \\ \vdots & \ddots & \vdots & \vdots & \vdots \\ I_1^{(1)}(x_q) & \cdots & I_m^{(1)}(x_q) & 1 & 0 \end{bmatrix} \begin{pmatrix} \widehat{\mathcal{C}} \\ \mathcal{B} \end{pmatrix}^{-1} \begin{pmatrix} \widehat{T} \\ T_{b1} \\ T_{b2} \\ \frac{\partial T_{b1}}{\partial x} \end{pmatrix}, \quad (2.25)$$

and

$$\begin{pmatrix} \frac{\partial^2 T_1}{\partial x^2} \\ \frac{\partial^2 T_2}{\partial x^2} \\ \vdots \\ \frac{\partial^2 T_q}{\partial x^2} \end{pmatrix} = \begin{bmatrix} I_1^{(2)}(x_1) & \cdots & I_m^{(2)}(x_1) & 0 & 0 \\ I_1^{(2)}(x_2) & \cdots & I_m^{(2)}(x_2) & 0 & 0 \\ \vdots & \ddots & \vdots & \vdots & \vdots \\ I_1^{(2)}(x_q) & \cdots & I_m^{(2)}(x_q) & 0 & 0 \end{bmatrix} \begin{pmatrix} \widehat{\mathcal{C}} \\ \mathcal{B} \end{pmatrix}^{-1} \begin{pmatrix} \widehat{T} \\ T_{b1} \\ T_{b2} \\ \frac{\partial T_{b1}}{\partial x} \end{pmatrix}. \quad (2.26)$$

The 1D-IRBFN expressions for derivatives are now written in terms of nodal values of  $T$  and they already satisfy the given boundary conditions. Thus one only needs to force them to satisfy the governing equation. By collocating the governing equation at interior points and Neumann boundary points (i.e. nodal points associated with unknown values of  $T$ ), a square system of algebraic equations is obtained, which is solved for the approximate temperature field. It is noted that, as with FDMs, FVMs, BEMs and FEMs, the global 1D-IRBFN approximations matrices are also formed through the assembly process.

### 2.2.2 Numerical examples

For all numerical examples studied, the width of the  $i$ th MQ-RBF,  $a_i$ , is simply chosen to be the grid size  $h$ , and we remove all interior points that fall within a distance of  $h/8$  to the boundary. Three types of problems, namely boundary-value problem with Dirichlet boundary conditions, boundary-value problem with Dirichlet and Neumann boundary conditions, and initial-value

problem with Dirichlet boundary conditions are considered.

The solution accuracy is measured by means of the discrete relative  $L_2$  norm of the error defined as

$$Ne = \frac{\sqrt{\sum_{i=1}^M (T_i^e - T_i)^2}}{\sqrt{\sum_{i=1}^M (T_i^e)^2}}, \quad (2.27)$$

where  $M$  is the number of unknown nodal values of  $T$ , and  $T^e$  and  $T$  denote the exact and approximate solutions, respectively. Another important measure is the convergence rate  $\alpha$  of the solution with respect to grid refinement

$$Ne(h) \approx \gamma h^\alpha = O(h^\alpha), \quad (2.28)$$

in which  $\alpha$  and  $\gamma$  are exponential model's parameters. Given a set of observations, these parameters can be found by the general linear least squares technique.

### Example 1 - A boundary value problem (Dirichlet)

The present technique is first verified through the solution of a test problem governed by

$$\frac{\partial^2 T}{\partial x^2} + \frac{\partial^2 T}{\partial y^2} = b(x, y), \quad (2.29)$$

on a multiply-connected domain and subject to Dirichlet boundary conditions. The problem domain chosen and its typical discretisation are shown in Figure 2.3. Two particular driving functions are considered.

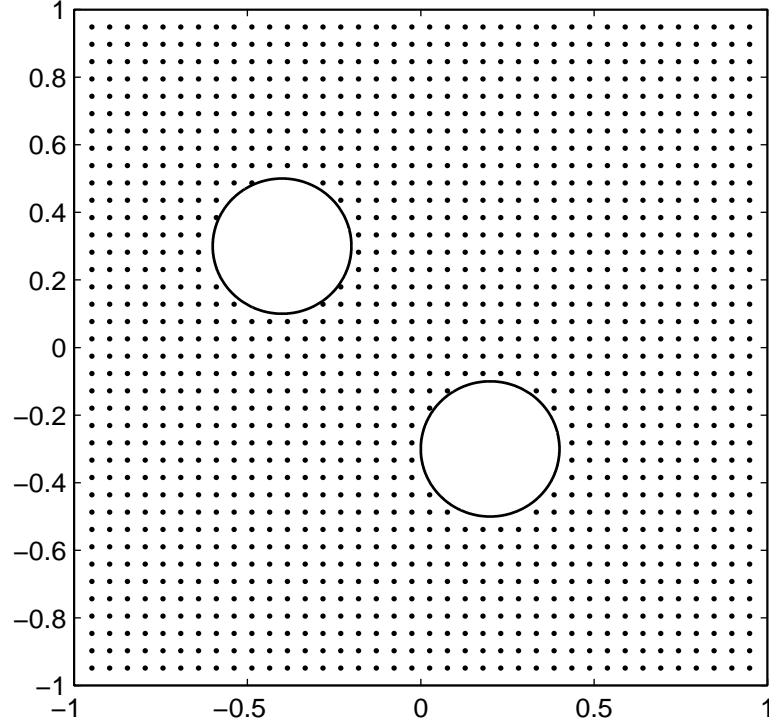


Figure 2.3: Example 1 (boundary value problem - Dirichlet boundary condition): Domain of interest and its typical discretisation. Two holes are of circular shapes with the same radius 0.2. The coordinates of the hole centres are  $(-0.4, 0.3)$  and  $(0.2; -0.3)$ . It is noted that the nodes outside the domain are removed.

Case 1:

$$\begin{aligned}
 b(x, y) = & 2\pi^2 \cos(\pi y) \cos(\pi(x - 0.5y)) + \pi^2 \sin(\pi y) \sin(\pi(x - 0.5y)) \\
 & + \pi^2 0.25 \cos(\pi y) \cos(\pi(x - 0.5y)).
 \end{aligned} \tag{2.30}$$

The exact solution is

$$T^e(x, y) = \cos(\pi(x - 0.5y)) \cos(\pi y), \tag{2.31}$$

from which boundary values of  $T$  can be easily derived.

Case 2:

$$b(x, y) = 0. \tag{2.32}$$

Analytic solution to this case is not available. The boundary conditions are set to one at the outer square boundary and to zero at the inner boundaries.

For Case 1, a number of uniform grids,  $(12 \times 12, 22 \times 22, \dots, 102 \times 102)$ , are considered. Table 2.1 presents the matrix condition (denoted by  $\text{cond}(A)$ ). It can be seen that condition numbers of the present matrix are relatively low (e.g.  $6.5 \times 10^3$  with grid  $102 \times 102$ ). Figure 2.4 shows the profile of the approximate solution. Figure 2.5 displays the behaviour of  $Ne$  against  $h$ , where the 1D-IRBFN solution converges apparently as  $O(h^{3.28})$ .

Table 2.1: Example 1 (boundary value problem - Dirichlet boundary condition - Case 1): Condition numbers of the IRBFN system matrix.

Grid	$\text{cond}(A)$
$12 \times 12$	$4.4 \times 10^1$
$22 \times 22$	$2.0 \times 10^2$
$32 \times 32$	$5.5 \times 10^2$
$42 \times 42$	$1.2 \times 10^3$
$52 \times 52$	$1.7 \times 10^3$
$62 \times 62$	$2.0 \times 10^3$
$72 \times 72$	$3.3 \times 10^3$
$82 \times 82$	$4.5 \times 10^3$
$92 \times 92$	$5.2 \times 10^3$
$102 \times 102$	$6.5 \times 10^3$

For Case 2, we present a visual comparison of the distribution of  $T$  between the present technique and FEM (Figure 2.6). It is noted that the FEM result is obtained using the PDE Toolbox in MATLAB. It can be seen that the two solutions have similar behaviours.

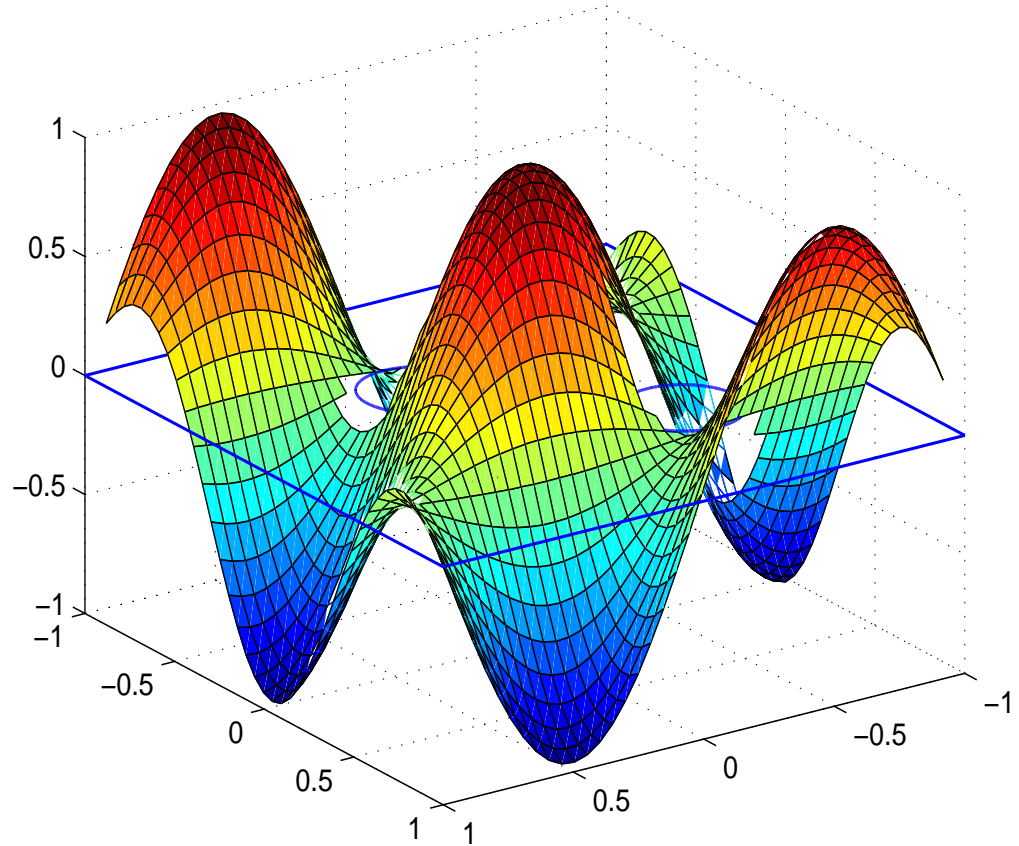


Figure 2.4: Example 1 (boundary value problem - Dirichlet boundary condition - Case 1): Profile of the approximate solution using a grid of  $42 \times 42$ .

**Example 2 - A boundary value problem (Dirichlet and Neumann)**

The driving function is taken as

$$\begin{aligned}
 b(x, y) = & -\frac{\cos(\sqrt{x^2 + y^2})}{(x^2 + y^2)} \left( \frac{1}{x^2} + \frac{1}{y^2} \right) + \frac{\sin(\sqrt{x^2 + y^2})}{(x^2 + y^2)^{3/2} y^2} \left( \frac{1}{x^2} + \frac{1}{y^2} \right) \\
 & - 2 \frac{\sin(\sqrt{x^2 + y^2})}{\sqrt{x^2 + y^2}}
 \end{aligned} \tag{2.33}$$

and the domain of interest is the region lying between a square of  $1 \times 1$  and a circle of radius  $1/8$  which are both centered at the origin (Figure 2.7). The

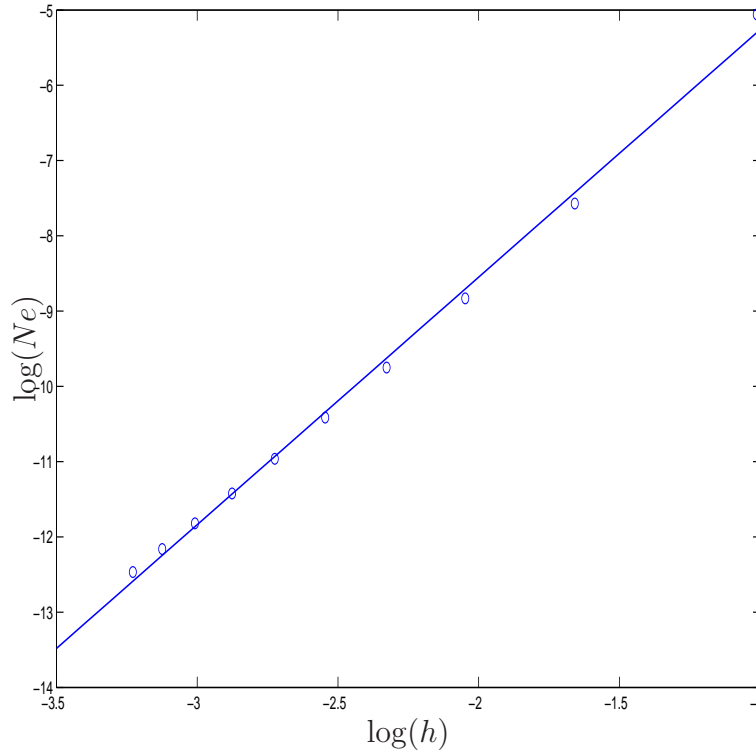


Figure 2.5: Example 1 (boundary value problem - Dirichlet boundary condition - Case 1): Convergence behaviour of the approximate solution with grid refinement.

exact solution for this problem can be verified to be

$$T^e(x, y) = \cos(\sqrt{x^2 + y^2}). \quad (2.34)$$

from which Dirichlet boundary conditions on the inner circular boundary and Neumann boundary conditions on the outer square boundary can be derived analytically.

A number of grids, namely  $(12 \times 12, 22 \times 22, \dots, 102 \times 102)$ , are employed to study the convergence behaviour of the solution. Results concerning the error  $Ne$  and condition numbers of the system matrix are given in Table 2.2. It can be seen that the 1D-IRBFN solution is very accurate even at coarse grids (e.g.  $Ne = 2.25 \times 10^{-4}$  using a grid of  $12 \times 12$ ) and condition numbers of the system

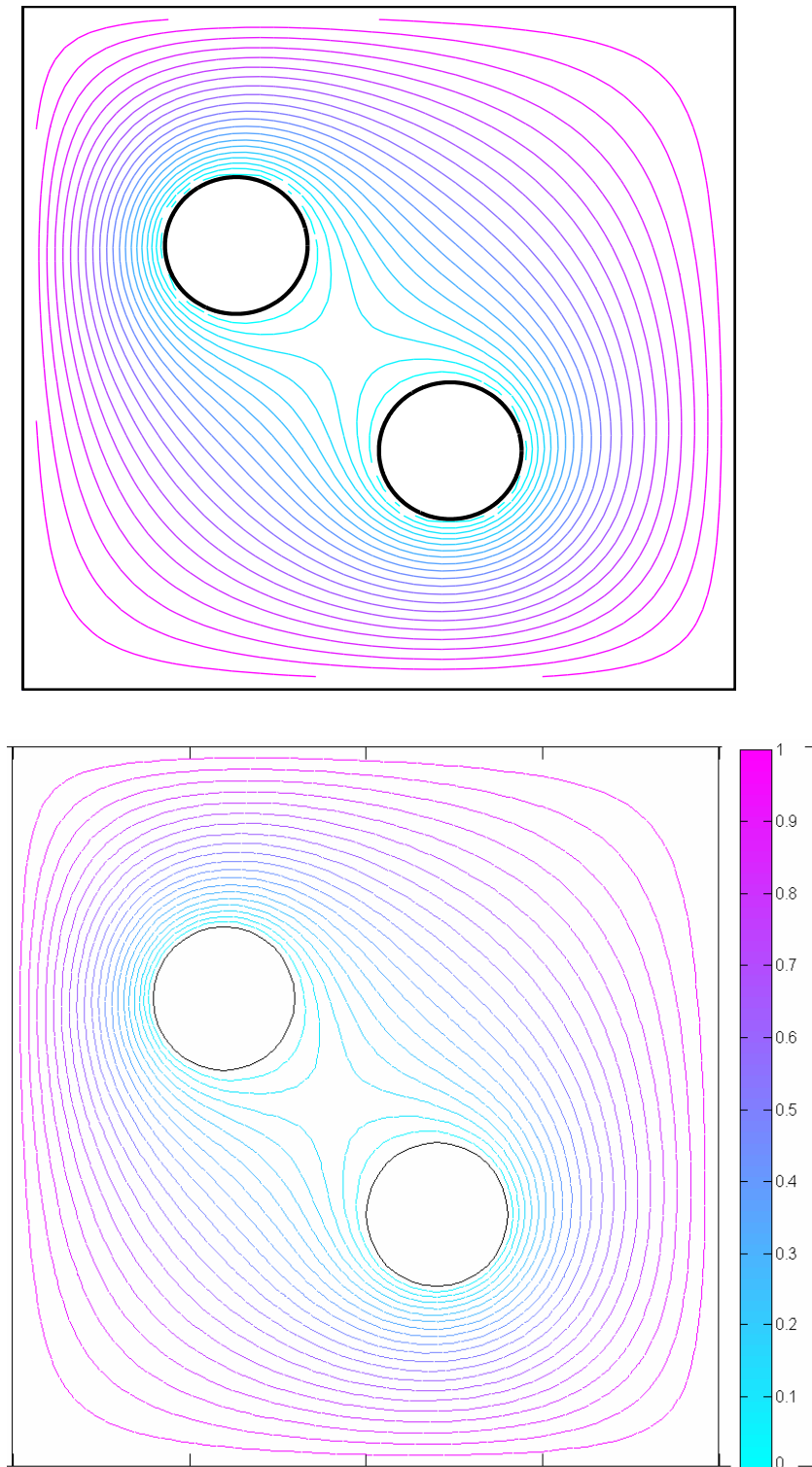


Figure 2.6: Example 1 (boundary value problem - Dirichlet boundary condition - Case 2): A contour plot of  $T$  by the 1D-IRBFN method using a grid of  $42 \times 42$  (top) and FEM (bottom).

matrix is relatively low (e.g.  $3.1 \times 10^4$  for a grid of  $102 \times 102$ ). A contour plot of  $T$  is shown in Figure 2.8

Table 2.2: Example 2 (boundary value problem - Dirichlet and Neumann boundary conditions): Overall accuracy of the solution  $T$  by the present technique. Condition numbers of the IRBFN system matrix are also included.

Grid	$Ne(T)$	$cond(A)$
$12 \times 12$	$2.2529 \times 10^{-4}$	$4.7 \times 10^2$
$22 \times 22$	$7.9877 \times 10^{-5}$	$1.4 \times 10^3$
$32 \times 32$	$3.9202 \times 10^{-5}$	$3.0 \times 10^3$
$42 \times 42$	$2.3111 \times 10^{-5}$	$5.2 \times 10^3$
$52 \times 52$	$1.5405 \times 10^{-5}$	$1.3 \times 10^4$
$62 \times 62$	$1.1084 \times 10^{-5}$	$1.8 \times 10^4$
$72 \times 72$	$8.2404 \times 10^{-6}$	$1.6 \times 10^4$
$82 \times 82$	$6.3450 \times 10^{-6}$	$2.0 \times 10^4$
$92 \times 92$	$5.0574 \times 10^{-6}$	$4.4 \times 10^4$
$102 \times 102$	$4.1250 \times 10^{-6}$	$3.1 \times 10^4$

### Example 3 - An initial-value problem

Consider the following PDE

$$\frac{\partial T}{\partial t} - \left( \frac{\partial^2 T}{\partial x^2} + \frac{\partial^2 T}{\partial y^2} \right) = (1 + 2\pi^2 k^2 t) \sin(k\pi x) \sin(k\pi y), \quad (2.35)$$

where  $k$  is a given number. We choose the domain to be the same as that in Example 1 (i.e. Figure 2.3). The exact solution is given by

$$T^e(x, y, t) = \sin(k\pi x) \sin(k\pi y)t, \quad (2.36)$$

from which the initial solution and Dirichlet boundary conditions are derived analytically.

The time derivative term in (2.35) is simply discretised using a first-order finite-difference scheme. It is noted that the system matrix, which is generated from

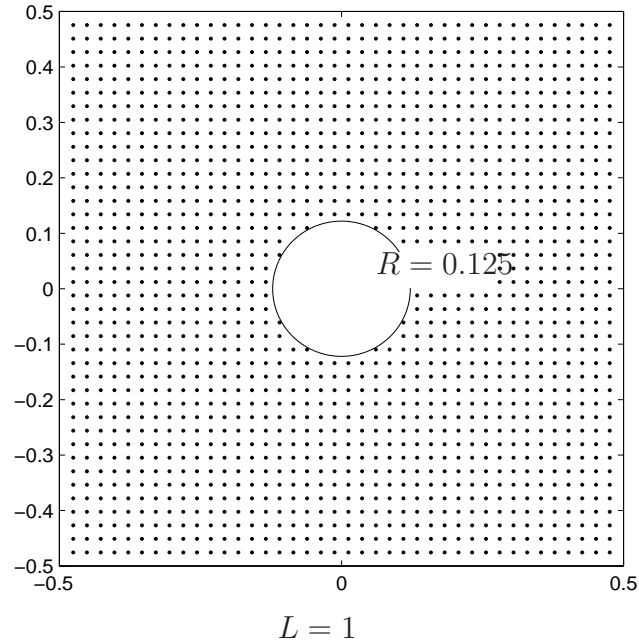


Figure 2.7: Example 2 (boundary value problem - Dirichlet and Neumann boundary conditions): Domain of interest and its typical discretisation. It is noted that the nodes outside the domain are removed.

the Laplacian and the time derivative term in (2.35), stays the same during the iterative process.

The spatial discretisation is based on Cartesian grids of  $32 \times 32$  and  $52 \times 52$ . Results concerning  $Ne$  for four values of  $k$ , namely 1, 2, 3, 4, using a time step of 0.1 are listed in Table 2.3 and Table 2.4 for grids of  $32 \times 32$  and  $52 \times 52$ , respectively. Condition numbers of the system matrix are  $5.5 \times 10^2$  for a grid of  $32 \times 32$  and  $1.6 \times 10^2$  for  $52 \times 52$ . Plots for  $T$  at  $t = 1$  are shown in Figure 2.9. It can be seen that the behaviour of the solution  $T$  grows complex quickly with increasing value of  $k$  and the present scheme is able to capture accurately a very complex function at  $k = 4$  using a relatively low number of nodes (about 900 nodes).

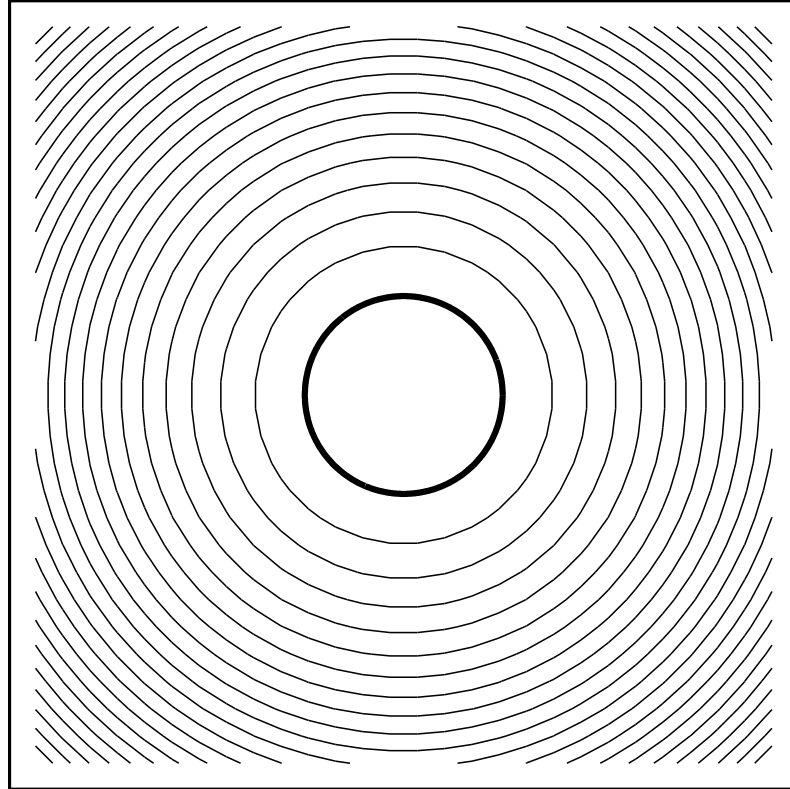


Figure 2.8: Example 2 (boundary value problem - Dirichlet and Neumann boundary conditions): Approximate solution using a grid of  $42 \times 42$ . This plot contains 21 contour lines whose levels vary linearly from the minimum to maximum values

Table 2.3: Example 3 (initial-value problem): Relative  $L_2$  errors of the solution (grid of  $32 \times 32$ ). It is noted that  $a(b)$  represents  $a \times 10^b$ .

t	$k = 1$	$k = 2$	$k = 3$	$k = 4$
0.1	6.1616(-5)	3.4048(-4)	8.7540(-4)	1.8977(-3)
0.2	6.6472(-5)	3.5274(-4)	8.9339(-4)	1.9259(-3)
0.3	6.8883(-5)	3.5777(-4)	9.0031(-4)	1.9368(-3)
0.4	7.0252(-5)	3.6040(-4)	9.0388(-4)	1.9425(-3)
0.5	7.1114(-5)	3.6200(-4)	9.0606(-4)	1.9460(-3)
0.6	7.1701(-5)	3.6308(-4)	9.0752(-4)	1.9483(-3)
0.7	7.2124(-5)	3.6385(-4)	9.0857(-4)	1.9500(-3)
0.8	7.2442(-5)	3.6443(-4)	9.0935(-4)	1.9513(-3)
0.9	7.2691(-5)	3.6488(-4)	9.0997(-4)	1.9522(-3)
1.0	7.2890(-5)	3.6524(-4)	9.1046(-4)	1.9530(-3)

Table 2.4: Example 3 (initial-value problem): Relative  $L_2$  errors of the solution (grid of  $52 \times 52$ ). It is noted that  $a(b)$  represents  $a \times 10^b$ .

t	$k = 1$	$k = 2$	$k = 3$	$k = 4$
0.1	2.7378(-5)	1.5101(-4)	3.9744(-4)	8.5594(-4)
0.2	2.9372(-5)	1.5589(-4)	4.0499(-4)	8.6748(-4)
0.3	3.0365(-5)	1.5789(-4)	4.0789(-4)	8.7195(-4)
0.4	3.0932(-5)	1.5893(-4)	4.0938(-4)	8.7428(-4)
0.5	3.1291(-5)	1.5957(-4)	4.1029(-4)	8.7571(-4)
0.6	3.1536(-5)	1.5999(-4)	4.1089(-4)	8.7667(-4)
0.7	3.1714(-5)	1.6030(-4)	4.1133(-4)	8.7736(-4)
0.8	3.1847(-5)	1.6053(-4)	4.1165(-4)	8.7788(-4)
0.9	3.1952(-5)	1.6071(-4)	4.1191(-4)	8.7828(-4)
1.0	3.2036(-5)	1.6085(-4)	4.1211(-4)	8.7861(-4)

## 2.3 Concluding remarks

In this chapter, we give a brief review of RBFNs and then present 1D-IRBFN calculations of heat problems governed by Poisson equation on irregular multiply-connected domains. Numerical examples show that (i) accurate results are obtained using relatively coarse grids; and (ii) condition numbers of the system matrix are relatively low. In the following chapters, 1D-IRBFNs are further developed for the simulation of fluid-flow problems.

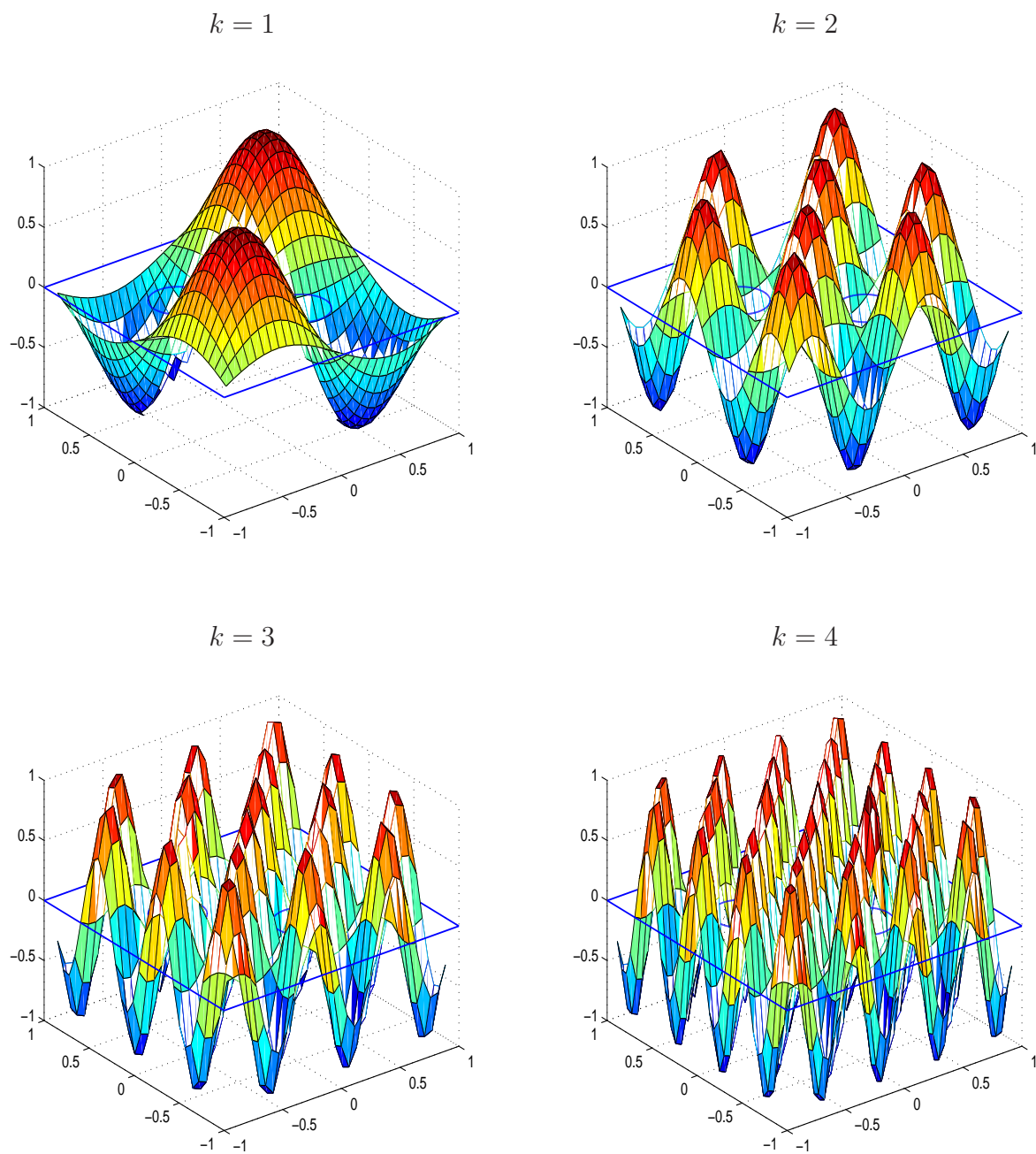


Figure 2.9: Example 3 (initial-value problem): 1D-IRBFN solution for four values of  $k$  at  $t = 1$  using a grid of  $32 \times 32$ .

# Chapter 3

## 1D-integrated-RBFN discretisation of stream-function - vorticity ( $\psi - \omega$ ) formulation in multiply-connected domains

This chapter presents a new numerical collocation procedure, based on Cartesian grids and one-dimensional integrated radial-basis-function networks (1D-IRBFNs), for the simulation of natural convection defined in two-dimensional multiply-connected domains and governed by the stream-function - vorticity - temperature ( $\psi - \omega - T$ ) formulation. Special emphasis is placed on the handling of vorticity values at boundary points that do not coincide with grid nodes. A suitable formula for computing vorticity boundary conditions, which is based on the approximations with respect to one coordinate direction only, is proposed. Normal derivative boundary conditions for the stream function are forced to be satisfied identically. Several test problems, including natural convection in an annulus between square and circular cylinders, are considered to investigate the accuracy of the proposed technique.

## 3.1 Introduction

Natural convection, where the motion of a fluid is caused by the combination of density variations and gravity, can be governed by the coupling of the momentum (velocity field) and energy (temperature field) equations within the Boussinesq approximation. In the momentum equation, the fluid is assumed to have a constant density except for the generation of buoyancy forces and in the energy equation, one neglects the viscous dissipation and compressibility effects. The governing equations can be written in different dependent variables, including the velocity - pressure - temperature ( $\mathbf{u} - p - T$ ), stream-function - vorticity - temperature ( $\psi - \omega - T$ ), and stream-function - temperature ( $\psi - T$ ) formulations. Each formulation has some strengths and weaknesses from a computational point of view.

With the introduction of the stream-function variable, the pressure variable does not have to be considered, resulting in an easy implementation. However, several issues arise, to which special attention should be paid. For example, in the  $\psi - T$  approach, one has to cope with fourth-order derivatives and double boundary conditions. Fourth-order systems are known to have higher matrix condition numbers than second-order systems. Errors for approximating higher-order derivatives are generally larger. In the implementation of double boundary conditions, special treatments are required because of two values given at a boundary point. For the  $\psi - \omega - T$  formulation, one has to derive computational boundary conditions for the vorticity transport equation. The boundary vorticity values are defined through the Poisson equation, which needs to be solved discretely on the boundaries. The  $\psi - \omega - T$  approach requires the approximations for derivatives of order up to 2 (instead of 4), leading to a significant improvement in the matrix condition number over the  $\psi - T$  approach. This feature is very attractive in dealing with flows with a fine structure as a large number of nodes is usually required for an accurate simulation.

Numerical solutions to these formulations can be achieved by means of discretisation, followed by solutions of the resultant algebraic equations. Results have been reported using different numerical techniques such as FDMs, FEMs, FVMs, BEMs, meshless methods and spectral methods (e.g. Kuehn and Goldstein, 1976); Manzari, 1999; Glakpe et al., 1986; Hribersek and Skerget, 1999; Šarler et al., 2004; Šarler, 2005; Kosec and Šarler, 2008a; Shu, 1999). These methods are based on a finite-element mesh, a finite-volume mesh, a Cartesian grid or a set of unstructured points. When dealing with non-rectangular domains, conventional FDMs and pseudospectral techniques require coordinate transformations to convert the physical domains into rectangular ones (e.g. Moukalled and Acharya, 1996; Shu and Zhu, 2002). The relationships between the physical and computational coordinates are given by a set of algebraic equations or a set of PDEs, depending on the level of complexity of the geometry. These transformation processes are, in general, complicated. It is very desirable that one is able to retain the PDEs in their original form (i.e. in terms of  $x$  and  $y$  coordinates) and then solve them on a Cartesian grid. Such a numerical solution procedure can be very economical. The use of Cartesian grids for solving problems defined on irregular domains has received much increased attention in recent decades.

It has been recognised that RBFN-based methods are easy to implement and capable of achieving a high level of accuracy using a relatively-small number of nodes. These approximators can work well with gridded and scattered points. RBFN solutions to fluid flow problems can be found in Ding et al., 2006; Divo and Kassab, 2006, 2007, 2008; Kosec and Šarler, 2008a,b; Orsini et al., 2009; Šarler et al., 2004; Šarler, 2005, 2009; Zahab et al., 2009; Erhart et al. (2010). One can construct the RBFN approximations through differentiation or integration. Since integration is a smoothing operator, the latter has higher approximation power than the former in the handling of derivative functions (e.g. Mai-Duy and Tran-Cong, 2003; Mai-Duy et al., 2008; Mai-Duy and Tanner, 2005).

This chapter reports a Cartesian-grid-based collocation technique incorporating 1D-IRBFNs on grid lines for the simulation of natural convection in multiply-connected domains. The technique combines strengths of the three approaches, namely 1D-IRBFNs (high-order accuracy), Cartesian grids (easy preprocessing) and the  $\psi - \omega - T$  formulation (low-order system). It should be emphasised that conventional RBFN methods lead to fully-populated matrices that tend to become ill-conditioned quickly with increasing numbers of RBFs. Instead of using conventional schemes, 1D-IRBFN approximation schemes (Mai-Duy and Tran-Cong, 2007) are utilised in the present work. We take the governing equations in the  $\psi - \omega - T$  formulation. A new formula for deriving computational vorticity boundary conditions on a Cartesian grid is developed. First derivatives of the stream function along the boundaries are incorporated into computational vorticity boundary values by means of integration constants. The present IRBFN approximations are constructed to satisfy all boundary conditions identically. The matrix condition number is significantly improved over that produced by the  $\psi - T$  formulation. Since there are no coordinate transformations required, the present technique works in a similar fashion for all domain shapes. Results obtained are compared well with available numerical data in literature.

The remainder of the chapter is organised as follows. Section 3.2 gives a brief review of the governing equations. In Section 3.3, the proposed technique is described. Emphasis is placed on the development of a novel formula for handling vorticity boundary conditions at irregular boundary points. Numerical results are presented in Section 3.4. Section 3.5 concludes the chapter.

## 3.2 Governing equations

The  $\psi - \omega - T$  formulation is used here. The non-dimensional basic equations for natural convection under the Boussinesq approximation in the Cartesian

$x - y$  coordinate system can be written as (e.g. Ostrach, 1988)

$$\frac{\partial^2 \psi}{\partial x^2} + \frac{\partial^2 \psi}{\partial y^2} = \omega, \quad (3.1)$$

$$\frac{\partial \omega}{\partial t} + u \frac{\partial \omega}{\partial x} + v \frac{\partial \omega}{\partial y} = \sqrt{\frac{Pr}{Ra}} \left( \frac{\partial^2 \omega}{\partial x^2} + \frac{\partial^2 \omega}{\partial y^2} \right) - \frac{\partial T}{\partial x}, \quad (3.2)$$

$$\frac{\partial T}{\partial t} + u \frac{\partial T}{\partial x} + v \frac{\partial T}{\partial y} = \frac{1}{\sqrt{RaPr}} \left( \frac{\partial^2 T}{\partial x^2} + \frac{\partial^2 T}{\partial y^2} \right), \quad (3.3)$$

where  $\psi$  is the stream function,  $\omega$  the vorticity,  $T$  the temperature,  $t$  the time,  $u$  and  $v$  the velocity components, and  $Pr$  and  $Ra$  the Prandtl and Rayleigh numbers defined as  $Pr = \nu/\alpha$  and  $Ra = \beta g \Delta T L^3 / \alpha \nu$ , in which  $\nu$  is the kinematic viscosity,  $\alpha$  the thermal diffusivity,  $\beta$  the thermal expansion coefficient and  $g$  the gravity, respectively. In this dimensionless scheme,  $L$ ,  $\Delta T$  (temperature difference),  $U = \sqrt{gL\beta\Delta T}$  and  $(L/U)$ , are taken as scale factors for length, temperature, velocity and time, respectively. Here, the velocity scale is chosen in such a way that the buoyancy and inertial forces are balanced (e.g. Ostrach, 1988).

The velocity components are defined in terms of the stream function as

$$u = \frac{\partial \psi}{\partial y}, \quad v = -\frac{\partial \psi}{\partial x}.$$

The given velocity boundary conditions can be transformed into two boundary conditions on the stream function and its normal derivative

$$\psi = \gamma, \quad \frac{\partial \psi}{\partial n} = \xi,$$

where  $n$  is the direction normal to the boundary, and  $\gamma$  and  $\xi$  prescribed functions. In the case of fixed concentric cylinders, non-slip boundary conditions usually lead to  $\gamma = 0$  and  $\xi = 0$ .

### 3.3 The present technique

The fluid domain is simply embedded in a Cartesian grid. Grid nodes outside the domain are removed from the computations. Boundary points are generated by the intersection of the grid lines and the boundaries of the domain. It can be seen that boundary conditions are over-prescribed for the stream-function equation (3.1) and under-prescribed for the vorticity equation (3.2). Normal derivative boundary conditions for the stream function are utilised to derive boundary conditions for the vorticity. For natural-convection problems employed in this study, boundary conditions for the energy equation (3.3) are the temperature values. Consequently, the three governing equations are all subject to Dirichlet boundary conditions. On a grid line, 1D-IRBFNs are employed to represent the stream function, vorticity and temperature variables.

#### 3.3.1 1D-IRBFN discretisation

All PDEs in the present governing equations are of second order. Consider an  $x$ -grid line. Making use of (2.5)-(2.9) with  $p = 2$ , second-order derivative of the field variable  $f$  along a grid line can be decomposed into RBFs

$$\frac{\partial^2 f(x)}{\partial x^2} = \sum_{i=1}^m w_i g_i(x) = \sum_{i=1}^m w_i I_i^{(2)}(x), \quad (3.4)$$

where  $m$  is the number of RBFs,  $\{g_i(x)\}_{i=1}^m \equiv \{I_i^{(2)}(x)\}_{i=1}^m$  the set of RBFs,  $\{w_i\}_{i=1}^m$  the set of weights to be found and  $f$  represents  $\psi$ ,  $\omega$  and  $T$ . Approximate expressions for first-order derivative and the field variable are then obtained

through integration

$$\frac{\partial f(x)}{\partial x} = \sum_{i=1}^m w_i I_i^{(1)}(x) + c_1, \quad (3.5)$$

$$f(x) = \sum_{i=1}^m w_i I_i^{(0)}(x) + c_1 x + c_2, \quad (3.6)$$

where  $I_i^{(1)}(x) = \int I_i^{(2)}(x) dx$  and  $I_i^{(0)}(x) = \int I_i^{(1)}(x) dx$ . As shown in Figure

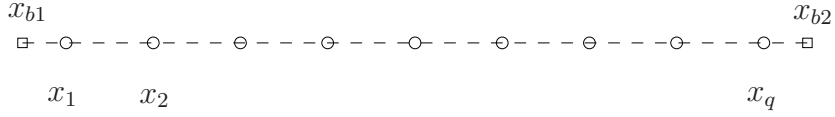


Figure 3.1: Points on a grid line consist of interior points  $x_i$  ( $\circ$ ) and boundary points  $x_{bi}$  ( $\square$ ).

3.1, a grid line contains two sets of points. The first set consists of  $q$  interior points that are also the grid nodes (regular nodes). The function values at the interior points ( $\{x_i\}_{i=1}^q$ ) are unknown. The second set is formed with the two boundary nodes that do not generally coincide with the grid nodes (irregular nodes). At the boundary nodes ( $x_{b1}$  and  $x_{b2}$ ), the function values are given (Dirichlet boundary conditions). The boundary conditions are incorporated into the IRBFN approximations through the process of conversion of the network-weight space into the physical space. Collocating (3.6) at the nodal points yields

$$\begin{pmatrix} \widehat{f} \\ \widehat{f}_b \end{pmatrix} = \widehat{\mathcal{I}}_{[2]}^{(0)} \begin{pmatrix} \widehat{w} \\ c_1 \\ c_2 \end{pmatrix}, \quad (3.7)$$

where

$$\begin{aligned}\widehat{f} &= (f(x_1), f(x_2), \dots, f(x_q))^T, \\ \widehat{f}_b &= (f(x_{b1}), f(x_{b2}))^T, \\ \widehat{w} &= (w_1, w_2, \dots, w_m)^T, \\ \widehat{\mathcal{I}}_{[2]}^{(0)} &= \begin{bmatrix} I_1^{(0)}(x_1) & I_2^{(0)}(x_1) & \cdots & I_m^{(0)}(x_1) & x_1 & 1 \\ I_1^{(0)}(x_2) & I_2^{(0)}(x_2) & \cdots & I_m^{(0)}(x_2) & x_2 & 1 \\ \vdots & \vdots & \ddots & \vdots & \vdots & \vdots \\ I_1^{(0)}(x_q) & I_2^{(0)}(x_q) & \cdots & I_m^{(0)}(x_q) & x_q & 1 \\ I_1^{(0)}(x_{b1}) & I_2^{(0)}(x_{b1}) & \cdots & I_m^{(0)}(x_{b1}) & x_{b1} & 1 \\ I_1^{(0)}(x_{b2}) & I_2^{(0)}(x_{b2}) & \cdots & I_m^{(0)}(x_{b2}) & x_{b2} & 1 \end{bmatrix},\end{aligned}$$

$m = q + 2$  and the subscript [2] indicates that the integral formulation starts with second-order derivatives. Solving (3.7) for the coefficient vector including the two integration constants results in

$$\begin{pmatrix} \widehat{w} \\ c_1 \\ c_2 \end{pmatrix} = \left( \widehat{\mathcal{I}}_{[2]}^{(0)} \right)^{-1} \begin{pmatrix} \widehat{f} \\ \widehat{f}_b \end{pmatrix}, \quad (3.8)$$

where  $\left( \widehat{\mathcal{I}}_{[2]}^{(0)} \right)^{-1}$  is the generalised inverse of  $\widehat{\mathcal{I}}_{[2]}^{(0)}$ .

The values of the first and second derivatives of  $f$  with respect to  $x$  at the interior points are thus computed in terms of nodal variable values

$$\begin{pmatrix} \frac{\partial f(x_1)}{\partial x} \\ \frac{\partial f(x_2)}{\partial x} \\ \vdots \\ \frac{\partial f(x_q)}{\partial x} \end{pmatrix} = \widehat{\mathcal{I}}_{[2]}^{(1)} \left( \widehat{\mathcal{I}}_{[2]}^{(0)} \right)^{-1} \begin{pmatrix} \widehat{f} \\ \widehat{f}_b \end{pmatrix}, \quad (3.9)$$

and

$$\begin{pmatrix} \frac{\partial^2 f(x_1)}{\partial x^2} \\ \frac{\partial^2 f(x_2)}{\partial x^2} \\ \vdots \\ \frac{\partial^2 f(x_q)}{\partial x^2} \end{pmatrix} = \widehat{\mathcal{I}}_{[2]}^{(2)} \left( \widehat{\mathcal{I}}_{[2]}^{(0)} \right)^{-1} \begin{pmatrix} \widehat{f} \\ \widehat{f}_b \end{pmatrix}, \quad (3.10)$$

where

$$\widehat{\mathcal{I}}_{[2]}^{(1)} = \begin{bmatrix} I_1^{(1)}(x_1) & I_2^{(1)}(x_1) & \cdots & I_m^{(1)}(x_1) & 1 & 0 \\ I_1^{(1)}(x_2) & I_2^{(1)}(x_2) & \cdots & I_m^{(1)}(x_2) & 1 & 0 \\ \vdots & \vdots & \ddots & \vdots & \vdots & \vdots \\ I_1^{(1)}(x_q) & I_2^{(1)}(x_q) & \cdots & I_m^{(1)}(x_q) & 1 & 0 \end{bmatrix},$$

and

$$\widehat{\mathcal{I}}_{[2]}^{(2)} = \begin{bmatrix} g_1(x_1) & g_2(x_1) & \cdots & g_m(x_1) & 0 & 0 \\ g_1(x_2) & g_2(x_2) & \cdots & g_m(x_2) & 0 & 0 \\ \vdots & \vdots & \ddots & \vdots & \vdots & \vdots \\ g_1(x_q) & g_2(x_q) & \cdots & g_m(x_q) & 0 & 0 \end{bmatrix}.$$

Expressions (3.9) and (3.10) can be rewritten in compact form

$$\frac{\widehat{\partial} f}{\partial x} = \widehat{\mathcal{D}}_{1x} \widehat{f} + \widehat{k}_{1x}, \quad (3.11)$$

and

$$\frac{\widehat{\partial}^2 f}{\partial x^2} = \widehat{\mathcal{D}}_{2x} \widehat{f} + \widehat{k}_{2x}, \quad (3.12)$$

where  $\widehat{\mathcal{D}}_{1x}$  and  $\widehat{\mathcal{D}}_{2x}$  are the first- and second-order differentiation matrices in the physical space, and  $\widehat{k}_{1x}$  and  $\widehat{k}_{2x}$  are the known vectors whose components are functions of given boundary conditions.

In the same manner, one can obtain the IRBFN expressions for  $\partial f / \partial y$  and

$\partial^2 f / \partial y^2$  at the interior points along a vertical grid line.

As with FDMs, FVMs, BEMs and FEMs, the IRBFN approximations will be gathered together to form the global matrices for the discretisation of the PDE.

### 3.3.2 A new formula for computing vorticity boundary conditions

The values of the vorticity on the boundaries can be computed via

$$\omega_b = \frac{\partial^2 \psi_b}{\partial x^2} + \frac{\partial^2 \psi_b}{\partial y^2}, \quad (3.13)$$

where the subscript  $b$  is used to indicate the boundary quantities. The handling of  $\omega_b$  thus involves the evaluation of second-order derivatives of the stream function in both  $x$  and  $y$  directions.

For regular boundary points (also grid nodes), one can apply (3.13) directly. The  $x$ - and  $y$ -grid lines passing through those points can be used for computing  $\partial^2 \psi_b / \partial x^2$  and  $\partial^2 \psi_b / \partial y^2$ , respectively. However, in general, the boundary points do not coincide with the grid nodes and hence they lie on either  $x$ - or  $y$ -grid lines. Information about  $\psi$  is thus given explicitly in one coordinate direction only. A great challenge here is how to compute second derivatives of  $\psi$  in (3.13) with respect to the direction without a grid line. A new formula to overcome this difficulty is proposed as follows.

Consider a curved boundary, along which the values for  $\psi$  and  $\partial\psi/\partial n$  are prescribed (Figure 3.2). It can be seen that the values of  $\partial\psi/\partial x$  and  $\partial\psi/\partial y$  on the boundary can then be obtained in a straightforward manner. Let  $s$  be the arc length of the boundary. By introducing an interpolating scheme (e.g. 1D-IRBFNs), one is able to derive derivatives of  $\partial\psi/\partial x$  and  $\partial\psi/\partial y$  with respect to  $s$  such as  $\partial^2\psi/\partial x\partial s$  and  $\partial^2\psi/\partial y\partial s$ .

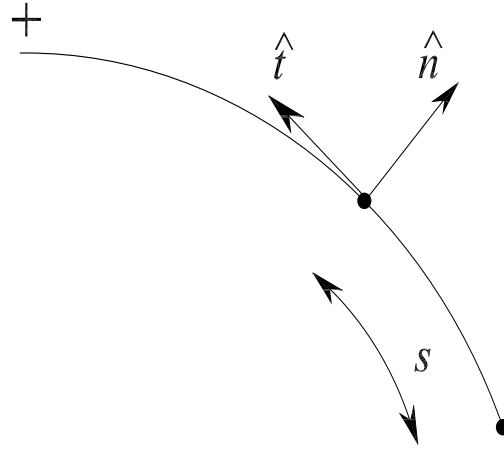


Figure 3.2: A curved boundary.

A tangential derivative of a function  $f$  at a boundary point can be computed using the following formula

$$\frac{\partial f}{\partial s} = \frac{\partial f}{\partial x} t_x + \frac{\partial f}{\partial y} t_y, \quad (3.14)$$

where  $t_x$  and  $t_y$  are the two  $x$  and  $y$  components of the unit vector  $\hat{t}$  tangential to the curve ( $t_x = \partial x / \partial s$  and  $t_y = \partial y / \partial s$ ).

Replacing  $f$  with  $\partial \psi_b / \partial x$ , one has

$$\frac{\partial^2 \psi_b}{\partial x \partial s} = \frac{\partial^2 \psi_b}{\partial x^2} t_x + \frac{\partial^2 \psi_b}{\partial x \partial y} t_y, \quad (3.15)$$

or

$$\frac{\partial^2 \psi_b}{\partial x \partial y} = \frac{1}{t_y} \left( \frac{\partial^2 \psi_b}{\partial x \partial s} - \frac{\partial^2 \psi_b}{\partial x^2} t_x \right), \quad (3.16)$$

where  $\partial^2 \psi_b / \partial x \partial s$  is considered as a known quantity.

Similarly, taking  $f$  as  $\partial \psi_b / \partial y$  results in

$$\frac{\partial^2 \psi_b}{\partial x \partial y} = \frac{1}{t_x} \left( \frac{\partial^2 \psi_b}{\partial y \partial s} - \frac{\partial^2 \psi_b}{\partial y^2} t_y \right), \quad (3.17)$$

where  $\partial^2\psi_b/\partial y\partial s$  is a known value.

From (3.16) and (3.17), one can derive the relationship between  $\partial^2\psi/\partial x^2$  and  $\partial^2\psi/\partial y^2$  at a boundary point

$$\frac{1}{t_y} \left( \frac{\partial^2\psi_b}{\partial x\partial s} - \frac{\partial^2\psi_b}{\partial x^2} t_x \right) = \frac{1}{t_x} \left( \frac{\partial^2\psi_b}{\partial y\partial s} - \frac{\partial^2\psi_b}{\partial y^2} t_y \right). \quad (3.18)$$

Consider an  $x$ -grid line. The interpolating scheme employed along this line does not facilitate the computation of second-order derivative of  $\psi$  with respect to the  $y$  coordinate. However, such a derivative at a boundary point can be found by using (3.18)

$$\frac{\partial^2\psi_b}{\partial y^2} = \left( \frac{t_x}{t_y} \right)^2 \frac{\partial^2\psi_b}{\partial x^2} + q_y, \quad (3.19)$$

where  $q_y$  is a known quantity defined by

$$q_y = -\frac{t_x}{t_y^2} \frac{\partial^2\psi_b}{\partial x\partial s} + \frac{1}{t_y} \frac{\partial^2\psi_b}{\partial y\partial s}. \quad (3.20)$$

By substituting (3.19) into (3.13), a boundary condition for the vorticity at a boundary point on a horizontal grid line will be computed by

$$\omega_b = \left[ 1 + \left( \frac{t_x}{t_y} \right)^2 \right] \frac{\partial^2\psi_b}{\partial x^2} + q_y, \quad (3.21)$$

where only the approximations in the  $x$  direction are needed.

In the same manner, on a vertical grid line, a boundary condition for the vorticity at a boundary point will be computed by

$$\omega_b = \left[ 1 + \left( \frac{t_y}{t_x} \right)^2 \right] \frac{\partial^2\psi_b}{\partial y^2} + q_x, \quad (3.22)$$

where  $q_x$  is a known quantity defined by

$$q_x = -\frac{t_y}{t_x^2} \frac{\partial^2 \psi_b}{\partial y \partial s} + \frac{1}{t_x} \frac{\partial^2 \psi_b}{\partial x \partial s}. \quad (3.23)$$

The boundary conditions for the vorticity are thus written in terms of second derivative of the stream function with respect to  $x$  or  $y$  only.

### 3.3.3 Numerical implementation of vorticity boundary conditions

As mentioned earlier, normal derivative boundary conditions for the stream function are used for solving the vorticity transport equation. As a result, the values of  $\partial\psi/\partial x$  and  $\partial\psi/\partial y$  at the boundary points have to be incorporated into (3.21) and (3.22), respectively.

It is well known that the computational vorticity boundary conditions strongly affect the performance of a numerical discretisation scheme. To evaluate the values of a second-order derivative using integrated RBFs only, the 1D-IRBFN scheme of at least second order needs to be employed. As shown in (Mai-Duy and Tanner, 2005), higher-order IRBFNs can give more accurate results. In this study, we attempt to employ 1D-IRBFNs of order 2 (Scheme 1) and 4 (Scheme 2), in which second and fourth derivatives of  $\psi$  are respectively decomposed into RBFs, to evaluate  $\partial^2\psi/\partial x^2$  and  $\partial^2\psi/\partial y^2$  in (3.21) and (3.22). A distinguishing feature here is that derivative boundary values,  $\partial\psi/\partial x$  and  $\partial\psi/\partial y$ , are incorporated into the IRBFN approximations by means of the constants of integration.

Along an  $x$ -grid line, the process of conversion of the network-weight space

into the physical space can be described as follows.

$$\widehat{\mathcal{B}} \begin{pmatrix} \widehat{w} \\ \widehat{c} \end{pmatrix} = \begin{pmatrix} \widehat{\psi} \\ \widehat{\psi}_b \\ \frac{\widehat{\partial\psi_b}}{\partial x} \end{pmatrix}, \quad (3.24)$$

where  $\widehat{c}$  is a vector of integration constants,  $\widehat{w}$  and  $\widehat{\psi}$  are defined as before,  $\widehat{\psi}_b = (\psi(x_{b1}), \psi(x_{b2}))^T$ ,

$$\frac{\widehat{\partial\psi_b}}{\partial x} = \left( \frac{\partial\psi(x_{b1})}{\partial x}, \frac{\partial\psi(x_{b2})}{\partial x} \right)^T,$$

and

$$\widehat{\mathcal{B}} = \begin{pmatrix} \widehat{\mathcal{B}}_1 \\ \widehat{\mathcal{B}}_2 \end{pmatrix},$$

in which

$$\widehat{\mathcal{B}}_1 = \widehat{\mathcal{I}}_{[2]}^{(0)},$$

$$\widehat{\mathcal{B}}_2 = \begin{bmatrix} I_1^{(1)}(x_{b1}) & I_2^{(1)}(x_{b1}) & \cdots & I_m^{(1)}(x_{b1}) & 1 & 0 \\ I_1^{(1)}(x_{b2}) & I_2^{(1)}(x_{b2}) & \cdots & I_m^{(1)}(x_{b2}) & 1 & 0 \end{bmatrix},$$

for Scheme 1, and

$$\widehat{\mathcal{B}}_1 = \widehat{\mathcal{I}}_{[4]}^{(0)} = \begin{bmatrix} I_1^{(0)}(x_1) & I_2^{(0)}(x_1) & \cdots & I_m^{(0)}(x_1) & x_1^3/6 & x_1^2/2 & x_1 & 1 \\ I_1^{(0)}(x_2) & I_2^{(0)}(x_2) & \cdots & I_m^{(0)}(x_2) & x_2^3/6 & x_2^2/2 & x_2 & 1 \\ \vdots & \vdots & \ddots & \vdots & \vdots & \vdots & \vdots & \vdots \\ I_1^{(0)}(x_m) & I_2^{(0)}(x_m) & \cdots & I_m^{(0)}(x_m) & x_m^3/6 & x_m^2/2 & x_m & 1 \end{bmatrix},$$

$$\widehat{\mathcal{B}}_2 = \begin{bmatrix} I_1^{(1)}(x_{b1}) & I_2^{(1)}(x_{b1}) & \cdots & I_m^{(1)}(x_{b1}) & x_{b1}^2/2 & x_{b1} & 1 & 0 \\ I_1^{(1)}(x_{b2}) & I_2^{(1)}(x_{b2}) & \cdots & I_m^{(1)}(x_{b2}) & x_{b2}^2/2 & x_{b2} & 1 & 0 \end{bmatrix},$$

for Scheme 2, where  $I_i^{(4)}(x) = g_i(x)$ ,  $I_i^{(3)}(x) = \int I_i^{(4)}(x)$ ,  $\cdots$ ,  $I_i^{(0)}(x) = \int I_i^{(1)}(x)$ .

Taking (3.24) into account, second derivatives of  $\psi$  at the two boundary points

can be expressed in terms of the values of  $\psi$  at every point on the grid line and the values of  $\partial\psi/\partial x$  at the two boundary points

$$\frac{\widehat{\partial^2\psi_b}}{\partial x^2} = \widehat{\mathcal{D}}\widehat{\mathcal{B}}^{-1} \begin{pmatrix} \widehat{\psi} \\ \widehat{\psi_b} \\ \frac{\widehat{\partial\psi_b}}{\partial x} \end{pmatrix}, \quad (3.25)$$

where

$$\widehat{\mathcal{D}} = \begin{bmatrix} g_1(x_{b1}) & g_2(x_{b1}) & \cdots & g_m(x_{b1}) & 0 & 0 \\ g_1(x_{b2}) & g_2(x_{b2}) & \cdots & g_m(x_{b2}) & 0 & 0 \end{bmatrix}$$

for Scheme 1, and

$$\widehat{\mathcal{D}} = \begin{bmatrix} I_1^{(2)}(x_{b1}) & I_2^{(2)}(x_{b1}) & \cdots & I_m^{(2)}(x_{b1}) & x_{b1} & 1 & 0 & 0 \\ I_1^{(2)}(x_{b2}) & I_2^{(2)}(x_{b2}) & \cdots & I_m^{(2)}(x_{b2}) & x_{b2} & 1 & 0 & 0 \end{bmatrix}$$

for Scheme 2.

It should be emphasised that the IRBFN approximation for  $\partial^2\psi/\partial x^2$  satisfies normal derivative of  $\psi$  at the two boundary points identically. Substituting (3.25) into (3.21), one is able to obtain the boundary conditions for the vorticity equation.

The process of computing the values of the vorticity at the two boundary points on a vertical line is similar to that on a horizontal line.

### 3.3.4 Solution procedure

The three governing equations must be solved simultaneously to find the values of the temperature, vorticity and stream function at the discrete points within the domain. In this chapter, a time marching approach is adopted and at each time step, to minimise the memory requirement, the three equations are solved

in a sequential manner. The solution procedure involves the following main steps.

1. Guess the distributions of  $T, \omega$  and  $\psi$ .
2. Discretise the governing equations in time using a first-order accurate finite-difference scheme, where the diffusive and convective terms are treated implicitly and explicitly, respectively.
3. Discretise the governing equations in space using 1D-IRBFNs. Since the differentiation matrices are the same for all variables, the construction process only needs to be carried out for one variable. The system matrices, which involve the IRBFN approximations for the Laplacian operator in the governing equations, stay the same during the iterative process. All equations are subject to Dirichlet boundary conditions.
4. Solve the energy equation (3.3) for  $T$ .
5. Derive computational boundary conditions for  $\omega$ .
6. Solve the vorticity equation (3.1) for  $\omega$ .
7. Solve the stream-function equation (3.2) for  $\psi$ .
8. Check to see whether the solution has reached a steady state using the following convergence measure ( $CM$ )

$$CM = \frac{\sqrt{\sum_{i=1}^{n_{ip}} \left( \psi_i^{(k)} - \psi_i^{(k-1)} \right)^2}}{\sqrt{\sum_{i=1}^{n_{ip}} \left( \psi_i^{(k)} \right)^2}} < \epsilon, \quad (3.26)$$

where  $n_{ip}$  is the number of interior points,  $k$  the time level and  $\epsilon$  the tolerance (in this study,  $\epsilon$  is taken to be  $10^{-12}$ ).

9. If it is not satisfied, advance time step and repeat from step 4. Otherwise, stop the computation and output the results.

### 3.4 Numerical examples

The first two examples, for which analytic solutions are available, are used to verify the vorticity boundary formula and its numerical implementations on both simply- and multiply-connected domains. In the last two examples, the proposed technique is applied for the simulation of natural convection in the region between two concentric cylinders. The thermal boundary conditions are prescribed as  $T = 0$  and  $T = 1$  along the stationary outer and inner walls, respectively.

The present technique implements the multiquadric (MQ) basis function whose form is

$$g_i(x) = \sqrt{(x - c_i)^2 + a_i^2}, \quad (3.27)$$

where  $c_i$  and  $a_i$  are the centre and the width of the  $i$ th MQ function.

For all numerical examples presented in this chapter, the problem domain is discretised with a uniform Cartesian grid. The width of the  $i$ th MQ-RBF,  $a_i$ , is simply chosen to be the grid spacing  $h$  (grid size), and the interior points that fall very close to the boundary (within a distance of  $h/8$ ) are removed from the set of nodal points. In the first two examples, the accuracy of an approximation scheme is measured by means of the discrete relative  $L_2$  norm of the error defined as

$$Ne = \frac{\sqrt{\sum_{i=1}^M (f_i^e - f_i)^2}}{\sqrt{\sum_{i=1}^M (f_i^e)^2}}, \quad (3.28)$$

where  $M$  is the number of unknown nodal values of  $f$ , and  $f^e$  and  $f$  are the exact and approximate solutions, respectively. Another important measure is the convergence rate  $\alpha$  of the solution with respect to the refinement of spatial

discretisation

$$Ne(h) \approx \gamma h^\alpha = O(h^\alpha), \quad (3.29)$$

in which  $\alpha$  and  $\gamma$  are exponential model's parameters. Given a set of observations, these parameters can be found by the general linear least squares technique.

### 3.4.1 Example 1: Circular shape domain

The present technique is first verified through the solution of the following test problem governed by

$$\frac{\partial^2 \psi}{\partial x^2} + \frac{\partial^2 \psi}{\partial y^2} = \omega, \quad (3.30)$$

$$\frac{\partial^2 \omega}{\partial x^2} + \frac{\partial^2 \omega}{\partial y^2} = b(x, y), \quad (3.31)$$

on a unit circular domain with the boundary conditions in terms of  $\psi$  and  $\partial\psi/\partial n$ . The exact solution of this problem is taken as

$$\psi_e = \cos(\sqrt{x^2 + y^2}), \quad (3.32)$$

from which the driving function  $b(x, y)$  and the boundary conditions can be derived analytically. The problem domain and its typical discretisation are shown in Figure 3.3, while the exact solution is shown in Figure 3.4. It can be seen that the two components of the unit vector  $\hat{t}$  tangential to the boundary of the present domain are simply computed by

$$t_x = \frac{-y}{\sqrt{x^2 + y^2}}, \quad (3.33)$$

$$t_y = \frac{x}{\sqrt{x^2 + y^2}}. \quad (3.34)$$

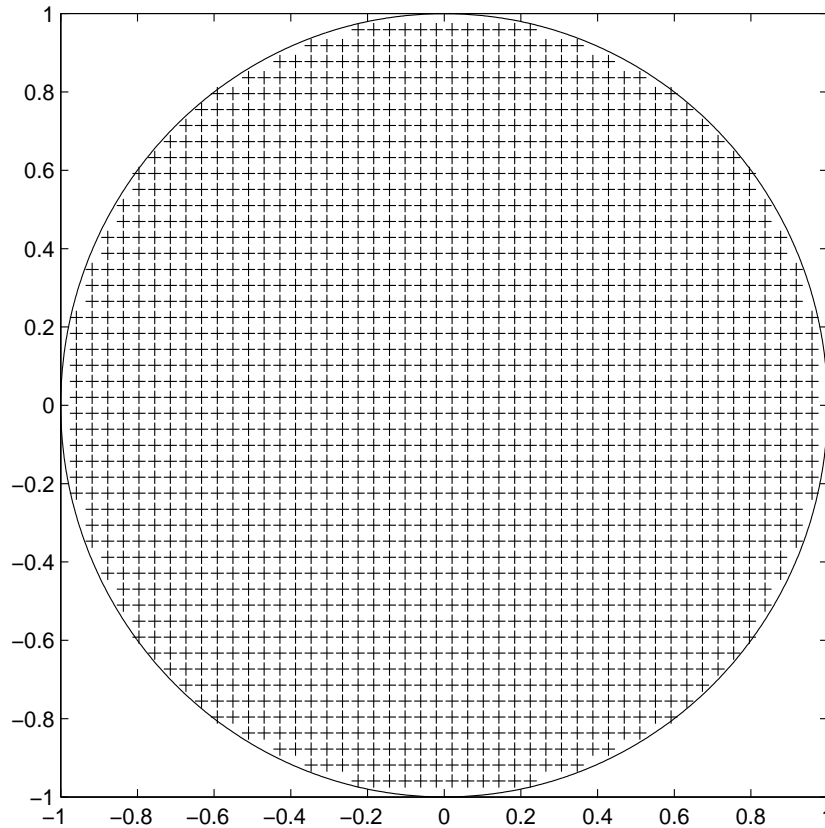


Figure 3.3: Example 1: Domain of interest and its typical discretisation. It is noted that the nodes outside the domain are removed.

Expressions for the vorticity at the boundary nodes on the  $x$ - and  $y$ -grid lines thus reduce to

$$\omega_b = \left[ 1 + \left( \frac{y}{x} \right)^2 \right] \frac{\partial^2 \psi_b}{\partial x^2} + q_y, \quad (3.35)$$

$$\omega_b = \left[ 1 + \left( \frac{x}{y} \right)^2 \right] \frac{\partial^2 \psi_b}{\partial y^2} + q_x, \quad (3.36)$$

each of which only requires the approximation of second-order derivative of  $\psi$  with respect to one coordinate direction. Both Scheme 1 and Scheme 2 are employed to compute the above expressions.

Two investigations are conducted here: (i) the accuracy of Scheme 1 and Scheme 2 for approximating  $\partial^2 \psi / \partial x^2$  in (3.35); and (ii) the accuracy of the RBF solution to the PDEs.

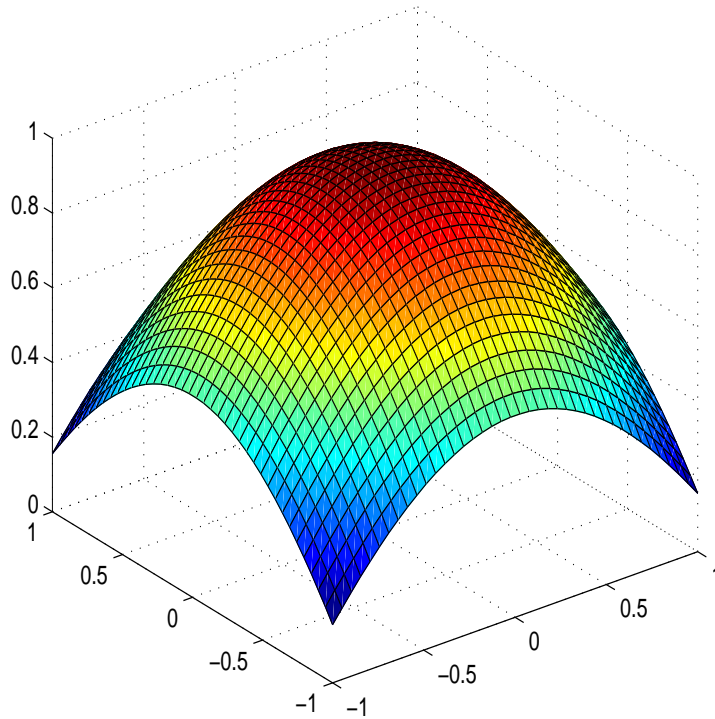


Figure 3.4: Example 1 (circular shape domain): Exact solution. It is noted that the exact solution is plotted over the square covering the problem domain.

For the former, calculations are carried out for various grids from  $5 \times 5$  to  $90 \times 90$ . Results of  $Ne$  obtained by the two different order interpolating schemes are displayed in Table 3.1, which shows that Scheme 2 gives much more accurate results than Scheme 1. Scheme 2 is thus recommended for use in practice.

For the latter, a number of grids, namely  $(12 \times 12, 22 \times 22, \dots, 62 \times 62)$ , are employed to study the convergence behaviour of the solution. Results concerning the condition number of the system matrix, denoted by  $\text{cond}(A)$ , and the error  $Ne$  are given in Table 3.2. The present technique produces system matrices with relatively-low condition numbers. For example, the matrix condition number is only  $6.0 \times 10^3$  for a grid of  $62 \times 62$ . It can be seen that the choice of Scheme 1 (1D-IRBFN-2s) and Scheme 2 (1D-IRBFN-4s) for computing  $\omega_b$  in (3.35) and (3.36) has a profound influence on the overall accuracy of the IRBFN solution.

Table 3.1: Example 1( circular shape domain): Errors by 1D-IRBFN-2s (Scheme 1) and 1D-IRBFN-4s (Scheme 2) in the computation of second derivatives of  $\psi$  at the boundary points. It is noted that  $a(b)$  represents  $a \times 10^b$ .

Grid	$Ne$	
	Scheme 1	Scheme 2
$5 \times 5$	3.5(-2)	4(-3)
$10 \times 10$	3.7(-2)	5.3(-4)
$30 \times 30$	6.8(-2)	1.1(-4)
$50 \times 50$	9.6(-2)	9.5(-5)
$70 \times 70$	6.9(-2)	1.9(-5)
$90 \times 90$	7.3(-2)	1.3(-5)

The fourth-order boundary scheme outperforms the second-order one regarding both accuracy and convergence rate. The recommended scheme 2 yields a fast rate of convergence,  $Ne$  of  $O(h^{3.1})$ , in comparison with that of Scheme 1,  $Ne$  of  $O(h^{1.8})$ .

### 3.4.2 Example 2: Multiply-connected domain

This test problem is also governed by the two coupled equations (3.30) and (3.31) with Dirichlet boundary conditions,  $\psi$  and  $\partial\psi/\partial n$ . The driving function is taken as

$$b(x, y) = 256(\pi^2 - 1)^2 [\sin(4\pi x) \cosh(4y) + \cos(4\pi x) \sinh(4y)], \quad (3.37)$$

and the domain of interest is the region lying between a circle of radius  $1/2$  and a square of dimensions  $1/2 \times 1/2$  which are both centered at the origin (Figure 3.5). The exact solution for this problem is

$$\psi_e = \sin(4\pi x) \cosh(4y) - \cos(4\pi x) \sinh(4y). \quad (3.38)$$

Table 3.2: Example 1 (circular shape domain): Overall accuracy of the solution  $\psi$  by the present technique employed with two different computational vorticity boundary schemes, namely Scheme 1 (1D-IRBFN-2s) and Scheme 2 (1D-IRBFN-4s). Condition numbers of the IRBFN system matrix are also included. It is noted that  $h$  is the spacing (grid size) and  $a(b)$  represents  $a \times 10^b$ .

Grid	$Ne(\psi)$		$\text{cond}(A)$
	Scheme 1	Scheme 2	
$12 \times 12$	1.5(-3)	6.5(-5)	8.9(1)
$22 \times 22$	9.4(-4)	1.1(-5)	3.6(2)
$32 \times 32$	7.4(-4)	3.9(-6)	8.0(2)
$42 \times 42$	6.4(-4)	1.4(-6)	2.4(3)
$52 \times 52$	6.4(-4)	6.4(-7)	3.3(3)
$62 \times 62$	4.5(-4)	3.1(-7)	6.0(3)
	$O(h^{1.8})$	$O(h^{3.1})$	

The variation of (3.38) over the extended square domain is plotted in Figure 3.6. A number of uniform grids, ( $10 \times 10, 20 \times 20, \dots, 50 \times 50$ ), are considered. Since inner boundaries are parallel to the  $x$  and  $y$  axes, one can use the original formula for deriving a computational vorticity boundary condition. The streamfunction equation can be rewritten as

$$\omega_b = \frac{\partial^2 \psi_b}{\partial n^2} + \frac{\partial^2 \psi_b}{\partial t^2}, \quad (3.39)$$

where  $\partial^2 \psi_b / \partial t^2$  is a known quantity derived from the boundary conditions for  $\psi$ , and  $\partial^2 \psi_b / \partial n^2$  can be evaluated using a grid line passing through that point. On the outer boundary, the handling of  $\omega_b$  is similar to that in the previous example. For brevity, only the recommended scheme (i.e. Scheme 2) for computing  $\omega_b$  is employed here. Results concerning  $Ne(\psi)$  are given in Table 3.3, from which one can also make remarks that are similar to those in the case of simply-connected domains. It can be seen that the present matrix condition numbers are relatively low and the approximate solution converges fast to the exact solution with  $Ne$  of  $O(h^{3.78})$ .

Table 3.3: Example 2 (multiply-connected domain): Condition numbers of the system matrix and relative  $L_2$  errors of the solution. It is noted that  $h$  is the spacing (grid size) and  $a(b)$  represents  $a \times 10^b$ .

Grid	$Ne$	$\text{cond}(A)$
$10 \times 10$	2.6(-2)	1.2(1)
$20 \times 20$	9.4(-4)	4.5(1)
$30 \times 30$	2.0(-4)	1.0(2)
$40 \times 40$	8.5(-5)	1.8(2)
$44 \times 44$	6.0(-5)	2.5(2)
$50 \times 50$	4.2(-5)	2.9(2)
$O(h^{3.78})$		

### 3.4.3 Example 3: Concentric annulus between two circular cylinders

The present method is now applied to the simulation of buoyancy-driven flow in an annulus between two concentric cylinders which are separated by a distance  $L$ , the inner cylinder heated ( $T = 1$ ) and the outer cylinder cooled ( $T = 0$ ) (Figure 3.7a). A comprehensive review of this problem can be found in (Kuehn and Goldstein, 1976). Most cases have been reported with  $Pr = 0.7$  and  $L/D_i = 0.8$ , in which  $D_i$  is the diameter of the inner cylinder. To these conditions, results by Kuehn and Goldstein (1976) using FDM for  $Ra = 10^2$  to  $Ra = 7 \times 10^4$  are often cited in the literature for comparison purposes. Later on, Shu (1999), who employed a differential quadrature method (DQM), has provided very accurate solutions for the values of  $Ra$  in the range of  $10^2$  to  $5 \times 10^4$ . It is noted that those works required a computational domain be rectangular.

The three governing equations (3.1), (3.2), (3.3) are presently solved with respect to Cartesian coordinates (Figure 3.7a). Numerical simulations are also conducted for  $Pr = 0.7$  and  $L/D_i = 0.8$ . Like in the case of Kuehn and Goldstein (1976), the values of the Rayleigh number varies from  $Ra = 10^2$  to  $Ra = 7 \times 10^4$ , which is broader than those reported in (Shu, 1999). Several

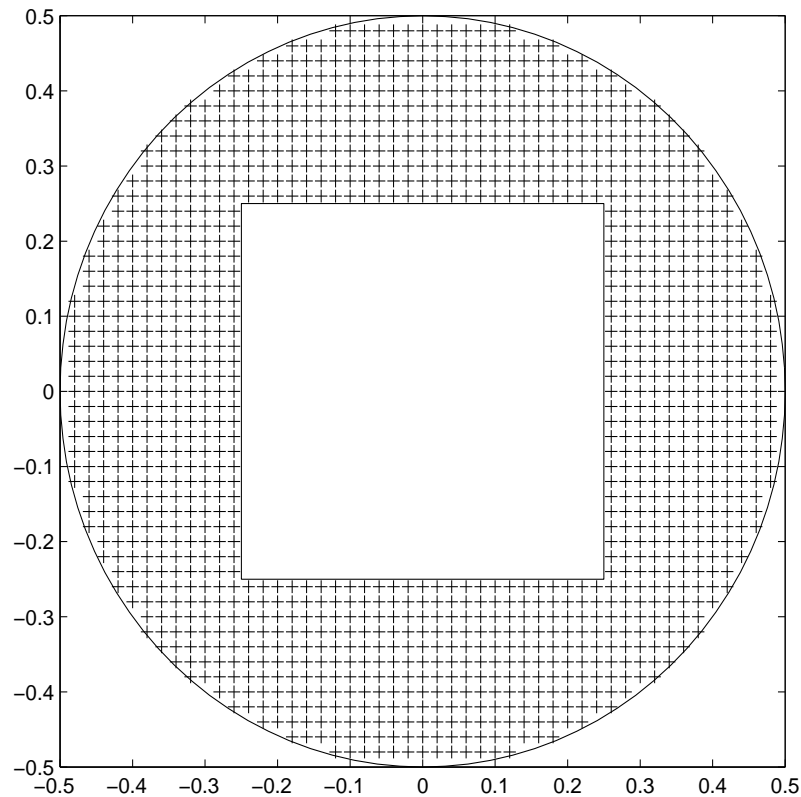


Figure 3.5: Example 2: Multiply-connected domain and its typical discretisation. It is noted that the nodes outside the domain are removed.

grids, namely  $(12 \times 12, 22 \times 22, \dots, 52 \times 52)$ , are employed.

The stream function and its normal derivative are set to zero along the inner and outer cylinders. Expressions (3.35) and (3.36) derived in Example 1 are applicable here to compute the values of the vorticity on the cylinder walls. Since the boundary values for  $\partial\psi/\partial x$  and  $\partial\psi/\partial y$  are simply zeros, the terms  $q_x$  and  $q_y$  vanish. The values for the vorticity at the boundary nodes on the  $x$ - and  $y$ -grid lines can thus be computed by

$$\omega_b = \left[1 + \left(\frac{y}{x}\right)^2\right] \frac{\partial^2 \psi_b}{\partial x^2}, \quad (3.40)$$

$$\omega_b = \left[1 + \left(\frac{x}{y}\right)^2\right] \frac{\partial^2 \psi_b}{\partial y^2}, \quad (3.41)$$

respectively. As mentioned earlier, Neumann boundary conditions for the stream

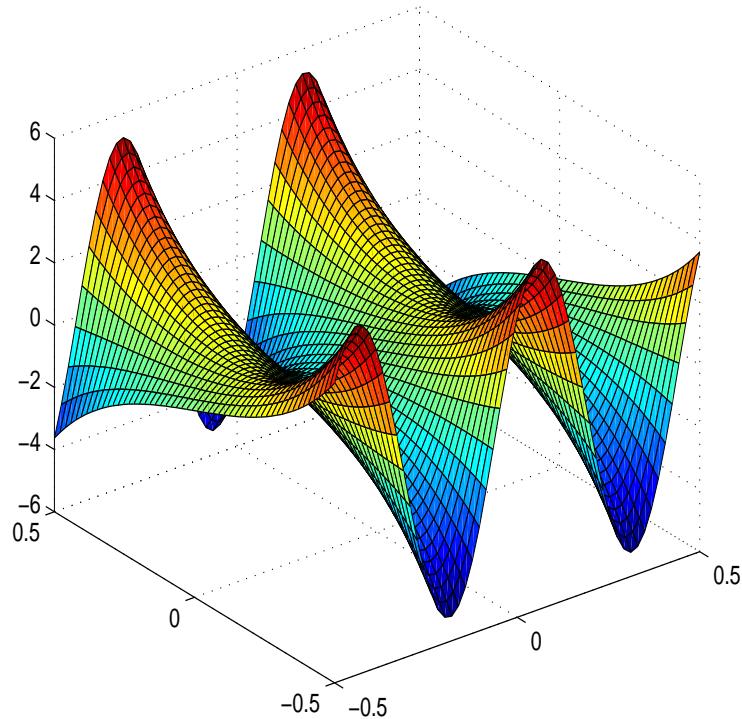


Figure 3.6: Example 2 (multiply-connected domain): Exact solution. It is noted that the exact solution is plotted over the square covering the problem domain.

function,  $\partial\psi/\partial x = 0$  and  $\partial\psi/\partial x = 0$ , are presently incorporated into the computational vorticity boundary conditions via integration constants and they are satisfied identically. Table 3.4 indicates a significant improvement in the matrix condition number of the present formulation over the  $\psi - T$  formulation reported in (Mai-Duy et al., 2008). The former yields the matrix condition number several orders of magnitude lower than the latter. This feature is very attractive in the context of RBFN techniques. One is thus able to use a larger number of nodes with the present approach in the RBFN simulation of fluid flow problems.

Both accuracy and grid convergence of the present technique are investigated.

The solution accuracy is assessed through the average equivalent conductivity

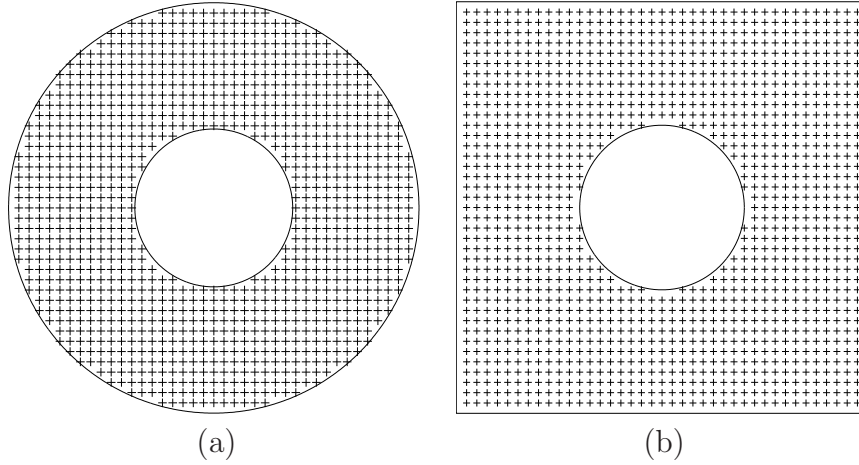


Figure 3.7: Computational domains and discretisations: Annulus between two circular cylinders (a) and annulus between inner circular cylinder and outer square cylinder (b).

Table 3.4: Example 3 (circular - circular cylinders): Condition numbers of the 1D-IRBFN system matrix by the two formulations.

Grid	cond( $A$ )	
	$\psi - \omega - T$	$\psi - T$
$12 \times 12$	$1.7 \times 10^1$	$8.4 \times 10^1$
$22 \times 22$	$9.1 \times 10^1$	$1.6 \times 10^3$
$32 \times 32$	$2.4 \times 10^2$	$6.9 \times 10^3$
$42 \times 42$	$6.7 \times 10^2$	$1.0 \times 10^5$
$52 \times 52$	$9.3 \times 10^2$	$2.1 \times 10^5$
$62 \times 62$	$1.7 \times 10^3$	$1.2 \times 10^6$

defined as e.g. (Kuehn and Goldstein, 1976; Shu, 1999)

$$\bar{k}_{eq} = \frac{-\ln(D_o/D_i)}{2\pi} \oint \frac{\partial T}{\partial n} ds, \quad (3.42)$$

in which  $D_o$  and  $D_i$  are the diameters of the outer cylinder and the inner cylinder, respectively. Results concerning  $\bar{k}_{eq}$  together with those of Kuehn and Goldstein (1976) and of Shu (1999) for  $Ra = \{10^2, 10^3, 3 \times 10^3, 6 \times 10^3, 10^4, 5 \times 10^4, 7 \times 10^4\}$  are presented in Table 3.5. It can be seen that there is a good agreement between these numerical solutions.

---

Figures 3.8 and 3.9 show the convergence of the stream function and temperature fields with respect to grid refinement for  $Ra = 10^4$  and  $Ra = 7 \times 10^4$ , respectively. It can be seen that the present technique is able to capture complex structures of the stream function and temperature fields even at coarse grids, and those patterns are improved in quality (smoothness) with increasing grid-densities. At a grid of  $42 \times 42$  for  $Ra = 10^4$  and a grid of  $52 \times 52$  for  $Ra = 7 \times 10^4$ , the plots look reasonable when compared with those reported in (Kuehn and Goldstein, 1976; Shu, 1999).

Table 3.5: Example 3 (circular - circular cylinders): Comparison of the average equivalent conductivity on the inner and outer cylinders,  $k_{eqi}$  and  $k_{eqo}$ , between the present IRBFN technique using a grid of  $52 \times 52$  and some other techniques for  $Ra$  in the range of  $10^2$  to  $7 \times 10^4$ . *KG* stands for Kuehn and Goldstein

$Ra$	$10^2$	$10^3$	$3 \times 10^3$	$6 \times 10^3$	$10^4$	$5 \times 10^4$	$7 \times 10^4$
	$k_{eqi}$						
Present Method	1.000	1.083	1.396	1.709	1.975	2.962	3.207
FDM							
(KG, 1976)	1.000	1.081	1.404	1.736	2.010	3.024	3.308
DQM							
(Shu, 1999)	1.001	1.082	1.397	1.715	1.979	2.958	
	$k_{eqo}$						
Present Method	0.999	1.080	1.393	1.712	1.970	2.942	3.246
FDM							
(KG, 1976)	1.002	1.084	1.402	1.735	2.005	2.973	3.226
DQM							
(Shu, 1999)	1.001	1.082	1.397	1.715	1.979	2.958	

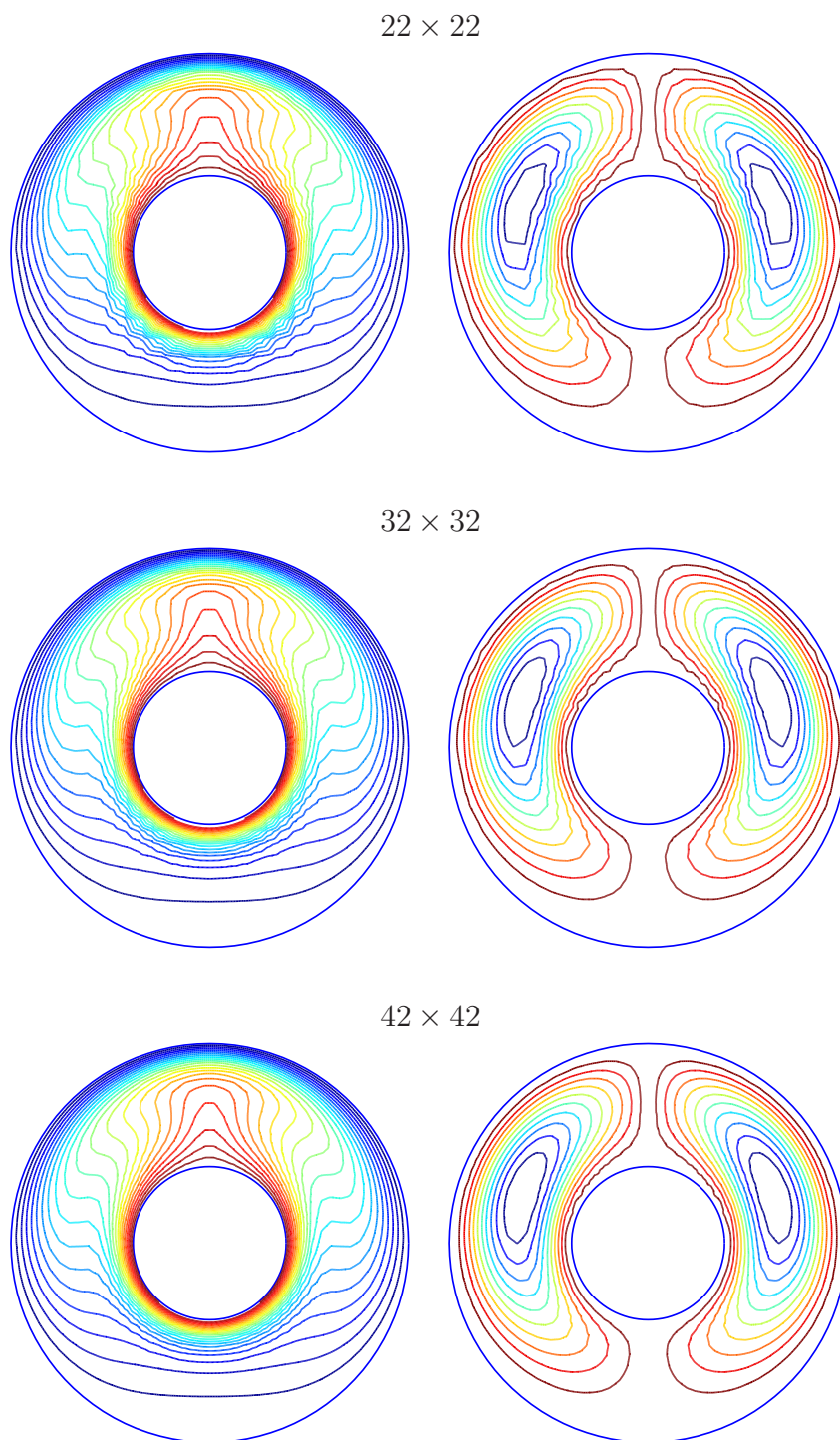


Figure 3.8: Example 3 (circular-circular cylinders): Convergence of the temperature (left) and stream-function (right) fields with respect to grid refinement for the flow at  $Ra = 10^4$ .

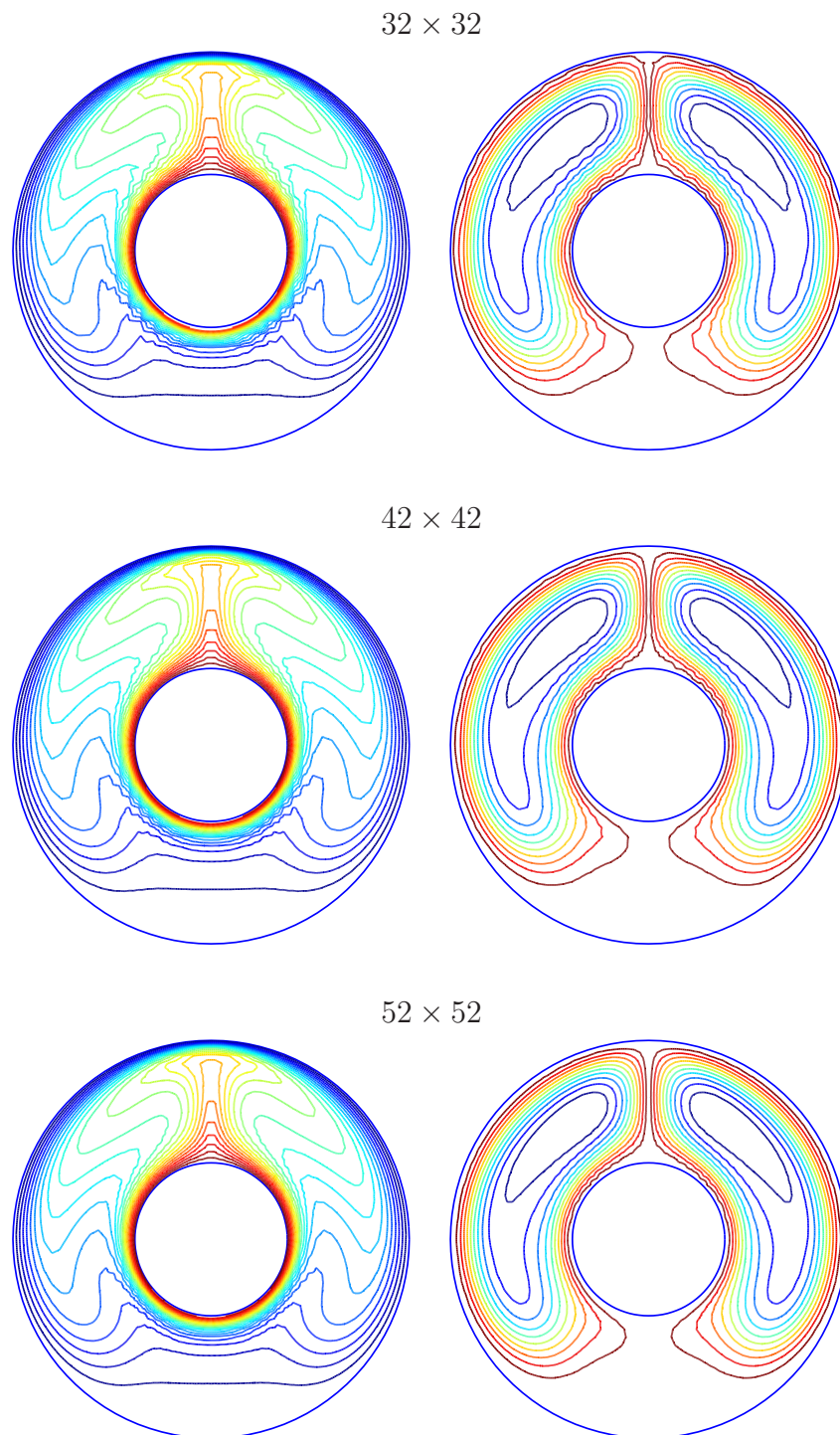


Figure 3.9: Example 3 (circular-circular cylinders): Convergence of the temperature (left) and stream-function (right) fields with respect to grid refinement for the flow at  $Ra = 7 \times 10^4$ .

### 3.4.4 Example 4: Concentric annulus between a square outer cylinder and a circular inner cylinder

For this example, natural convection between a heated inner circular cylinder and a cooled square enclosure is considered (Figure 3.7b). It is noted that the transformation of this domain into a rectangular one in other methods where it is required is much more complicated than that in the previous problem.

An aspect ratio of  $H/D_i = 2.5$  ( $H$ : the side length of the outer square and  $D_i$ : the diameter of the inner circle),  $Pr = 0.71$  and  $Ra = \{10^4, 5 \times 10^4, 10^5, 5 \times 10^5, 10^6\}$  are employed here to investigate the accuracy of the technique.

An attractive feature here is that the present technique does not require any coordinate transformations. The problem domain is simply represented by a Cartesian grid (Figure 3.7b). Numerical results are obtained for three uniform grids of  $32 \times 32$ ,  $42 \times 42$ , and  $52 \times 52$ .

For  $Ra = 10^4$ , the solution is started from rest to simulate the flow. For higher values of  $Ra$ , the initial solution is taken as the solution obtained at the nearest lower  $Ra$ . Figure 3.10 presents the behaviour of the convergence measure  $CM$  against the number of time steps. It can be seen that the decrease in  $CM$  is rather monotonic. As expected, the simulation of high- $Ra$  flows requires a larger number of iterations.

The obtained results are presented in Table 3.6, and Figures 3.11 and 3.12. Table 3.6 is concerned with the accuracy of the solution. Following the work of Moukalled and Acharya (1996), the local heat transfer coefficient is defined as

$$h = -k \frac{\partial T}{\partial n}, \quad (3.43)$$

where  $k$  is the thermal conductivity. The average Nusselt number (the ratio of the temperature gradient at the wall to a reference temperature gradient) is

Table 3.6: Example 4 (square-circular cylinders): Comparison of the average Nusselt number on the outer and inner cylinders,  $Nu_o$  and  $Nu_i$ , for  $Ra$  from  $10^4$  to  $10^6$  between the present technique (grid  $52 \times 52$ ) and some other techniques.

$Ra$	$10^4$	$5 \times 10^4$	$10^5$	$5 \times 10^5$	$10^6$
	$Nu_o$				
Present Method	3.22	4.04	4.89	7.43	8.70
DQM (Shu and Zhu, 2002)	3.24		4.86		8.90
FVM (Moukalled and Acharya, 1996)	3.33		5.08		9.37
	$Nu_i$				
Present Method	3.21	4.04	4.89	7.51	8.85
DQM (Shu and Zhu, 2002)	3.24		4.86		8.90
FVM (Moukalled and Acharya, 1996)	3.33		5.08		9.37

computed by

$$Nu = \frac{\bar{h}}{k}, \quad (3.44)$$

where  $\bar{h} = -\oint \frac{\partial T}{\partial n} ds$ . Since the computational domain in (Moukalled and Acharya, 1996) is taken as one-half of the physical domain, the values of  $Nu$  in the present work (Table 3.6) are divided by 2 for comparison purposes. The present results agree well with those in (Moukalled and Acharya, 1996) and (Shu and Zhu, 2002).

Figures 3.11 and 3.12 display streamlines and isotherms versus grid densities for  $Ra = 5 \times 10^5$  and  $Ra = 10^6$ , which show a very fast convergence of all fields. The qualitative behaviour of these fields and those in (Shu and Zhu, 2002) is similar.

## 3.5 Concluding remarks

In this chapter, a new numerical discretisation scheme for the  $\psi - \omega - T$  formulation using Cartesian grids and 1D-IRBFNs is reported. Attractive features of the proposed technique include (i) the preprocessing is simple; and (ii) the boundary conditions for the vorticity are implemented in a new and effective manner. Numerical results show that (i) the matrix condition number is significantly improved over the  $\psi - T$  formulation; and (ii) accurate results are obtained using a relatively-coarse grid.

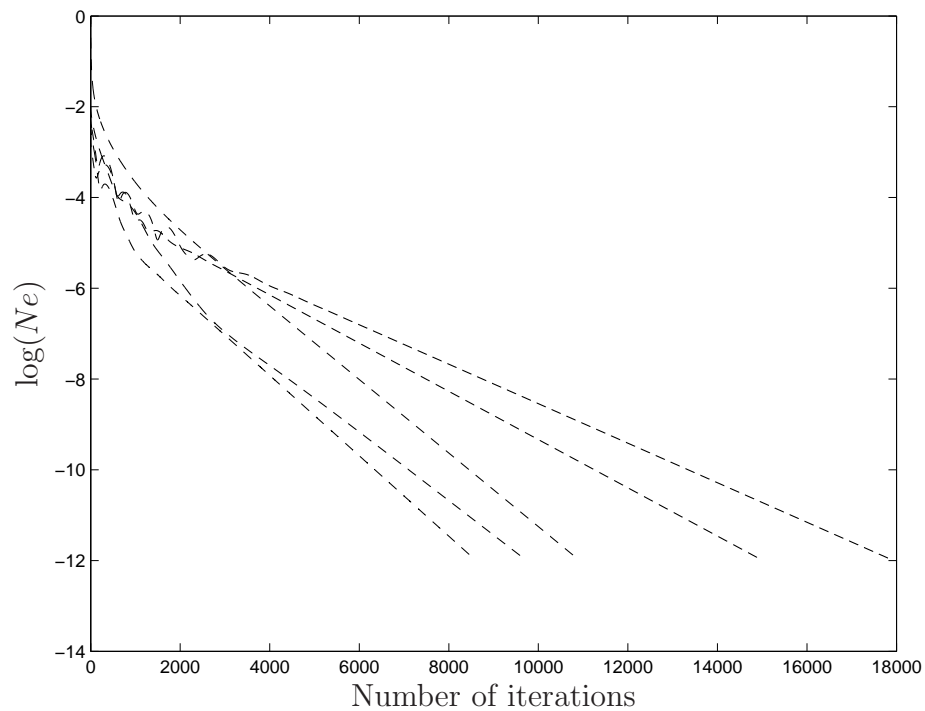


Figure 3.10: Example 4 (square-circular cylinders): Iterative convergence. Time steps used are 0.002 for  $Ra = 10^4$ , 0.005 for  $Ra = 5 \times 10^4$ , and 0.008 for  $Ra = \{10^5, 5 \times 10^5, 10^6\}$ . The values of CM become less than  $10^{-12}$  when the numbers of iterations reach 10925, 9740, 8609, 15017, and 17938 for  $Ra = \{10^4, 5 \times 10^4, 10^5, 5 \times 10^5, 10^6\}$ , respectively. Using the last point on the curves as a positional indicator, from left to right the curves correspond to  $Ra = \{10^4, 5 \times 10^4, 10^5, 5 \times 10^5, 10^6\}$ .

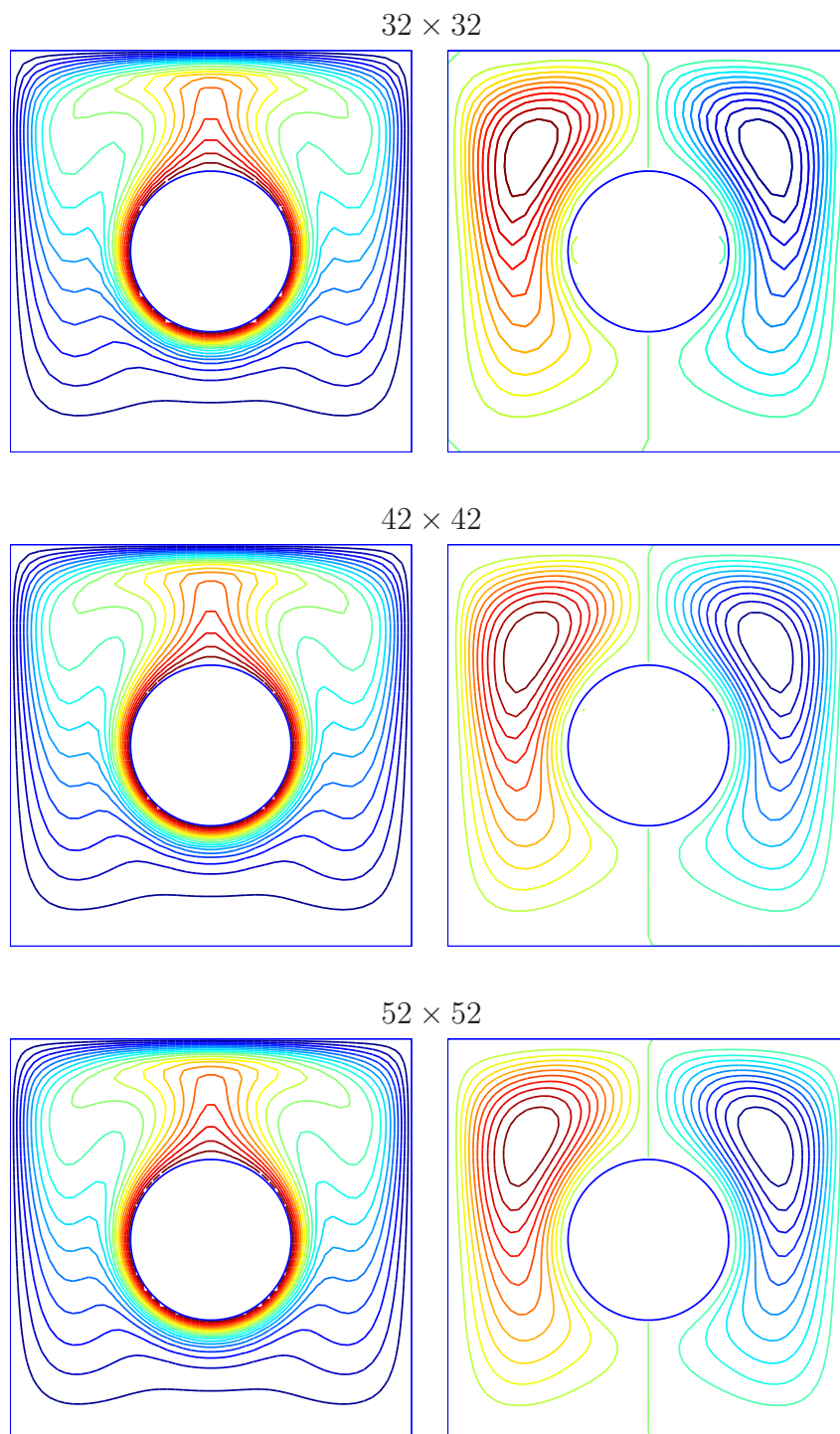


Figure 3.11: Example 4 (square-circular cylinders): Convergence of the temperature (left) and stream-function (right) fields with respect to grid refinement for the flow at  $Ra = 5 \times 10^5$ .

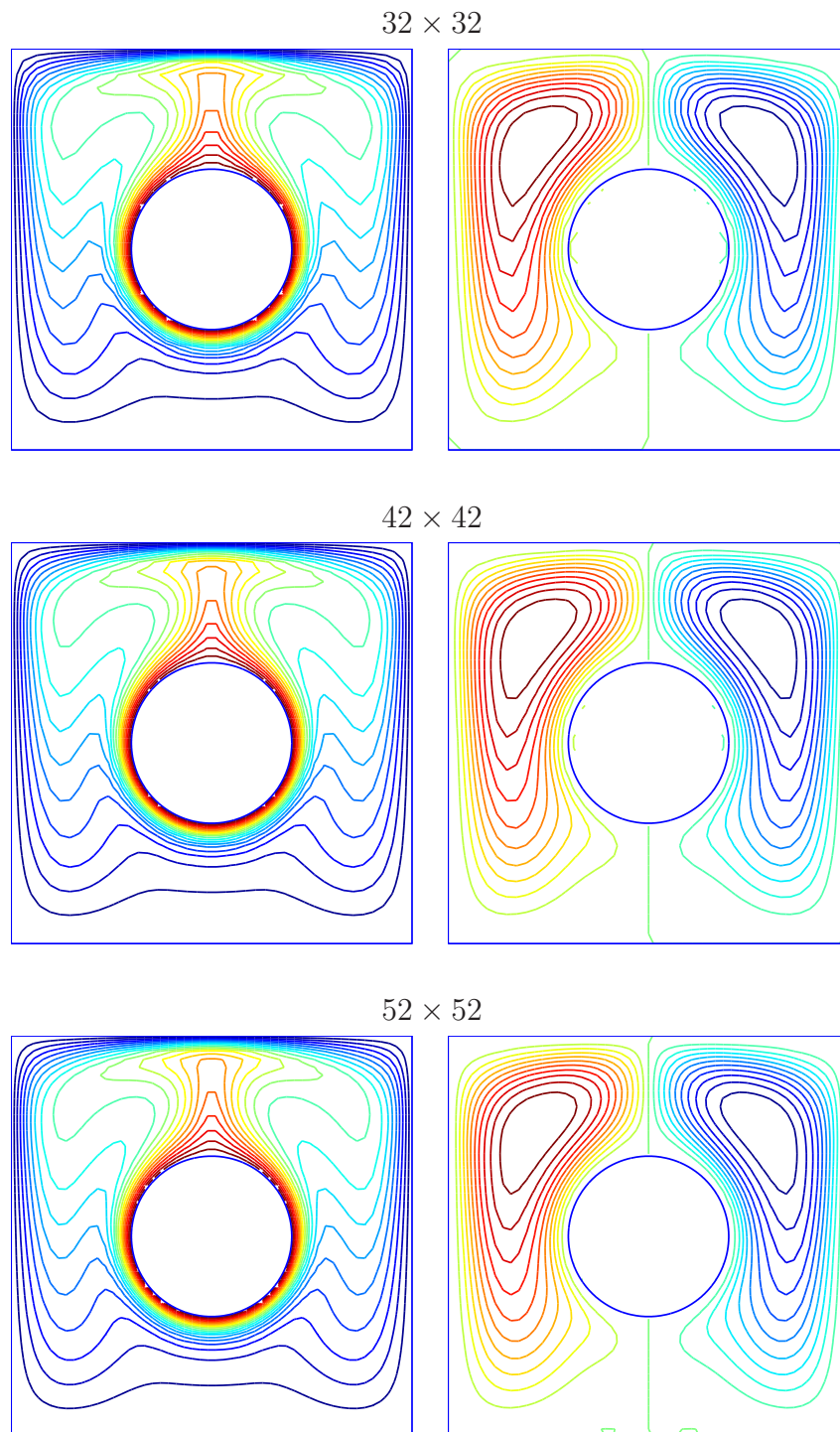


Figure 3.12: Example 4 (square-circular cylinders): Convergence of the temperature (left) and stream-function (right) fields with respect to grid refinement for the flow at  $Ra = 10^6$ .

# Chapter 4

## 1D-integrated-RBFN discretisation of stream-function ( $\psi$ ) formulation in multiply-connected domains

This chapter describes a new numerical procedure, based on point collocation, integrated multiquadric functions and Cartesian grids, for the discretisation of the stream-function formulation for flows of a Newtonian fluid in multiply-connected domains. Three particular issues, namely (i) the derivation of the stream-function values on separate boundaries; (ii) the implementation of cross derivatives in irregular regions; and (iii) the treatment of double boundary conditions, are studied in the context of Cartesian grids and approximants based on integrated multiquadric functions in one dimension. Several test problems, i.e. steady flows between a rotating circular cylinder and a fixed square cylinder and also between eccentric cylinders maintained at different temperatures, are investigated. Results obtained are compared well with numerical data available in the literature.

## 4.1 Introduction

The motion of a Newtonian fluid is governed by the Navier-Stokes equations which can be written in terms of different dependent variables, including the velocity - pressure ( $\mathbf{u} - p$ ) formulation, the stream-function - vorticity ( $\psi - \omega$ ) formulation and the stream-function ( $\psi$ ) formulation. The  $\mathbf{u} - p$  formulation is able to work for two- and three-dimension flows in a similar manner. One main concern is that there are no explicit transport equation and boundary conditions for the pressure variable. The resultant algebraic system could be solved iteratively where the pressure value is corrected using the continuity equation. For two-dimensional (2D) problems, by introducing the stream-function variable, one can eliminate the pressure and reduce the number of unknowns, i.e. from three (for the  $\mathbf{u} - p$  formulation) to two (the  $\psi - \omega$  formulation) and only one (the  $\psi$  formulation). However, the last two formulations have some drawbacks. Special attention should be given to the handling of the vorticity boundary condition for the  $\psi - \omega$  formulation and the double boundary conditions as well as high-order derivatives including the cross ones for the  $\psi$  formulation. Furthermore, the pressure field needs be computed after solving the governing equations, which is generally regarded as a complicated process. In the case of multiply-connected domains, an added difficulty is that the stream-function variable generally has different values, which are unknown, on separate boundaries.

The governing differential equations can be transformed into sets of algebraic equations by means of discretisation. To support the approximations, the problem domain needs be represented by a set of finite elements, a Cartesian grid or a collection of discrete points. For problems with complicated geometries such as flows in multiply-connected domains, it has been recognised that the task of dividing the spatial domain into a number of finite elements can be the most time-consuming part of the solution process. Generating a Cartesian grid or a set of discrete points is clearly much more economical.

In recent years, RBFNs have been developed to solve different types of differential problems encountered in applied mathematics, science and engineering. Details can be found in (Divo and Kassab, 2005, 2006, 2007, 2008; Kosec and Šarler, 2008a,b, 2009; Šarler et al., 2004; Šarler, 2005; Šarler et al., 2010; Wu and Liu, 2003; Siraj-ul-Islam et al., 2010; Yao et al., 2011). As shown in (Driscoll and Fornberg, 2002; Schaback, 2005; Wright and Fornberg, 2006), there is a relation between the RBFN collocation method and the finite difference method (FDM). For 1D approximations, the standard RBF interpolant converges to the Lagrange interpolating polynomial as the RBF width goes to infinity, which means that all classical FD formulas can be recovered by the limiting RBF interpolant. In the case of two and higher dimensions, the situation is not clear due to the fact that multivariate polynomial interpolations are not well-posed.

In (Le-Cao et al., 2009; Mai-Duy et al., 2008; Mai-Duy and Tran-Cong, 2001b, 2003, 2007), the RBFN approximations are constructed using integration (integrated RBFNs (IRBFNs)) rather than the usual differentiation. This approach has the ability to overcome the problem of reduced convergence rates caused by differentiation and to provide effective ways to implement derivative boundary conditions. IRBFNs have been developed for the simulation of flows in simply-connected domains governed by the  $\psi$  formulation and the  $\psi - \omega$  formulation (e.g. Mai-Duy and Tran-Cong, 2001b) as well as natural convection governed by the  $\psi - \omega$  formulation in a region between concentric cylinders (symmetrical flows) (e.g. Le-Cao et al., 2009).

This chapter is concerned with the simulation of unsymmetrical flows of a Newtonian fluid in multiply-connected domains using the  $\psi$  formulation, Cartesian grids and 1D-IRBFNs. Unlike the symmetrical case, the stream-function variable has different values on separate boundaries. These values can be found using the single-value condition for the pressure, whose implementations are known to be difficult (e.g. Peyret, 2002). Further difficulties include the implementation of cross derivatives in regions bounded by irregular surfaces as the

boundary points do not generally coincide with the grid nodes. New treatments for these difficulties and their 1D-IRBFN-based implementations are the focal point of this study.

An outline of this chapter is as follows. The  $\psi$  formulation and 1D-IRBFNs are briefly reviewed in Section 4.2 and Section 4.3, respectively. The proposed procedure is described in Section 4.4 and then numerically verified through the simulation of steady flows between a rotating circular cylinder and a fixed square cylinder and also between eccentric cylinders maintained at different temperatures in Section 4.5. Section 4.6 concludes the chapter.

## 4.2 Governing equations

The non-dimensional basic equations for natural convection under the Boussinesq approximation in the Cartesian  $x - y$  coordinate system can be written as (e.g. Ostrach, 1988)

$$\frac{\partial u}{\partial x} + \frac{\partial v}{\partial y} = 0, \quad (4.1)$$

$$\frac{\partial u}{\partial t} + u \frac{\partial u}{\partial x} + v \frac{\partial u}{\partial y} = -\frac{\partial p}{\partial x} + \sqrt{\frac{Pr}{Ra}} \left( \frac{\partial^2 u}{\partial x^2} + \frac{\partial^2 u}{\partial y^2} \right), \quad (4.2)$$

$$\frac{\partial v}{\partial t} + u \frac{\partial v}{\partial x} + v \frac{\partial v}{\partial y} = -\frac{\partial p}{\partial y} + \sqrt{\frac{Pr}{Ra}} \left( \frac{\partial^2 v}{\partial x^2} + \frac{\partial^2 v}{\partial y^2} \right) + T, \quad (4.3)$$

$$\frac{\partial T}{\partial t} + u \frac{\partial T}{\partial x} + v \frac{\partial T}{\partial y} = \frac{1}{\sqrt{RaPr}} \left( \frac{\partial^2 T}{\partial x^2} + \frac{\partial^2 T}{\partial y^2} \right), \quad (4.4)$$

where  $u$  and  $v$  are the velocity components,  $p$  the dynamic pressure,  $T$  the temperature, and  $Pr$  and  $Ra$  the Prandtl and Rayleigh numbers defined as  $Pr = \nu/\alpha$  and  $Ra = \beta g \Delta T L^3 / \alpha \nu$ , respectively in which  $\nu$  is the kinematic viscosity,  $\alpha$  the thermal diffusivity,  $\beta$  the thermal expansion coefficient,  $g$  the gravity, and  $L$  and  $\Delta T$  the characteristic length and temperature difference, respectively. In this dimensionless scheme, the velocity scale is taken as  $U =$

$\sqrt{gL\beta\Delta T}$  for the purpose of balancing the buoyancy and inertial forces.

By writing the velocity components in terms of a stream function  $\psi$  defined as

$$u = \frac{\partial\psi}{\partial y}, \quad (4.5)$$

$$v = -\frac{\partial\psi}{\partial x}. \quad (4.6)$$

the continuity equation is satisfied identically and the momentum equations reduce to

$$\begin{aligned} & \frac{\partial}{\partial t} \left( \frac{\partial^2\psi}{\partial x^2} + \frac{\partial^2\psi}{\partial y^2} \right) + \frac{\partial\psi}{\partial y} \left( \frac{\partial^3\psi}{\partial x^3} + \frac{\partial^3\psi}{\partial x\partial y^2} \right) - \frac{\partial\psi}{\partial x} \left( \frac{\partial^3\psi}{\partial x^2\partial y} + \frac{\partial^3\psi}{\partial y^3} \right) \\ & = \sqrt{\frac{Pr}{Ra}} \left( \frac{\partial^4\psi}{\partial x^4} + 2\frac{\partial^4\psi}{\partial x^2\partial y^2} + \frac{\partial^4\psi}{\partial y^4} \right) - \frac{\partial T}{\partial x}, \end{aligned} \quad (4.7)$$

Using the equivalent stream-function formulation, the set of four equations (4.1)-(4.4) reduces to a set of two equations: (4.4) and (4.7).

For iso-thermal flows, the non-dimensional basic equations reduce to

$$\begin{aligned} & \frac{\partial}{\partial t} \left( \frac{\partial^2\psi}{\partial x^2} + \frac{\partial^2\psi}{\partial y^2} \right) + \frac{\partial\psi}{\partial y} \left( \frac{\partial^3\psi}{\partial x^3} + \frac{\partial^3\psi}{\partial x\partial y^2} \right) - \frac{\partial\psi}{\partial x} \left( \frac{\partial^3\psi}{\partial x^2\partial y} + \frac{\partial^3\psi}{\partial y^3} \right) = \\ & \frac{1}{Re} \left( \frac{\partial^4\psi}{\partial x^4} + 2\frac{\partial^4\psi}{\partial x^2\partial y^2} + \frac{\partial^4\psi}{\partial y^4} \right), \end{aligned} \quad (4.8)$$

where  $Re$  is the Reynolds number defined as  $Re = UL/\nu$ .

The given velocity boundary conditions for  $u$  and  $v$  can be transformed into two boundary conditions on the stream function and its normal derivative

$$\psi = \gamma, \quad (4.9)$$

$$\frac{\partial\psi}{\partial n} = \xi, \quad (4.10)$$

where  $n$  is the direction normal to the boundary, and  $\gamma$  and  $\xi$  prescribed functions. For the case of fixed concentric cylinders, non-slip boundary conditions usually lead to  $\gamma = 0$  and  $\xi = 0$  at walls. For the case of rotating cylinders and eccentric cylinders, because of the existence of a global circulation flow, the stream-function values on the inner and outer cylinder walls cannot be the same.

### 4.3 Brief review of 1D-integrated RBFNs

The present governing equations consist of of a fourth order PDE (4.8) and a second order PDE (4.4). We employ an 1D-IRBFN-4 scheme for the discretisation of (4.8) and an 1D-IRBFN-2 scheme for (4.4).

#### 4.3.1 1D-IRBFN-4

The following expressions are obtained by using (2.5)-(2.9) with  $p = 4$

$$\frac{d^4 f(x)}{dx^4} = \sum_{i=1}^m w_i g_i(x) = \sum_{i=1}^m w_i I_i^{(4)}(x), \quad (4.11)$$

$$\frac{d^3 f(x)}{dx^3} = \sum_{i=1}^m w_i I_i^{(3)}(x) + c_1, \quad (4.12)$$

$$\frac{d^2 f(x)}{dx^2} = \sum_{i=1}^m w_i I_i^{(2)}(x) + c_1 x + c_2, \quad (4.13)$$

$$\frac{df(x)}{dx} = \sum_{i=1}^m w_i I_i^{(1)}(x) + c_1 \frac{x^2}{2} + c_2 x + c_3, \quad (4.14)$$

$$f(x) = \sum_{i=1}^m w_i I_i^{(0)}(x) + c_1 \frac{x^3}{6} + c_2 \frac{x^2}{2} + c_3 x + c_4, \quad (4.15)$$

where there are four integration constants that are treated like the RBF weights.

### 4.3.2 1D-IRBFN-2

The following expressions are obtained by using (2.5)-(2.9) with  $p = 2$

$$\frac{d^2 f(x)}{dx^2} = \sum_{i=1}^m w_i I_i^{(2)}(x), \quad (4.16)$$

$$\frac{df(x)}{dx} = \sum_{i=1}^m w_i I_i^{(1)}(x) + c_1, \quad (4.17)$$

$$f(x) = \sum_{i=1}^m w_i I_i^{(0)}(x) + c_1 x + c_2, \quad (4.18)$$

where there are two integration constants that are treated like the RBF weights.

Both 1D-IRBFN-4 and 1D-IRBFN-2 implement the multiquadric (MQ) function whose form is

$$g_i(x) = \sqrt{(x - c_i)^2 + a_i^2}, \quad (4.19)$$

where  $c_i$  and  $a_i$  are, respectively, the centre and the width of the  $i$ th MQ basis function.

## 4.4 Proposed numerical procedure

Calculations for unsymmetrical flows in multiply-connected domains are carried out on Cartesian grids. Grid nodes inside the domain of interest are taken to be interior nodes. Boundary points are generated by the intersection of the grid lines and boundaries. Boundary nodes are thus comprised of two sets of points. The first set is generated by the  $x$ -grid lines; the other by the  $y$ -grid lines.

1D-IRBFNs of orders 4 (i.e. equations (4.11)-(4.15)) and 2 (i.e. equations (4.16)-(4.18)) are employed on the grid lines to represent the stream-function and temperature variables, respectively. The governing differential equations,

which involve high-order and cross derivatives, are discretised by means of point collocation. Emphasis is placed on the following issues: (i) the implementation of cross derivatives in irregular regions; (ii) the derivation of the stream-function values on separate boundaries; and (iii) the treatment of double boundary conditions. Formulas are derived in terms of Cartesian coordinates and they are implemented with 1D-IRBFNs.

It is noted that conventional RBFN methods are global and lead to full populated matrices. Unlike conventional methods, at a grid node, the proposed method only uses RBF centres on the two associated grid lines rather than the whole set of RBF centres to construct the approximations at that point. The present method thus possesses some local approximation properties. In comparison with conventional RBFN methods, relatively-large numbers of nodes can be employed here. However, the resultant system matrix is still not as sparse as those produced by finite-difference methods. The present technique needs to be combined with domain decompositions for handling large-scale engineering problems.

#### **4.4.1 Boundary values for stream function**

Since there is no flow in the direction normal to a solid boundary, the stream function is constant at a wall. The stream-function variable has different values on different walls. The value of  $\psi$  on the outer wall is simply set to zero, while the values of  $\psi$  on inner walls are considered as unknowns. Consider an inner wall. The associated unknown there cannot be determined from the governing equation; an independent equation/integral condition is needed. To find the value of  $\psi$  on the wall, Lewis (1979) suggested using the condition that the pressure is a single-valued function of position. This condition can be

mathematically described as

$$\oint_{\Gamma} \frac{\partial p}{\partial s} ds = \oint_{\Gamma} \nabla p \cdot d\vec{s} = 0, \quad (4.20)$$

where  $p$  is the pressure,  $s$  the arc length,  $ds$  the length of an infinitesimal part of the boundary  $\Gamma$ . It should be pointed out that  $\Gamma$  can be any closed path. In the present work, the inner cylinder boundary is taken to be  $\Gamma$ . The pressure gradient  $\nabla p$  can be obtained from the momentum equations. The reader is referred to, for example, (Lewis, 1979; Shu et al., 2002; Shu and Wu, 2002) for further details. In the Cartesian coordinate system, equation (4.20) becomes

$$\oint \frac{\partial p}{\partial x} dx + \oint \frac{\partial p}{\partial y} dy = 0. \quad (4.21)$$

From the primitive variable formulation, we have

$$\frac{\partial p}{\partial x} = \frac{1}{Re} \left( \frac{\partial^2 u}{\partial x^2} + \frac{\partial^2 u}{\partial y^2} \right) - \left( u \frac{\partial u}{\partial x} + v \frac{\partial u}{\partial y} \right), \quad (4.22)$$

$$\frac{\partial p}{\partial y} = \frac{1}{Re} \left( \frac{\partial^2 v}{\partial x^2} + \frac{\partial^2 v}{\partial y^2} \right) - \left( u \frac{\partial v}{\partial x} + v \frac{\partial v}{\partial y} \right). \quad (4.23)$$

Substituting (4.22) and (4.23) into (4.21) and then making use of (4.5) and (4.6) lead to

$$\begin{aligned} & \oint \frac{\partial^3 \psi}{\partial x^2 \partial y} dx + \oint \frac{\partial^3 \psi}{\partial y^3} dx - Re \oint \frac{\partial \psi}{\partial y} \frac{\partial^2 \psi}{\partial x \partial y} dx + Re \oint \frac{\partial \psi}{\partial x} \frac{\partial^2 \psi}{\partial y^2} dx - \\ & \oint \frac{\partial^3 \psi}{\partial x^3} dy - \oint \frac{\partial^3 \psi}{\partial y^2 \partial x} dy + Re \oint \frac{\partial \psi}{\partial y} \frac{\partial^2 \psi}{\partial x^2} dy - Re \oint \frac{\partial \psi}{\partial x} \frac{\partial^2 \psi}{\partial y \partial x} dy = 0. \end{aligned} \quad (4.24)$$

In the case of a fixed cylinder, the convection term vanishes on its wall. Equation (4.24) thus reduces to

$$\oint \frac{\partial^3 \psi}{\partial x^2 \partial y} dx + \oint \frac{\partial^3 \psi}{\partial y^3} dx - \oint \frac{\partial^3 \psi}{\partial x^3} dy - \oint \frac{\partial^3 \psi}{\partial y^2 \partial x} dy = 0. \quad (4.25)$$

By expressing integrals in (4.24)/(4.25) in terms of the values of  $\psi$  at the interior points, the resultant equation can be used as an extra equation to determine the value of  $\psi$  on the wall.

#### 4.4.2 Cross derivatives

In the present formulations, the governing equations and the single-valued pressure condition involve cross derivatives, namely  $\partial^4\psi/\partial^2x\partial^2y$ ,  $\partial^3\psi/\partial^2x\partial y$ , and  $\partial^3\psi/\partial x\partial y^2$ . As mentioned earlier, the IRBFN approximations are constructed on the grid lines. It is necessary to transform the computation of these mixed derivatives to that of pure derivatives. This can be achieved through the following relations

$$\frac{\partial^4\psi}{\partial x^2\partial y^2} = \frac{1}{2} \left[ \frac{\partial^2}{\partial x^2} \left( \frac{\partial^2\psi}{\partial y^2} \right) + \frac{\partial^2}{\partial y^2} \left( \frac{\partial^2\psi}{\partial x^2} \right) \right], \quad (4.26)$$

$$\frac{\partial^3\psi}{\partial x^2\partial y} = \frac{\partial^2}{\partial x^2} \left( \frac{\partial\psi}{\partial y} \right), \quad (4.27)$$

$$\frac{\partial^3\psi}{\partial x\partial y^2} = \frac{\partial^2}{\partial y^2} \left( \frac{\partial\psi}{\partial x} \right). \quad (4.28)$$

In (4.26)-(4.28), there are two terms, namely  $\partial^2 (\partial^2\psi/\partial y^2) / \partial x^2$  and  $\partial^2 (\partial\psi/\partial y) / \partial x^2$ , to be evaluated on the  $x$ -grid lines and two terms, namely  $\partial^2 (\partial^2\psi/\partial x^2) / \partial y^2$  and  $\partial^2 (\partial\psi/\partial x) / \partial y^2$ , to be evaluated on the  $y$ -grid lines.

Consider an  $x$ -grid line. To carry out the approximation of  $\partial^2 (\partial^2\psi/\partial y^2) / \partial x^2$  and  $\partial^2 (\partial\psi/\partial y) / \partial x^2$ , the values of  $\partial^2\psi/\partial y^2$  and  $\partial\psi/\partial y$  at the interior and boundary nodes on the  $x$ -grid line are assumed to be given (i.e. they are known values or can be expressed in terms of the nodal values of  $\psi$ ). For nodal interior points, these values can be obtained straightforwardly by using the approximations on the vertical grid lines. For the boundary points, the value of  $\partial\psi/\partial y$  is known as it can be easily computed from the given boundary conditions  $\psi$  and  $\partial\psi/\partial n$ , while one does not generally know the value of  $\partial^2\psi/\partial y^2$ . For the latter, there are two possible cases. If the boundary point is also a grid

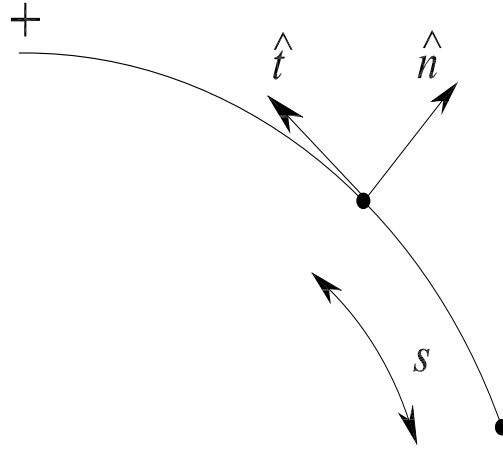


Figure 4.1: A curved boundary.

node, the computation of  $\partial^2\psi/\partial y^2$  is similar to that of an interior point. If the boundary point is not a grid node, special treatment is required. A new formula for computing  $\partial^2\psi/\partial y^2$  is derived as follows. Along a curved boundary (Figure 4.1), the values of  $\partial\psi/\partial x$  and  $\partial\psi/\partial y$  can be easily obtained from the prescribed boundary values for  $\psi$  and  $\partial\psi/\partial n$ . By introducing an interpolating scheme (e.g. 1D-IRBFNs) on the boundary, one is able to get derivatives of  $\partial\psi/\partial x$  and  $\partial\psi/\partial y$  along the boundary such as  $\partial^2\psi/\partial x\partial s$  and  $\partial^2\psi/\partial y\partial s$  in which  $s$  is the arc-length of the curved boundary. The following expressions were derived in section 3.3.2 of Chapter 3 and are reproduced here for convenience.

$$\frac{\partial^2\psi(x_b)}{\partial y^2} = \left(\frac{t_x}{t_y}\right)^2 \frac{\partial^2\psi(x_b)}{\partial x^2} + q_y, \quad (4.29)$$

where  $q_y$  is a known value defined by

$$q_y = -\frac{t_x}{t_y^2} \frac{\partial^2\psi(x_b)}{\partial x\partial s} + \frac{1}{t_y} \frac{\partial^2\psi(x_b)}{\partial y\partial s}. \quad (4.30)$$

Formula (4.29) facilitates the computation of the value of  $\partial^2\psi/\partial y^2$  at a boundary point  $x_b$  using the approximations on the  $x$ -grid line.

Consider a  $y$ -grid line. In the same manner, the value of  $\partial^2\psi/\partial x^2$  at a boundary point  $y_b$  can be computed by

$$\frac{\partial^2\psi(y_b)}{\partial x^2} = \left(\frac{t_y}{t_x}\right)^2 \frac{\partial^2\psi(y_b)}{\partial y^2} + q_x, \quad (4.31)$$

where  $q_x$  is a known value defined by

$$q_x = -\frac{t_y}{t_x^2} \frac{\partial^2\psi(y_b)}{\partial y\partial s} + \frac{1}{t_x} \frac{\partial^2\psi(y_b)}{\partial x\partial s}. \quad (4.32)$$

It can be seen that, given a Cartesian grid, expressions (4.29) and (4.31) allow the approximations of mixed derivatives in regions bounded by irregular surfaces to be expressed in terms of the nodal values of  $\psi$  and the boundary conditions.

### 4.4.3 1D-IRBFN expressions

1D-IRBFN expressions on the  $x$ - and  $y$ -grid lines have similar forms. In the following, the process of deriving 1D-IRBFN expressions for the stream-function variable and its derivatives on the  $x$ -grid lines is presented in detail.

#### Pure derivatives

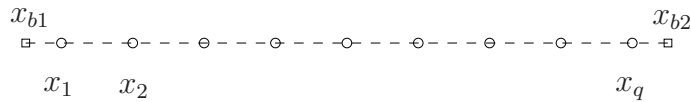


Figure 4.2: Points on a grid line consist of interior points  $x_i$  ( $\circ$ ) and boundary points  $x_{bi}$  ( $\square$ ).

Along an  $x$ -grid line (Figure 4.2), the set of RBF centres consists of the interior points  $\{x_i\}_{i=1}^q$  and the two boundary points  $\{x_{bi}\}_{i=1}^2$ . The stream-function variable is approximated using 1D-IRBFN-4s (equations (4.11)-(4.15) and  $f$  is replaced with  $\psi$ ). At a boundary point  $x_b$ , there are double boundary condi-

tions,  $\psi(x_b)$  and  $\partial\psi(x_b)/\partial x$ . Unlike conventional differentiated RBFNs, there are four integration constants in the 1D-IRBFN formulation. These extra coefficients allows for the addition of some extra equations to the process of conversion of the coefficient space into the physical space. The extra equations are utilised here to implement derivative boundary conditions. The conversion system is thus formed by not only collocating (4.15) at  $\{x_i\}_{i=1}^q$  and  $\{x_{bi}\}_{i=1}^2$  but also collocating (4.14) at  $\{x_{bi}\}_{i=1}^2$

$$\begin{pmatrix} \widehat{\psi} \\ \widehat{\psi}_b \\ \widehat{\frac{\partial\psi_b}{\partial x}} \end{pmatrix} = \widehat{\mathcal{C}} \widehat{w}, \quad (4.33)$$

where

$$\begin{aligned} \widehat{\psi} &= (\psi(x_1), \psi(x_2), \dots, \psi(x_q))^T, \\ \widehat{\psi}_b &= (\psi(x_{b1}), \psi(x_{b2}))^T, \\ \widehat{\frac{\partial\psi_b}{\partial x}} &= \left( \frac{\partial\psi(x_{b1})}{\partial x}, \frac{\partial\psi(x_{b2})}{\partial x} \right)^T, \\ \widehat{\mathcal{C}} &= \begin{bmatrix} I_1^{(0)}(x_1) & \cdots & I_m^{(0)}(x_1) & x_1^3/6 & x_1^2/2 & x_1 & 1 \\ I_1^{(0)}(x_2) & \cdots & I_m^{(0)}(x_2) & x_2^3/6 & x_2^2/2 & x_2 & 1 \\ \vdots & \ddots & \vdots & \vdots & \vdots & \vdots & \vdots \\ I_1^{(0)}(x_q) & \cdots & I_m^{(0)}(x_q) & x_q^3/6 & x_q^2/2 & x_q & 1 \\ I_1^{(0)}(x_{b1}) & \cdots & I_m^{(0)}(x_{b1}) & x_{b1}^3/6 & x_{b1}^2/2 & x_{b1} & 1 \\ I_1^{(0)}(x_{b2}) & \cdots & I_m^{(0)}(x_{b2}) & x_{b2}^3/6 & x_{b2}^2/2 & x_{b2} & 1 \\ I_1^{(1)}(x_{b1}) & \cdots & I_m^{(1)}(x_{b1}) & x_{b1}^2/2 & x_{b1} & 1 & 0 \\ I_1^{(1)}(x_{b2}) & \cdots & I_m^{(1)}(x_{b2}) & x_{b2}^2/2 & x_{b2} & 1 & 0 \end{bmatrix}, \\ \widehat{w} &= (w_1, w_2, \dots, w_m, c_1, c_2, c_3, c_4)^T, \end{aligned}$$

and  $m = q + 2$ . The values of the  $l$ th-order derivative ( $l = \{1, 2, 3, 4\}$ ) of  $\psi$  at

the interior points on the grid line are evaluated as

$$\frac{\widehat{\partial^l \psi}}{\partial x^l} = \widehat{\mathcal{I}}_{[4]}^{(l)} \widehat{\mathcal{C}}^{-1} \begin{pmatrix} \widehat{\psi} \\ \widehat{\psi}_b \\ \frac{\widehat{\partial \psi_b}}{\partial x} \end{pmatrix}, \quad (4.34)$$

where

$$\widehat{\mathcal{I}}_{[4]}^{(4)} = \begin{bmatrix} I_1^{(4)}(x_1) & \cdots & I_m^{(4)}(x_1) & 0 & 0 & 0 & 0 \\ I_1^{(4)}(x_2) & \cdots & I_m^{(4)}(x_2) & 0 & 0 & 0 & 0 \\ \vdots & \ddots & \vdots & \vdots & \vdots & \vdots & \vdots \\ I_1^{(4)}(x_q) & \cdots & I_m^{(4)}(x_q) & 0 & 0 & 0 & 0 \end{bmatrix},$$

$$\widehat{\mathcal{I}}_{[4]}^{(3)} = \begin{bmatrix} I_1^{(3)}(x_1) & \cdots & I_m^{(3)}(x_1) & 1 & 0 & 0 & 0 \\ I_1^{(3)}(x_2) & \cdots & I_m^{(3)}(x_2) & 1 & 0 & 0 & 0 \\ \vdots & \ddots & \vdots & \vdots & \vdots & \vdots & \vdots \\ I_1^{(3)}(x_q) & \cdots & I_m^{(3)}(x_q) & 1 & 0 & 0 & 0 \end{bmatrix},$$

$$\widehat{\mathcal{I}}_{[4]}^{(2)} = \begin{bmatrix} I_1^{(2)}(x_1) & \cdots & I_m^{(2)}(x_1) & x_1 & 1 & 0 & 0 \\ I_1^{(2)}(x_2) & \cdots & I_m^{(2)}(x_2) & x_2 & 1 & 0 & 0 \\ \vdots & \ddots & \vdots & \vdots & \vdots & \vdots & \vdots \\ I_1^{(2)}(x_q) & \cdots & I_m^{(2)}(x_q) & x_q & 1 & 0 & 0 \end{bmatrix},$$

and

$$\widehat{\mathcal{I}}_{[4]}^{(1)} = \begin{bmatrix} I_1^{(1)}(x_1) & \cdots & I_m^{(1)}(x_1) & x_1^2/2 & x_1 & 1 & 0 \\ I_1^{(1)}(x_2) & \cdots & I_m^{(1)}(x_2) & x_2^2/2 & x_2 & 1 & 0 \\ \vdots & \ddots & \vdots & \vdots & \vdots & \vdots & \vdots \\ I_1^{(1)}(x_q) & \cdots & I_m^{(1)}(x_q) & x_q^2/2 & x_q & 1 & 0 \end{bmatrix}.$$

Expressions (4.34) can be rewritten in compact form

$$\frac{\widehat{\partial^l \psi}}{\partial x^l} = \widehat{\mathcal{D}}_{lx} \widehat{\psi} + \widehat{k}_{lx}, \quad (4.35)$$

where  $\widehat{\mathcal{D}}_{lx}$  are the differentiation matrices in the physical space, and  $\widehat{k}_{lx}$  the vectors whose components are functions of boundary conditions. It is noted that, for the grid lines which cross over the inner cylinder, only the values of  $\psi$  on the outer cylinder are given.

Similarly, 1D-IRBFN expressions for pure derivatives on the  $y$ -grid lines take the following forms

$$\frac{\widehat{\partial^l \psi}}{\partial y^l} = \widehat{\mathcal{D}}_{ly} \widehat{\psi} + \widehat{k}_{ly}, \quad (4.36)$$

where  $l = \{1, 2, 3, 4\}$ .

The temperature variable is represented by 1D-IRBFN-2s, i.e. equations (4.16)-(4.18), where  $f$  is replaced with  $T$ . It is noted that the present energy equation (4.4) is subject to the Dirichlet boundary condition only. The process of deriving 1D-IRBFNs for  $T$  is similar to that for  $\psi$ , except that no extra equations are employed in the process of conversion (4.33).

### Mixed derivatives

On an  $x$ -grid line, it can be seen from (4.26)-(4.28) that relevant mixed derivative to be evaluated here are  $\partial^2 (\partial\psi/\partial y) / \partial x^2$  and  $\partial^2 (\partial^2\psi/\partial y^2) / \partial x^2$ . Approximate expressions for  $\partial\psi/\partial y$  and  $\partial^2\psi/\partial y^2$  can be obtained at the interior points using (4.36) with  $l = \{1, 2\}$ . At the boundary points, the values of  $\partial\psi/\partial y$  are given, while the values of  $\partial^2\psi/\partial y^2$  can be computed using (4.29) in which

$\partial^2\psi/\partial x^2$  is evaluated using the nodal values of  $\psi$  on the  $x$ -grid line

$$\frac{\partial^2\psi(x_b)}{\partial x^2} = \left[ I_1^{(2)}(x_b) \cdots I_m^{(2)}(x_b) \quad x_b \quad 1 \quad 0 \quad 0 \right] \widehat{\mathcal{C}}^{-1} \begin{pmatrix} \widehat{\psi} \\ \widehat{\psi}_b \\ \widehat{\frac{\partial\psi_b}{\partial x}} \end{pmatrix}, \quad (4.37)$$

where  $x_b$  is a boundary point and  $\widehat{\psi}$ ,  $\widehat{\partial\psi_b/\partial x}$ ,  $\widehat{w}$  and  $\widehat{\mathcal{C}}$  are defined as before.

Let  $g$  represent  $\partial^2\psi/\partial y^2$  and  $\partial\psi/\partial y$ . The remaining task is to form an 1D-IRBFN expression for  $\partial^2g/\partial x^2$ . This process is similar to that for the stream function which is described in Section 4.4.3, except that there are no extra equations representing derivative boundary values in (4.33).

### Single-valued pressure equation

As shown in (4.24)/(4.25), this pressure condition involves pure and mixed derivatives on the wall.

Using 1D-IRBFN expressions which are derived above, one can express derivatives in (4.24)/(4.25) in terms of the nodal values of  $\psi$ . For example, the integrand of the third term in (4.25) can be written as

$$\frac{\partial^3\psi(x_b)}{\partial x^3} = \left[ I_1^{(3)}(x_b) \cdots I_m^{(3)}(x_b) \quad 1 \quad 0 \quad 0 \quad 0 \right] \widehat{\mathcal{C}}^{-1} \begin{pmatrix} \widehat{\psi} \\ \widehat{\psi}_b \\ \widehat{\frac{\partial\psi_b}{\partial x}} \end{pmatrix}, \quad (4.38)$$

where  $x_b$  is the boundary point on the inner wall and  $\widehat{\psi}$ ,  $\widehat{\partial\psi_b/\partial x}$ ,  $\widehat{w}$  and  $\widehat{\mathcal{C}}$  are defined as before. The vector  $\widehat{\psi}_b$  in (4.38) contains the value of the stream function on the inner cylinder, i.e.  $\psi(x_b)$ , that is an unknown to be found.

All associated integrals in (4.24)/(4.25) are then evaluated using the Gauss quadrature scheme.

The pressure condition leads to a relation where the value of  $\psi$  on the inner wall is expressed as a linear combination of the values of  $\psi$  at the interior points.

#### 4.4.4 Solution Procedure

The set of algebraic equations resulting from the discretisation of the stream-function formulation is nonlinear because of the presence of the convective terms. There are two approaches widely used to handle this nonlinearity. In the first approach, all time derivative terms are dropped out and nonlinear solvers such as Newton iterations can be applied. In the second approach, the solution is obtained by means of time marching. Each approach has some advantages over the other for certain problems. In this study, fluid flow problems are considered and the second approach is applied.

1. Guess initial values of  $T, \psi$  and their spatial derivatives at time  $t = 0$ .
2. Discretise the governing equations in time using a first-order accurate finite-difference scheme, where the diffusive and convective terms are treated implicitly and explicitly, respectively.
3. Discretise the governing equations in space using 1D-IRBFN schemes,  
Solve the energy equation (4.4) for  $T$ , and  
Solve the momentum equation (4.7) for  $\psi$ .

The two equations are solved separately in order to keep matrix sizes to a minimum.

4. Check to see whether the solution has reached a steady state

$$CM = \frac{\sqrt{\sum_{i=1}^{n_{ip}} \left( \psi_i^{(k)} - \psi_i^{(k-1)} \right)^2}}{\sqrt{\sum_{i=1}^{n_{ip}} \left( \psi_i^{(k)} \right)^2}} < \epsilon, \quad (4.39)$$

where  $k$  is the time level and  $\epsilon$  is the prescribed tolerance.

5. If it is not satisfied, advance time step and repeat from step 2. Otherwise, stop the computation and output the results.

## 4.5 Numerical results

The present method is verified through the simulation of steady iso-thermal flows between a rotating circular cylinder and a fixed square cylinder, and steady buoyancy-driven flows in eccentric annuli with a wide range of the eccentricity parameter. The computed solution at the nearest lower value of  $Re/Ra$  is taken to be the initial solution. Internal grid points that fall very close—within a distance of  $h/8$ —to the boundary are removed.

It is well known that RBFN-based schemes suffer from the so-called uncertainty or trade-off principle. As the value of the RBF-width/shape-parameter increases, the approximation error reduces while the condition number of the system matrix grows. Unfortunately, there is still a lack of theory to determine the optimal value for the RBF width. The RBF width is usually chosen by trial and error or some other ad-hoc means. In this study, the grid size  $h$  is taken to be the MQ-RBF width.

For conventional FDMs and pseudo-spectral techniques, coordinate transformations are required to convert non-rectangular domains into rectangular ones (Shu et al., 2002; Moukalled and Acharya, 1996). The relationships between the physical and computational coordinates are given by a set of algebraic equations or a set of partial differential equations (PDEs), depending on the level of complexity of the geometry. Such transformation processes are, in general, complicated. The proposed technique can work with irregular domains in a direct manner, i.e. without the need for using coordinate transformations. However, the proposed technique is restricted to structured uniform or non-uniform Cartesian grids.

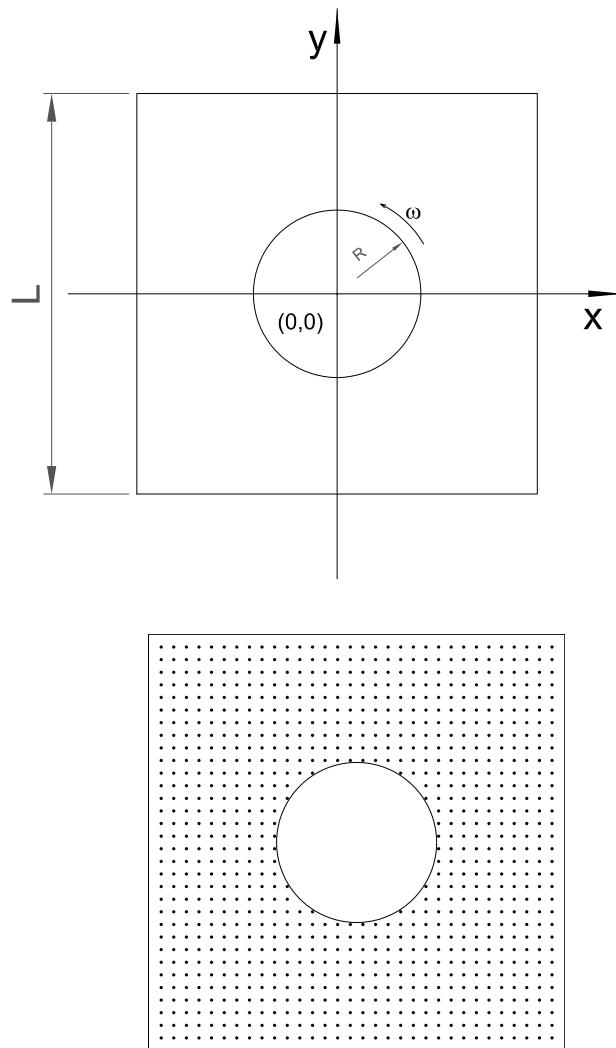


Figure 4.3: Example 1 (rotating cylinder): geometry (top) and discretisation (bottom).

### 4.5.1 Example 1: Steady flow between a rotating circular cylinder and a fixed square cylinder

This test problem is employed for the investigation of accuracy of the proposed technique in computing the value of the stream function on the inner cylinder. The flow geometry and discretisation are shown in Figure 4.3. The inner cylinder rotates at a unit angular velocity. The stream function on the outer wall is set to zero. Formula (4.24) is utilised to determine the value of the stream function on the inner wall, denoted by  $\psi_w$ . This flow is governed by (4.8) and subject to the boundary conditions

$$\psi = \frac{\partial\psi}{\partial x} = \frac{\partial\psi}{\partial y} = 0,$$

on the outer cylinder and

$$\psi = \psi_w, \quad \frac{\partial\psi}{\partial x} = -x, \quad \frac{\partial\psi}{\partial y} = -y,$$

on the inner cylinder. The flow is simulated with  $R = 0.25$  and  $L = \{0.55, 1.0\}$  using a uniform grid of  $52 \times 52$ . Several values of the Reynolds number, namely 1, 100, 500, 700 and 1000, are considered. Results concerning  $\psi_w$  obtained by the proposed technique and the finite-difference technique (Lewis, 1979) are presented in Table 4.1, showing a satisfactory agreement. Plots for the velocity and vorticity fields for the case of  $L = 1$  and  $R = 0.25$  at  $Re = \{1, 700\}$  are given in Figure 4.4.

Table 4.1: Example 1 (rotating cylinder): Comparison of the stream-function values at the inner cylinder,  $\psi_w$ , for  $Re$  from 1 to 1000 between the present technique (grid of  $52 \times 52$ ) and finite difference technique.

$Re$	1	100	500	1000
$(R, L)$	$(0.25, 0.55)$			
	$\psi_w$			
Present method	0.0581	0.0582	0.0586	0.0596
FDM (Lewis, 1979)	0.0625	0.0626	0.0621	0.0600
$(R, L)$	$(0.25, 1)$			
	$\psi_w$			
Present method	0.4622	0.4617	0.4500	0.4264
FDM (Lewis, 1979)	0.4656	0.4577	0.4465	0.4375

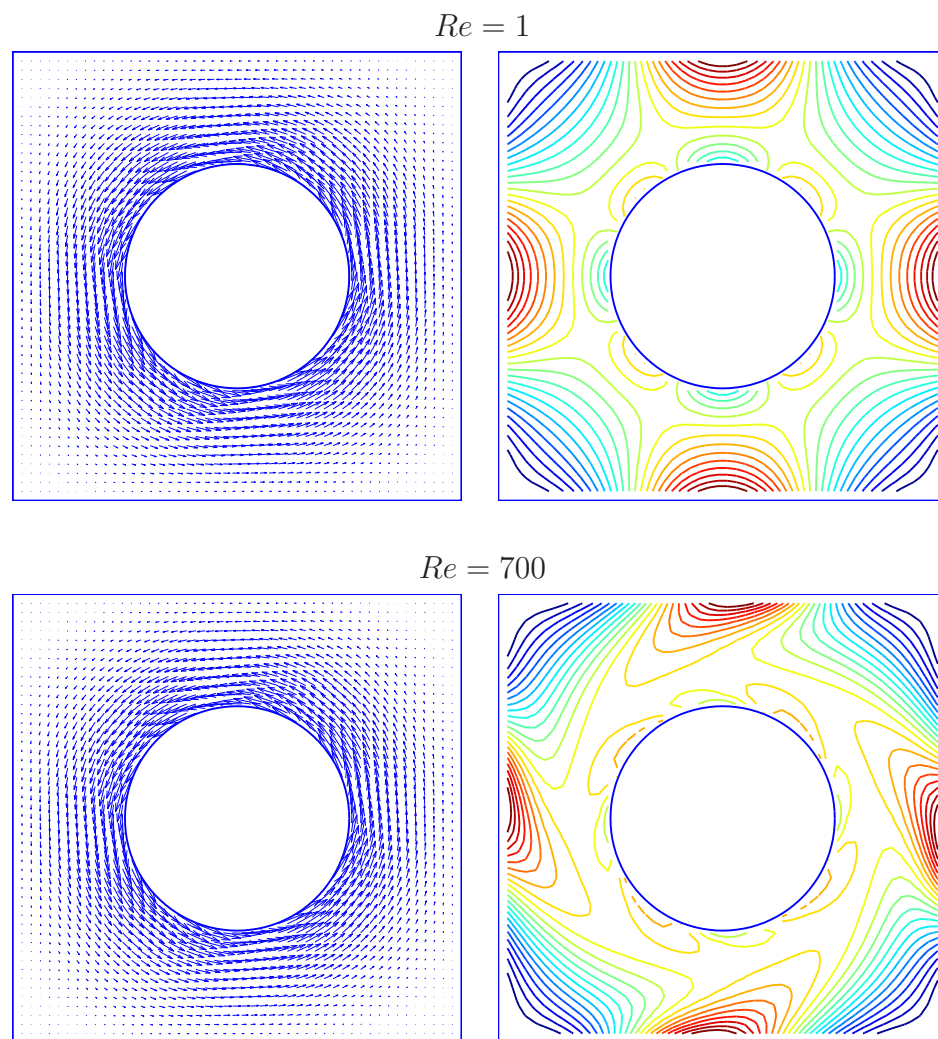


Figure 4.4: Example 1 (rotating cylinder,  $R=0.25$ ,  $L=1$ ): Velocity field (left) and vorticity field (right) for the flow at  $Re = 1$  and  $Re = 700$ .

### 4.5.2 Example 2: Natural convection in an eccentric annulus between two circular cylinders

Natural convection is governed by the coupling of the momentum equation (velocity field) (4.7) and energy equation (temperature field) (4.4). Solutions to natural convection have been reported using various discretisation techniques such as FDMs (e.g. Kuehn and Goldstein, 1976; de Vahl Davis, 1983), FEMs (e.g. Manzari, 1999; Sammouda et al., 1999), FVMs (e.g. Glakpe et al., 1986; Kaminski and Prakash, 1986), BEMs (e.g. Kitagawa et al., 1988; Hribersek and Skerget, 1999), spectral methods (e.g. Shu, 1999; Shu et al., 2002; Shu and Wu, 2002) and meshless methods (e.g. Divo and Kassab, 2008; Šarler et al., 2004; Šarler, 2005).

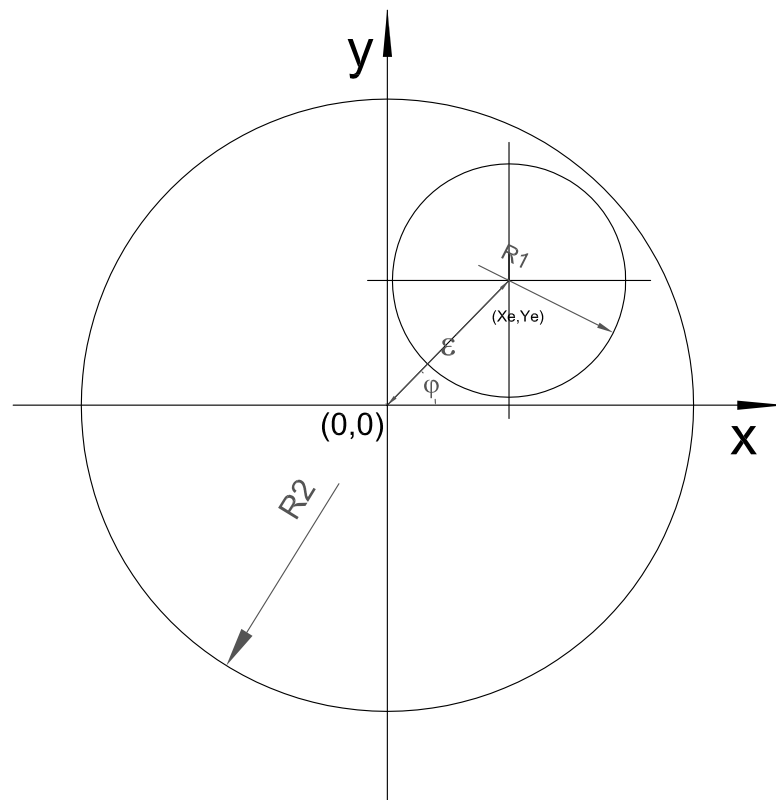
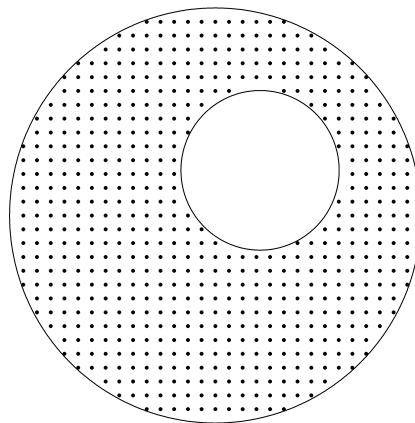
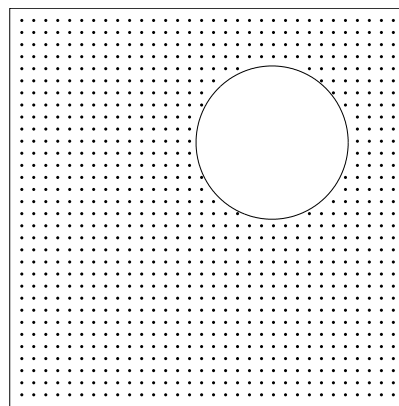


Figure 4.5: Example 2 (eccentric circular-circular annulus): geometry.



(a)



(b)

Figure 4.6: Schematic spatial discretisations for an annulus between two circular cylinders (a) and an annulus between inner circular and outer square cylinders (b).

Consider buoyancy-driven flows of a Newtonian fluid between two cylinders whose centres are separated by a distance  $\varepsilon$  (Figure 4.5). As shown in Figure 4.5, the flow geometry is defined by the following geometrical parameters: the eccentricity  $\varepsilon$ , angular position  $\varphi$ , the diameter of the outer cylinder  $D_o$  and the diameter of the inner cylinder  $D_i$ . In the present work, the numerical results are reported with  $Pr = 0.71$  and  $D_o/D_i = 2.6$ . A typical discretisation is shown on Figure 4.6a, where no coordinate transformations are employed.

The inner and outer cylinders are heated ( $T = 1$ ) and cooled ( $T = 0$ ), respectively. The stream-function value at the outer cylinder is set to zero. The stream-function value at the inner cylinder is a part of the solution and can be determined by the single-valued pressure condition (4.25). The normal derivatives of the stream function are set to zero at both walls.

Both trust region and time marching techniques are applied here to solve the nonlinear equation set. For the trust region technique, it takes about 5 to 10 iterations to get a converged solution. For the time marching technique, much more iterations are required as shown in Figure 4.7. However, a single iteration of the decoupled approach consumes much less CPU time than that of the coupled approach. Overall, the decoupled approach is more efficient than the coupled approach. For example, in the case of simulating the flow at  $Ra = 10^4$  using a grid of  $41 \times 41$ , the decoupled approach is about 9.2 times faster than the coupled approach.

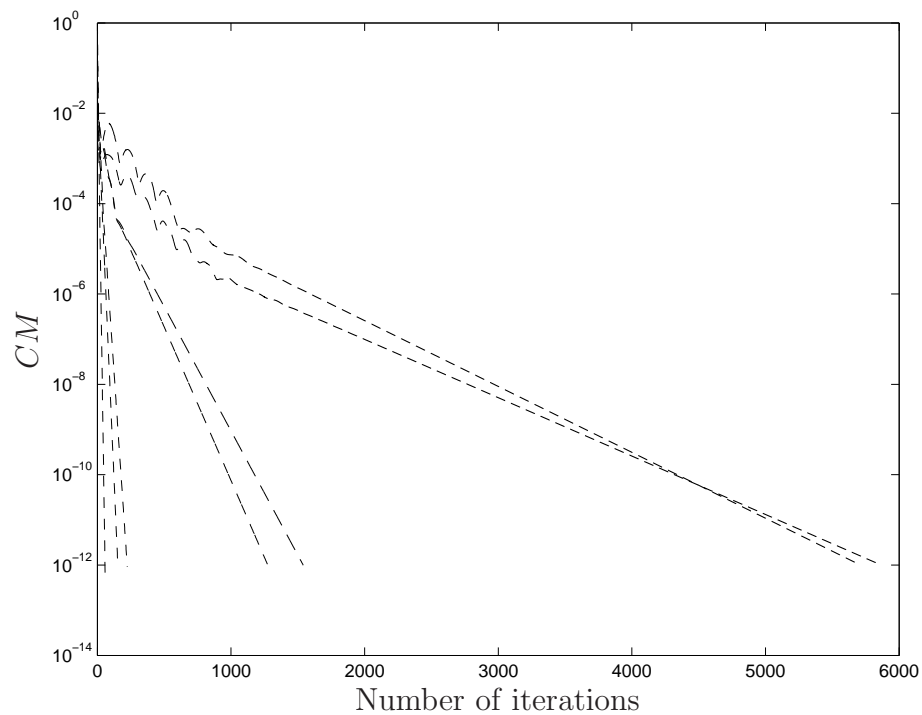


Figure 4.7: Example 2 (circular-circular annulus):  $61 \times 61$ , decoupled approach, iterative convergence. Time steps used are 0.5 for  $Ra = \{10^2, 10^3, 3 \times 10^3\}$ , 0.1 for  $Ra = \{6 \times 10^3, 10^4\}$ , and 0.05 for  $Ra = \{5 \times 10^4, 7 \times 10^4\}$ . The values of CM become less than  $10^{-12}$  when the numbers of iterations reach 58, 154, 224, 1276, 1541, 5711 and 5867 for  $Ra = \{10^2, 10^3, 3 \times 10^3, 6 \times 10^3, 10^4, 5 \times 10^4, 7 \times 10^4\}$ , respectively. Using the last point on the curves as a positional indicator, from left to right the curves correspond to  $Ra = \{10^2, 10^3, 3 \times 10^3, 6 \times 10^3, 10^4, 5 \times 10^4, 7 \times 10^4\}$

Table 4.2: Condition numbers of the RBFN matrices associated with the harmonic and biharmonic operators.

Grid	$\text{cond}(\mathcal{L}_2 T)$	$\text{cond}(\mathcal{L}_4 \psi)$
$11 \times 11$	$1.3 \times 10^1$	$7.4 \times 10^1$
$21 \times 21$	$1.2 \times 10^2$	$5.0 \times 10^3$
$31 \times 31$	$3.3 \times 10^2$	$3.3 \times 10^4$
$41 \times 41$	$5.1 \times 10^2$	$7.9 \times 10^4$
$51 \times 51$	$7.5 \times 10^2$	$1.6 \times 10^5$
$61 \times 61$	$1.0 \times 10^3$	$3.2 \times 10^5$

The condition numbers of the system matrix associated with the energy equation (4.4) and momentum equation (4.7) are reported in Table 4.2.

One typical quantity associated with this type of flow is the average equivalent conductivity denoted by  $\bar{k}_{eq}$ . This quantity is defined as (e.g. Kuehn and Goldstein, 1976)

$$\bar{k}_{eq} = \frac{-\ln(D_o/D_i)}{2\pi} \oint \frac{\partial T}{\partial n} ds \quad (4.40)$$

Table 4.3: Example 2 (symmetric flow, concentric circular-circular annuli): Convergence of  $\bar{k}_{eq}$  with grid refinement for the flow at  $Ra = 10^2$ .

Grid	Outer cylinder, $k_{eqo}$	Inner cylinder, $k_{eqi}$
$11 \times 11$	0.969	0.972
$21 \times 21$	0.994	0.989
$31 \times 31$	0.997	0.997
$41 \times 41$	0.999	0.999
FDM (Kuehn and Goldstein, 1976)	1.002	1.000
DQM (Shu, 1999)	1.001	1.001

The present method is first tested with the case of symmetrical flows, where the exact value of  $\psi$  at the inner wall is known (i.e.  $\psi_w = 0$  for the present case). Three uniform grids of  $41 \times 41$ ,  $51 \times 51$  and  $61 \times 61$  are employed to represent the

Table 4.4: Example 2 (symmetric flow, concentric circular-circular annuli): Convergence of  $\bar{k}_{eq}$  with grid refinement for the flow at  $Ra = 10^3$ .

Grid	Outer cylinder, $k_{eqo}$	Inner cylinder, $k_{eqi}$
$11 \times 11$	1.133	1.046
$21 \times 21$	1.072	1.069
$31 \times 31$	1.078	1.077
$41 \times 41$	1.080	1.079
$51 \times 51$	1.081	1.080
FDM (Kuehn and Goldstein, 1976)	1.084	1.081
DQM (Shu, 1999)	1.082	1.082

Table 4.5: Example 2 (symmetric flow, concentric circular-circular annuli): Convergence of  $\bar{k}_{eq}$  with grid refinement for the flow at  $Ra = 3 \times 10^3$ .

Grid	Outer cylinder, $k_{eqo}$	Inner cylinder, $k_{eqi}$
$11 \times 11$	1.745	1.200
$21 \times 21$	1.365	1.378
$31 \times 31$	1.387	1.386
$41 \times 41$	1.391	1.390
$51 \times 51$	1.393	1.393
FDM (Kuehn and Goldstein, 1976)	1.402	1.404
DQM (Shu, 1999)	1.397	1.397

flow field. For concentric cylinders, results concerning  $\bar{k}_{eq}$  together with those of (Kuehn and Goldstein, 1976) and of (Shu, 1999) for various Rayleigh numbers from  $10^2$  to  $7 \times 10^4$  are presented in Tables 4.3-4.9. It can be seen that there is a good agreement between these numerical solutions. For each Rayleigh number, the convergence of the average equivalent conductivity with grid refinement is fast, e.g. the solution  $k_{eqo}$  for the last two Rayleigh numbers (i.e.  $Ra = 10^4$  and  $Ra = 5 \times 10^4$ ) converges as  $O(h^{2.71})$  and  $O(h^{3.36})$  in which  $h$  is the grid spacing (errors are computed relative to the spectral results). Variations of the local equivalent conductivity on the inner and outer cylinder surfaces using a grid of  $51 \times 51$  for  $Ra = 10^3$  and  $Ra = 5 \times 10^4$  are shown in Figures 4.8 and

Table 4.6: Example 2 (symmetric flow, concentric circular-circular annuli): Convergence of  $\bar{k}_{eq}$  with grid refinement for the flow at  $Ra = 6 \times 10^3$ .

Grid	Outer cylinder, $k_{eqo}$	Inner cylinder, $k_{eqi}$
$31 \times 31$	1.698	1.702
$41 \times 41$	1.704	1.705
$51 \times 51$	1.709	1.709
$61 \times 61$	1.711	1.711
FDM (Kuehn and Goldstein, 1976)	1.735	1.736
DQM (Shu, 1999)	1.715	1.715

Table 4.7: Example 2 (symmetric flow, concentric circular-circular annuli): Convergence of  $\bar{k}_{eq}$  with grid refinement for the flow at  $Ra = 10^4$ .

Grid	Outer cylinder, $k_{eqo}$	Inner cylinder, $k_{eqi}$
$41 \times 41$	1.961	1.967
$51 \times 51$	1.969	1.971
$61 \times 61$	1.973	1.973
FDM (Kuehn and Goldstein, 1976)	2.005	2.010
DQM (Shu, 1999)	1.979	1.979

4.9, respectively. It can be seen that they are compared well with those of (Kuehn and Goldstein, 1976). The present solutions converge well and are in close agreement with the other solutions. It can be seen that the IRBFN results are more agreeable to the DQ ones than the FD results. Figure 4.10 shows the streamlines and isotherms of the flow for  $Ra = \{10^3, 6 \times 10^3, 5 \times 10^4, 7 \times 10^4\}$  using a grid of  $51 \times 51$ . Each plot contains 21 contour lines whose levels vary linearly from the minimum to maximum values. The plots look reasonable in comparison with those of the FD and DQ methods. For eccentric cylinders (i.e. the centres of inner and outer cylinders lie on the vertical symmetrical axis), results obtained show that the value of  $\psi_w$  is less than  $10^{-6}$ , which is close to zero. Table 4.10 compares the maximum value of  $\psi$  for  $Ra = 10^4$  between the proposed method and the DQM (Shu, 1999). Good agreement is achieved.

Table 4.8: Example 2 (symmetric flow, concentric circular-circular annuli): Convergence of  $\bar{k}_{eq}$  with grid refinement for the flow at  $Ra = 5 \times 10^4$ .

Grid	Outer cylinder, $k_{eqo}$	Inner cylinder, $k_{eqi}$
$41 \times 41$	3.089	3.045
$51 \times 51$	2.936	2.946
$61 \times 61$	2.922	2.941
FDM (Kuehn and Goldstein, 1976)	2.973	3.024
DQM (Shu, 1999)	2.958	2.958

Table 4.9: Example 2 (symmetric flow, concentric circular-circular annuli): Convergence of  $\bar{k}_{eq}$  with grid refinement for the flow at  $Ra = 7 \times 10^4$ .

Grid	Outer cylinder, $k_{eqo}$	Inner cylinder, $k_{eqi}$
$41 \times 41$	3.465	3.254
$51 \times 51$	3.241	3.187
$61 \times 61$	3.167	3.174
FDM (Kuehn and Goldstein, 1976)	3.226	3.308

For the case of unsymmetrical flows, the value of  $\psi$  at the inner wall has non-zero value that varies with the location of the inner cylinder. Different amounts of eccentricity ( $\varepsilon$ ), namely  $\{0.25, 0.5, 0.75, 0.95\}$ , and angular direction  $\varphi$ , namely  $\{-45^\circ, 0^\circ, 45^\circ\}$ , are employed. In Table 4.11, the values of  $\psi$  at the inner walls are presented and agree satisfactorily with those conducted by the DQM (Shu et al., 2002) and the domain free discretisation method (DFD) (Shu and Wu, 2002). Figure 4.11 shows the streamlines and isotherms of the flow at  $Ra = 10^4$  using a grid of  $61 \times 61$ , where several values of eccentricity and angular directions are employed. Each plot contains 21 contour lines whose levels vary linearly from the minimum to maximum values. All plots look reasonable when compared with those of the DQM (Shu et al., 2002).

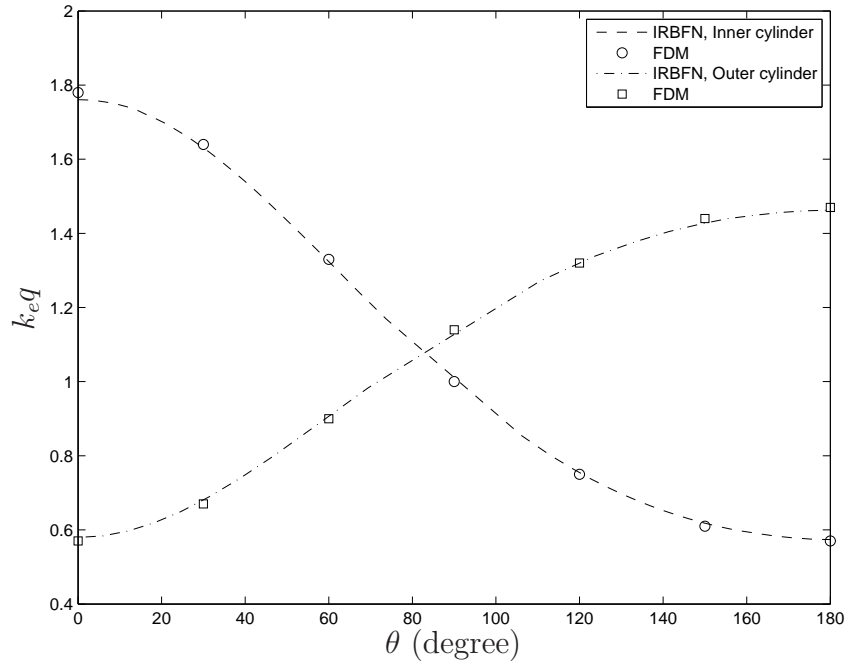


Figure 4.8: Example 2 (concentric circular-circular annulus): Local equivalent conductivities for  $Ra = 10^3$  by 1D-IRBFN and FDM.

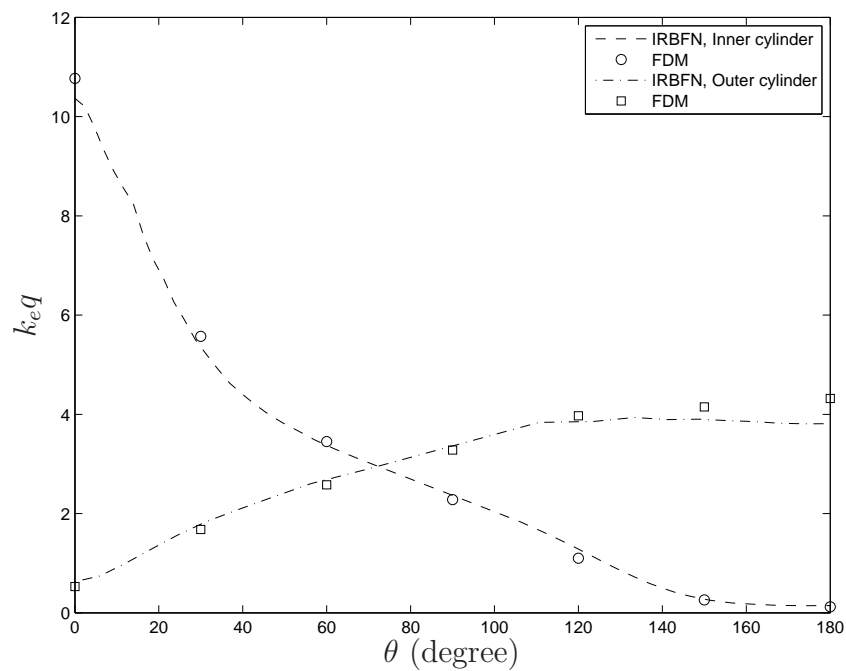


Figure 4.9: Example 2 (concentric circular-circular annulus): Local equivalent conductivities for  $Ra = 5 \times 10^4$  by 1D-IRBFN and FDM.

Table 4.10: Example 2 (symmetric flow, eccentric circular-circular annuli): Comparison of the maximum stream-function values,  $\psi_{max}$ , for two special cases  $\varphi = \{-90^0, 90^0\}$  between the present technique and DQM technique.

$\varepsilon$	0.25	0.5	0.75	0.95
$\varphi$	$-90^0$			
	$\psi_{max}$			
Present method	22.19	20.72	18.50	15.71
DQM (Shu et al., 2002)	22.16	20.62	18.32	15.50
$\varphi$	$90^0$			
	$\psi_{max}$			
Present method	11.26	9.64	8.25	7.28
DQM (Shu et al., 2002)	11.13	9.55	8.12	7.17

Table 4.11: Example 2 (unsymmetrical flow, eccentric circular-circular annuli): Comparison of the stream-function values at the inner cylinders,  $\psi_w$ , for  $\varepsilon = \{0.25, 0.5, 0.75, 0.95\}$  and  $\varphi = \{-45^0, 0^0, 45^0\}$  between the present, DQM and DFD techniques.

$\varepsilon$	0.25	0.5	0.75	0.95
$\varphi$	$45^0$			
	$\psi_w$			
Present method	0.52	1.25	1.01	0.01
DQM (Shu et al., 2002)	0.52	1.31	1.07	0.03
DFD (Shu and Wu, 2002)	0.54	1.29	1.09	0.03
$\varphi$	$0^0$			
	$\psi_w$			
Present method	0.60	1.28	1.18	0.01
DQM (Shu et al., 2002)	0.72	1.15	1.30	0.06
DFD (Shu and Wu, 2002)	0.72	1.10	1.26	0.06
$\varphi$	$-45^0$			
	$\psi_w$			
Present method	0.48	0.80	1.05	0.6
DQM (Shu et al., 2002)	0.51	0.92	0.99	0.08
DFD (Shu and Wu, 2002)	0.51	0.77	0.77	0.04

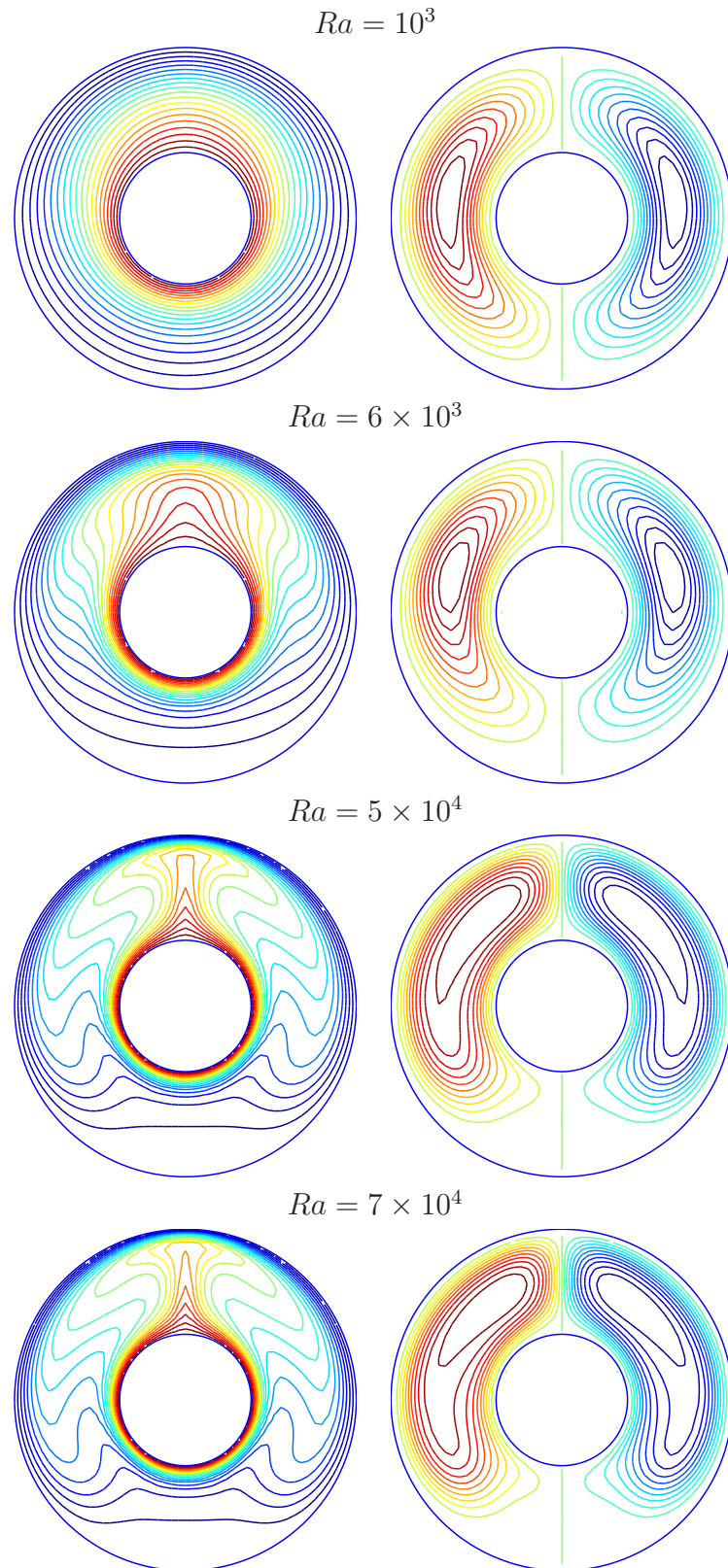


Figure 4.10: Example 2 (concentric circular-circular annulus): Contour plots of temperature (left) and stream function (right) for four different Rayleigh numbers using a grid of  $51 \times 51$ . Each plot contains 21 contour lines whose levels vary linearly from the minimum to maximum values.

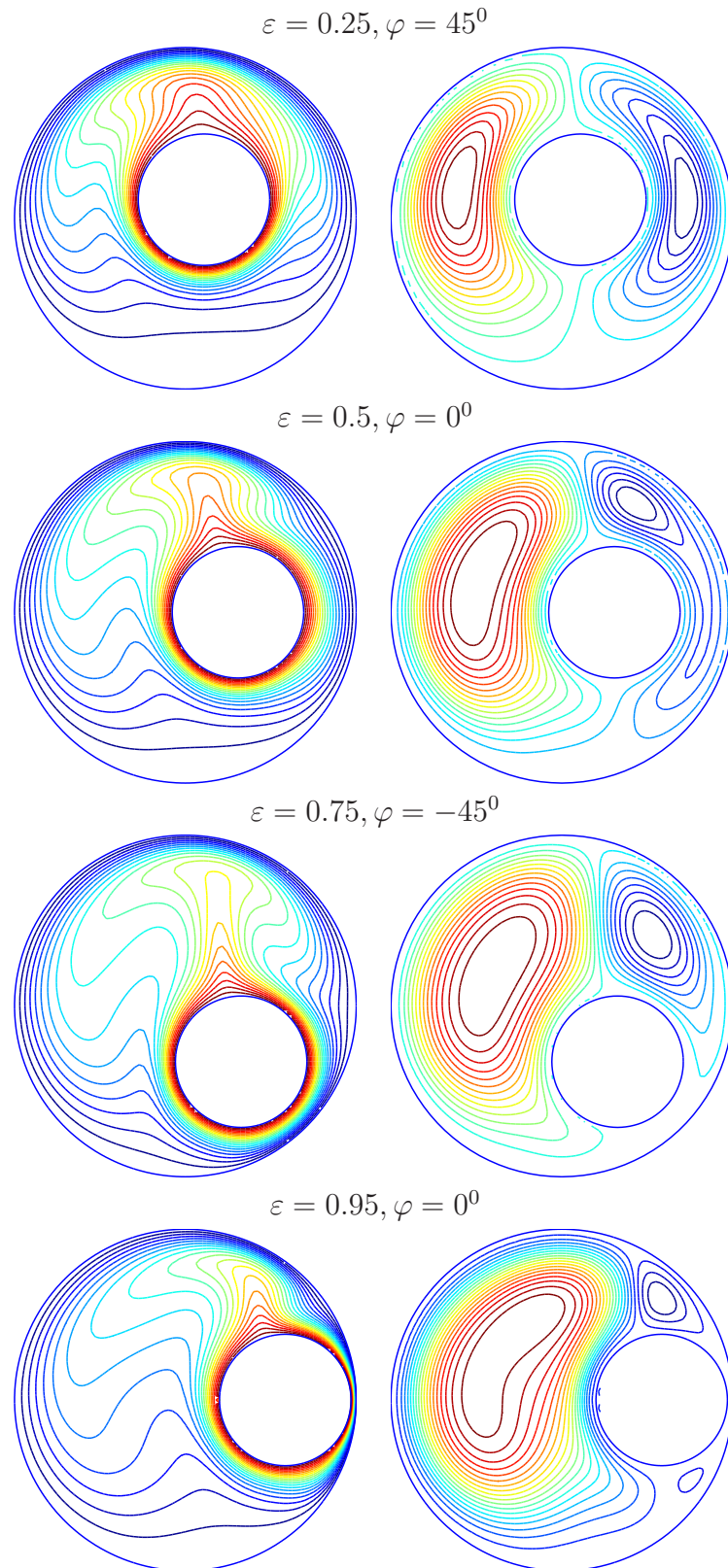


Figure 4.11: Example 2 (eccentric circular-circular annuli): Contour plots for the temperature (left) and stream-function (right) fields for several values of eccentricity  $\varepsilon$  and angular directions  $\varphi$  for the flow at  $Ra = 1 \times 10^4$ . Each plot contains 21 contour lines whose levels vary linearly from the minimum to maximum values.

### 4.5.3 Example 3: Natural convection in eccentric annuli between a square outer and a circular inner cylinder

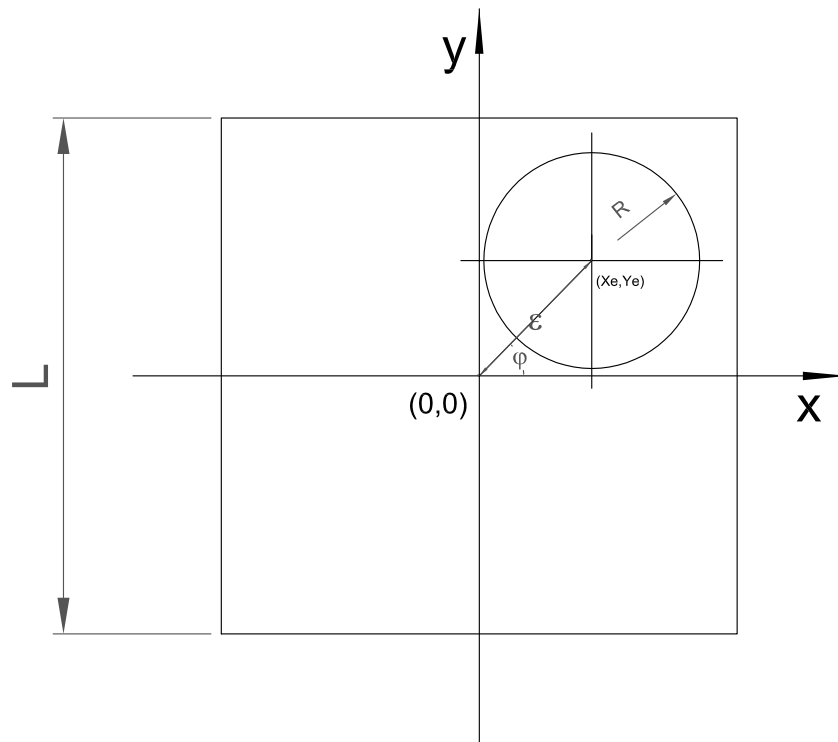


Figure 4.12: Example 3 (eccentric square-circular domain): geometry.

In this example, natural convection between a heated inner circular cylinder and a cooled square enclosure (Figure 4.12) is considered. An aspect ratio of  $L/2R = 2.6$  ( $L$ : the side length of the outer square and  $R$ : the radius of the inner circle),  $Pr = 0.71$  and  $Ra = 3 \times 10^5$  are used.

The problem domain is simply replaced with a Cartesian grid (Figure 4.6b), where no coordinate transformations are employed.

For the concentric case, the obtained results are presented in the forms of streamlines and isotherms (Figure 4.13). In Figure 4.13, each plot contains 21 contour lines whose levels vary linearly from the minimum to maximum val-

Table 4.12: Example 3 (symmetric flow, eccentric square-circular annuli): Comparison of the maximum stream-function values,  $\psi_{max}$ , for special cases  $\varphi = \{-90^0, 90^0\}$  between the present technique and MQ-DQ technique.

$\varepsilon$	0.25	0.5	0.75	0.95
$\varphi$	$-90^0$			
	$\psi_{max}$			
Present method	18.63	21.30	23.47	24.48
MQ-DQ (Ding et al., 2005)	18.64	21.29	23.52	
$\varphi$	$90^0$			
	$\psi_{max}$			
Present method	12.37	11.36	10.10	9.289
MQ-DQ (Ding et al., 2005)	12.39	11.38	10.09	

ues. For special cases of eccentric square-circular annuli, where the centre of the inner cylinder lies on the vertical symmetrical axis of the outer square cylinder, the values of  $\psi_{max}$  are given in Table 4.12. It can be seen that the present results are in very good agreement with those of Ding et al., 2005.

Table 4.13: Example 3 (concentric square-circular annuli): Comparison of the average Nusselt number on the outer and inner cylinders,  $Nu_o$  and  $Nu_i$ , for  $Ra$  from  $10^4$  to  $10^6$  between the present technique (grid of  $62 \times 62$ ) and some other techniques.

$Ra$	$10^4$	$5 \times 10^4$	$10^5$	$5 \times 10^5$	$10^6$
	$Nu_o$				
Present method	3.22	4.04	4.89	7.43	8.70
MQ-DQ (Ding et al., 2005)	3.24		4.86		8.90
FVM (Moukalled and Acharya, 1996)	3.33		5.08		9.37
	$Nu_i$				
Present method	3.21	4.04	4.89	7.51	8.85
MQ-DQ (Ding et al., 2005)	3.24		4.86		8.90
FVM (Moukalled and Acharya, 1996)	3.33		5.08		9.37

Following the work of Moukalled and Acharya (Moukalled and Acharya, 1996),

Table 4.14: Example 3 (unsymmetrical flow, eccentric square-circular annuli): Comparison of the maximum stream-function values,  $\psi_{max}$ , for  $\varepsilon = \{0.25, 0.5, 0.75, 0.95\}$  and  $\varphi = \{-45^0, 0^0, 45^0\}$  between the present technique and MQ-DQ technique.

$\varepsilon$	0.25	0.5	0.75	0.95
$\varphi$	$45^0$			
	$\psi_{max}$			
Present method	15.31	14.23	13.52	12.91
MQ-DQ (Ding et al., 2005)	15.32	14.35	13.61	12.98
$\varphi$	$0^0$			
	$\psi_{max}$			
Present method	17.00	16.99	16.87	17.18
MQ-DQ (Ding et al., 2005)	17.00	16.97	16.84	
$\varphi$	$-45^0$			
	$\psi_{max}$			
Present method	18.50	20.09	21.02	21.61
MQ-DQ (Ding et al., 2005)	18.50	20.03	21.01	21.68

the local heat transfer coefficient is defined as

$$\theta = -k \frac{\partial T}{\partial n}, \quad (4.41)$$

where  $k$  is the thermal conductivity. The average Nusselt number (the ratio of the temperature gradient at the wall to a reference temperature gradient) is computed by

$$Nu = \frac{\bar{\theta}}{k}, \quad (4.42)$$

where  $\bar{\theta} = -\oint \frac{\partial T}{\partial n} ds$ . Since the computational domain in (Moukalled and Acharya, 1996) is taken as one-half of the physical domain, the values of  $Nu$  in the present work (Table 4.13) are divided by 2 for comparison purposes. The present results agree well with those in (Moukalled and Acharya, 1996) and (Ding et al., 2005).

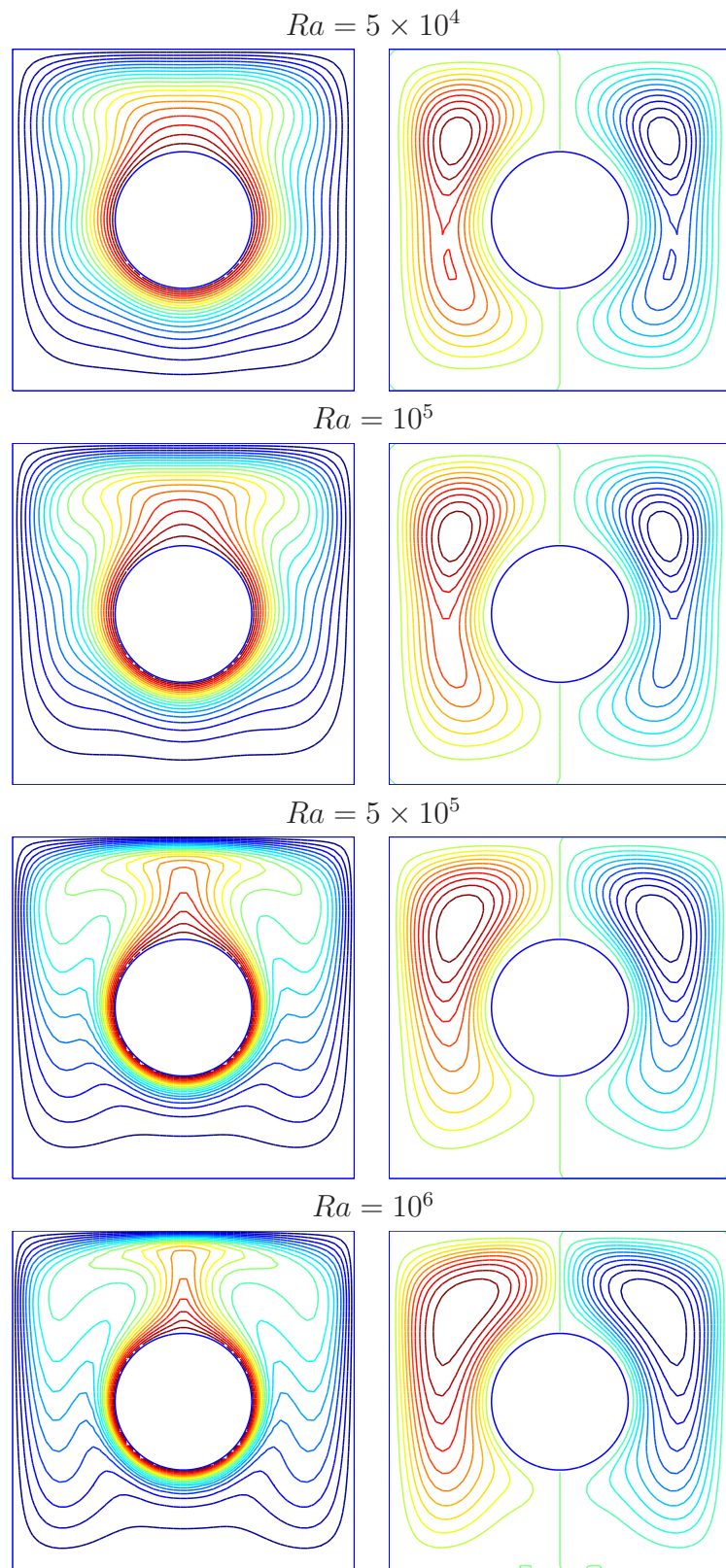


Figure 4.13: Example 3 (concentric square-circular annulus): Contour plots of temperature (left) and stream function (right) for four different Rayleigh numbers using a grid of  $61 \times 61$ . Each plot contains 21 contour lines whose levels vary linearly from the minimum to maximum values.

Similar to Example 2, the eccentricity values used are  $\varepsilon = \{0.25, 0.5, 0.75, 0.95\}$  and the angular positions are  $\varphi = \{-45^0, 0^0, 45^0\}$ . The value of  $\psi$  along the inner wall is considered as an unknown and the values of  $\psi$  along the outer boundary can be taken to be zero. Calculations are performed on a uniform Cartesian grid of  $62 \times 62$ . In Table 4.14, the maximum values of the stream function are presented and compared very well with those obtained by Ding et al. (2005).

In Figure 4.14, the effects of time step on convergence behaviour of the proposed technique are investigated for the case of  $Ra = 1 \times 10^5$  using a grid of  $53 \times 53$ . It can be seen that the present technique can work with a wide range of values of time step. As expected, convergence is faster but less stable when the length of time step increases. In relation to CPU times, the present technique consumes 0.013715 (s) per iteration for a grid of  $33 \times 33$ , 0.0599 for  $49 \times 49$  and 0.0807 for  $53 \times 53$  (Intel Core 2 6300-1.86 Ghz). Figures 4.15 displays streamline and isotherm fields for several positions of the inner cylinder for  $Ra = 3 \times 10^5$ . The qualitative behaviours of these fields and those in (Ding et al., 2005) are similar.

For all values of the Reynolds/Rayleigh number employed in these examples, it is observed that the solution evolves in a stable manner with relatively-large time steps. As a result, the use of special treatments for the convection term such as the upwind scheme is not necessary here.

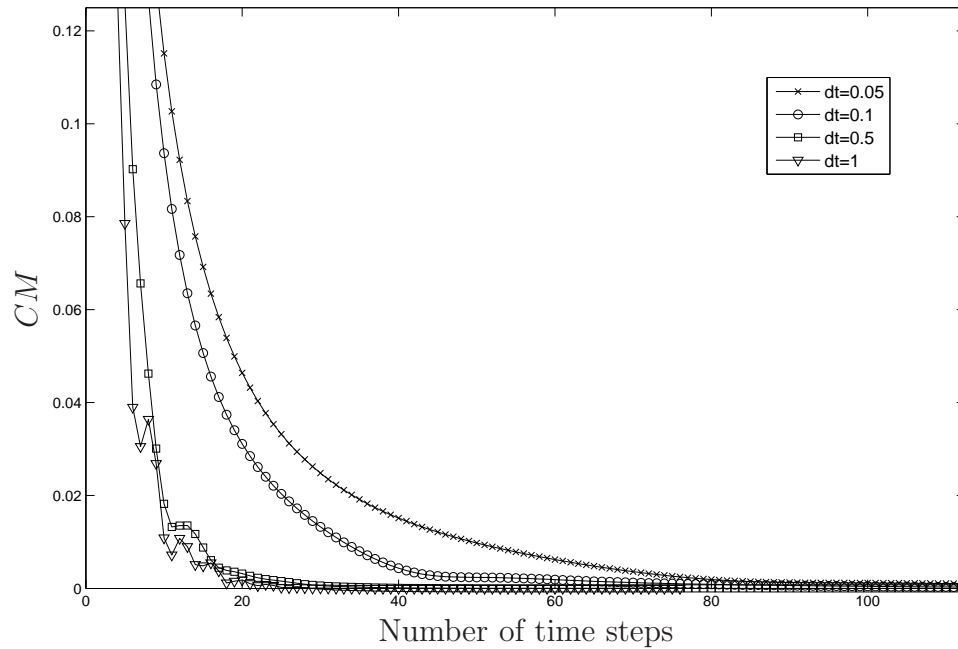


Figure 4.14: Example 3 (eccentric square-circular annulus): the effects of time-step length on convergence behaviour.

## 4.6 Concluding Remarks

In this chapter, flows in multiply-connected domains are studied using the stream-function formulation, one-dimensional integrated RBFN approximations and Cartesian grids. Formulas for handling mixed derivatives in irregular regions and boundary conditions for the stream-function variable are derived under the Cartesian framework, and they are implemented effectively with 1D-IRBFNs. Attractive features of the proposed technique include (i) simple pre-processing; and (ii) the ability to retain the PDEs in their Cartesian forms, and thus to work in a similar fashion for different shapes of annuli. Various solutions are reported to demonstrate the capabilities of the proposed technique.

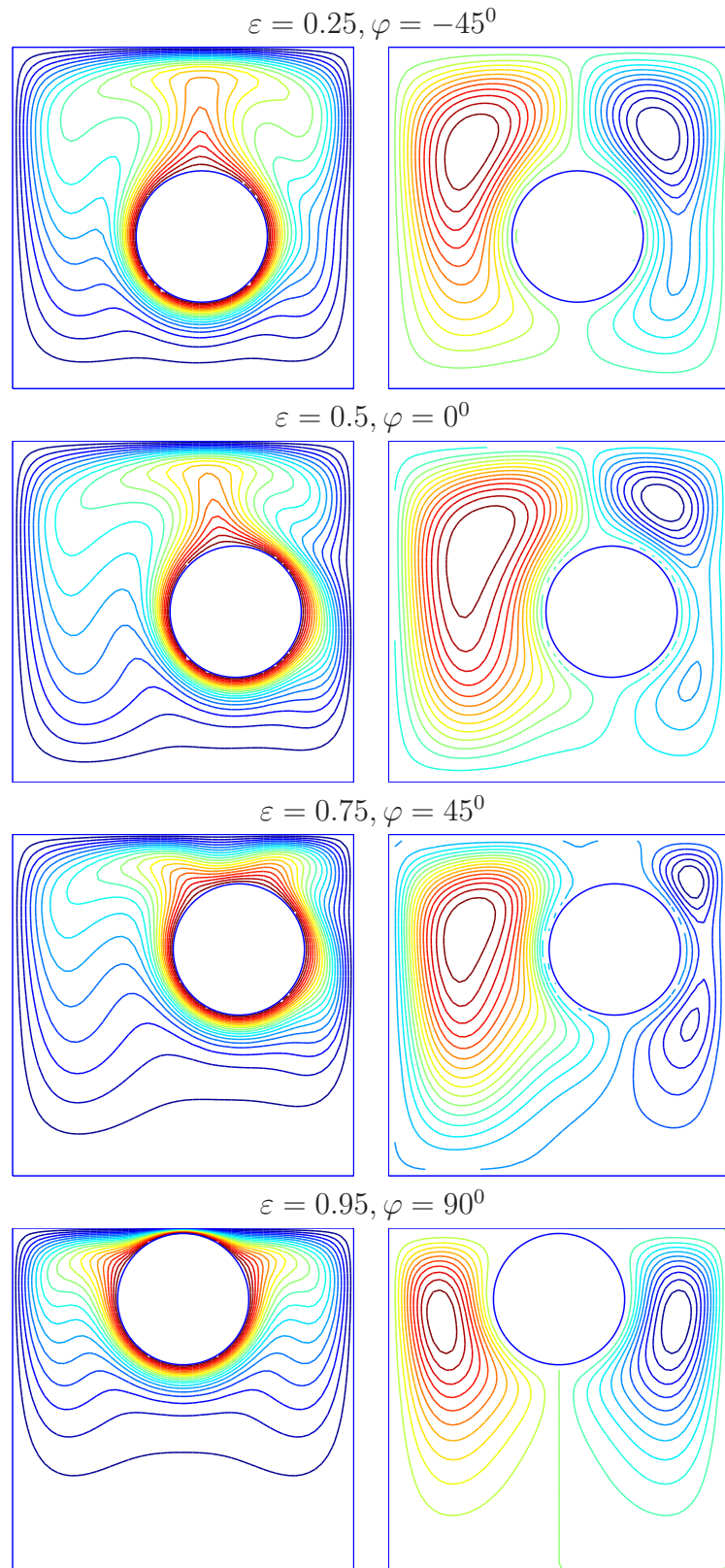


Figure 4.15: Example 3 (eccentric square-circular annuli): The temperature (left) and stream-function (right) fields for several values of eccentricity  $\varepsilon$  and angular direction  $\varphi$  for the flow at  $Ra = 3 \times 10^5$ . Each plot contains 21 contour lines whose levels vary linearly from the minimum to maximum values.

## Chapter 5

# 1D-integrated-RBFN-based domain embedding technique

This chapter presents a new domain embedding numerical technique for solving PDEs in multiply-connected domains. The problem domain is converted into a simply-connected domain that is then discretised using a Cartesian grid. The field variable in a given PDE is assumed to vary over interior holes according to appropriate analytic functions that are constructed to satisfy the boundary conditions. Point collocation and 1D-IRBFNs are applied to discretise the PDE in a resultant simple domain. Several linear boundary-value and initial-value problems, some of which have exact solutions, are considered to validate the proposed technique.

## 5.1 Introduction

There are two general approaches of handling geometrically-complex multiply-connected domains in solving PDEs, namely boundary fitted and domain embedding. The former was considered in the previous three chapters, while the latter is studied in the context of 1D-IRBFNs in this chapter.

The use of the domain embedding approach for solving differential problems defined on irregular domains has received much increased attention in recent years (e.g. Glowinski et al., 1994; Maury, 2001; Parvizian et al., 2007; Husain et al., 2009; Mai-Duy et al., 2009; Buffat and Penven, 2010). The concept of domain embedding or fictitious domain is known to provide an efficient way to handle complex geometries. The basic idea of domain-embedding/fictitious-domain based methods is to extend the problem defined on a geometrically-complex domain to that on a larger, but simpler shaped domain. However, special attention is paid to the imposition of given boundary conditions in order to match the solution on the extended domain with that on the original domain. The extended domain allows the use of a regular grid/mesh, and one can thus employ fast direct solvers for the resultant algebraic system. In the case of multiply-connected domains with moving interior holes, the mesh/grid may remain fixed. As a result, the discrete system matrix may be formed once and stay unchanged through the computation process.

Domain-embedding-based methods have been very successful in solving complicated engineering problems. Glowinski et al. (1994, 1998) presented a family of fictitious-domain techniques which are based on the explicit use of Lagrange multipliers defined on the actual boundary and associated with the boundary conditions for Dirichlet elliptic problems. Since then, Lagrange multiplier/fictitious-domain methods have become increasingly popular. They were applied successfully to simulate practical problems including fluid/rigid-body interactions (e.g. Patankar et al., 2000), fluid/flexible-body interactions (e.g. Yu, 2005), and par-

ticulate suspension flows (e.g. Wan and Turek, 2006). Parvizian et al. (2007) proposed a finite cell method with  $h$ - and  $p$ - extension for embedded domain problems in solid mechanics. Duster et al. (2008) extended the finite cell method to 3D problems of linear elasticity. Maury (2001) introduced a fat boundary method (FBM) for solving PDEs in a domain with holes. Bertoluzza et al. (2005) gave some numerical results on a semi-discrete FBM in the framework of a FE discretisation. Vos et al. (2008) combined the classic fictitious domain method and FBM to form an implicit FBM.

This chapter reports a new domain-embedding-based technique for the solution of PDEs in multiply-connected domains. The proposed technique combines strengths of the three approaches, namely 1D-IRBFNs (high-order approximator), Cartesian grids (simple preprocessing) and fictitious domains (complex geometry). Unlike other domain-embedding-based techniques, the variations of the field variable over interior holes are presently represented by appropriate analytic functions that are constructed to satisfy the boundary conditions. Results obtained are compared well with analytic and other numerical solutions.

The remainder of this chapter is organised as follows. In Section 5.2, the proposed method is presented for the solution of elliptic and parabolic equations. Emphasis is placed on the construction of analytic functions representing the solution over fictitious regions. Details for 1D-IRBFN discretisations of PDEs in extended (rectangular) domains are also included. Numerical results are presented in Section 5.3. Section 5.4 concludes the chapter.

## 5.2 Proposed domain-embedding technique

Consider a multiply-connected domain such as the one shown in Figure 5.1. This physical domain is embedded in a rectangular domain that is used for computation. The computational domain thus involves two kinds of subregion: the

first made up of the holes (fictitious) and the second by the multiply-connected domain (real). One thus needs to ensure that all boundary conditions on the boundaries of the inner holes are taken into account.

Let  $f_f$  and  $f_r$  represent the solution  $f$  in the holes and in the real domain, respectively. We assume that (i) the function  $f$  is at least  $C^0$ -continuous (i.e.  $f_f = f_r$ ) across the interfaces between the real domain and fictitious regions; and (ii) the solution in the holes can be represented by suitable analytic functions.

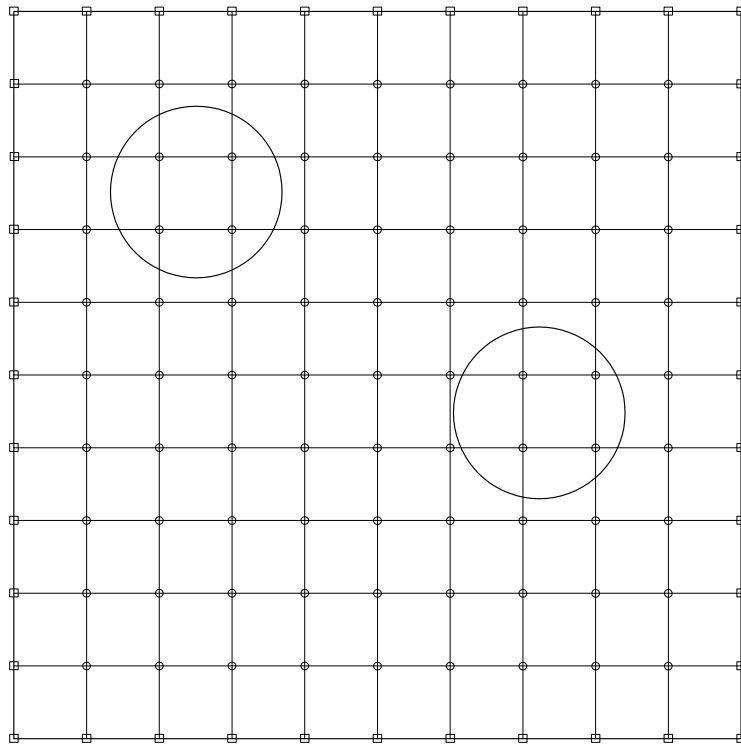


Figure 5.1: A multiply-connected domain. Its extension is a rectangular domain that is represented by a Cartesian discretisation.

Cartesian grids are employed to represent the extended/computational domain and IRBFNs are then utilised to approximate the field variable  $f$  on each grid line. In the following, details are presented for two main parts, namely (i) 1D-IRBFN discretisation for the PDE in a rectangular domain (i.e. extended domain); and (ii) imposition of boundary conditions on the interfaces between the real domain and fictitious regions.

### 5.2.1 1D-IRBFN discretisation for extended domain

All PDEs in the present chapter are of second order. Consider an  $x$ -grid line. Making use of (2.5)-(2.9) with  $p = 2$ , second-order derivative of the field variable  $f$  along a grid line can be decomposed into RBFs

$$\frac{\partial^2 f(x)}{\partial x^2} = \sum_{i=1}^m w_i g_i(x) = \sum_{i=1}^m w_i I_i^{(2)}(x), \quad (5.1)$$

where  $m$  is the number of RBFs,  $\{g_i(x)\}_{i=1}^m \equiv \{I_i^{(2)}(x)\}_{i=1}^m$  the set of RBFs,  $\{w_i\}_{i=1}^m$  the set of weights to be found. Approximate expressions for the first-order derivative and the field variable are then obtained through integration

$$\frac{\partial f(x)}{\partial x} = \sum_{i=1}^m w_i I_i^{(1)}(x) + c_1, \quad (5.2)$$

$$f(x) = \sum_{i=1}^m w_i I_i^{(0)}(x) + c_1 x + c_2, \quad (5.3)$$

where  $I_i^{(1)}(x) = \int I_i^{(2)}(x) dx$ ,  $I_i^{(0)}(x) = \int I_i^{(1)}(x) dx$  and  $\{c_1, c_2\}$  are the constants of integration.

Collocating (5.3) at the nodal points yields

$$\hat{f} = \hat{\mathcal{I}}^{(0)} \begin{pmatrix} \hat{w} \\ c_1 \\ c_2 \end{pmatrix}, \quad (5.4)$$

where

$$\begin{aligned}\widehat{f} &= (f(x_1), f(x_2), \dots, f(x_m))^T, \\ \widehat{w} &= (w_1, w_2, \dots, w_m)^T, \\ \widehat{\mathcal{I}}^{(0)} &= \begin{bmatrix} I_1^{(0)}(x_1) & I_2^{(0)}(x_1) & \cdots & I_m^{(0)}(x_1) & x_1 & 1 \\ I_1^{(0)}(x_2) & I_2^{(0)}(x_2) & \cdots & I_m^{(0)}(x_2) & x_2 & 1 \\ \vdots & \vdots & \ddots & \vdots & \vdots & \vdots \\ I_1^{(0)}(x_m) & I_2^{(0)}(x_m) & \cdots & I_m^{(0)}(x_m) & x_m & 1 \end{bmatrix}.\end{aligned}$$

Solving (5.4) for the coefficient vector including the two integration constants results in

$$\begin{pmatrix} \widehat{w} \\ c_1 \\ c_2 \end{pmatrix} = \left(\widehat{\mathcal{I}}^{(0)}\right)^{-1} \widehat{f}, \quad (5.5)$$

where  $\left(\widehat{\mathcal{I}}^{(0)}\right)^{-1}$  is the generalised inverse of  $\widehat{\mathcal{I}}^{(0)}$ . The values of the first and second derivatives of  $f$  with respect to  $x$  at the nodal points are thus computed in terms of nodal variable values

$$\frac{\widehat{\partial f}}{\partial x} = \widehat{\mathcal{I}}^{(1)} \left(\widehat{\mathcal{I}}^{(0)}\right)^{-1} \widehat{f} = \widehat{\mathcal{D}}_{1x} \widehat{f}, \quad (5.6)$$

and

$$\frac{\widehat{\partial^2 f}}{\partial x^2} = \widehat{\mathcal{I}}^{(2)} \left(\widehat{\mathcal{I}}^{(0)}\right)^{-1} \widehat{f} = \widehat{\mathcal{D}}_{2x} \widehat{f}, \quad (5.7)$$

where

$$\frac{\widehat{\partial f}}{\partial x} = \left( \frac{\partial f(x_1)}{\partial x}, \frac{\partial f(x_2)}{\partial x}, \dots, \frac{\partial f(x_m)}{\partial x} \right)^T,$$

$$\frac{\widehat{\partial^2 f}}{\partial x^2} = \left( \frac{\partial^2 f(x_1)}{\partial x^2}, \frac{\partial^2 f(x_2)}{\partial x^2}, \dots, \frac{\partial^2 f(x_m)}{\partial x^2} \right)^T,$$

$$\widehat{\mathcal{I}}^{(1)} = \begin{bmatrix} I_1^{(1)}(x_1) & I_2^{(1)}(x_1) & \cdots & I_m^{(1)}(x_1) & 1 & 0 \\ I_1^{(1)}(x_2) & I_2^{(1)}(x_2) & \cdots & I_m^{(1)}(x_2) & 1 & 0 \\ \vdots & \vdots & \ddots & \vdots & \vdots & \vdots \\ I_1^{(1)}(x_m) & I_2^{(1)}(x_m) & \cdots & I_m^{(1)}(x_m) & 1 & 0 \end{bmatrix},$$

$$\widehat{\mathcal{I}}^{(2)} = \begin{bmatrix} g_1(x_1) & g_2(x_1) & \cdots & g_m(x_1) & 0 & 0 \\ g_1(x_2) & g_2(x_2) & \cdots & g_m(x_2) & 0 & 0 \\ \vdots & \vdots & \ddots & \vdots & \vdots & \vdots \\ g_1(x_m) & g_2(x_m) & \cdots & g_m(x_m) & 0 & 0 \end{bmatrix},$$

and  $\widehat{\mathcal{D}}_{1x}$ ,  $\widehat{\mathcal{D}}_{2x}$  are the first- and second-order differentiation matrices in the physical space.

In the same manner, one can obtain the IRBFN expressions for  $\partial f/\partial y$  and  $\partial^2 f/\partial y^2$  along a vertical line.

The 1D-IRBFN approximations of derivatives at a grid point are expressed in terms of the nodal values of  $f$  along the grid lines that go through that point. As with finite-difference and finite-element techniques, one will gather these approximations together to form the global matrices. This task is relatively simple since the grid used here is regular. For example, in the case of the Laplacian, the corresponding global matrix can be generated by means of tensor

products

$$\tilde{\mathcal{A}} = \widehat{\mathcal{D}}_{2x} \otimes \mathbf{1} + \mathbf{1} \otimes \widehat{\mathcal{D}}_{2y}, \quad (5.8)$$

where  $\mathbf{1}$  is the identity matrix of dimension of  $m \times m$ . In (5.8), the grid nodes are numbered from left to right and from bottom to top. The next task is to impose the boundary conditions. It is straightforward to implement the boundary conditions on the outer boundary. However, special treatments are required when imposing the boundary conditions on the inner boundaries as the grid nodes do not generally lie on these boundaries.

### 5.2.2 Imposition of the boundary conditions on the inner boundaries

Two types of equations, namely elliptic and parabolic, with Dirichlet boundary conditions are considered. Using 1D-IRBFNs and point collocation, the PDE reduces to a set of algebraic equations that can be written in the following form

$$\tilde{\mathcal{A}}\tilde{f} = \tilde{b}, \quad (5.9)$$

where  $\tilde{\mathcal{A}}$  is the system matrix,  $\tilde{f}$  the vector consisting of nodal values of  $f$  over the whole 2D computational domain and  $\tilde{b}$  the known vector generated by the driving function.

This system can be rearranged for unknown values of  $f$  in the real domain as

$$\tilde{\mathcal{A}}(idr, idr)\tilde{f}(idr) = \tilde{b}(idr) - \tilde{\mathcal{A}}(idr, idb)\tilde{f}(idb) - \tilde{\mathcal{A}}(idr, idf)\tilde{f}(idf), \quad (5.10)$$

where  $idr$ ,  $idb$  and  $idf$  are the sets whose elements are the indices of nodes in the real domain, on the outer boundary and in the fictitious regions, respectively. We assume that the solution in inner holes is known and can be described

by polynomials of third order in one dimension. The construction of these polynomials is presented in detail for a typical case: an  $x$ -grid line that crosses several inner holes as shown in Figure 5.2.

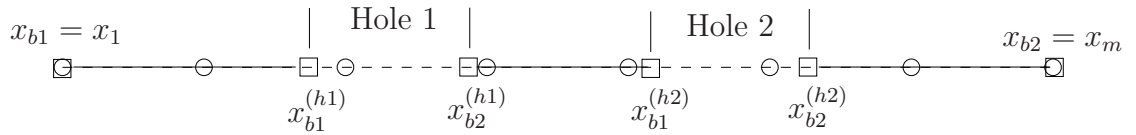


Figure 5.2: Points on a grid line consist of interior points  $x_i$  ( $\circ$ ) and boundary points  $x_{bi}$  ( $\square$ ).

Let  $x_{b1}^{(hi)}$  and  $x_{b2}^{(hi)}$  ( $i = (1, 2)$ ) be the coordinates of the boundary points of the  $i$ th hole on the  $x$ -grid line (Figure 5.2). We seek a function  $f_f(x)$  over the interval  $x_{b1}^{(hi)} \leq x \leq x_{b2}^{(hi)}$  in the form

$$f_f^{(hi)}(x) = ax^3 + bx^2 + cx + d, \quad (5.11)$$

where  $\{a, b, c, d\}$  are unknown values. Two schemes for determining these coefficients, namely Scheme 1 and Scheme 2, are proposed.

**Scheme 1:** This scheme is based on function values only. The coefficients in

(5.11) can be found through

$$\begin{pmatrix} a \\ b \\ c \\ d \end{pmatrix} = \mathcal{P}^{-1} \begin{pmatrix} f_{b1} \\ f_{b1}^{(hi)} \\ f_{b2}^{(hi)} \\ f_{b2} \end{pmatrix}, \quad (5.12)$$

where  $f_{b1} = f(x_1)$ ,  $f_{b2} = f(x_m)$ ,  $f_{b1}^{(hi)} = f(x_{b1}^{(hi)})$ ,  $f_{b2}^{(hi)} = f(x_{b2}^{(hi)})$ , and

$$\mathcal{P} = \begin{bmatrix} x_{b1}^3 & x_{b1}^2 & x_{b1} & 1 \\ \left(x_{b1}^{(hi)}\right)^3 & \left(x_{b1}^{(hi)}\right)^2 & x_{b1}^{(hi)} & 1 \\ \left(x_{b2}^{(hi)}\right)^3 & \left(x_{b2}^{(hi)}\right)^2 & x_{b2}^{(hi)} & 1 \\ x_{b2}^3 & x_{b2}^2 & x_{b2} & 1 \end{bmatrix}.$$

The values of  $f_f^{(hi)}$  at the interior nodes  $x_i$  are thus computed by

$$f_f^{(hi)}(x_i) = [x_i^3 \ x_i^2 \ x_i \ 1] \mathcal{P}^{-1} \begin{pmatrix} f_{b1} \\ f_{b1}^{(hi)} \\ f_{b2}^{(hi)} \\ f_{b2} \end{pmatrix}, \quad (5.13)$$

where  $x_{b1}^{(hi)} < x_i < x_{b2}^{(hi)}$ . It can be seen that there are two values of  $f_f^{(hi)}$  at a grid point located within the  $i$ th hole: one associated with the  $x$ -grid line (i.e. (5.13)) and one with the  $y$ -grid line. The nodal value of  $f_f^{(hi)}$  at a fictitious point is thus taken in an average sense.

By substituting nodal values of  $f_f$  within holes into (5.10) and then replacing the boundary conditions with given values, the right hand side of (5.13) becomes known. One can now apply linear algebra to solve the system (5.10) for the nodal values of  $f_r$ .

**Scheme 2:** This scheme is based on not only function values but also derivative

values. The coefficients in (5.11) can be found through

$$\begin{pmatrix} a \\ b \\ c \\ d \end{pmatrix} = \mathcal{P}^{-1} \begin{pmatrix} f_{b1}^{(hi)} \\ f_{b2}^{(hi)} \\ \frac{\partial f_{b1}^{(hi)}}{\partial x} \\ \frac{\partial f_{b2}^{(hi)}}{\partial x} \end{pmatrix}, \quad (5.14)$$

where  $\partial f_{b1}^{(hi)}/\partial x = \partial f(x_{b1}^{(hi)})/\partial x$ ,  $\partial f_{b2}^{(hi)}/\partial x = \partial f(x_{b2}^{(hi)})/\partial x$ , and

$$\mathcal{P} = \begin{bmatrix} \left(x_{b1}^{(hi)}\right)^3 & \left(x_{b1}^{(hi)}\right)^2 & x_{b1}^{(hi)} & 1 \\ \left(x_{b2}^{(hi)}\right)^3 & \left(x_{b2}^{(hi)}\right)^2 & x_{b2}^{(hi)} & 1 \\ 3\left(x_{b1}^{(hi)}\right)^2 & 2x_{b1}^{(hi)} & 1 & 0 \\ 3\left(x_{b2}^{(hi)}\right)^2 & 2x_{b2}^{(hi)} & 1 & 0 \end{bmatrix}.$$

It is noted that Scheme 2 uses local data only, i.e. the values of  $f$  and  $\partial f/\partial x$  at  $x_{b1}^{(hi)}$  and at  $x_{b2}^{(hi)}$ , to construct the polynomials. Derivative values need be obtained in advance and how to compute these values will be discussed in next section. The remaining steps of the solution procedure are similar to those for Scheme 1.

### 5.3 Numerical examples

For all examples in this chapter, 1D-IRBFNs are implemented with the multiquadric (MQ) function. A grid size is taken to be the MQ width. Both boundary-value and initial-value problems are considered to validate the present technique.

The solution accuracy is measured by means of the discrete relative  $L_2$  norm of

the error defined as

$$Ne = \frac{\sqrt{\sum_{i=1}^{n_{ip}} (f_i^e - f_i)^2}}{\sqrt{\sum_{i=1}^{n_{ip}} (f_i^e)^2}}, \quad (5.15)$$

where  $n_{ip}$  is the number of interior points in the physical domain, and  $f^e$  and  $f$  are the exact and approximate solutions, respectively.

The convergence rate of the solution with respect to grid refinement is measured by  $\alpha$  in

$$Ne(h) \approx \gamma h^\alpha = O(h^\alpha), \quad (5.16)$$

in which  $\alpha$  and  $\gamma$  are exponential model's parameters and  $h$  the average nodal spacing. Given a set of observations, these parameters can be found by the general linear least squares technique.

### Example 1 - A boundary-value problem

This problem is governed by Poisson equation

$$\frac{\partial^2 f}{\partial x^2} + \frac{\partial^2 f}{\partial y^2} = b(x, y), \quad (5.17)$$

where  $b(x, y)$  is a given function. A domain of interest is a square region,  $[-0.5, 0.5] \times [-0.5, 0.5]$ , with a circular hole of radius  $R = 0.2$  and its centre located at position  $(-0.2, -0.2)$ . This physical domain is embedded in a square computational one that can be conveniently represented by a uniform Cartesian grid (Figure 5.3).

Two particular driving functions are considered.

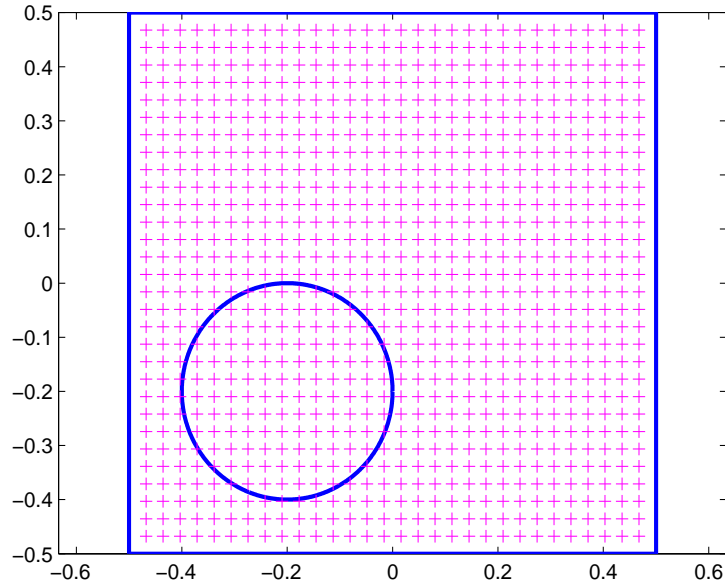


Figure 5.3: Example 1 (boundary-value problem): Domain of interest and a typical discretisation

Case 1:

$$b(x, y) = -8\pi^2(\sin(3\pi x) \cosh(\pi y) - \cos(3\pi x) \sinh(\pi y)). \quad (5.18)$$

The exact solution to this case is available

$$f^e(x, y) = \sin(3\pi x) \cosh(\pi y) - \cos(3\pi x) \sinh(\pi y), \quad (5.19)$$

from which Dirichlet boundary conditions can be derived analytically.

Case 2:

$$b(x, y) = 0. \quad (5.20)$$

Analytic solution to this case is not available. On the outer and inner boundaries,  $f = 1$  and  $f = 0$  are prescribed, respectively.

For Case 1, Scheme 1 is employed to construct the fictitious solution over the hole. Results of the matrix condition number and the solution accuracy are presented in Table 5.1. In terms of stability, the proposed method yields relatively low condition numbers (e.g. about  $1.0 \times 10^3$  for a grid of  $66 \times 66$ ). In terms of accuracy, errors obtained are relatively small, varying from  $2.09 \times 10^{-2}$  (grid of  $22 \times 22$ ) to  $3.73 \times 10^{-3}$  (grid of  $66 \times 66$ ). Figure 5.4 displays the computed solution using a grid of  $42 \times 42$ . It can be seen that the present scheme is able to capture a complex function.

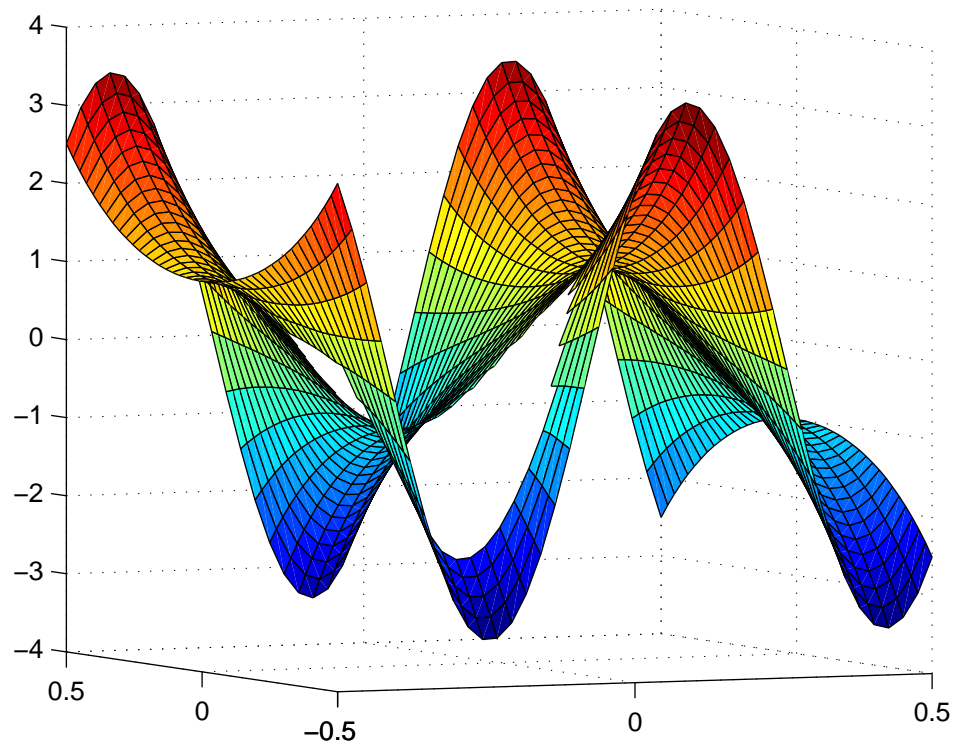


Figure 5.4: Example 1 (boundary-value problem - Case 1): A plot of the approximate solution using a grid of  $42 \times 42$

For Case 2, Scheme 2 is employed. As mentioned earlier, one needs to have the values of  $\partial f / \partial x$  at  $x_{b1}^{(hi)}$  and at  $x_{b2}^{(hi)}$  in advance. An iterative procedure is employed here for this purpose. At the beginning, these derivative values are set to zero. Through (5.14), a function  $f_f$  is obtained. By substituting nodal values of  $f_f$  into (5.10), one is able to acquire the solution  $f_r$ . These  $f_f$  and  $f_r$

Table 5.1: Example 1 (boundary-value problem - Case 1): Errors of the solution and condition numbers of the system matrix.

Grid	Error	Cond(A)
$22 \times 22$	$2.0903 \times 10^{-2}$	$1.1 \times 10^2$
$26 \times 26$	$1.3029 \times 10^{-2}$	$1.5 \times 10^2$
$30 \times 30$	$1.0792 \times 10^{-2}$	$2.0 \times 10^2$
$34 \times 34$	$1.0584 \times 10^{-2}$	$2.7 \times 10^2$
$38 \times 38$	$1.0076 \times 10^{-2}$	$3.4 \times 10^2$
$42 \times 42$	$9.1317 \times 10^{-3}$	$4.3 \times 10^2$
$46 \times 46$	$8.1338 \times 10^{-3}$	$5.1 \times 10^2$
$50 \times 50$	$8.0598 \times 10^{-3}$	$6.1 \times 10^2$
$54 \times 54$	$7.9912 \times 10^{-3}$	$7.1 \times 10^2$
$58 \times 58$	$5.6866 \times 10^{-3}$	$8.3 \times 10^2$
$62 \times 62$	$6.9334 \times 10^{-3}$	$9.4 \times 10^2$
$66 \times 66$	$3.7331 \times 10^{-3}$	$1.0 \times 10^3$

constitute a solution  $f$  along a grid line, from which the values of  $\partial f / \partial x$  at  $x_{b1}^{(hi)}$  and at  $x_{b2}^{(hi)}$  are updated. This procedure is repeated a few times to pick up one among many possible third-order polynomial representations for the fictitious solution  $f_f$ .

Figure 5.5 displays a visual comparison of the distribution of  $f_r$  between the present technique and FEM. It is noted that the FEM result is obtained using the PDE Toolbox in MATLAB. It can be seen that the two solutions have similar variations.

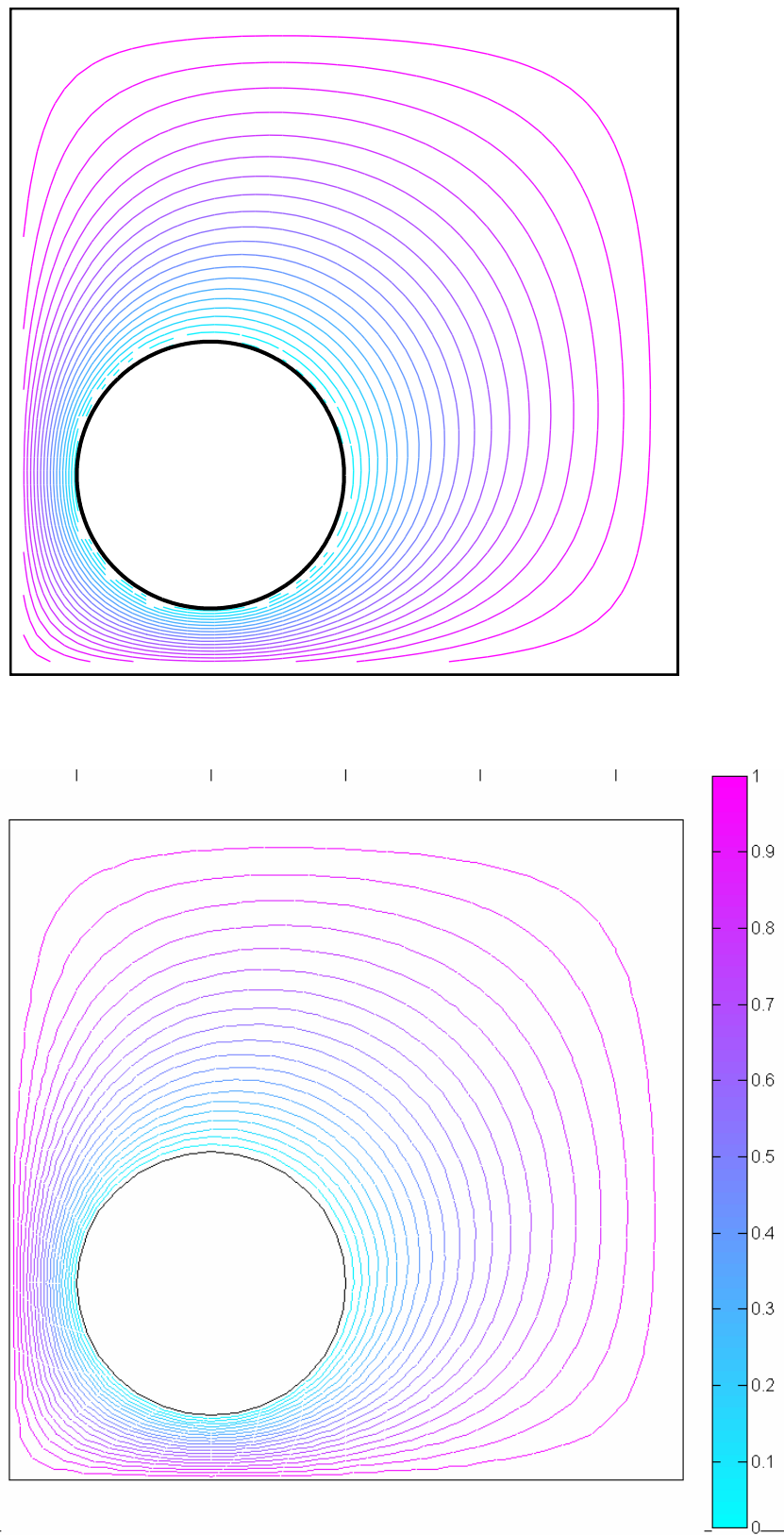


Figure 5.5: Example 1 (boundary-value problem - Case 2): A contour plot of  $f_r$  by the 1D-IRBFN method using grid of  $40 \times 40$  (top) and FEM (bottom).

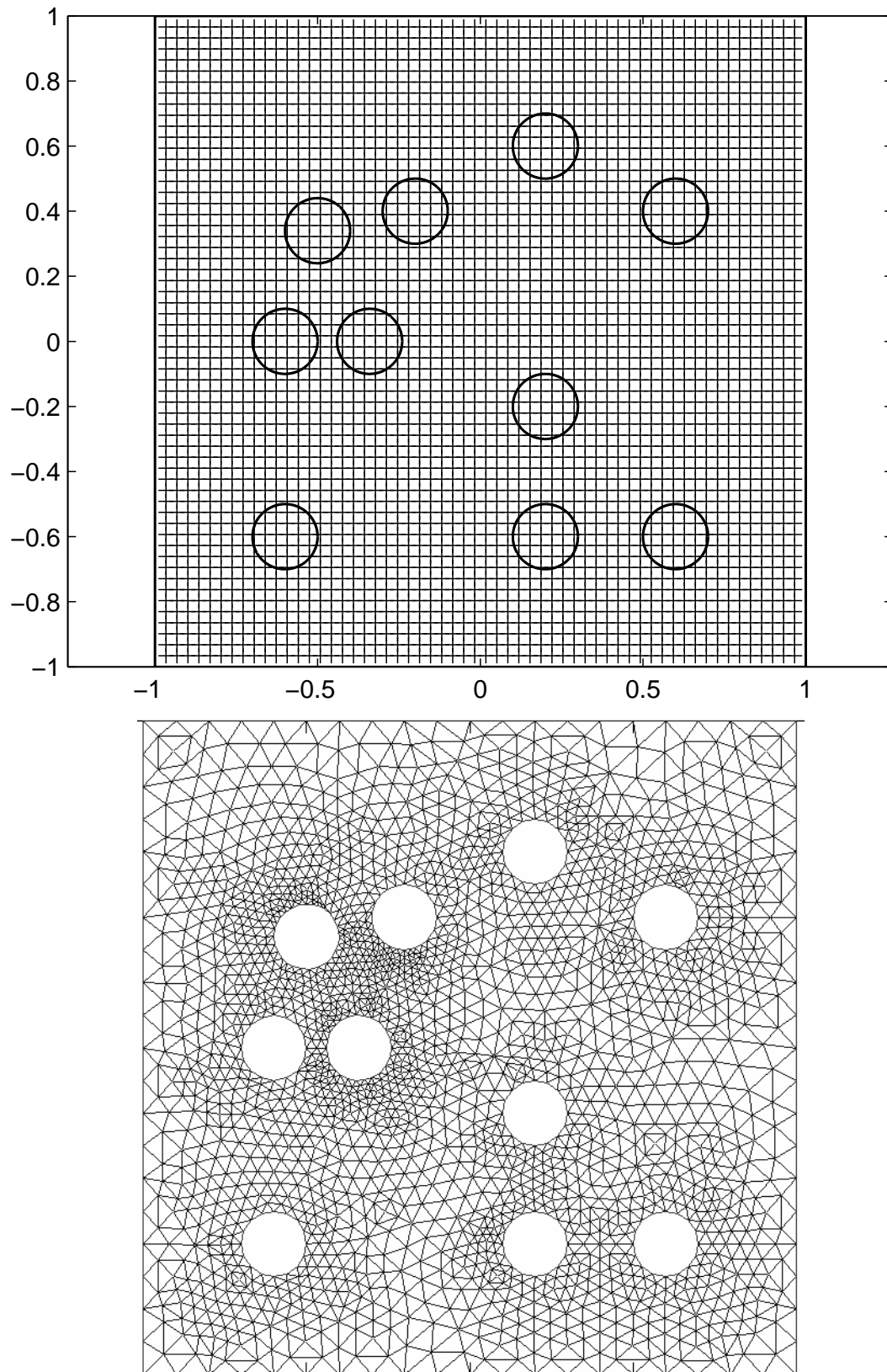


Figure 5.6: Example 2 (boundary value problem): Discretisation by the present 1D-IRBFN method (top) and FEM (bottom)

**Example 2 - A boundary value problem**

This problem is governed by Poisson equation with the driving function  $b(x, y) = -1$  and homogeneous Dirichlet boundary conditions. The domain of interest is a unit square with 10 holes of radius 0.1. This example provides a good means of testing the capability of the proposed technique in dealing with geometrically-complex-domain problems. It is noted that multi-hole domains occur in many practical modelling situations such as thermal conductivity for composite materials, fluid flow in porous medium and particulate flows.

In Figure 5.6, a typical discretisation of the present technique and that of FEM are shown. The pre-processing for the present technique is much more economical than that for FEM. Since there is no exact solution available here, we present a visual comparison of the distribution of  $f_r$  between the present technique (Scheme 1, grid of  $80 \times 80$ ) and FEM (Figure 5.7). It is noted that the FEM result is obtained using the PDE Toolbox in MATLAB. It can be seen that the two solutions have similar behaviours.

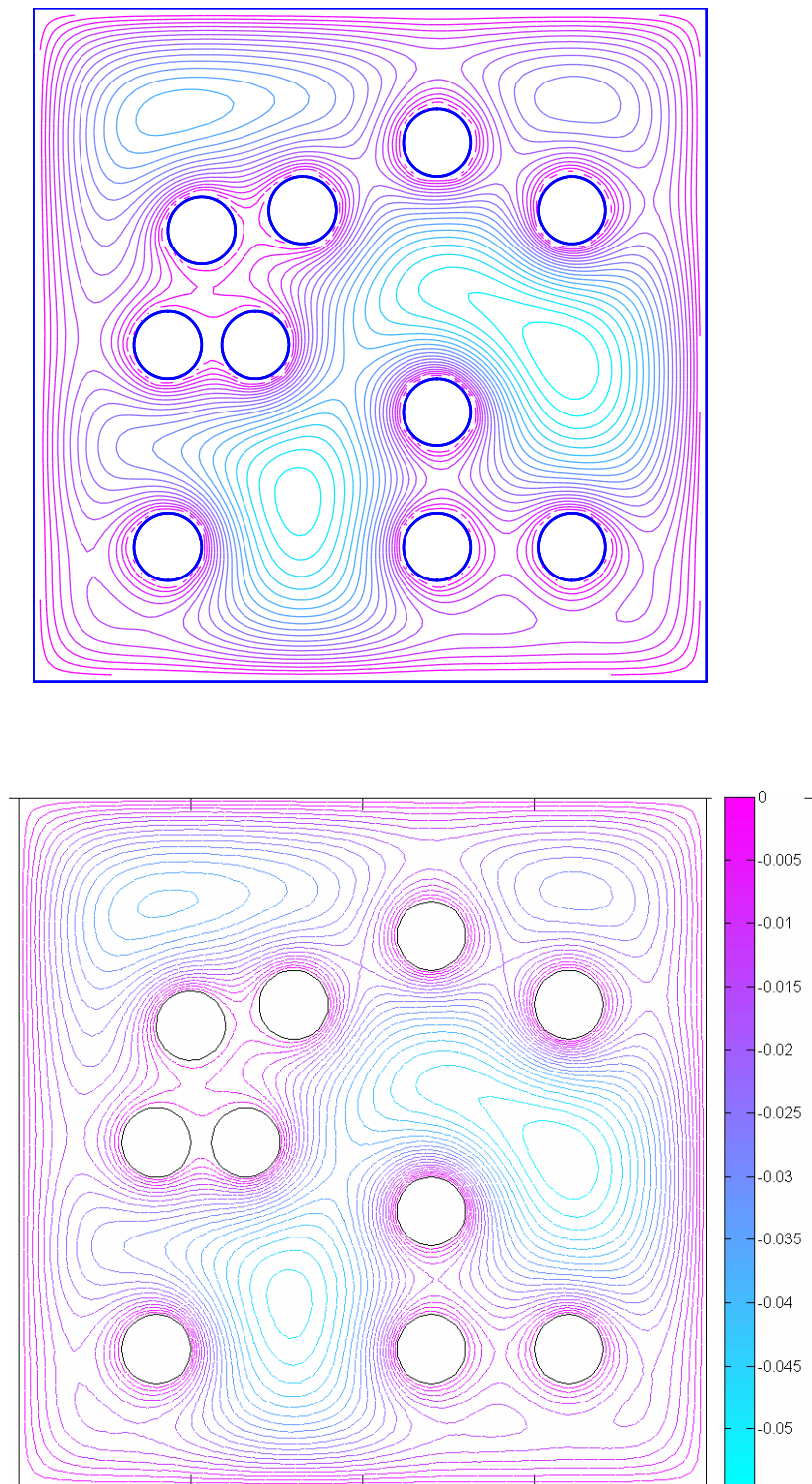


Figure 5.7: Example 2 (boundary value problem): A contour plot of  $f_r$  by the present 1D-IRBFN method using grid of  $80 \times 80$  (top) and FEM (bottom)

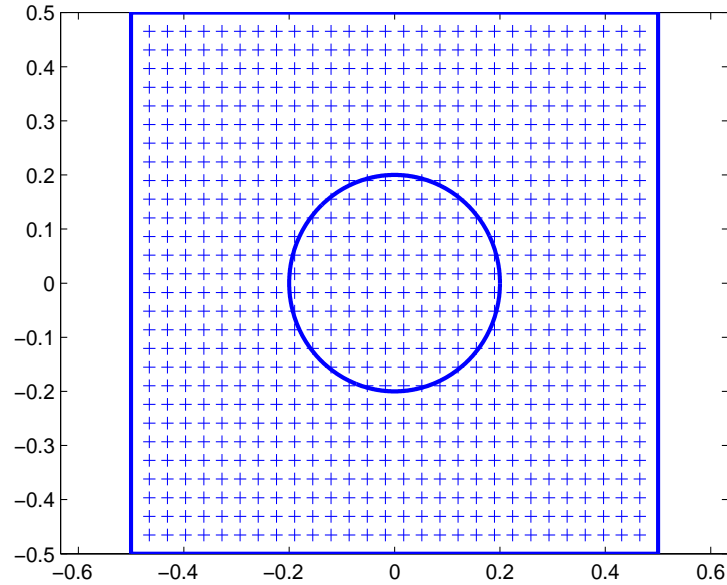


Figure 5.8: Example 3 (initial-value problem): Domain of interest and a typical discretisation

### Example 3 - An initial-value problem

This problem is governed by the following parabolic PDE

$$\frac{\partial f}{\partial t} - \left( \frac{\partial^2 f}{\partial x^2} + \frac{\partial^2 f}{\partial y^2} \right) = (1 + 2\pi^2 k^2 t) \sin(k\pi x) \sin(k\pi y), \quad (5.21)$$

where  $k$  is a given number. The problem domain is the region lying between a square of  $1 \times 1$  and a circle of radius 0.2 which are both centered at the origin (Figure 5.8). The exact solution is given by

$$f^e(x, y, t) = \sin(k\pi x) \sin(k\pi y)t, \quad (5.22)$$

from which the initial solution and Dirichlet boundary conditions are derived analytically.

The spatial discretisation is carried out using a Cartesian grid of  $40 \times 40$ . Both Scheme 1 and Scheme 2 for calculating the function  $f_f$  in (5.10) are employed.

For the latter, the values of  $\partial f/\partial x$  at  $x_{b1}^{(hi)}$  and at  $x_{b2}^{(hi)}$  are simply taken from the previous time level. Results of  $Ne$  for  $k = 2$  and  $k = 3$  using a time step of 0.1 are presented in Table 5.2, which shows that Scheme 2 gives more accurate results than Scheme 1. Scheme 2 is thus recommended for use in practice. It is noted that the matrix condition number is only  $3.8 \times 10^2$  for a grid of  $40 \times 40$ . Plots for  $f$  with two values of  $k$  at  $t = 1$  are shown in Figure 5.9.

## 5.4 Concluding remarks

In this chapter, Cartesian grids and 1D-IRBFNs are incorporated into the domain embedding framework to solve elliptic and parabolic equations of second order on multiply-connected domains. The preprocessing is simple as the multiply-connected domain is converted into a rectangular one. We employ polynomials of third order to represent the fictitious solution within holes. Two schemes to construct polynomials are proposed. The first is based on function values while the second relies on both function and derivative values. The system matrix is expressed in terms of the values of the field variable at grid nodes only. The technique is validated successfully through several boundary-value and initial-value problems. Numerical results indicate that the inclusion of derivative values in constructing the polynomials leads to an improvement in accuracy. In comparison with the 1D-IRBFN-based boundary fitted method, the 1D-IRBFN-based domain embedding method is seen to be less accurate, but appears to be more convenient for solving multiply-connected domain problems with many moving inner holes.

Table 5.2: Example 3 (initial-value problem): Errors of  $f$  with  $k = 2$  and  $k = 3$  by Scheme 1 and Scheme 2 using grid of  $40 \times 40$ . It is noted that  $a(b)$  represents  $a \times 10^b$ .

Time	$k = 2$		$k = 3$	
	Scheme 1	Scheme 2	Scheme 1	Scheme 2
0.2	1.4690(-3)	8.1363e(-3)	1.1299(-2)	3.9580e(-3)
0.4	1.4858(-3)	4.0864e(-3)	1.1435(-2)	3.9580e(-3)
0.6	1.4915(-3)	2.7144e(-3)	1.1481(-2)	2.5376e(-3)
0.8	1.4943(-3)	2.0333e(-3)	1.1504(-2)	1.8324e(-3)
1.0	1.4961(-3)	1.6249e(-3)	1.1518(-2)	1.4103e(-3)
1.2	1.4972(-3)	1.3527e(-3)	1.1528(-2)	1.1297e(-3)
1.4	1.4980(-3)	1.1583e(-3)	1.1534(-2)	9.2994e(-4)
1.6	1.4986(-3)	1.0125e(-3)	1.1539(-2)	7.8087e(-4)
1.8	1.4991(-3)	8.9925e(-4)	1.1543(-2)	6.6565e(-4)
2.0	1.4995(-3)	8.0867e(-4)	1.1546(-2)	5.7421e(-4)
2.2	1.4998(-3)	7.3460e(-4)	1.1549(-2)	5.0016e(-4)
2.4	1.5001(-3)	6.7292e(-4)	1.1551(-2)	4.3925e(-4)
2.6	1.5003(-3)	6.2077e(-4)	1.1553(-2)	3.8855e(-4)
2.8	1.5005(-3)	5.7610e(-4)	1.1554(-2)	3.4597e(-4)
3.0	1.5007(-3)	5.3742e(-4)	1.1555(-2)	3.1000e(-4)
3.2	1.5008(-3)	5.0361e(-4)	1.1557(-2)	2.7951e(-4)
3.4	1.5009(-3)	4.7381e(-4)	1.1558(-2)	2.5366e(-4)
3.6	1.5010(-3)	4.4735e(-4)	1.1559(-2)	2.3178e(-4)
3.8	1.5011(-3)	4.2370e(-4)	1.1559(-2)	2.1335e(-4)
4.0	1.5012(-3)	4.0244e(-4)	1.1560(-2)	1.9795e(-4)

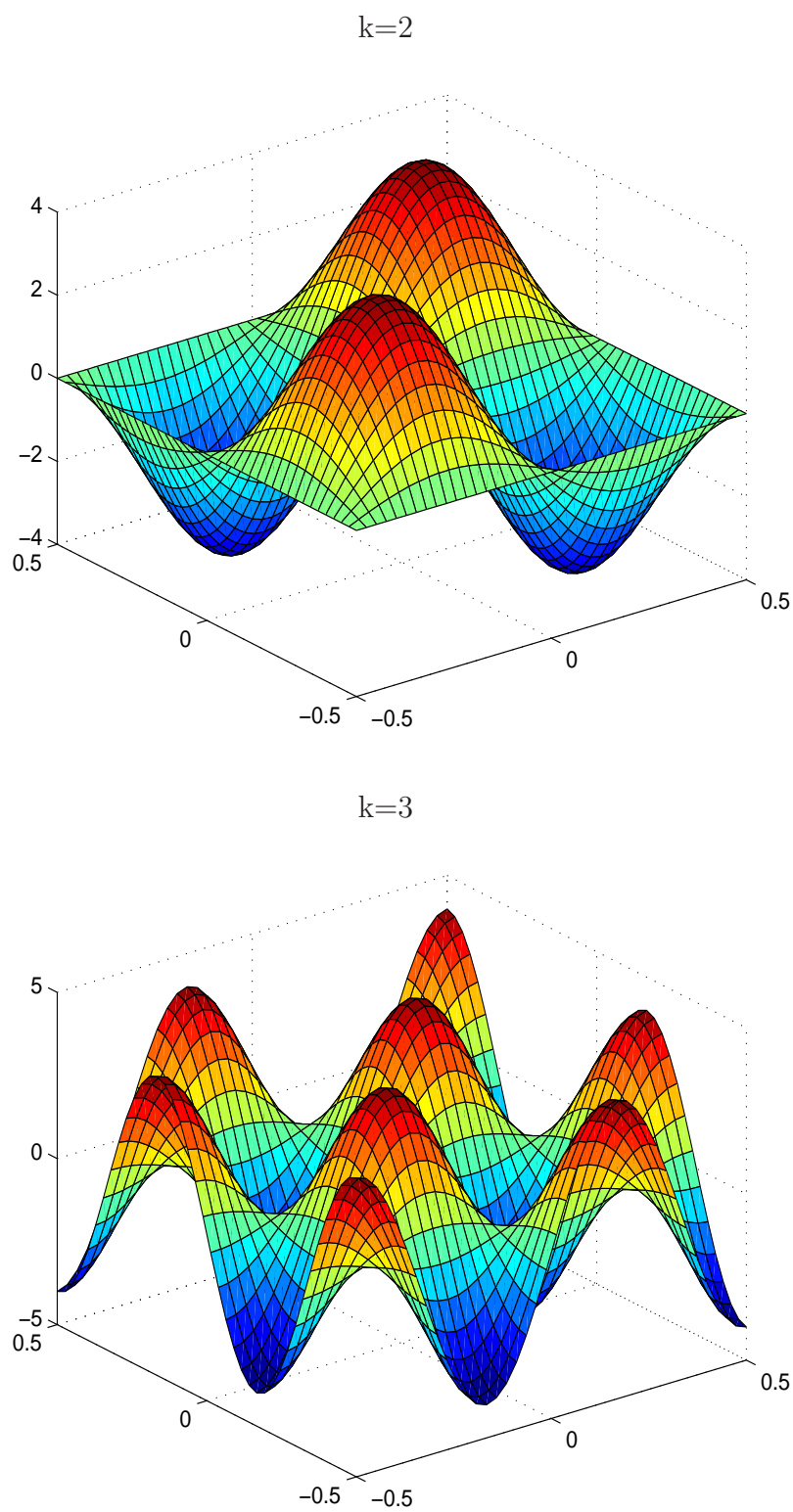


Figure 5.9: Example 3 (initial-value problem): Plots of the approximate solution for two values of  $k$  using a grid of  $40 \times 40$ .

## Chapter 6

# 1D-integrated-RBFN calculation of particulate suspension flows

In this chapter, 1D-IRBFN methods are applied for the numerical prediction of bulk properties of particulate suspensions under simple shear conditions. The suspending fluid is Newtonian and the suspended particles are rigid. Results obtained are compared well with those based on finite elements in the literature.

## 6.1 Introduction

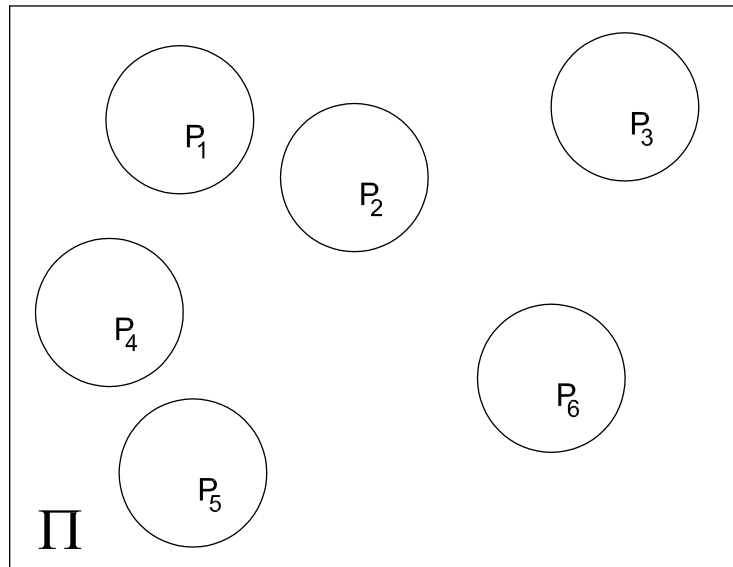


Figure 6.1: A particle-fluid system

Particulate suspensions, which involve transport of rigid particles suspended in a fluid medium, occur in many industrial processes such as slurries, colloids, fluidised beds, etc. Due to their great structural and physical variety, the use of experiments to determine the macroscopic rheological properties of these multiphase materials was seen to be impractical (Phan-Thien and Kim, 1994). However, it may be possible to employ numerical simulations to predict the bulk properties of multiphase materials. Various numerical models have been proposed. Among them are direct numerical simulations (DNSs) which have received a great deal of attention. In DNSs, the fundamental equations for particles (Newton-Euler equation) and a fluid (Navier-Stokes equation) are solved in a direct and fully-coupled manner. Two main advantages of DNSs are that (i) they can handle particles of different shapes and sizes as well as any type of fluid; and (ii) hydrodynamic forces and moments can be calculated directly

from the fluid flow. Difficulties faced by DNSs include (i) a very large number of particles is typically required for a proper simulation; and (ii) the fluid domain is of very complex shape due to the presence of particles and the change of their positions with time. Based on the fluid-phase solver employed, DNSs can be classified into two categories. In the first category, a mesh follows the movement of the particles, i.e. a moving mesh is used. Methods based on the Arbitrary Lagrangian-Eulerian (ALE) moving mesh approach proposed by Hu et al. (1992) are widely used, (e.g. Hu, 1995; Huang et al., 1997; Huang et al., 1998). In the second category, a mesh covers the whole domain and is independent of the position of particles, i.e. a fixed mesh is used. Methods based on the fictitious domain approach proposed by Glowinski et al. (1998) are widely employed, (e.g. Hwang et al., 2004; Patankar et al., 2000; Singh et al., 2000). Hwang et al. (2004) incorporated sliding bi-periodic frames, introduced by Lees and Edwards (1972) for molecular dynamics, into the simulation of particulate flows. This concept allows the modelling of suspension systems with infinite numbers of particles to be conducted through a small number of particles in a representative reference sliding frame. The computational fluid domain is thus small with bi-periodic conditions on the frame and no-slip conditions on the surfaces of the particles.

In recent years, RBFN-based methods, which are extremely easy to implement and capable of achieving a high level of accuracy using a relatively-small number of nodes, have been successfully applied to solve complex problems encountered in engineering, (e.g. Šarler et al., 2004; Šarler, 2005; Šarler et al., 2010; Gerace et al., 2009; Kosec and Šarler, 2008a,b; Orsini et al., 2009; Divo and Kassab, 2005, 2006, 2007, 2008; Pepper and Sarler, 2005; Zahab et al., 2009; Yao et al., 2011 and the references therein). In this chapter, we report a new numerical method based on 1D integrated RBFNs and point collocation in the context of boundary fitted Cartesian grids and sliding bi-periodic frames for the direct simulation of flows of Newtonian-based particulate systems.

The remainder of the chapter is organised as follows. Section 6.2 gives a brief review of the governing equations and the concept of sliding frames. In Section 6.3, the proposed numerical procedure is described. Numerical results are presented in Section 6.4. Section 6.5 concludes the chapter.

## 6.2 Governing equations and sliding frames concept

### 6.2.1 Governing equations

Let  $\Pi$  be the entire computational domain, including the interior regions occupied by the particles. Let  $P_i(t)$  and  $\partial P_i(t)$  be the region and its boundary of the  $i$ th particle of time  $t$ , where  $i = (1, 2, \dots, N)$  and  $N$  is the number of particles (Figure 6.1).

**Fluid motion:** The laws of mass and momentum conservation for an incompressible fluid lead to

$$\nabla \cdot \mathbf{u} = 0, \quad (6.1)$$

$$\rho_f \frac{D\mathbf{u}}{Dt} = \nabla \cdot \boldsymbol{\sigma}, \quad (6.2)$$

where  $\mathbf{u}$  is the velocity vector,  $\rho_f$  the density of the fluid,  $\boldsymbol{\sigma}$  the total stress tensor, and  $D[.]/Dt$  the material derivative defined as

$$\frac{D[.]}{Dt} = \frac{\partial[.]}{\partial t} + (\mathbf{u} \cdot \nabla)[.]. \quad (6.3)$$

For a Newtonian fluid, the total stress tensor is given by

$$\boldsymbol{\sigma} = -p\mathbf{I} + 2\eta\mathbf{D}, \quad (6.4)$$

where  $p$  is the hydrodynamic pressure,  $\mathbf{I}$  the unit tensor,  $\eta$  the viscosity, and  $\mathbf{D}$  the strain rate tensor defined as

$$\mathbf{D} = \frac{1}{2}[\nabla\mathbf{u} + (\nabla\mathbf{u})^T]. \quad (6.5)$$

In the case of 2D problems, the  $\psi - \omega$  formulation has been widely employed because of its simplicity. The governing equations (6.1), (6.2) and (6.4) can be rewritten as follows.

$$\frac{\partial^2\psi}{\partial x^2} + \frac{\partial^2\psi}{\partial y^2} = \omega, \quad (6.6)$$

$$\frac{\partial\omega}{\partial t} + u\frac{\partial\omega}{\partial x} + v\frac{\partial\omega}{\partial y} = \frac{1}{Re} \left( \frac{\partial^2\omega}{\partial x^2} + \frac{\partial^2\omega}{\partial y^2} \right), \quad (6.7)$$

where  $\psi$  is the stream function,  $\omega$  the vorticity,  $Re$  the Reynolds number, and  $u$  and  $v$  the components of  $\mathbf{u}$ , which are defined in terms of the stream function as

$$u = \frac{\partial\psi}{\partial y}, \quad v = -\frac{\partial\psi}{\partial x}.$$

The given velocity boundary conditions can be transformed into two boundary conditions on the stream function and its normal derivative

$$\psi = \gamma, \quad \frac{\partial\psi}{\partial n} = \xi,$$

where  $n$  is the direction normal to the boundary, and  $\gamma$  and  $\xi$  prescribed functions.

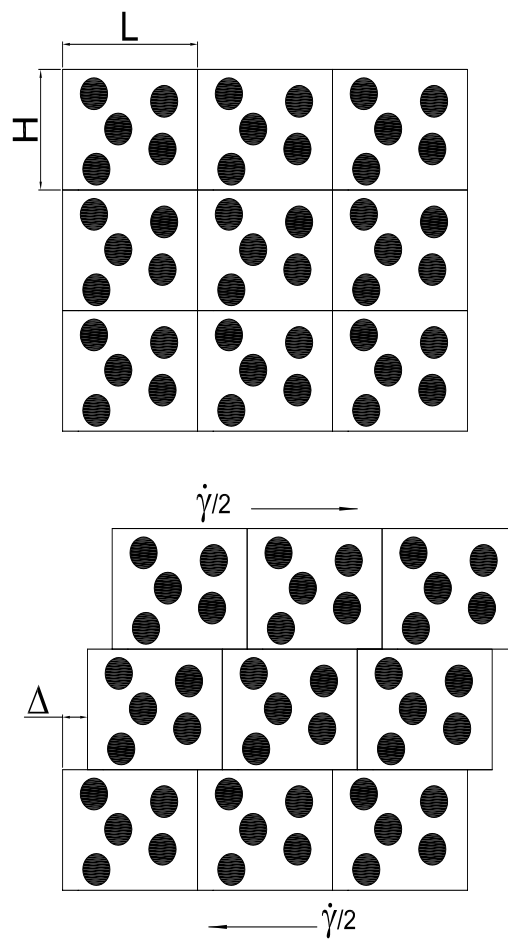


Figure 6.2: Shear bi-periodic frames.

**Particle motion:** Consider an  $i$ th particle. The motion of the particle can be described by the Newton-Euler equations

$$M_i \frac{d\mathbf{U}_i}{dt} = \mathbf{F}_i, \quad (6.8)$$

$$\mathbf{I}_i \frac{d\boldsymbol{\Omega}_i}{dt} = \mathbf{T}_i, \quad (6.9)$$

where  $M_i$ ,  $\mathbf{I}_i$ ,  $\mathbf{U}_i$  and  $\boldsymbol{\Omega}_i$  are the mass, inertia tensor, translational velocity vector of the mass centre and angular velocity vector of the  $i$ th particle, respectively, and  $\mathbf{F}_i$  and  $\mathbf{T}_i$  the force and torque vectors acting on the  $i$ th particle.

The force and torque vectors can be computed from the fluid flow as

$$\mathbf{F}_i = \oint_{\partial P_i(t)} \boldsymbol{\sigma} \cdot \mathbf{n} ds, \quad (6.10)$$

$$\mathbf{T}_i = \oint_{\partial P_i(t)} \mathbf{r} \times (\boldsymbol{\sigma} \cdot \mathbf{n}) ds, \quad (6.11)$$

where  $\mathbf{r}$  is the position vector,  $\mathbf{n}$  the outward unit vector normal to the boundary  $\partial P_i$  and  $ds$  the length of an infinitesimal part of  $\partial P_i$ .

Non-slip boundary conditions on the interface between the fluid and the  $i$ th particle are given by

$$\mathbf{u} = \mathbf{U}_i + \boldsymbol{\Omega}_i \times \mathbf{r}, \quad (6.12)$$

where

$$\mathbf{U}_i = \frac{d\mathbf{X}_i}{dt},$$

$$\boldsymbol{\Omega}_i = \frac{d\boldsymbol{\Theta}_i}{dt},$$

in which  $\mathbf{X}_i$  is the position vector of the mass center and  $\boldsymbol{\Theta}_i$  the orientation of

the  $i$ th particle. In terms of the stream function, (6.12) becomes

$$\frac{\partial\psi}{\partial y} = U_i - \Omega_i y \quad (6.13)$$

$$\frac{\partial\psi}{\partial x} = -V_i - \Omega_i x, \quad (6.14)$$

where  $U_i$  and  $V_i$  are the two components of  $\mathbf{U}$  and  $\Omega_i$  the magnitude of  $\mathbf{\Omega}_i$ .

### 6.2.2 Sliding bi-periodic frames concept

Consider a particulate flow of very large domain under simple shear conditions in the  $x$  direction. One possible way to make such a large problem tractable is to simplify it using the concept of sliding bi-periodic frames. The problem domain can be divided into a set of identical sliding frames of width  $L$  and height  $H$  (Figure 6.2). Each frame translates along the shear direction at its own average velocity. Rows of frames slide relatively to one another by an amount  $\Delta = \dot{\gamma}Ht$ , where  $\dot{\gamma}$  is the given shear rate,  $H$  height of the frame and  $t$  shear time (Hwang et al., 2004).

Because frames have similar solutions, only one frame is considered. If particles in a frame are ignored, it can be seen that the velocity profile is linear

$$u = u_0 + \dot{\gamma}y, \quad (6.15)$$

$$v = 0, \quad (6.16)$$

where the origin of the  $x - y$  coordinate system is located at the centre of the frame;  $u_0$  the translation velocity of the frame and  $-H/2 \leq y \leq H/2$ . With the presence of particles, one has

$$u = \hat{u} + u_0 + \dot{\gamma}y, \quad (6.17)$$

$$v = \hat{v}, \quad (6.18)$$

where  $\hat{u}$  and  $\hat{v}$  are the perturbations from the linear profile.

Since the solution is continuous across sliding frames, the following bi-periodic boundary conditions for the velocity  $\mathbf{u}$  and the traction  $\boldsymbol{\tau}$  can be applied to each frame

$$\mathbf{u}(-L/2, y, t) = \mathbf{u}(L/2, y, t), \quad -H/2 \leq y \leq H/2, \quad (6.19)$$

$$\boldsymbol{\tau}(-L/2, y, t) = \boldsymbol{\tau}(L/2, y, t), \quad -H/2 \leq y \leq H/2, \quad (6.20)$$

for the two vertical faces, and

$$\mathbf{u}(x, -H/2, t) = \mathbf{u}(x + \dot{\gamma}Ht, H/2, t) + (\dot{\gamma}H, 0)^T, \quad -L/2 \leq x \leq L/2, \quad (6.21)$$

$$\boldsymbol{\tau}(x, -H/2, t) = \boldsymbol{\tau}(x + \dot{\gamma}Ht, H/2, t), \quad -L/2 \leq x \leq L/2, \quad (6.22)$$

for the two horizontal faces.

### 6.3 Proposed numerical procedure

In this chapter, we propose a numerical procedure based on IRBFNs and sliding frames for the simulation of particulate suspensions under simple shear conditions. The fluid domain in a reference frame is simply discretised using a Cartesian grid  $n_x \times n_y$ . Let  $\Gamma_1, \Gamma_2, \Gamma_3$  and  $\Gamma_4$  be the sides of the reference frame (Figure 6.3). IRBFNs are employed on each grid line to represent the field variables  $\psi$  and  $\omega$  (one-dimensional IRBFNs). Sliding bi-periodic boundary conditions are presently implemented by means of point collocation rather than the Lagrange multipliers used in (Hwang et al., 2004). The proposed procedure combines strengths of three approaches, namely IRBFNs (high-order accuracy), Cartesian grids (easy preprocessing) and the sliding bi-periodic frames concept

(infinite number of particles). To our best knowledge, this is a first attempt to use RBFs for the analysis of shear particulate flows. In the following, details are presented for the three constituent components of the proposed procedure. 1D-IRBFNs are first described. Sliding bi-periodic boundary conditions are then expressed in terms of the stream function and implemented with IRBFs and point collocation. Finally, suitable formulas and their IRBFN implementation are presented for computing the boundary values on the particles.

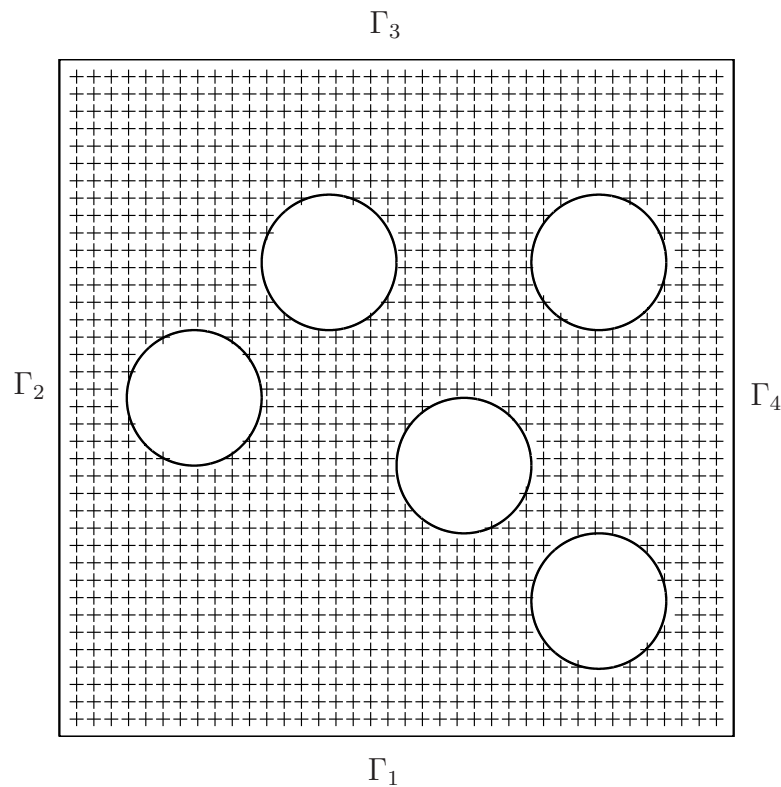


Figure 6.3: A reference frame and its typical Cartesian-grid discretisation.

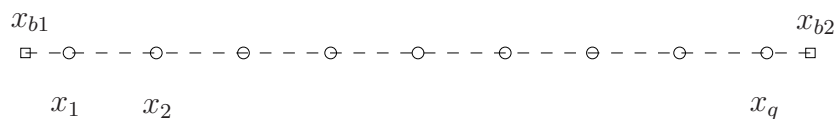


Figure 6.4: Nodal points on a grid line consisting of interior points  $x_i$  (○) and boundary points  $x_{bi}$  (□).

### 6.3.1 1D-IRBFNs

Consider a grid line that can be bounded by two faces of the frame, the boundaries of two particles, or the boundary of the particle and the frame. Assume a grid line in the  $x$  direction and let  $f$  be the field variable. IRBFNs are employed to approximate  $f$ . The construction procedure is as follows.

Second-order derivative of  $f$  along a grid line can be decomposed into RBFs

$$\frac{\partial^2 f(x)}{\partial x^2} = \sum_{i=1}^m w_i g_i(x) = \sum_{i=1}^m w_i I_i^{(2)}(x), \quad (6.23)$$

where  $m$  is the number of RBFs,  $\{g_i(x)\}_{i=1}^m \equiv \{I_i^{(2)}(x)\}_{i=1}^m$  the set of RBFs,  $\{w_i\}_{i=1}^m$  the set of weights to be found and  $f$  represents  $\psi$  and  $\omega$ . Approximate expressions for the first-order derivative and the field variable are then obtained through integration

$$\frac{\partial f(x)}{\partial x} = \sum_{i=1}^m w_i I_i^{(1)}(x) + c_1, \quad (6.24)$$

$$f(x) = \sum_{i=1}^m w_i I_i^{(0)}(x) + c_1 x + c_2, \quad (6.25)$$

where  $I_i^{(1)}(x) = \int I_i^{(2)}(x) dx$  and  $I_i^{(0)}(x) = \int I_i^{(1)}(x) dx$ . In this study, IRBFNs are implemented with the multiquadric (MQ) function and one thus has

$$I_i^{(2)}(x) = \sqrt{(x - c_i)^2 + a_i^2}, \quad (6.26)$$

$$I_i^{(1)}(x) = \frac{(x - c_i)}{2} A + \frac{a_i^2}{2} B, \quad (6.27)$$

$$I_i^{(0)}(x) = \left( \frac{-a_i^2}{3} + \frac{(x - c_i)^2}{6} \right) A + \frac{a_i^2 (x - c_i)}{2} B, \quad (6.28)$$

where  $c_i$  and  $a_i$  are the centre and the width of the  $i$ th MQ, respectively,  $A = \sqrt{(x - c_i)^2 + a_i^2}$ , and  $B = \ln \left( (x - c_i) + \sqrt{(x - c_i)^2 + a_i^2} \right)$ . The grid size  $h$  is chosen as the RBF width  $a_i$ . The set of collocation points  $\{x_i\}_{i=1}^m$  is taken to be the same as the set of centres  $\{c_i\}_{i=1}^m$ .

As shown in Figure 6.4, a grid line contains two sets of nodal points. The first set consists of  $q$  interior points that are also the grid nodes (regular nodes). The function values at the interior points ( $\{x_i\}_{i=1}^q$ ) are unknown. The second set consists of the two nodes  $x_{b1}$  and  $x_{b2}$  which are generated by the intersection of the grid line and the boundaries.

Collocating (6.25) at the nodal points yields

$$\begin{pmatrix} \hat{f} \\ f(x_{b1}) \\ f(x_{b2}) \end{pmatrix} = \hat{\mathcal{I}}^{(0)} \begin{pmatrix} \hat{w} \\ c_1 \\ c_2 \end{pmatrix}, \quad (6.29)$$

where

$$\begin{aligned} \hat{f} &= (f(x_1), f(x_2), \dots, f(x_q))^T, \\ \hat{w} &= (w_1, w_2, \dots, w_m)^T, \\ \hat{\mathcal{I}}^{(0)} &= \begin{bmatrix} I_1^{(0)}(x_1) & I_2^{(0)}(x_1) & \cdots & I_m^{(0)}(x_1) & x_1 & 1 \\ I_1^{(0)}(x_2) & I_2^{(0)}(x_2) & \cdots & I_m^{(0)}(x_2) & x_2 & 1 \\ \vdots & \vdots & \ddots & \vdots & \vdots & \vdots \\ I_1^{(0)}(x_q) & I_2^{(0)}(x_q) & \cdots & I_m^{(0)}(x_q) & x_q & 1 \\ I_1^{(0)}(x_{b1}) & I_2^{(0)}(x_{b1}) & \cdots & I_m^{(0)}(x_{b1}) & x_{b1} & 1 \\ I_1^{(0)}(x_{b2}) & I_2^{(0)}(x_{b2}) & \cdots & I_m^{(0)}(x_{b2}) & x_{b2} & 1 \end{bmatrix}, \\ m &= q + 2. \end{aligned}$$

Solving (6.29) for the coefficient vector, including the two integration constants, results in

$$\begin{pmatrix} \hat{w} \\ c_1 \\ c_2 \end{pmatrix} = \left(\hat{\mathcal{I}}^{(0)}\right)^{-1} \begin{pmatrix} \hat{f} \\ f(x_{b1}) \\ f(x_{b2}) \end{pmatrix}, \quad (6.30)$$

where  $\left(\hat{\mathcal{I}}^{(0)}\right)^{-1}$  is the generalised inverse of  $\hat{\mathcal{I}}^{(0)}$ .

Making use of (6.30), the values of the first and second derivatives of  $f$  at the interior points are computed in terms of nodal variable values

$$\begin{pmatrix} \frac{\partial f(x_1)}{\partial x} \\ \frac{\partial f(x_2)}{\partial x} \\ \vdots \\ \frac{\partial f(x_q)}{\partial x} \end{pmatrix} = \widehat{\mathcal{I}}^{(1)} \left( \widehat{\mathcal{I}}^{(0)} \right)^{-1} \begin{pmatrix} \widehat{f} \\ f(x_{b1}) \\ f(x_{b2}) \end{pmatrix}, \quad (6.31)$$

and

$$\begin{pmatrix} \frac{\partial^2 f(x_1)}{\partial x^2} \\ \frac{\partial^2 f(x_2)}{\partial x^2} \\ \vdots \\ \frac{\partial^2 f(x_q)}{\partial x^2} \end{pmatrix} = \widehat{\mathcal{I}}^{(2)} \left( \widehat{\mathcal{I}}^{(0)} \right)^{-1} \begin{pmatrix} \widehat{f} \\ f(x_{b1}) \\ f(x_{b2}) \end{pmatrix}, \quad (6.32)$$

where

$$\widehat{\mathcal{I}}^{(1)} = \begin{bmatrix} I_1^{(1)}(x_1) & I_2^{(1)}(x_1) & \cdots & I_m^{(1)}(x_1) & 1 & 0 \\ I_1^{(1)}(x_2) & I_2^{(1)}(x_2) & \cdots & I_m^{(1)}(x_2) & 1 & 0 \\ \vdots & \vdots & \ddots & \vdots & \vdots & \vdots \\ I_1^{(1)}(x_q) & I_2^{(1)}(x_q) & \cdots & I_m^{(1)}(x_q) & 1 & 0 \end{bmatrix},$$

and

$$\widehat{\mathcal{I}}^{(2)} = \begin{bmatrix} g_1(x_1) & g_2(x_1) & \cdots & g_m(x_1) & 0 & 0 \\ g_1(x_2) & g_2(x_2) & \cdots & g_m(x_2) & 0 & 0 \\ \vdots & \vdots & \ddots & \vdots & \vdots & \vdots \\ g_1(x_q) & g_2(x_q) & \cdots & g_m(x_q) & 0 & 0 \end{bmatrix}.$$

It can be seen from (6.31) and (6.32) that Dirichlet conditions at  $x_{b1}$  and  $x_{b2}$  are incorporated into the IRBFN approximations. Depending on how a grid line is bounded, the boundary points  $x_{b1}$  and  $x_{b2}$  have particular locations. For example, one has ( $x_{b1} \in \Gamma_2$  and  $x_{b2} \in \Gamma_4$ ) if a grid line is bounded by the two vertical faces of the frame, and ( $x_{b1} \in \Gamma_2$  and  $x_{b2} \in \partial P_i$ ) if the bounding surfaces

are the left face and the  $i$ th particle boundary.

In the same manner, one can obtain the IRBFN expressions for a  $y$ -grid line.

### 6.3.2 Sliding bi-periodic boundary conditions

The continuity of the stream function and the vorticity across two adjacent sliding frames leads to the following periodic boundary conditions (Anderson et al., 2006)

$$\psi(-L/2, y, t) = \psi(L/2, y, t), \quad -H/2 \leq y \leq H/2, \quad (6.33)$$

$$\frac{\partial \psi}{\partial x}(-L/2, y, t) = \frac{\partial \psi}{\partial x}(L/2, y, t), \quad -H/2 \leq y \leq H/2, \quad (6.34)$$

$$\omega(-L/2, y, t) = \omega(L/2, y, t), \quad -H/2 \leq y \leq H/2, \quad (6.35)$$

$$\frac{\partial \omega}{\partial x}(-L/2, y, t) = \frac{\partial \omega}{\partial x}(L/2, y, t), \quad -H/2 \leq y \leq H/2, \quad (6.36)$$

for the two vertical faces and

$$\psi(x, -H/2, t) = \psi(x + \dot{\gamma}Ht, H/2, t), \quad -L/2 \leq x \leq L/2, \quad (6.37)$$

$$\frac{\partial \psi}{\partial y}(x, -H/2, t) = \frac{\partial \psi}{\partial y}(x + \dot{\gamma}Ht, H/2, t) + \dot{\gamma}H, \quad -L/2 \leq x \leq L/2, \quad (6.38)$$

$$\omega(x, -H/2, t) = \omega(x + \dot{\gamma}Ht, H/2, t), \quad -L/2 \leq x \leq L/2, \quad (6.39)$$

$$\frac{\partial \omega}{\partial y}(x, -H/2, t) = \frac{\partial \omega}{\partial y}(x + \dot{\gamma}Ht, H/2, t), \quad -L/2 \leq x \leq L/2, \quad (6.40)$$

for the two horizontal faces.

Consider the stream function  $\psi$ . The values of  $\psi$  are unknown not only at the interior points  $(x_i, y_j)$  with  $2 \leq i \leq n_x - 1$  and  $2 \leq j \leq n_y - 1$  but also at the boundary points of the reference frame  $(-L/2, y_j)$ ,  $(L/2, y_j)$ ,  $(x_i, -H/2)$  and  $(x_i, H/2)$  with  $1 \leq j \leq n_y$  and  $2 \leq i \leq n_x - 1$ . There are  $2n_y + 2(n_x - 2)$  unknowns for the latter, leading to  $n_{ip} + 2n_y + 2(n_x - 2)$  unknowns in total,

where  $n_{ip}$  is the number of interior points. Apart from collocating the governing equation for  $\psi$  at the interior points, one also needs to generate  $2n_y + 2(n_x - 2)$  extra equations which can be achieved by using the bi-periodic boundary conditions (6.33), (6.34), (6.37) and (6.38). Details are as follows.

$$\psi(-L/2, y_j) - \psi(L/2, y_j) = 0, \quad 1 \leq j \leq n_y, \quad (6.41)$$

$$\frac{\partial \psi}{\partial x}(-L/2, y_j) - \frac{\partial \psi}{\partial x}(L/2, y_j) = 0, \quad 1 \leq j \leq n_y, \quad (6.42)$$

$$\psi(x_i, -H/2) - \psi(x_i + \dot{\gamma}Ht, H/2) = 0, \quad 2 \leq i \leq n_x - 1, \quad (6.43)$$

$$\frac{\partial \psi}{\partial y}(x_i, -H/2) - \frac{\partial \psi}{\partial y}(x_i + \dot{\gamma}Ht, H/2) - \dot{\gamma}H = 0, \quad 2 \leq i \leq n_x - 1, \quad (6.44)$$

where the time variable  $t$  is left out for the sake of simplicity.

In (6.41)-(6.44), one needs to express  $\partial\psi(L/2, y_j)/\partial x$ ,  $\partial\psi(-L/2, y_j)/\partial x$ ,  $\partial\psi(x_i, -H/2)/\partial y$ ,  $\psi(x_i + \dot{\gamma}Ht, H/2)$  and  $\partial\psi(x_i + \dot{\gamma}Ht, H/2)/\partial y$  in terms of nodal values of  $\psi$ .

For  $\partial\psi(\pm L/2, y_j)/\partial x$ , the following IRBFN expressions are obtained by collocating (6.24) at  $x = \pm L/2$  and then making use of (6.30)

$$\frac{\partial \psi}{\partial x}(L/2, y_j) = [I_1^{(1)}(L/2), \dots, I_m^{(1)}(L/2), 1, 0] \left( \widehat{\mathcal{I}}^{(0)} \right)^{-1} \begin{pmatrix} \widehat{\psi} \\ \psi(x_{b1}, y_j) \\ \psi(L/2, y_j) \end{pmatrix}, \quad (6.45)$$

$$\frac{\partial \psi}{\partial x}(-L/2, y_j) = [I_1^{(1)}(-L/2), \dots, I_m^{(1)}(-L/2), 1, 0] \left( \widehat{\mathcal{I}}^{(0)} \right)^{-1} \begin{pmatrix} \widehat{\psi} \\ \psi(-L/2, y_j) \\ \psi(x_{b2}, y_j) \end{pmatrix}. \quad (6.46)$$

Similarly, one can obtain

$$\frac{\partial \psi}{\partial y}(x_i, -H/2) = [I_1^{(1)}(-H/2), \dots, I_m^{(1)}(-H/2), 1, 0] \left( \widehat{\mathcal{I}}^{(0)} \right)^{-1} \begin{pmatrix} \widehat{\psi} \\ \psi(x_i, -H/2) \\ \psi(x_i, y_{b2}) \end{pmatrix}.$$

(6.47)

For  $\psi(x_i + \dot{\gamma}Ht, H/2)$ , collocating (6.25) at  $x_i + \dot{\gamma}Ht$  and then making use of (6.30) lead to

$$\psi(\bar{x}, H/2) = [I_1^{(0)}(\bar{x}_i), \dots, I_m^{(0)}(\bar{x}_i), \bar{x}_i, 1] \left( \widehat{\mathcal{I}}^{(0)} \right)^{-1} \begin{pmatrix} \widehat{\psi} \\ \psi(-L/2, H/2) \\ \psi(L/2, H/2) \end{pmatrix}, \quad (6.48)$$

where  $\bar{x}_i = x_i + \dot{\gamma}Ht$ . The process of deriving the IRBFN expression for  $\partial\psi(x_i + \dot{\gamma}Ht, H/2)/\partial y$  is similar to that for  $\psi(x_i + \dot{\gamma}Ht, H/2)$ .

Sliding bi-periodic boundary conditions for the vorticity are also obtained in a similar fashion.

### 6.3.3 Boundary conditions on the particles' boundaries

#### Boundary conditions for the stream function

The values of the stream function  $\psi$  on the boundary of each particle  $P_i$  are constant due to no-slip condition at the particle surface. Particles have their own boundary values of  $\psi$  which are unknown. To find these unknowns, Lewis (1979) suggested using the condition that the pressure is a single-valued function on the boundary of a particle. This condition can be mathematically described as

$$\oint_{\partial P_i} \frac{\partial p}{\partial s} ds = \oint_{\partial P_i} \nabla p \cdot d\vec{s} = 0, \quad (6.49)$$

where  $p$  is the pressure and  $s$  the arc length. In the Cartesian coordinate system, (6.49) becomes

$$\oint \frac{\partial p}{\partial x} dx + \oint \frac{\partial p}{\partial y} dy = 0. \quad (6.50)$$

The pressure gradient  $\nabla p$  can be obtained from the momentum equations in the primitive variable form. By replacing  $u = \partial\psi/\partial y$  and  $v = -\partial\psi/\partial x$ , one can express the components of  $\nabla p$  in terms of the stream function and its derivatives.

### Boundary conditions for the vorticity

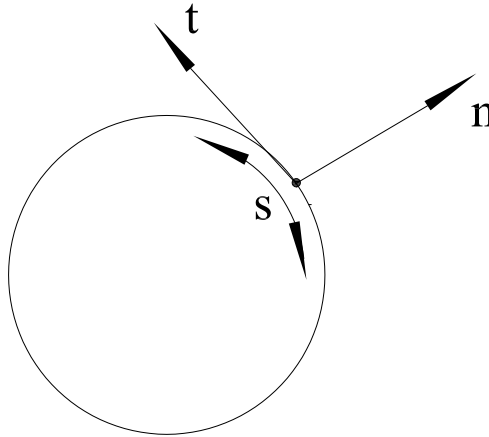


Figure 6.5: A curved boundary of the particle: arclength, and unit normal and tangential vectors.

The values of the vorticity on  $\partial P_i$  can be computed via

$$\omega = \frac{\partial^2 \psi}{\partial x^2} + \frac{\partial^2 \psi}{\partial y^2}, \quad \mathbf{x} \in \partial P_i. \quad (6.51)$$

The handling of (6.51) thus involves the evaluation of second-order derivatives of the stream function in both  $x$  and  $y$  directions. Unfortunately, the boundary points on  $\partial P_i$  do not generally coincide with the grid nodes and hence they lie

on either  $x$ - or  $y$ -grid lines. In (Le-Cao et al., 2009), the following formulae were proposed

$$\omega = \left[ 1 + \left( \frac{t_x}{t_y} \right)^2 \right] \frac{\partial^2 \psi}{\partial x^2} - \frac{t_x}{t_y^2} \frac{\partial^2 \psi}{\partial x \partial s} + \frac{1}{t_y} \frac{\partial^2 \psi}{\partial y \partial s}, \quad \mathbf{x} \in \partial P_i, \quad (6.52)$$

for the  $x$ -grid lines, and

$$\omega = \left[ 1 + \left( \frac{t_y}{t_x} \right)^2 \right] \frac{\partial^2 \psi}{\partial y^2} - \frac{t_y}{t_x^2} \frac{\partial^2 \psi}{\partial y \partial s} + \frac{1}{t_x} \frac{\partial^2 \psi}{\partial x \partial s}, \quad \mathbf{x} \in \partial P_i, \quad (6.53)$$

for the  $y$ -grid lines. In (6.52) and (6.53),  $t_x$  and  $t_y$  are the  $x$  and  $y$  components of the unit tangential vector and  $\partial(\cdot)/\partial s$  represents the derivative of  $(\cdot)$  on  $\partial P_i$  which is known (Figure 6.5). The boundary conditions for the vorticity are thus written in terms of the second derivative of  $\psi$  with respect to  $x$  or  $y$  only.

In the case that the  $i$ th particle is of circular shape of radius  $R_i$  and rotates about the centre of the reference frame at the angular velocity  $\Omega_i$ . Expressions for computing  $t_x$ ,  $t_y$ ,  $\partial^2 \psi / \partial x \partial s$  and  $\partial^2 \psi / \partial y \partial s$  become

$$t_x = \frac{-y}{\sqrt{x^2 + y^2}}, \quad (6.54)$$

$$t_y = \frac{x}{\sqrt{x^2 + y^2}}, \quad (6.55)$$

$$\frac{\partial^2 \psi}{\partial x \partial s} = \frac{1}{R_i} \Omega_i y, \quad (6.56)$$

$$\frac{\partial^2 \psi}{\partial y \partial s} = -\frac{1}{R_i} \Omega_i x. \quad (6.57)$$

Substitution of (6.54)-(6.57) into (6.52) and (6.53) yields

$$\omega = \left[ 1 + \left( \frac{y}{x} \right)^2 \right] \frac{\partial^2 \psi}{\partial x^2} + \left[ \left( \frac{y}{x} \right)^2 - 1 \right] \Omega_i, \quad \mathbf{x} \in \partial P_i, \quad (6.58)$$

$$\omega = \left[ 1 + \left( \frac{x}{y} \right)^2 \right] \frac{\partial^2 \psi}{\partial y^2} + \left[ \left( \frac{x}{y} \right)^2 - 1 \right] \Omega_i, \quad \mathbf{x} \in \partial P_i. \quad (6.59)$$

The IRBFN implementation of (6.50) is straightforward, while special treat-

ments are required in handling (6.52)-(6.53) and (6.58)-(6.59). For the latter, normal derivative boundary conditions for the stream function, i.e.  $\partial\psi/\partial n$ , need be incorporated into expressions (6.52), (6.53), (6.58) and (6.59). Since  $\psi$  and  $\partial\psi/\partial n$  are known from the previous iteration, one can easily obtain the values of  $\partial\psi/\partial x$  and  $\partial\psi/\partial y$  on  $\partial P_i$ . The proposed procedure imposes  $\partial\psi/\partial n$ , i.e.  $\partial\psi/\partial x$  and  $\partial\psi/\partial y$ , using the constants of integration. On an  $x$ -grid line, one needs to incorporate  $\partial\psi/\partial x$  into  $\partial^2\psi/\partial x^2$ , while on a  $y$ -grid line,  $\partial\psi/\partial y$  is incorporated into  $\partial^2\psi/\partial y^2$ . Because these two processes are similar, details are given here for an  $x$ -grid line only, e.g. the one with  $x_{b1} \in \Gamma_2$  and  $x_{b2} \in \partial P_i$ . The system for the conversion of the RBF space into the physical space (6.29) now takes the form

$$\begin{pmatrix} \widehat{\psi} \\ \psi(x_{b1}) \\ \psi(x_{b2}) \\ \frac{\partial\psi}{\partial x}(x_{b2}) \end{pmatrix} = \begin{pmatrix} \widehat{\mathcal{I}}^{(0)} \\ \mathcal{B} \end{pmatrix} \begin{pmatrix} \widehat{w} \\ c_1 \\ c_2 \end{pmatrix}, \quad (6.60)$$

where the conversion matrix is of dimensions  $(m+1) \times (m+2)$  and

$$\mathcal{B} = \left[ I_1^{(1)}(x_{b2}), I_2^{(1)}(x_{b2}), \dots, I_m^{(1)}(x_{b2}), 1, 0 \right].$$

Using (6.60), one obtains the following from (6.23) (in which  $f \equiv \psi$  and  $x \equiv x_{b2}$ )

$$\frac{\partial^2\psi}{\partial x^2}(x_{b2}) = [g_1(x_{b2}), g_2(x_{b2}), \dots, g_m(x_{b2}), 0, 0] \begin{pmatrix} \widehat{\mathcal{I}}^{(0)} \\ \mathcal{B} \end{pmatrix}^{-1} \begin{pmatrix} \widehat{\psi} \\ \psi(x_{b1}) \\ \psi(x_{b2}) \\ \frac{\partial\psi}{\partial x}(x_{b2}) \end{pmatrix}. \quad (6.61)$$

Since the conversion matrix in (6.60) is not over-determined, the IRBFN approximation for  $\partial^2\psi(x_{b2})/\partial x^2$  satisfies  $\partial\psi/\partial x$  at  $x = x_{b2}$  identically. This imposition shows a clear advantage of IRBFNs over the usual differentiated approximations.

Substituting (6.61) into (6.52), one is able to obtain the boundary conditions on  $\partial P_i$  for the vorticity equation. It is noted that given  $\partial\psi/\partial x$  and  $\partial\psi/\partial y$  on  $\partial P_i$ , the terms  $\partial^2\psi/\partial x\partial s$  and  $\partial^2\psi/\partial y\partial s$  in (6.52) and (6.53) are known.

## 6.4 Numerical examples

In this section, the proposed procedure is validated through three examples. The first example examines the performance of the present technique in the implementation of sliding bi-periodic boundary conditions of the frame. The second example investigates the accuracy of the present technique in the handling of boundary conditions that are similar to those on the particles' boundaries. In the third example, the proposed method is applied to simulate a shear flow of a Newtonian-based particulate system, which is modelled by one particle suspended in a sliding rectangular frame. For all numerical examples, the problem domain is discretised using a uniform Cartesian grid. The interior points that fall very close to the curved/irregular boundary (within a distance of  $h/8$ ,  $h$  - the grid size) are removed from the set of nodal points.

### 6.4.1 Example 1: Sliding bi-periodic boundary conditions

In this example, the 1D-IRBFN implementation of shear bi-periodic boundary conditions is validated. The test problem is governed by

$$\frac{\partial^2\psi}{\partial x^2} + \frac{\partial^2\psi}{\partial y^2} = b(x, y). \quad (6.62)$$

The domain of interest is the region lying between a circle of radius  $1/2$  and a square of dimensions  $2 \times 2$  which are both centered at the origin. The exact

solution is

$$\psi(x, y) = \sin(\pi(x - \dot{\gamma}yt)) \sin(\pi y), \quad (6.63)$$

from which the driving function  $b(x, y)$  in (6.62) and the Dirichlet boundary conditions on the hole can be easily derived. The value of  $\dot{\gamma}$  is set to 1. This problem is taken from (Anderson et al., 2006).

The accuracy of an approximation scheme is measured by means of the discrete relative  $L_2$  norm of the error defined as

$$Ne = \frac{\sqrt{\sum_{i=1}^M (\psi_i^e - \psi_i)^2}}{\sqrt{\sum_{i=1}^M (\psi_i^e)^2}}, \quad (6.64)$$

where  $M$  is the number of unknown nodal values of  $\psi$ , and  $\psi^e$  and  $\psi$  are the exact and approximate solutions, respectively. Another important measure is the convergence rate  $\alpha$  of the solution with respect to grid refinement

$$Ne(h) \approx \gamma h^\alpha = O(h^\alpha), \quad (6.65)$$

in which  $\alpha$  and  $\gamma$  are exponential model's parameters. Given a set of observations, these parameters can be found by the general linear least squares technique.

Table 6.1: Example 1 (sliding bi-periodic boundary conditions): Errors of the solution and condition numbers of the system matrix denoted by  $\text{Cond}(A)$ . It is noted that  $h$  is the spacing (grid size).

Grid	$Ne$	$\text{Cond}(A)$
$12 \times 12$	$3.1078 \times 10^{-3}$	$1.6 \times 10^3$
$22 \times 22$	$4.9660 \times 10^{-4}$	$5.1 \times 10^3$
$32 \times 32$	$1.5234 \times 10^{-4}$	$1.8 \times 10^4$
$42 \times 42$	$6.6599 \times 10^{-5}$	$2.2 \times 10^4$
$52 \times 52$	$3.6510 \times 10^{-5}$	$5.2 \times 10^4$
$62 \times 62$	$1.9881 \times 10^{-5}$	$5.9 \times 10^4$
$O(h^{2.94})$		

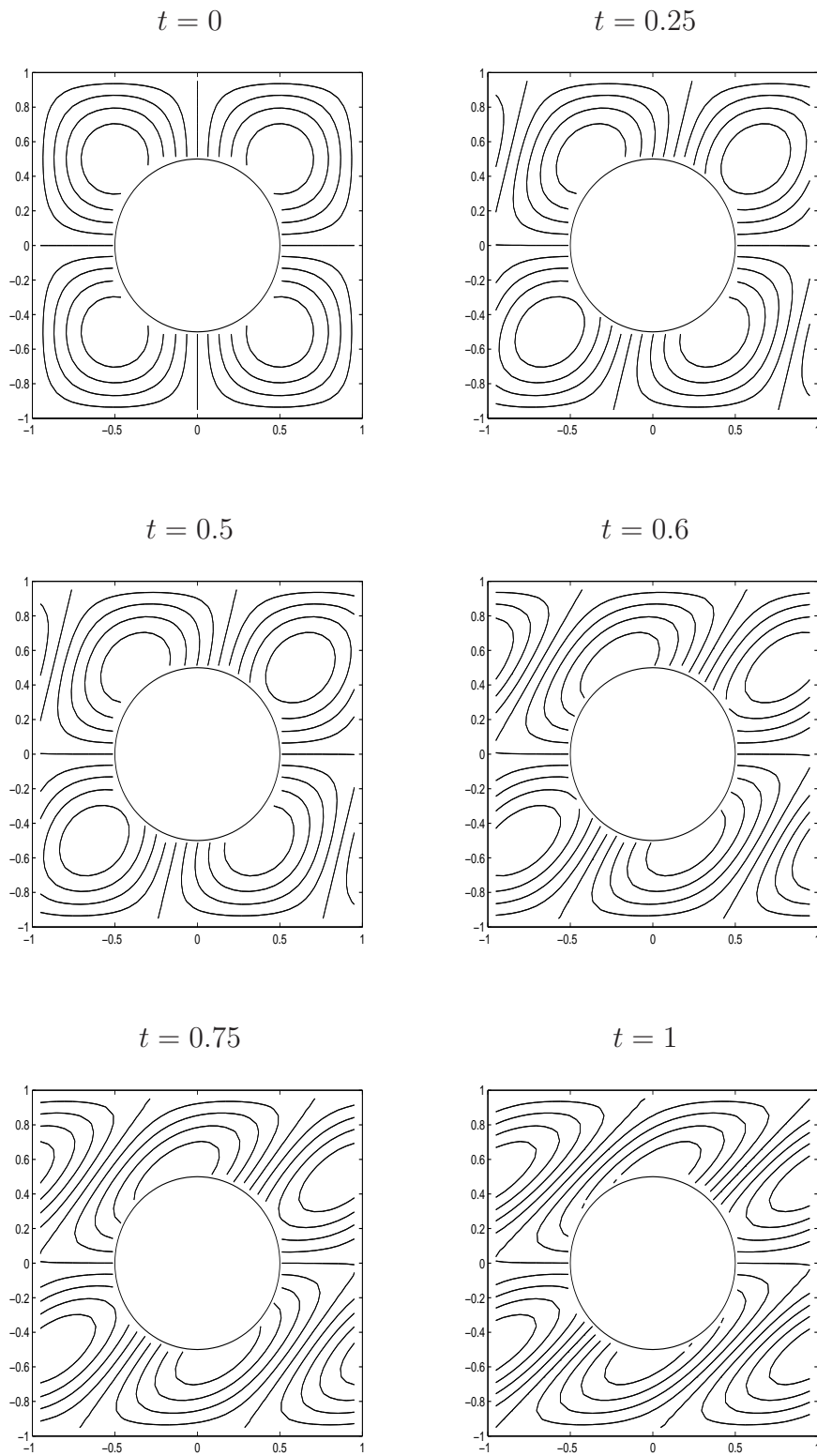


Figure 6.6: Example 1 (sliding bi-periodic boundary conditions): Contour plots of the approximate and exact solutions at different time values. The two plots are indistinguishable.

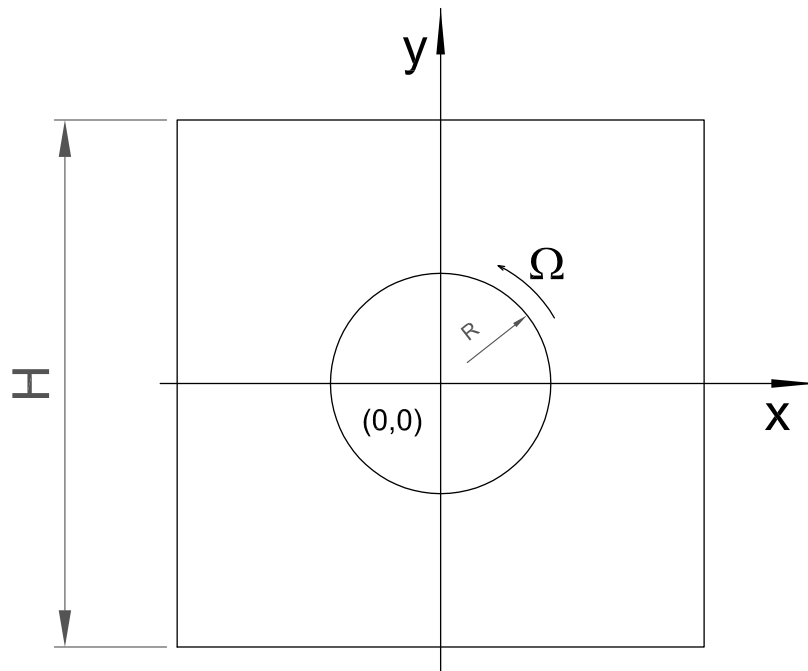


Figure 6.7: Example 2 (rotating cylinder): geometry.

A number of grids, namely  $(12 \times 12, 22 \times 22, \dots, 62 \times 62)$ , are employed for the convergence study. Results concerning the condition number of the system matrix, denoted by  $\text{cond}(A)$ , and the error  $Ne$  at  $t = 0$  are listed in Table 6.1. It can be seen that the present system matrix has relatively-low condition numbers and the solution converges fast at the rate of 2.94.

Contour plots for  $\psi$  at several values of the shear time  $t$ , namely  $(0, 0.5, 0.75, 1)$ , using a grid of  $42 \times 42$  are shown in Figure 6.6. Exact solutions are also included. The two solutions are indistinguishable.

### 6.4.2 Example 2: A rotating circular cylinder

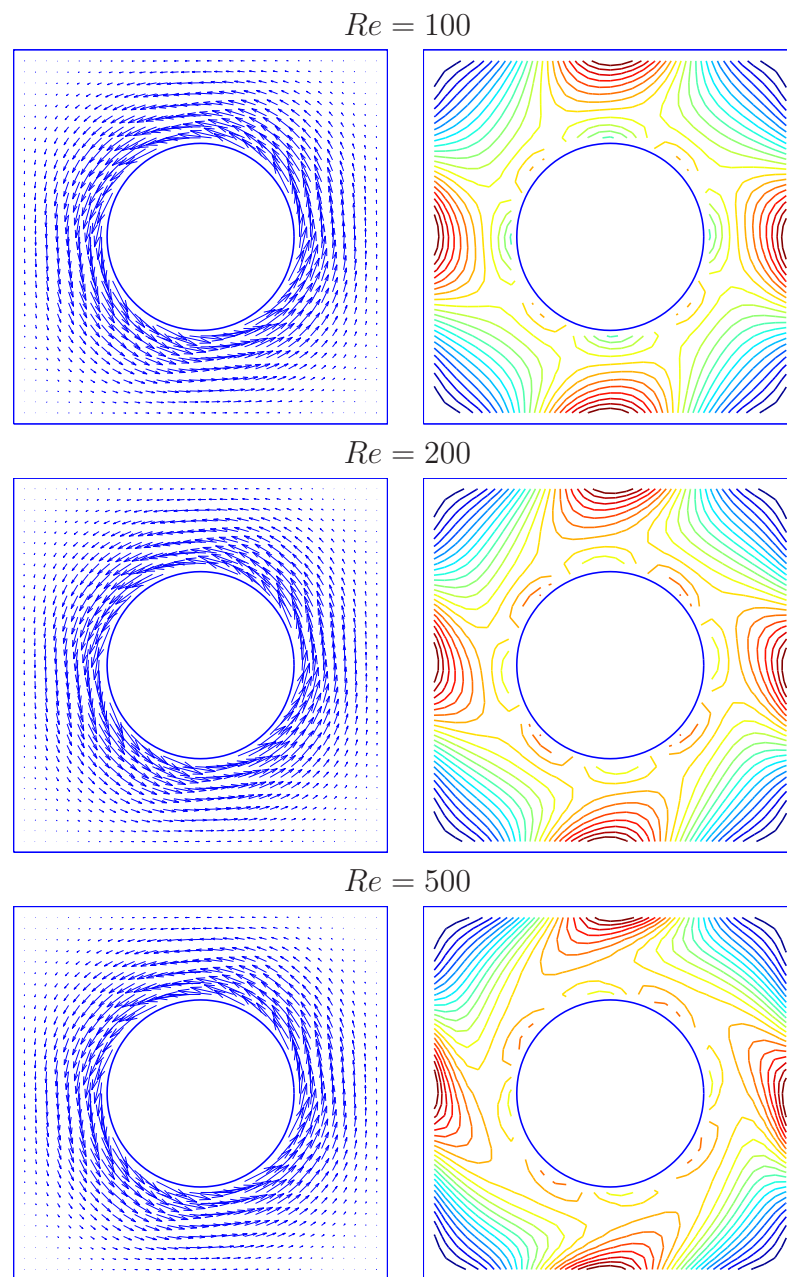


Figure 6.8: Example 2 (rotating cylinder): Velocity vector field (left) and vorticity field (right) for the flow at  $Re = 100, 200$  and  $500$ .

Table 6.2: Example 2 (rotating cylinder): Comparison of the stream-function value at the inner cylinder,  $\psi_{wall}$ , between the present technique (grid of  $36 \times 36$ ) and finite difference technique for several values of  $Re$ .

$Re$	100	200	500
	$\psi_{wall}$		
Present	0.4637	0.4632	0.4550
(Lewis, 1979)	0.4577	0.4539	0.4465

In this test problem, the 1D-IRBFN implementation of boundary conditions of particles is validated through the simulation of the flow of a Newtonian fluid shown in Figure 6.7. The inner cylinder rotates at a unit angular velocity while the outer cylinder is stationary. The value of  $\psi$  on the outer wall is simply set to zero, while the value of  $\psi$  on the inner wall is considered as an unknown, denoted by  $\psi_{wall}$ . The flow is governed by (6.6) and (6.7) and subject to the boundary conditions

$$\psi = \frac{\partial\psi}{\partial x} = \frac{\partial\psi}{\partial y} = 0,$$

on the outer cylinder and

$$\psi = \psi_{wall}, \quad \frac{\partial\psi}{\partial x} = -x, \quad \frac{\partial\psi}{\partial y} = -y,$$

on the inner cylinder. Using (6.58) and (6.59) with  $\Omega = 1$ , the vorticity boundary conditions on the rotating cylinder can be computed by

$$\omega = \left[ 1 + \left(\frac{y}{x}\right)^2 \right] \frac{\partial^2\psi}{\partial x^2} + \left[ \left(\frac{y}{x}\right)^2 - 1 \right],$$

$$\omega = \left[ 1 + \left(\frac{x}{y}\right)^2 \right] \frac{\partial^2\psi}{\partial y^2} + \left[ \left(\frac{x}{y}\right)^2 - 1 \right].$$

The value of  $\psi_{wall}$  is found using the single-valued pressure condition as discussed earlier.

The flow is simulated with  $R = 0.25$  and  $L = 1.0$  using a uniform grid of  $36 \times 36$ . Several values of the Reynolds number, namely (100, 200, 500), are considered. Results concerning  $\psi_{wall}$  obtained by the proposed technique and the finite-difference technique (Lewis, 1979) are presented in Table 6.2, showing a good agreement. Plots for the velocity vector and vorticity fields for the case of  $Re = \{100, 200, 500\}$  are given in Figure 6.8.

### 6.4.3 Example 3: Shear suspension flow

In this example, a single particle of radius  $R$  is suspended freely at the center of the reference sliding bi-periodic frame of dimensions  $1 \times 1$ . The fluid domain is the region lying between the particle and the frame boundary (Figure 6.9). The fluid is Newtonian and moves under a shear rate  $\dot{\gamma} = 1$ . This configuration can represent the system of an infinite number of particles as described in Figure 6.10. It can be seen that the initial configuration is reproduced after the time period  $K = 1/\dot{\gamma}$ . The inertia of the particle and fluid are ignored. This problem was studied using the fictitious-domain/finite-element method in (Hwang et al., 2004). The governing equations for the motion of a fluid thus reduce to

$$\frac{\partial^2 \psi}{\partial x^2} + \frac{\partial^2 \psi}{\partial y^2} = \omega, \quad (6.66)$$

$$\frac{\partial^2 \omega}{\partial x^2} + \frac{\partial^2 \omega}{\partial y^2} = 0. \quad (6.67)$$

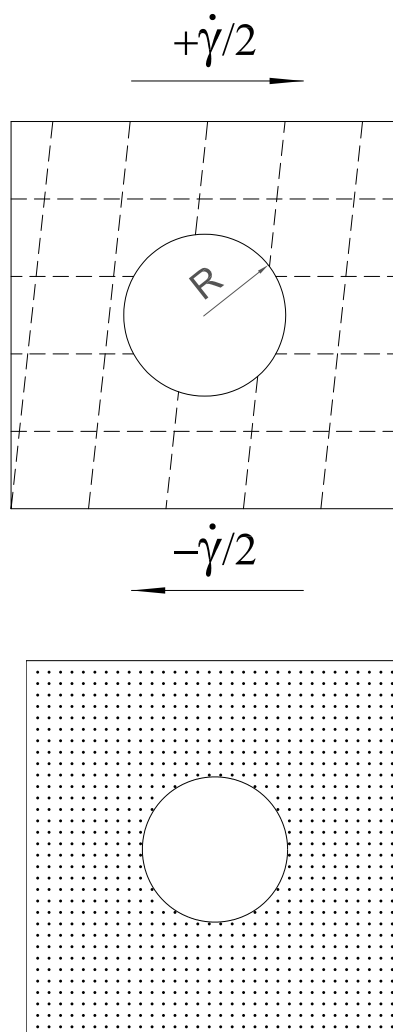


Figure 6.9: Example 3 (shear suspension): A reference frame (top) and its discretisation (bottom).

The boundary conditions for the frame are bi-periodic and determined through (6.33)-(6.40), while the boundary conditions for the particle are computed using (6.50), (6.58) and (6.59). However, as only one particle is considered, the value of  $\psi$  on  $\partial P$  is simply set to 0. The stress tensor can be written in terms of the stream function and pressure as

$$\boldsymbol{\sigma} = \begin{bmatrix} \left(-p + 2\frac{\partial^2\psi}{\partial x\partial y}\right) & \left(\frac{\partial^2\psi}{\partial y^2} - \frac{\partial^2\psi}{\partial x^2}\right) \\ \left(\frac{\partial^2\psi}{\partial y^2} - \frac{\partial^2\psi}{\partial x^2}\right) & \left(-p + 2\frac{\partial^2\psi}{\partial x\partial y}\right) \end{bmatrix}. \quad (6.68)$$

Conventionally, the interacting hydrodynamic force and moment are first calculated from the fluid flow, and the movement of the particle is then determined from these force and moment using the Newton-Euler equations. Because the inertia of the particle is neglected and there is no external force acting on the particle, the hydrodynamic force and torque are zero (force free and torque free). It can be seen that the particle rotates about the frame centre at the angular velocity  $\Omega$  and does not translate relative to the frame, i.e.  $U = 0$  and  $V = 0$ . One thus only needs to use the torque-free condition to determine the value of  $\Omega$

$$\mathbf{T} = \int_{\partial P} \mathbf{r} \times (\boldsymbol{\sigma} \cdot \mathbf{n}) ds = 0. \quad (6.69)$$

The reader is referred to (Hwang et al., 2004) for further details. Substitution of (6.68) into (6.69) yields

$$\oint (x^2 - y^2) \left( \frac{\partial^2\psi}{\partial y^2} - \frac{\partial^2\psi}{\partial x^2} \right) ds = 0. \quad (6.70)$$

In this study, a new way of obtaining  $\Omega$  is proposed. On the particle boundary (Figure 6.5), one can have

$$\frac{\partial f}{\partial s} = \frac{\partial f}{\partial x} t_x + \frac{\partial f}{\partial y} t_y, \quad (6.71)$$

where  $f$  is a generic function, and  $s$ ,  $t_x$  and  $t_y$  are defined as before. By replacing

$f = \partial\psi/\partial x$ , (6.71) becomes

$$\frac{\partial^2\psi}{\partial s\partial x} = \frac{\partial^2\psi}{\partial x^2}t_x + \frac{\partial^2\psi}{\partial y\partial x}t_y. \quad (6.72)$$

Since  $U = 0$  and  $V = 0$ , (6.13) and (6.14) reduce to

$$\frac{\partial\psi}{\partial y} = -\Omega y, \quad (6.73)$$

$$\frac{\partial\psi}{\partial x} = -\Omega x. \quad (6.74)$$

Substituting (6.73) and (6.74) into (6.72) and making use of  $t_x = -y/R$  and  $t_y = x/R$  give

$$\Omega = -\frac{\partial^2\psi}{\partial x^2}. \quad (6.75)$$

Similarly, by replacing  $f = \partial\psi/\partial y$ , one has

$$\Omega = -\frac{\partial^2\psi}{\partial y^2}. \quad (6.76)$$

These conditions (6.75) and (6.76) can be used as an alternative to (6.70). In practice, (6.75) and (6.76) are applied to the boundary points of the particle on the  $x$ - and  $y$ -grid lines, respectively, from which the angular velocity is derived in an average sense.

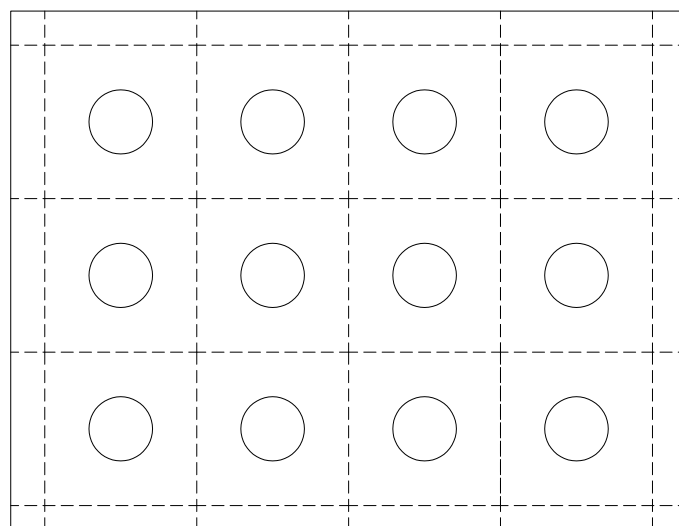
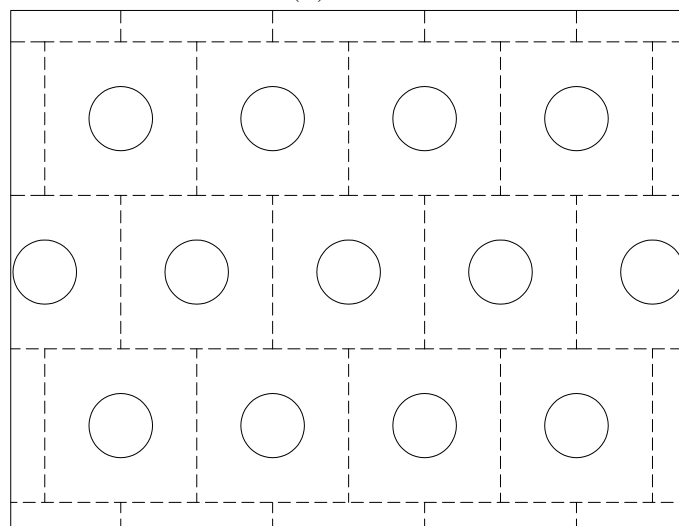
(a)  $t = 0$ (b)  $t = K/2$ 

Figure 6.10: Example 3 (shear suspension): Problem description with two instances during a period of shearing.

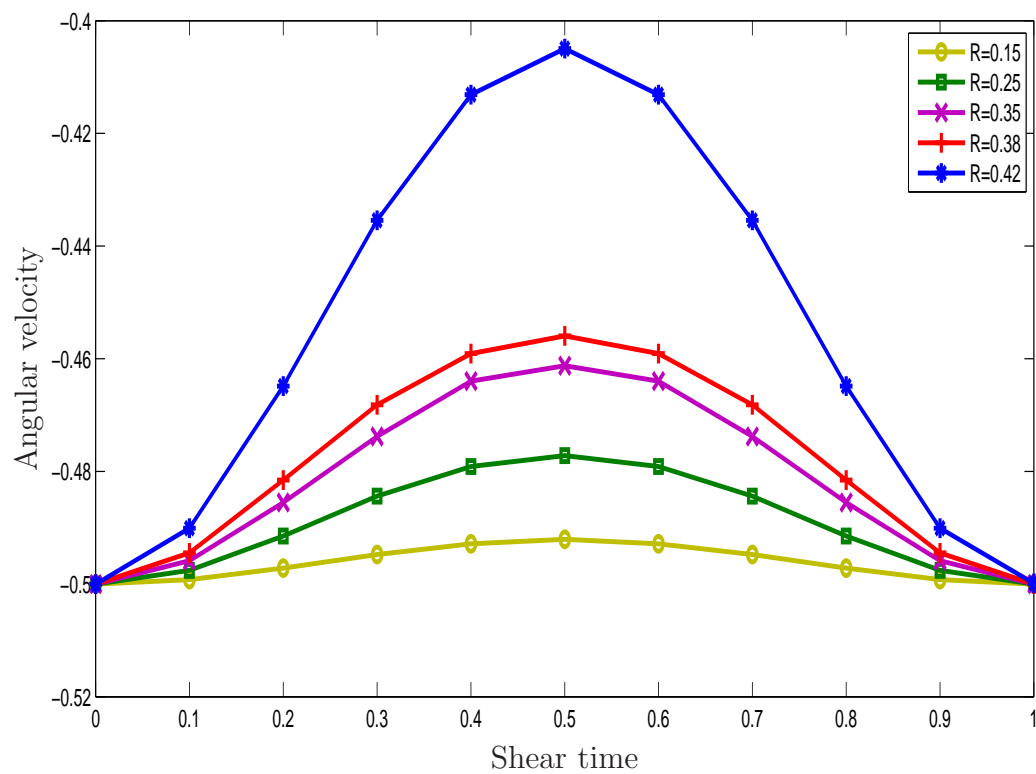


Figure 6.11: Example 3 (shear suspension): Profile of the angular velocity over the period  $K$ .

For each shear interval, the solution procedure is as follows.

1. Guess the distribution of  $\omega$  and  $\psi$ .
2. Discretise (6.66) and (6.67) using 1D-IRBFNs. The two system matrices arising from the discretisation of the Laplace operator are identical and remain unchanged during the iterative process.
3. Impose the sliding bi-periodic boundary conditions for  $\psi$  and  $\omega$  on the frame.
4. Derive computational boundary conditions for  $\omega$  on  $\partial P$ .
5. Solve (6.66) for  $\omega$  and (6.67) for  $\psi$ .
6. Compute  $\Omega$  from (6.75) and (6.76).
7. Check the following convergence measure

$$CM = \frac{\sqrt{\sum_{i=1}^{n_{ip}} (\psi_i^{(k)} - \psi_i^{(k-1)})^2}}{\sqrt{\sum_{i=1}^{n_{ip}} (\psi_i^{(k)})^2}} < \epsilon,$$

where  $n_{ip}$  is the number of interior points,  $k$  the current iteration and  $\epsilon$  the tolerance. In this study,  $\epsilon$  is taken to be  $10^{-12}$ .

8. If not, relax the field solution

$$\psi_i^{(k)} = \alpha \psi_i^{(k)} + (1 - \alpha) \psi_i^{(k-1)},$$

where  $\alpha$  is a given number ( $0 < \alpha < 1$ ), and repeat from step 4. Otherwise, stop the computation and save the results.

The particle's radius  $R$  is considered in the range of 0.15 to 0.42. Simulations are carried out using Cartesian grids whose densities vary from  $50 \times 50$  to  $72 \times 72$ . Denser grids are used for larger values of  $R$ .

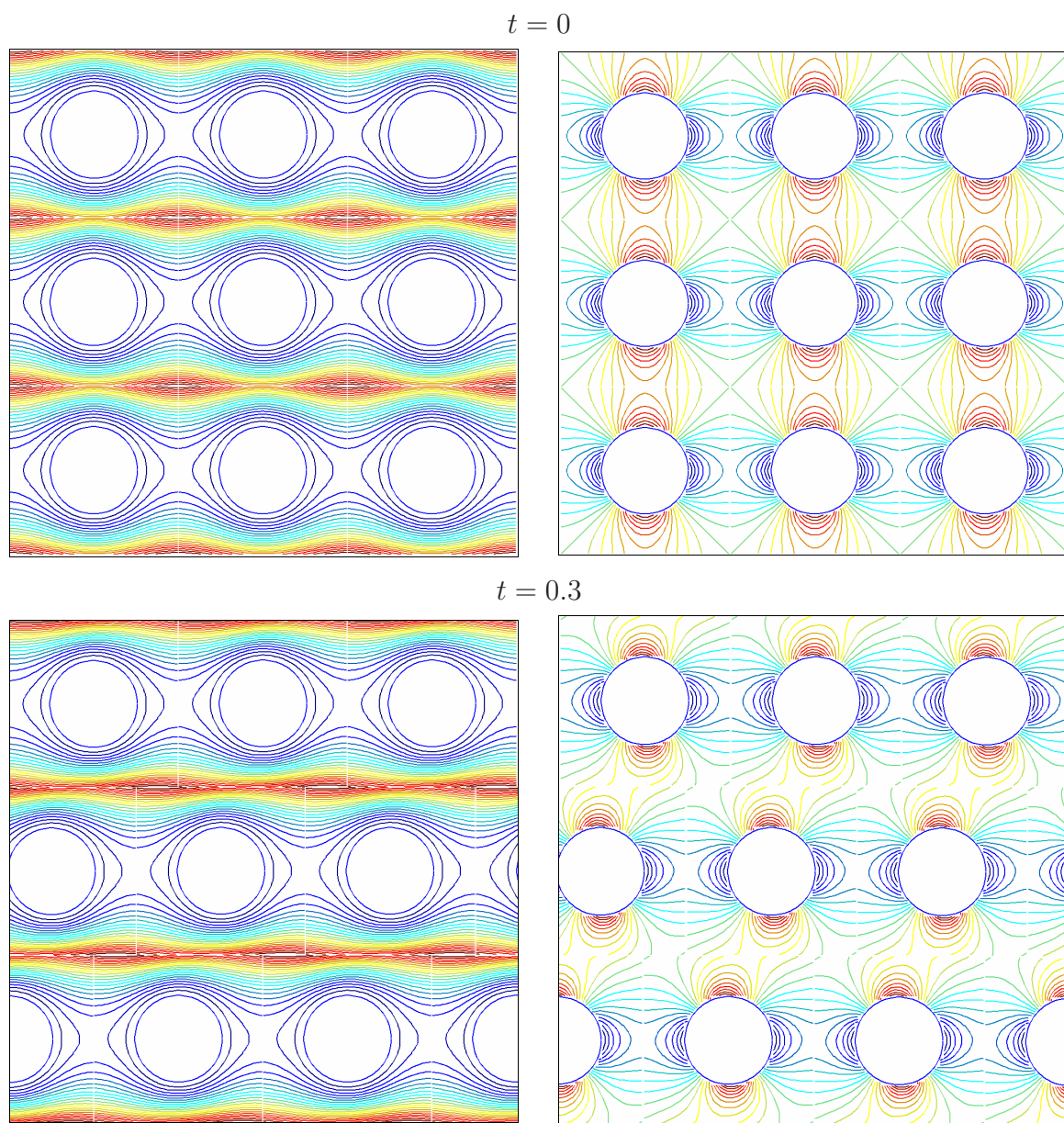


Figure 6.12: Example 3 (shear suspension): Streamlines and iso-vorticity lines at the shear time of 0 and 0.3.

Figure 6.11 shows the variation of  $\Omega$  with respect to the shear time for several values of  $R$  over the period  $K$ . It can be seen that the profile of  $\Omega$  is symmetric about the vertical line  $t = K/2$ . The largest value of  $\Omega$  occurs when the frames line up in the vertical direction (Figure 6.10a). Furthermore, the fluctuation of  $\Omega$  is an increasing function of  $R$ , indicating stronger hydrodynamic interaction between particles at shorter range. In Figure 6.12, the distribution of  $\psi$  and  $\omega$  over a reference frame are multiplied to produce the  $\psi$  and  $\omega$  fields on the original large domain, where the sliding bi-periodic boundary conditions are clearly observed.

### Prediction of the bulk material properties

Following the work of Hwang et al. (2004), the bulk stress can be computed by

$$\langle \boldsymbol{\sigma} \rangle = \frac{1}{A} \int_{\Gamma} \mathbf{x} \boldsymbol{\tau}^T ds, \quad (6.77)$$

where  $\Gamma = \Gamma_1 \cap \Gamma_2 \cap \Gamma_3 \cap \Gamma_4$  and  $A$  is the area of the frame domain,  $\mathbf{x}$  the position vector and  $\boldsymbol{\tau}$  the traction vector. In terms of  $\psi$ , (6.77) takes the form

$$\langle \sigma_{xy} \rangle = \frac{1}{A} \int_{\Gamma} y t_x ds = \int_{\Gamma_1} \left( \frac{\partial^2 \psi}{\partial y^2} - \frac{\partial^2 \psi}{\partial x^2} \right) dy, \quad (6.78)$$

$$\begin{aligned} \langle \sigma_{xx} \rangle = \frac{1}{A} \int_{\Gamma} x t_x ds = & \int_{\Gamma_2} \left( -p + \frac{\partial^2 \psi}{\partial x \partial y} \right) dy + \int_{\Gamma_3} x \left( \frac{\partial^2 \psi}{\partial y^2} - \frac{\partial^2 \psi}{\partial x^2} \right) dx \\ & - \int_{\Gamma_1} x \left( \frac{\partial^2 \psi}{\partial y^2} - \frac{\partial^2 \psi}{\partial x^2} \right) dx, \end{aligned} \quad (6.79)$$

$$\langle \sigma_{yy} \rangle = \frac{1}{A} \int_{\Gamma} y t_y ds = \frac{1}{2} \int_{\Gamma_3} \left( -p + \frac{\partial^2 \psi}{\partial x \partial y} \right) dx - \frac{1}{2} \int_{\Gamma_1} \left( -p + \frac{\partial^2 \psi}{\partial x \partial y} \right) dx, \quad (6.80)$$

where the pressure on  $\Gamma_2$  and  $\Gamma_1$  are computed using

$$\begin{aligned} p &= \int_{\Gamma_2} \frac{\partial p}{\partial y} dy = - \int_{\Gamma_2} \left( \frac{\partial^3 \psi}{\partial x^3} + \frac{\partial^3 \psi}{\partial y^2 \partial x} \right) dy, \\ p &= \int_{\Gamma_1} \frac{\partial p}{\partial x} dx = \int_{\Gamma_1} \left( \frac{\partial^3 \psi}{\partial y^3} + \frac{\partial^3 \psi}{\partial x^2 \partial y} \right) dx, \end{aligned}$$

and the pressure on  $\Gamma_3$  is derived from the pressure on  $\Gamma_1$  and the sliding periodic condition.

Results for the bulk shear stress  $\langle\sigma_{xy}\rangle$  and the normal stress difference  $\langle\sigma_{xx}-\sigma_{yy}\rangle$  are plotted in Figure 6.13 and 6.14. When the distance from a given particle in a sliding layer to the nearest particle in an adjacent layer is maximum (Figure 6.10b), the bulk shear stress becomes maximum and the bulk normal stress difference becomes minimum. Both the bulk shear and normal stress difference become larger when the particle radius increases and they oscillate with the period  $K$ .

The bulk shear viscosity can be obtained by taking the time average of the bulk shear stress over the period  $K$  (Hwang et al., 2004),

$$\frac{\langle\eta\rangle}{\eta} = \frac{1}{K} \int_0^K \langle\sigma_{xy}\rangle dt. \quad (6.81)$$

In Figure 6.15,  $\langle\eta\rangle/\eta$  is plotted against the solid area fraction  $\phi$  ( $\phi = \pi R^2$ ). In the case of dilute suspensions with circular disks, the bulk shear viscosity can be computed by  $\langle\eta\rangle = (1 + 2\phi)\eta$  (Hwang et al., 2004). The dilute suspension results are also plotted in Figure 6.15. It can be seen that the present model produces larger values of  $\langle\eta\rangle/\eta$  than the dilute model. This looks reasonable as the present simulations take the interaction between the particles into account and the dilute result is only valid for small  $\phi$ .

The observations presented above are similar to those reported in (Hwang et al., 2004). Since the finite-element results were presented in graph, we are not able to reproduce them here. However, numerical results by the two techniques appear to be of comparable values, judging from the graphical presentations.

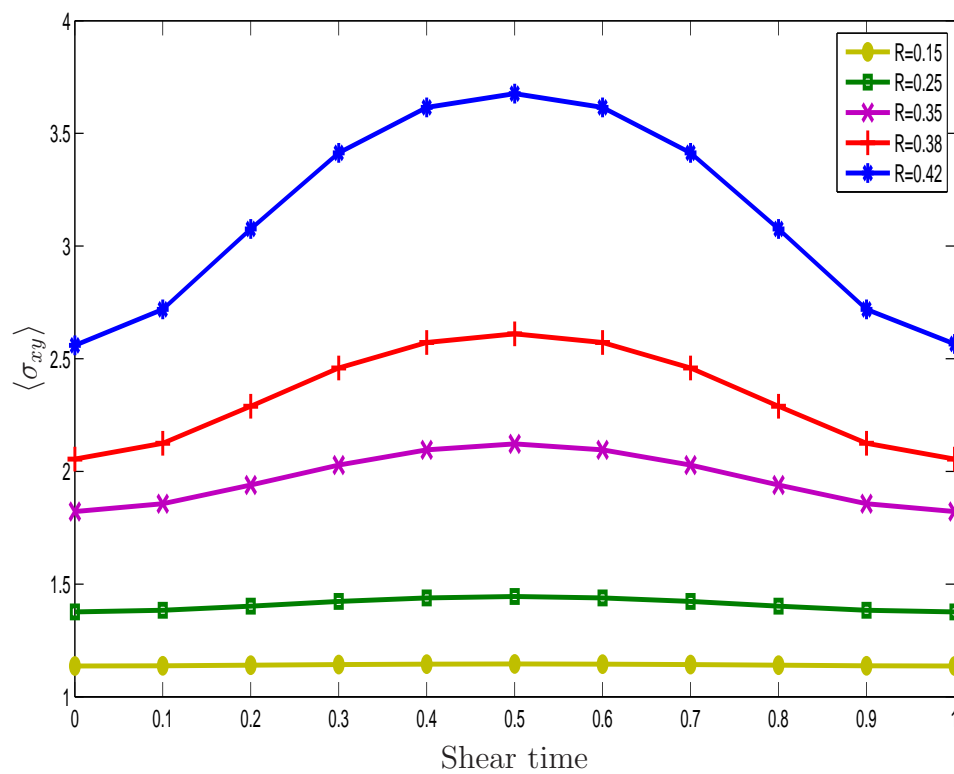


Figure 6.13: Example 3 (shear suspension): Variations of the bulk shear stresses over the period  $K$ .

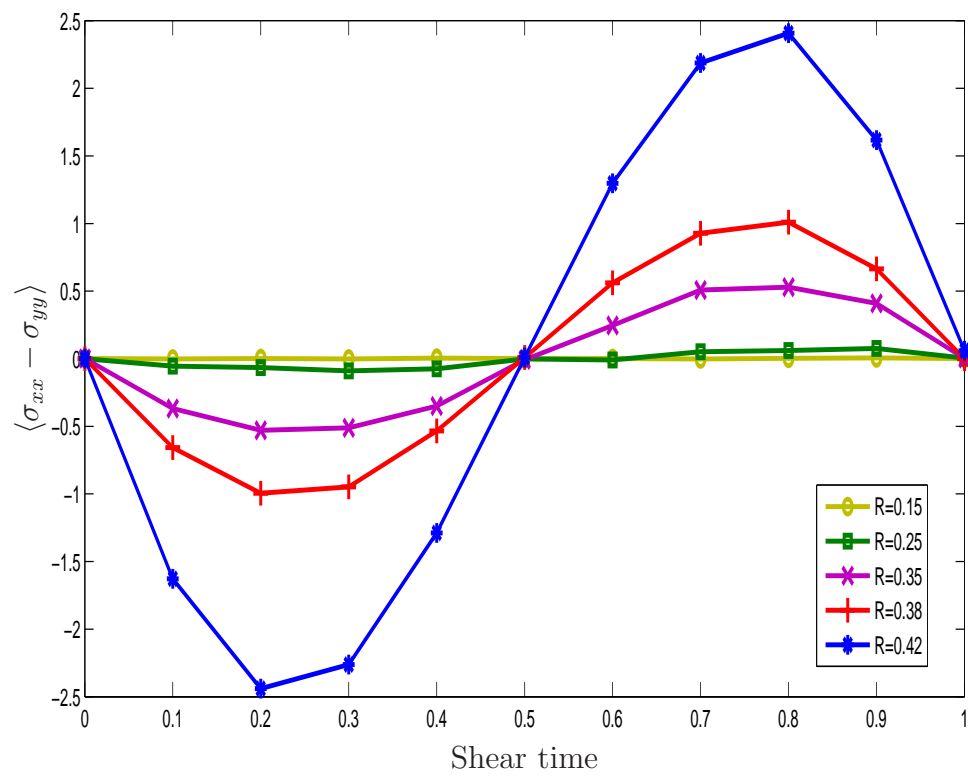


Figure 6.14: Example 3 (shear suspension): Variations of the bulk normal stress difference over the period  $K$ .

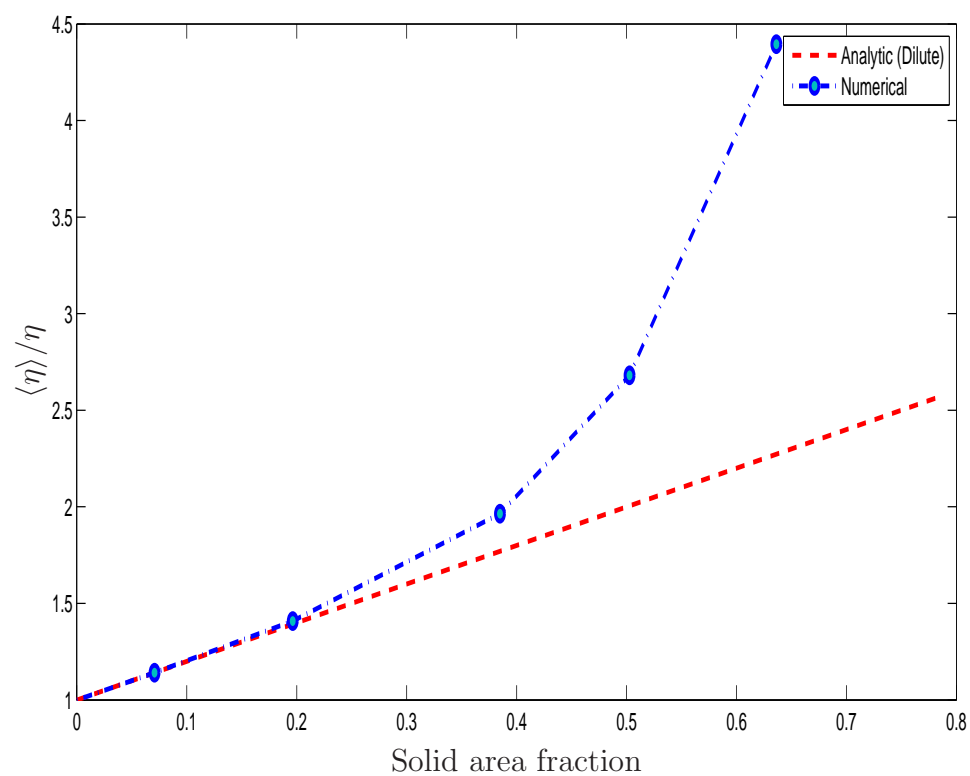


Figure 6.15: Example 3 (shear suspension): Computed bulk viscosity. Analytic results for the dilute case are also included.

## 6.5 Concluding remarks

In this chapter, a new computational procedure based on 1D-IRBFNs is developed for the simulation of 2D particulate flows under simple shear conditions. Sliding bi-periodic frames are applied to reduce the large domain to a small one. For the fluid component, the governing equations are taken in the stream-function - vorticity formulation and the multiply-connected domain is simply discretised using a Cartesian grid. For the particle component, a new efficient way, based on direct point-wise calculations rather than line/surface integrals, is proposed to compute the angular velocity. Three examples concerning sliding bi-periodic conditions, particle-like boundary conditions and shear particulate suspensions modelled by one particle in each frame are simulated successfully. The presently predicted bulk properties are in good agreement with those by the fictitious-domain/finite-element method.

# Chapter 7

## Conclusion

This chapter concludes the thesis. We will briefly summarise research contributions of the project and also present some suggestions for improvement.

## 7.1 Research contributions

The outcome of the present research project is the successful development of accurate and efficient numerical methods based on Cartesian grids and 1D-IRBFNs for the simulation of heat and viscous flows defined on two-dimensional multiply-connected domains. Significant applications of the proposed methods include the simulation of natural convection flows and the prediction of material properties of particulate flows. Research works in this project are briefly outlined below.

### **Development of 1D-IRBFNs for solving heat transfer problems in multiply-connected domains**

This research work has been presented in Chapter 2. A multiply-connected domain is simply discretised by a Cartesian grid, in which all boundaries are represented by sets of points that are generated by the intersections between the grid lines and the boundaries. We employ IRBFNs in one dimension on each grid line to approximate the field variable and point collocation to discretise the governing equation. Advantages of the proposed method include (i) very economical preprocessing (Cartesian grids for multiply-connected domains); (ii) high order of accuracy (RBFNs); (iii) avoidance of the reduction in convergence rate caused by differentiation (integral formulation); (iv) accurate imposition of Neumann boundary conditions (integration constants); and (v) achievement of some degree of local approximation (IRBFNs in one dimension). The proposed method is validated successfully through the solution of second-order elliptic and parabolic equations. Numerical results show that high rates of convergence with respect to grid refinement are obtained and condition numbers of the system matrix are relatively low, e.g. in the range of  $O(10^1)$  to  $O(10^3)$  for grids with densities of  $12 \times 12$  to  $62 \times 62$ , respectively.

### **Development of 1D-IRBFNs for discretising the stream-function -**

**vorticity ( $\psi - \omega$ ) formulation in multiply-connected domains**

This research work has been presented in Chapter 3. The Navier-Stokes equations are employed in the  $\psi - \omega$  formulation. We devise a new formula to compute a boundary condition for  $\omega$  on an irregular boundary. It should be emphasised that the boundary vorticity formula requires information about  $\psi$  on one grid line only. The accuracy of the proposed technique is demonstrated through several linear and non-linear problems, including natural convection in annuli between circular-circular and square-circular cylinders. Results obtained by the present 1D-IRBFN technique are compared well with numerical data available in the literature.

**Development of 1D-IRBFNs for discretising the stream-function ( $\psi$ ) formulation in multiply-connected domains**

This research work has been presented in Chapter 4. The Navier-Stokes equations are employed in the  $\psi$  formulation. We employ 1D-IRBFNs of order 4 and utilise the integral constants to incorporate double boundary conditions into the approximations. Formulas for computing mixed derivatives in irregular regions using 1D-IRBFNs are derived in the Cartesian system. We use the condition that the pressure is a single-valued function of position to find the values of  $\psi$  at inner boundaries. To verify the proposed technique, simulations of buoyancy flows in several annuli of various shapes are carried out. High Rayleigh-number solutions are achieved and they are in good agreement with previously published numerical data.

**Incorporation of 1D-IRBFNs into the domain embedding framework**

This research work has been presented in Chapter 5. The multiply-connected domain is now transformed into a simply-connected one. Solutions over interior holes are assumed to be represented by third-order polynomials. These polynomials are constructed to satisfy the boundary conditions. Several boundary-

value and initial-value problems are considered. Preliminary results indicate that this method is more suitable for the handling of problems with moving interior holes.

### **Application of 1D-IRBFNs for the prediction of material properties**

This research work has been presented in Chapter 6, which seems to be a first RBFN report on the prediction of macro properties of particulate suspensions. The concept of sliding bi-periodic frames is adopted. We impose sliding bi-periodic boundary conditions in the collocation form and use a direct point-wise way to calculate the angular velocity of a rigid particle in a reference frame. Bulk properties are predicted numerically and they agree well with those by the finite-element method.

## **7.2 Suggested work**

The following works are suggested for possible further developments

- The 1D-IRBFN discretisation methods lead to matrices that are not as sparse as those yielded through FDMs and FVMs. To improve the sparseness of the matrix, one possible way is to introduce domain decompositions into the methods.
- The 1D-IRBFN boundary fitted methods are presently developed for the simulation of 2D fluid flows governed by the  $\psi - \omega$  and  $\psi$  formulations. Extension of the methods to the discretisation of the velocity - pressure ( $\mathbf{u} - p$ ) or velocity - vorticity ( $\mathbf{u} - \omega$ ) formulations is possible. Such  $\mathbf{u} - p$  and  $\mathbf{u} - \omega$  formulations are known to suit 3D problems.
- The 1D-IRBFN domain embedding techniques are seen to be more efficient in solving multiply-connected domain problems with moving interior boundaries (e.g. particulate suspensions). More accurate imposition

---

of the inner boundary conditions can be achieved by using T-splines and infinitely smooth functions over fictitious subregions.

- 1D-IRBFNs are presently formulated for the direct simulation of particulate shear flows modelled by one particle in a reference frame. Extension of this formulation to a more sophisticated model, i.e. two or more particles in a reference frame, is possible. In this case, one needs to pay extra attention to deal with collision among rigid particles.

# References

- Aidun, C. K. and Lu, Y. (1995). Lattice Boltzmann simulation of solid particles suspended in fluid, *Journal of Statistical Physics* **81**(1-2): 49–61.
- Aidun, C. K., Lu, Y. and Ding, E. (1998). Direct analysis of particulate suspensions with inertia using the discrete Boltzmann equation, *Journal of Fluid Mechanics* **373**: 287–311.
- Anderson, P. D., Keestra, B. J. and Hulsen, M. A. (2006). On the stream function-vorticity formulation in sliding bi-period frames: Application to bulk behavior for polymer blends, *Journal of Computational Physics* **212**: 268–287.
- Beatson, R. K., Cherrie, J. B. and Mouat, C. T. (1999). Fast fitting of radial basis functions: Methods based on preconditioned GMRES iteration, *Advances in Computational Mathematics* **11**(2-3): 253–270.
- Bernal, F. and Kindelan, M. (2007). RBF meshless modeling of non-Newtonian Hele-Shaw flow, *Engineering Analysis with Boundary Elements* **31**(10): 863–874.
- Bert, C. W. and Malik, M. (1996). Differential quadrature method in computational mechanics: A review, *Applied Mechanics Reviews* **49**(1): 1–27.
- Bertoluzza, S., Ismail, M. and Maury, B. (2005). *The Fat Boundary Method: Semi-Discrete Scheme and Some Numerical Experiments*, Vol. 40 of *Lecture Notes in Computational Science and Engineering*, Springer Berlin Heidelberg.

- Beskos, D. E. (1997). Boundary element methods in dynamic analysis: Part II (1986-1996), *Applied Mechanics Reviews* **50**(3): 149–197.
- Brown, D., Ling, L., Kansa, E. J. and Levesley, J. (2005). On approximate cardinal preconditioning methods for solving PDEs with radial basis functions, *Engineering Analysis with Boundary Elements* **29**(4): 343–353.
- Buffat, M. and Penven, L. L. (2010). A spectral fictitious domain method with internal forcing for solving elliptic PDEs, *Journal of Computational Physics* **In Press**: –.
- Calhoun, D. (2002). A Cartesian grid method for solving the two-dimensional streamfunction-vorticity equations in irregular regions, *Journal of Computational Physics* **176**(2): 231–275.
- Chen, W., Ye, L. and Sun, H. (2010). Fractional diffusion equations by the Kansa method, *Computers and Mathematics with Applications* **59**(5): 1614–1620.
- Chinchapatnam, P., Djidjeli, K. and Nair, P. (2007). Domain decomposition for time-dependent problems using radial based meshless methods, *Numerical Methods for Partial Differential Equations* **23**: 38–59.
- Chinchapatnam, P., Djidjeli, K., Nair, P. and Tan, M. (2009). A compact RBF-FD based meshless method for the incompressible Navier-Stokes equations, *Proceedings of the Institution of Mechanical Engineers Part M: Journal of Engineering for the Maritime Environment* **223**(3): 275–290.
- Conn, A. R., Gould, N. I. M. and Toint, P. L. (2000). *Trust-Region Methods (MPS-SIAM Series on Optimization)*, Society for Industrial Mathematics.
- D’Avino, G., Maffettone, P. L., Hulsen, M. A. and Peters, G. W. M. (2008). Numerical simulation of planar elongational flow of concentrated rigid particle suspensions in a viscoelastic fluid, *Journal of Non-Newtonian Fluid Mechanics* **150**: 65–79.

- de Vahl Davis, G. (1983). Natural convection of air in a square cavity: a benchmark numerical solution, *International Journal for Numerical Methods in Fluids* **3**: 249–264.
- Demirdzic, I. and Peric, M. (1990). Finite volume method for prediction of fluid flow in arbitrarily shaped domains with moving boundaries, *International Journal for Numerical Methods in Fluids* **10**(7): 771–790.
- Ding, H., Shu, C., Yeo, K. S. and Lu, Z. L. (2005). Simulation of natural convection in eccentric annuli between a square outer cylinder and a circular inner cylinder using local MQ-DQ method, *Numerical Heat Transfer, Part A: Applications* **47**(3): 291–313.
- Ding, H., Shu, C., Yeo, K. and Xu, D. (2006). Numerical computation of three-dimensional incompressible viscous flows in the primitive variable form by local multiquadric differential quadrature method, *Computer Methods in Applied Mechanics and Engineering* **195**(7-8): 516–533.
- Divo, E. and Kassab, A. (2008). Localized meshless modeling of natural-convective viscous flows, *Numerical Heat Transfer, Part B: Fundamentals* **53**(6): 487–509.
- Divo, E. and Kassab, A. J. (2005). A meshless method for conjugate heat transfer problems, *Engineering Analysis with Boundary Elements* **29**(2): 136 – 149.
- Divo, E. and Kassab, A. J. (2006). Iterative domain decomposition meshless method modeling of incompressible viscous flows and conjugate heat transfer, *Engineering Analysis with Boundary Elements* **30**(6): 465–478.
- Divo, E. and Kassab, A. J. (2007). An efficient localized radial basis function meshless method for fluid flow and conjugate heat transfer, *Journal of Heat Transfer* **129**(2): 124–136.

- Driscoll, T. A. and Fornberg, B. (2002). Interpolation in the limit of increasingly flat radial basis functions, *Computers and Mathematics with Applications* **43**: 413–422.
- Duster, A., Parvizian, J., Yang, Z. and Rank, E. (2008). The finite cell method for three-dimensional problems of solid mechanics, *Computer Methods in Applied Mechanics and Engineering* **197**(45-48): 3768 – 3782.
- Erhart, K. J., Gerace, S. A., Divo, E. A. and Kassab, A. J. (2010). An RBF interpolated generalized finite difference meshless method for compressible turbulent flows, *ASME International Mechanical Engineering Congress and Exposition, Proceedings*, Vol. 9, pp. 571–581.
- Fasshauer, G. (2007). *Meshfree Approximation Methods with Matlab*, Interdisciplinary Mathematical Sciences, World Scientific Publishers.
- Feng, J., Hu, H. H. and Joseph, D. D. (1994a). Direct simulation of initial value problems for the motion of solid bodies in a Newtonian fluid. Part 1: Sedimentation, *Journal of Fluid Mechanics* **261**: 95–134.
- Feng, J., Hu, H. H. and Joseph, D. D. (1994b). Direct simulation of initial value problems for the motion of solid bodies in a Newtonian fluid. Part 2: Couette and Poiseuille flows, *Journal of Fluid Mechanics* **277**: 271–301.
- Fornberg, B. (1998). *A Practical Guide to Pseudospectral Methods*, Cambridge University Press.
- Franke, R. (1982). Scattered data interpolation: Tests of some method, *Mathematics of Computation* **38**: 181–200.
- Gerace, S., Erhart, K., Divo, E. and Kassab, A. (2009). Local and virtual RBF meshless method for high-speed flows, *WIT Transactions on Modelling and Simulation* **49**: 83–94.

- Ghosh, S., Hossain, M. and Matthaeus, W. H. (1993). The application of spectral methods in simulating compressible fluid and magnetofluid turbulence, *Computer Physics Communications* **74**(1): 18–40.
- Glakpe, E. K., Watkins, C. B. and Cannon, J. N. (1986). Constant heat flux solutions for natural convection between concentric and eccentric horizontal cylinders, *Numerical Heat Transfer: Part B: Fundamentals* **10**: 279–295.
- Glowinski, R. (2008). *Lectures on Numerical Methods for Non-Linear Variational Problems*, Springer.
- Glowinski, R., Pan, T. W. and Periaux, J. (1998). Distributed Lagrange multiplier methods for incompressible viscous flow around moving rigid bodies, *Computer Methods in Applied Mechanics and Engineering* **151**(1-2): 181–194.
- Glowinski, R., Pan, T.-W. and Piaux, J. (1994). A fictitious domain method for external incompressible viscous flow modeled by Navier-Stokes equations., *Computer Methods in Applied Mechanics and Engineering* **112**: 133–148.
- Harlow, F. H. and Welch, J. E. (1965). Numerical calculation of time-dependent viscous incompressible flow of fluid with free surface, *Physics of Fluids* **8**(12): 2182–2189.
- Haykin, S. (1998). *Neural networks: a comprehensive foundation*, Prentice Hall.
- Ho-Minh, D., Mai-Duy, N. and Tran-Cong, T. (2009). A Galerkin-RBF approach for the streamfunction-vorticity-temperature formulation of natural convection in 2D enclosed domains, *CMES: Computer Modeling in Engineering & Sciences* **44**(3): 219–248.
- Hortmann, M., Peric, M. and Scheuerer, G. (1990). Finite volume multigrid prediction of laminar natural convection. Bench-mark solutions, *International Journal for Numerical Methods in Fluids* **11**(2): 189–207.
- Hribersek, M. and Skerget, L. (1999). Fast boundary-domain integral algorithm

- for the computation of incompressible fluid flow problems, *International Journal for Numerical Methods in Fluids* **31**: 891–907.
- Hu, H. H. (1995). Motion of a circular cylinder in a viscous liquid between parallel plates, *Theoretical and Computational Fluid Dynamics* **7**: 441–455.
- Hu, H. H. (1996). Direct simulation of flows of solid-liquid mixtures, *International Journal of Multiphase Flow* **22**(2): 335–352.
- Hu, H. H., Joseph, D. D. and Crochet, M. J. (1992). Direct simulation of fluid particle motions, *Theoretical and Computational Fluid Dynamics* **3**: 285–306.
- Hu, H. H., Patankar, N. A. and Zhu, M. Y. (2001). Direct numerical simulations of fluid-solid systems using the arbitrary Lagrangian-Eulerian technique, *Journal of Computational Physics* **169**(2): 427–462.
- Hu, H. Y., Chen, J. S. and Hu, W. (2004). Weighted radial basis collocation method for boundary value problems, *International Journal for Numerical Methods in Engineering* **69**(13): 2736–2757.
- Huang, P. Y., Feng, J., Hu, H. H. and Joseph, D. D. (1997). Direct simulation of the motion of solid particles in Couette and Poiseuille flows of viscoelastic fluids, *Journal of Fluid Mechanics* **343**: 73–94.
- Huang, P. Y., Hu, H. H. and Joseph, D. D. (1998). Direct simulation of the sedimentation of elliptic particles in Oldroyd-B fluids, *Journal of Fluid Mechanics* **362**: 297–325.
- Husain, S., Floryan, J. and Szumbariski, J. (2009). Over-determined formulation of the immersed boundary conditions method, *Computer Methods in Applied Mechanics and Engineering* **199**(1-4): 94 – 112.
- Hwang, W. R., Hulsen, M. A. and Meijer, H. E. H. (2004). Direct simulation of particle suspensions in sliding bi-periodic frames, *Journal of Computational Physics* **194**: 742–772.

- Issa, R. I. (1986). Solution of the implicitly discretised fluid flow equations by operator-splitting, *Journal of Computational Physics* **62**: 40–65.
- Ito, K., Lai, M. C. and Li, Z. (2009). A well-conditioned augmented system for solving Navier-Stokes equations in irregular domains, *Journal of Computational Physics* **228**(7): 2616–2628.
- Kaminski, D. A. and Prakash, C. (1986). Conjugate natural convection in a square enclosure: Effect of conduction in one of the vertical walls, *International Journal for Heat and Mass Transfer* **29**(12): 1979–1988.
- Kansa, E. J. (1990a). Multiquadrics- A scattered data approximation scheme with applications to computational fluid-dynamics-I. surface approximations and partial derivative estimates, *Computers and Mathematics with Applications* **19**(8/9): 127–145.
- Kansa, E. J. (1990b). Multiquadrics- A scattered data approximation scheme with applications to computational fluid-dynamics-II. solutions to parabolic, hyperbolic and elliptic partial differential equations, *Computers and Mathematics with Applications* **19**(8/9): 147–161.
- Kitagawa, K., Wrobel, L. C., Brebbia, C. A. and Tanaka, M. (1988). A boundary element formulation for natural convection problems, *International Journal for Numerical Methods in Fluids* **8**: 139–149.
- Kosec, G. and Šarler, B. (2008a). Local RBF collocation method for Darcy flow, *CMES: Computer Modeling in Engineering & Sciences* **25**(3): 197–207.
- Kosec, G. and Šarler, B. (2008b). Solution of thermo-fluid problems by collocation with local pressure correction, *International Journal of Numerical Methods for Heat & Fluid Flow* **18**(7/8): 868–882.
- Kosec, G. and Šarler, B. (2009). Solution of phase change problems by collocation with local pressure correction, *CMES: Computer Modeling in Engineering & Sciences* **47**(2): 191–216.

- Kuehn, T. and Goldstein, R. (1976). An experimental and theoretical study of natural convection in the annulus between horizontal concentric cylinders, *Journal of Fluids Mechanics* **74**(4): 695–719.
- Ladd, A. J. C. (1994). Numerical simulations of particulate suspensions via a discretized Boltzmann equation. I. Theoretical foundation, *Journal of Fluid Mechanics* **271**: 285–309.
- Lan, C. W. (1994). Newton’s method for solving heat transfer, fluid flow and interface shapes in a floating molten zone, *International Journal for Numerical Methods in Fluids* **19**(1): 41–65.
- Layton, W. and Lenferink, W. (1995). Two-level Picard and modified Picard methods for the Navier-Stokes equations, *Applied Mathematics and Computation* **69**(2-3): 263–274.
- Le-Cao, K., Mai-Duy, N. and Tran-Cong, T. (2009). An effective integrated-RBFN Cartesian-grid discretization for the stream function-vorticity-temperature formulation in nonrectangular domains, *Numerical Heat Transfer, Part B: Fundamentals* **55**(6): 480–502.
- Le, H. and Moin, P. (1991). An improvement of fractional step methods for the incompressible Navier-Stokes equations, *Journal of Computational Physics* **92**(2): 369–379.
- Lees, A. W. and Edwards, S. F. (1972). The computer study of transport processes under extreme conditions, *Journal of Physics C: Solid State Physics* **5**(15): 1921.
- LeQuéré, P. (1991). Accurate solutions to the square thermally driven cavity at high Rayleigh number, *Computers & Fluids* **20**(1): 29–41.
- Lewis, E. (1979). Steady flow between a rotating circular cylinder and fixed square cylinder, *Journal of Fluid Mechanics* **95**: 497–513.

- Li, J. and Chen, C. S. (2003). Some observations on unsymmetric radial basis function collocation methods for convection-diffusion problems, *International Journal for Numerical Methods in Engineering* **57**(8): 1085–1094.
- Li, J. and Hon, Y. (2004). Domain decomposition for radial basis meshless methods, *Numerical Methods for Partial Differential Equations* **20**: 450–462.
- Li, K., Huang, Q., Wang, J. and Lin, L. (2011). An improved localized radial basis function meshless method for computational aeroacoustics, *Engineering Analysis with Boundary Elements* **35**(1): 47 – 55.
- Liao, C. C., Chang, Y. W., Lin, C. A. and McDonough, J. M. (2010). Simulating flows with moving rigid boundary using immersed-boundary method, *Computers & Fluids* **39**(1): 152–167.
- Libre, N. A., Emdadi, A., Rahimian, E. K. M. and Shekarchi, M. (2008). A stabilized RBF collocation scheme for Neumann type boundary value problems, *CMES: Computer Modeling in Engineering & Sciences* **24**(1): 61–80.
- Ling, L. and Kansa, E. (2005). A least-squares preconditioner for radial basis functions collocation methods, *Advances in Computational Mathematics* **23**(1-2): 31–54.
- Madych, W. R. and Nelson, S. A. (1988). Multivariate interpolation and conditionally positive definite functions, *Approximation Theory and its Applications* **4**: 77–89.
- Mai-Duy, N. (2004). Indirect RBFN method with scattered points for numerical solution of PDEs., *CMES: Computer Modeling in Engineering & Sciences* **6**(2): 209–226.
- Mai-Duy, N., Le-Cao, K. and Tran-Cong, T. (2008). A Cartesian grid technique based on one-dimensional integrated radial basis function networks for natural convection in concentric annuli, *International Journal for Numerical Methods in fluids* **57**: 1709–1730.

- Mai-Duy, N., See, H. and Tran-Cong, T. (2009). A spectral collocation technique based on integrated Chebyshev polynomials for biharmonic problems in irregular domains, *Applied Mathematical Modelling* **33**(1): 284 – 299.
- Mai-Duy, N. and Tanner, R. I. (2005). Solving high order partial differential equations with indirect radial basis function networks, *International Journal for Numerical Methods in Engineering* **63**: 1636–1654.
- Mai-Duy, N. and Tran-Cong, T. (2001a). Numerical solution of differential equations using multiquadric radial basic function networks, *Neural Networks* **14**: 185–199.
- Mai-Duy, N. and Tran-Cong, T. (2001b). Numerical solution of Navier-Stokes equations using multiquadric radial basis function networks, *International Journal for Numerical Methods in Fluids* **37**(1): 65–86.
- Mai-Duy, N. and Tran-Cong, T. (2003). Approximation of function and its derivatives using radial basis function networks, *Applied Mathematical Modelling* **27**: 197–220.
- Mai-Duy, N. and Tran-Cong, T. (2007). A Cartesian-grid collocation method based on radial-basis-function networks for solving PDEs in irregular domains, *Numerical Methods for Partial Differential Equations* **23**(5): 1192–1210.
- Mai-Duy, N. and Tran-Cong, T. (2008). A multidomain integrated-radial-basis-function collocation method for elliptic problems, *Numerical Methods for Partial Differential Equations* **24**(5): 1301–1320.
- Mai-Duy, N. and Tran-Cong, T. (2010). A simple and effective preconditioner for integrated-rbf-based cartesian-grid schemes, *International Conference on Computational & Experimental Engineering and Sciences* **14**(2): 51–56.
- Manzari, M. T. (1999). An explicit finite element algorithm for convection heat transfer problems, *International Journal of Numerical Methods for Heat and Fluid Flow* **9**(8): 860–877.

- Marella, S., Krishnan, S., Liu, H. and Udaykumar, H. S. (2005). Sharp interface Cartesian grid method I: An easily implemented technique for 3D moving boundary computations, *Journal of Computational Physics* **210**(1): 1–31.
- Maury, B. (2001). A fat boundary method for the Poisson problem in a domain with holes, *Journal of Scientific Computing* **16**(3): 319–339.
- Michelli, C. A. (1986). Interpolation of scattered data: Distance matrices and conditionally positive definite functions, *Constructive Approximation* **2**(1): 11–22.
- Moukalled, F. and Acharya, S. (1996). Natural convection in the annulus between concentric horizontal circular and square cylinders, *Journal of Thermophysics and Heat Transfer* **10**(3): 524–531.
- Noye, B. J. and Tan, H. H. (1989). Finite difference methods for solving the two-dimensional advection-diffusion equation, *International Journal for Numerical Methods in Fluids* **9**(1): 75–98.
- Orsini, P., Power, H., Lees, M. and Morvan, H. (2009). A control volume radial basis function techniques for the numerical simulation of saturated flows in semi-confined aquifer, *Transport in Porous Media* **79**(2): 171–196.
- Ostrach, S. (1988). Natural convection in enclosures, *Journal of Heat Transfer* **110**: 1175–1190.
- Paik, S., Nguyen, H. D. and Chung, J. N. (1994). A spectral method for unsteady flow and heat transfer past a spherical droplet: primitive variable formulation, *International Journal of Computational Fluid Dynamics*, **3**(3): 171–192.
- Park, J. and Sandberg, I. W. (1991). Universal approximation using radial basis function networks, *Neural Computation* **3**(2): 246–257.
- Park, J. and Sandberg, I. W. (1993). Approximation and radial basis function networks, *Neural Computation* **5**: 305–316.

- Parvizian, J., Duster, A. and Rank, E. (2007). Finite cell method h - and p -extension for embedded domain problems in solid mechanics, *Computational Mechanics* **41**: 121–133.
- Patankar, N. A., Singh, P., Joseph, D. D., Glowinski, R. and Pan, T. W. (2000). A new formulation of the distributed Lagrange multiplier/ fictitious domain method for particulate flows, *International Journal Multiphase Flow* **26**: 1509–1524.
- Patankar, S. V. and Spalding, D. B. (1972). A calculation procedure for heat, mass and momentum transfer in three-dimensional parabolic flows, *International Journal of Heat and Mass Transfer* **15**: 1787–1806.
- Pepper, D. W. and Sarler, B. (2005). Application of meshless methods for thermal analysis, *Strojnicki Vestnik/Journal of Mechanical Engineering* **51**(7-8): 476–483.
- Peyret, R. (2002). *Spectral Methods for Incompressible Viscous Flow*, Vol. 148 of *Applied Mathematical Sciences*, New York Springer-Verlag.
- Phan-Thien, N. and Kim, S. (1994). *Microstructures in Elastic media principles and computational methods*, Oxford University Press.
- Poggio, T. and Girosi, F. (1990). Networks for approximation and learning, *Proceedings of the IEEE* **78**: 1481–1497.
- Power, H. and Barraco, V. (2002). A comparison analysis between unsymmetric and symmetric radial basis function collocation methods for the numerical solution of partial differential equations, *Computers and Mathematics with Applications* **43**(3-5): 551–583.
- Power, H., Hernandez, A. and Rocca, A. L. (2007). Non-overlapping domain decomposition scheme for the symmetric radial basis function meshless approach with double collocation at the sub-domain interfaces, *WIT Transactions on Modelling and Simulation* **44**: 13–22.

- Prasad, V. R., Reddy, N. B., Muthucumaraswamy, R. and Vasu, B. (2011). Finite difference analysis of radiative free convection flow past an impulsively started vertical plate with variable heat and mass flux, *Journal of Applied Fluid Mechanics* **4**(1): 59–68.
- Roache, P. J. (1998). *Fundamentals of Computational Fluid Dynamics*, Hermosa Publishers.
- Roque, C. M. C., Ferreira, A. J. M. and Jorge, R. M. N. (2010). An optimized shape parameter radial basis function formulation for composite and sandwich plates using higher order formulations, *Journal of Sandwich Structures and Materials* **12**(3): 279–306.
- Sadeghirad, A. and Kani, I. M. (2009). Modified equilibrium on line method for imposition of Neumann boundary conditions in meshless collocation methods, *Communications in Numerical Methods in Engineering* **25**(2): 147–171.
- Sahin, M. and Wilson, H. J. (2007). A semi-staggered dilation-free finite volume method for the numerical solution of viscoelastic fluid flows on all-hexahedral elements, *Journal of Non-Newtonian Fluid Mechanics* **147**(1-2): 79–91.
- Sammouda, H., Belghith, A. and Surry, C. (1999). Finite element simulation of transient natural convection of low-Prandtl-number fluids in heated cavity, *International Journal of Numerical Methods for Heat and Fluid Flow* **9**(5): 612–624.
- Šarler, B. (2005). A radial basis function collocation approach in computational fluid dynamics, *CMES: Computer Modeling in Engineering & Sciences* **7**(2): 185–194.
- Šarler, B. (2009). Solution of potential flow problems by the modified method of fundamental solutions: Formulations with the single layer and the double layer fundamental solutions, *Engineering Analysis with Boundary Elements* **33**(12): 1374–1382.

- Šarler, B., Jelic, N., Kovacevic, I., Lakner, M. and Perko, J. (2006). Axisymmetric multiquadrics, *Engineering Analysis with Boundary Elements* **30**(2): 137 – 142.
- Šarler, B., Kosec, G., Lorbicka, A. and Vertnik, R. (2010). A meshless approach in solution of multiscale solidification modeling, *Materials Science Forum* **649**: 211–216.
- Šarler, B., Perko, J. and Chen, C. S. (2004). Radial basis function collocation method solution of natural convection in porous media, *International Journal of Numerical Methods for Heat and Fluid Flow* **14**(2): 187–212.
- Šarler, B. and Vertnik, R. (2006). Meshfree explicit local radial basis function collocation method for diffusion problems, *Computers and Mathematics with Applications* **51**(8 SPEC. ISS.): 1269–1282.
- Schaback, R. (2005). Multivariate interpolation by polynomials and radial basis functions, *Constructive Approximation* **21**: 293–317.
- Shinn, A., Goodwin, M. and Vanka, S. (2009). Immersed boundary computations of shear- and buoyancy-driven flows in complex enclosures, *International Journal of Heat and Mass Transfer* **52**(17-18): 4082 – 4089.
- Shu, C. (1999). Application of differential quadrature method to simulate natural convection in a concentric annulus, *International Journal for Numerical Methods in Fluids* **30**: 977–993.
- Shu, C., Ding, H. and Yeo, K. (2003). Local radial basis function-based differential quadrature method and its application to solve two-dimensional incompressible Navier-Stokes equations, *Computer Methods in Applied Mechanics and Engineering* **192**(7-8): 941–954.
- Shu, C. and Richards, B. E. (1992). Application of generalized differential quadrature to solve two-dimensional incompressible Navier-Stokes equations, *International Journal for Numerical Methods in Fluids* **15**(7): 791–798.

- Shu, C. and Wu, Y. L. (2002). Domain-free discretization method for doubly connected domain and its application to simulate natural convection in eccentric annuli, *Computer Methods in Applied Mechanics and Engineering* **191**(17-18): 1827–1841.
- Shu, C., Yao, Q., Yeo, K. S. and Zhu, Y. D. (2002). Numerical analysis of flow and thermal fields in arbitrary eccentric annulus by differential quadrature method, *Journal of Heat and Mass Transfer* **38**: 597–608.
- Shu, C. and Zhu, Y. D. (2002). Efficient computation of natural convection in a concentric annulus between an outer square cylinder and an inner circular cylinder, *International Journal for Numerical Methods in Fluids* **38**: 429–445.
- Singh, P., Joseph, D. D., Hesla, T. I., Glowinski, R. and Pan, T. W. (2000). A distributed Lagrange multiplier/fictitious domain method for viscoelastic particulate flows, *Journal of Non-Newtonian Fluid Mechanics* **91**: 165–188.
- Siraj-ul-Islam, Aziz, I. and Šarler, B. (2010). The numerical solution of second-order boundary-value problems by collocation method with the Haar wavelets, *Mathematical and Computer Modelling* **52**(9-10): 1577 – 1590.
- Siraj-ul-Islam, Khattak, A. J. and Tirmizi, I. A. (2008). A meshfree method for numerical solution of KdV equation, *Engineering Analysis with Boundary Elements* **32**(10): 849–855.
- Skouras, E., Bourantas, G., Loukopoulos, V. and Nikiforidis, G. (2011). Truly meshless localized type techniques for the steady-state heat conduction problems for isotropic and functionally graded materials, *Engineering Analysis with Boundary Elements* **35**(3): 452 – 464.
- Sugiyama, K., Ii, S., Takeuchi, S., Takagi, S. and Matsumoto, Y. (2011). A full Eulerian finite difference approach for solving fluid-structure coupling problems, *Journal of Computational Physics* **230**(3): 596–627.

- Tran-Cong, T. and Phan-Thien, N. (1989). Stokes problems of multiparticle systems: A numerical method for arbitrary flows, *Physics of Fluids A* **1**(3): 453–461.
- Udaykumar, H. S., Krishnan, S. and Marella, S. V. (2009). Adaptively refined, parallelised sharp interface Cartesian grid method for three-dimensional moving boundary problems, *International Journal of Computational Fluid Dynamics* **23**(1): 1–24.
- Udaykumar, H. S., Mittal, R., Rampunggoon, P. and Khanna, A. (2001). A sharp interface Cartesian grid method for simulating flows with complex moving boundaries, *Journal of Computational Physics* **174**(1): 345 – 380.
- Vertnik, R. and Šarler, B. (2006). Meshless local radial basis function collocation method for convective-diffusive solid-liquid phase change problems, *International Journal of Numerical Methods for Heat and Fluid Flow* **16**(5): 617–640.
- Vertnik, R., Založnik, M. and Šarler, B. (2006). Solution of transient direct-chill aluminium billet casting problem with simultaneous material and interphase moving boundaries by a meshless method, *Engineering Analysis with Boundary Elements* **30**(10): 847–855.
- Vos, P., van Loon, R. and Sherwin, S. (2008). A comparison of fictitious domain methods appropriate for spectral/hp element discretisations, *Computer Methods in Applied Mechanics and Engineering* **197**(25-28): 2275 – 2289.
- Wan, D. and Turek, S. (2006). Direct numerical simulation of particulate flow via multigrid FEM techniques and the fictitious boundary method, *International Journal of Numerical Method Fluids* **51**: 531–566.
- Wan, D. and Turek, S. (2007). Fictitious boundary and moving mesh methods for the numerical simulation of rigid particulate flows, *Journal of Computational Physics* **222**(1): 28–56.

- Wendland, H. (1995). Piecewise polynomial, positive definite and compactly supported radial functions of minimal degree, *Advances in Computational Mathematics* **4**(1): 389–396.
- Wendland, H. (1998). Error estimates for interpolation by compactly supported radial basis functions of minimal degree, *Journal of Approximation Theory* **93**(2): 258 – 272.
- Wright, G. B. and Fornberg, B. (2006). Scattered node compact finite difference-type formulas generated from radial basis functions, *Journal of Computational Physics* **212**: 99–123.
- Wu, Y. L. and Liu, G. R. (2003). A meshfree formulation of local radial point interpolation method (LRPIM) for incompressible flow simulation, *Computational Mechanics* **30**(5-6): 355–365.
- Yao, G., Šarler, B. and Chen, C. (2011). A comparison of three explicit local meshless methods using radial basis functions, *Engineering Analysis with Boundary Elements* **35**(3): 600 – 609.
- Yu, Z. A. (2005). DLM/FD method for fluid / flexible-body interactions, *Journal of Computational Physics* **207**: 1–27.
- Yu, Z. and Shao, X. (2007). A direct-forcing fictitious domain method for particulate flows, *Journal of Computational Physics* **227**(1): 292–314.
- Yun-Xin, Z. and Yong-Ji, T. (2006). Meshless schemes for unsteady Navier-Stokes equations in vorticity formulation using radial basis functions, *Journal of Computational and Applied Mathematics* **192**(2): 328–338.
- Zahab, Z. E., Divo, E. and Kassab, A. (2009). A localized collocation meshless method (LCMM) for incompressible flows CFD modeling with applications to transient hemodynamics, *Engineering Analysis with Boundary Elements* **33**(8-9): 1045 – 1061.

- 
- Zerroukat, M., Power, H. and Chen, C. (1998). A numerical method for heat transfer problems using collocation and radial basis functions, *International Journal for Numerical Methods in Engineering* **42**: 1263–1728.